

THE UNIVERSITY
OF BIRMINGHAM

INCOHERENT PROCESSING OF SYNTHETIC APERTURE SONAR

by

KAE YEET, FOO

A thesis submitted to the School of Engineering
of the University of Birmingham for the degree of
DOCTOR OF PHILOSOPHY

Dept. of Electronic, Electrical and Computer Engineering
School of Engineering
The University of Birmingham
Edgbaston, Birmingham, B15 2TT, U.K.
June, 2004.

UNIVERSITY OF
BIRMINGHAM

University of Birmingham Research Archive

e-theses repository

This unpublished thesis/dissertation is copyright of the author and/or third parties. The intellectual property rights of the author or third parties in respect of this work are as defined by The Copyright Designs and Patents Act 1988 or as modified by any successor legislation.

Any use made of information contained in this thesis/dissertation must be in accordance with that legislation and must be properly acknowledged. Further distribution or reproduction in any format is prohibited without the permission of the copyright holder.

Acknowledgements

This research work is jointly sponsored and funded by the Overseas Research Students (ORS) Awards Scheme and the University of Birmingham, United Kingdom.

I would like to convey my highest gratitude to both supervisors, Mr. Phil Atkins and Dr. Tim Collins. Throughout the entire course of this research, they have offered timely guidance, unfailing support, and motivational inspirations.

Special thanks also go to Mr. David Prowse from QinetiQ (formerly the Defence Evaluation Research Agency, DERA) in Winfrith, UK, for carrying out the sea-trials and providing the trial data, without which the accomplishments of this research work would not have been possible.

Much appreciation goes to my fellow colleague and friends in the department for their great company and helping hand.

Finally, I would like to thank my family for their unfailing encouragement and support, and especially my wife, Elaine, for her understanding, patience and excellent cooking!

Abstract

The technique of synthetic aperture imaging is well applied in radar to produce images with high along-track resolution. However, when applied in sonar imaging, maintaining phase coherence across the length of the synthetic aperture had proven to be the greatest challenge due to the relatively much slower speed of sound waves and the instability inherent in an underwater towed platform.

This work aims to study, analytically and experimentally, the potential of reconstructing synthetic aperture images, by the exact reconstruction algorithm in the time-domain, without the use of phase information. The absence of phase information results in images with a relatively lower along-track resolution. However, the benefits of hardware simplicity and higher mapping rate, not present with the use of side-scan sonar, are still enjoyed. In addition, greater flexibility and robustness is achieved as compared to a coherent synthetic aperture system. This is manifested in its resilience to path deviations, tolerance to sparse arrangement of elements in the aperture, and consequently higher achievable mapping rate.

Software simulations were performed to study the impact of key parameters on the performance of an incoherent synthetic aperture system. Concepts such as the point-target energy response and signal to self-noise ratio were formed, which led to the formulation of design methodologies and tools for such a system. A novel algorithm is introduced to address the problems of false targets and long processing time. A new bulk motion compensation method is presented for situations where large path deviations cause severe image degradation and compensation is necessary.

This technique, together with the algorithms developed in this work, was implemented with data from a sea-survey of the Aeolian Sky wreck. Results gave a positive indication of the theoretical frameworks established. This technique was then extended to achieve 3-D imaging capability. Results from laboratory tank trials that were carried out were encouraging, and led to the development of an original concept of incoherent synthetic aperture synthesis that is practical, robust, economical, and has 3-D imaging capability.

Table of Contents

Acknowledgements

Abstract

List of Figures

List of Acronyms

Chapter 1: Introduction **1**

1.1 Background.....1

1.2 Objectives.....2

1.3 Thesis Organisation.....3

1.4 Statement of Originality.....4

Chapter 2: Synthetic Aperture Sonar Background and Review **6**

2.1 The Concept of Synthetic Aperture.....6

2.2 Synthetic Aperture Sonar Developments.....10

2.2.1 In the Beginning

2.2.2 Medium Instabilities

2.2.3 Platform Instabilities

2.2.3.1 Coverate rate

2.2.3.2 Image degradation

2.3 Synthetic Aperture Sonar Processing 17

2.3.1 Cross-track Processing

2.3.2 Along-track Processing

2.4 Motion Estimation and Compensation.....23

2.5 Incoherent Synthetic Aperture Processing.....26

2.6 Conclusion.....28

Chapter 3: Incoherent Synthetic Aperture Sonar Processing **30**

3.1 Introduction.....30

3.2 Phase Removal.....30

3.3 Time-Domain Back-projection.....31

3.3.1 Coordinate Mapping

3.3.2 Image Reconstruction
3.3.3 Two way propagation distance in bi-static Configuration
3.3.4 Interpolation
3.3.5 Computational Complexity
3.3.6 Processing Gain
3.4 Pulse Design....39
3.5 Along-track Resolution 41
3.6 Dynamic Focussing....47
3.7 Self-noise....48
3.8 Grating Lobes....49
3.9 Tolerance to Motion Errors....50
3.10 SAS Imaging Modes....53
3.11 Weighting Function....54
3.12 Point-target Energy Response....58
3.13 Image Quality Benchmark....61
3.14 Design Considerations in Incoherent SAS Imaging....63
3.15 Core Advantages and Disadvantages of Incoherent SAS Processing....65
3.16 Conclusion....69

Chapter 4: Fast Reduced-Elements Back-projection 70

4.1 Introduction....70
4.2 Fast Reduced-Elements Back-projection (FREB)....71
4.3.1 The principle
4.3.2 The application
4.3 Analysis of FREB....74
4.4.1 Improvement of self-noise energy pattern
4.4.2 Reduction of processing time
4.4 Implications of FREB....82
4.5 Conclusion....83

Chapter 5: A Correlation-Based Bulk Motion Compensation Algorithm **85**

5.1 Introduction....85
5.2 Motion Errors....86
5.3 The Principle....89
5.4 The Estimation Algorithm....94
5.5 Simulation Example and Results....97
5.6 Discussion....100
5.7 Conclusion....102

Chapter 6: Sea Trials of a Bi-static, Time-Domain, Incoherent Synthetic Aperture Sonar **104**

6.1 Introduction....104
6.2 The Aeolian Sky Wreck....104
6.3 The Survey....105
6.4 Synthetic Aperture Processing....108
6.4.1 Raw image formation
6.4.2 Cross-track processing
6.4.3 Along-track processing
6.4.4 Analysis of results
6.5 Bi-static Processing....115
6.6 Conclusion....120

Chapter 7: Incoherent Synthetic Aperture Sonar 3-D Imaging with 2-D Synthetic Aperture **122**

7.1 Introduction....122
7.2 Beyond Linear Synthetic Aperture....123
7.3 Monostatic 2-D Synthetic Aperture....125
7.3.1 Concept and simulation
7.3.2 Laboratory tank trial
7.3.3 FREB algorithm with 2-D monostatic synthetic aperture
7.4 3-D Image Representation....133
7.4.1 The issue of dynamic detection

7.4.2 Moving averaging-window CFAR detector
7.4.3 Normalisation of incoherent SAS images
7.5 Multi-static 2-D Synthetic Aperture.....138
7.5.1 A practical concept
7.5.2 Point-target energy response of a multi-static planar synthetic aperture
7.5.3 Applying multi-static weightings
7.5.4 Laboratory tank trial
7.5.5 Analysis of results
7.6 Conclusion.....153

Chapter 8: Conclusions and Further Work 155

8.1 Key Conclusions.....155
8.2 Further Work.....159

References

Appendix A: Along-track Resolution of an Incoherent Synthetic Aperture

Appendix B: K.Y.Foo, P.R.Atkins and T.Collins, "Robust underwater imaging with fast broadband incoherent synthetic aperture sonar," *IEEE Proceedings of ICASSP-03*, vol. 5, pp. v17-v20, Apr. 2003.

Appendix C: K.Y.Foo, P.R.Atkins and T.Collins, "Sea Trials of a Bi-Static, Time-Domain, Incoherent Synthetic Aperture Sonar," *IEE Electronics Letter,* vol. 40, no. 5, pp. 341-343, 4th Mar 2004.

List of Acronyms

2-D – Two-dimensional

3-D – Three-dimensional

AUV – Autonomous Underwater Vehicle

CFAR – Constant False Alarm Rate

CPA – Closest Point of Approach

CPU – Central Processing Unit

FFT – Fast Fourier Transform

FREB – Fast Reduced-Element Back-projection

Matlab – Matrix Laboratory software developed by Mathworks Inc.

NASA – National Aeronautics and Space Administration, United States of America.

PFA – Probability of False Alarm

Q-factor – Quality factor

RADAR – Radio Detection and Ranging

RMS – Root Mean Square

SAR – Synthetic Aperture Radar

SAS – Synthetic Aperture Sonar

SEASAT – Sea satellite

SNR – Signal to Noise Ratio

SONAR – Sound Navigation and Ranging

Chapter 1

Introduction

1.1 Background of Synthetic Aperture

In the pursuit for a large antenna to detect and receive very weak radio signals from space, the idea of synthesizing, rather than building, a large antenna by using many spatially-varying samples first came to light in radio-astronomy. In 1951, Carl Wiley observed that a radar beam (in active radar) oblique to the radar platform velocity vector will return signals having frequency offset from the carrier frequency due to Doppler effect. He realised that the varying Doppler shift in echoes from a target made it possible to narrow the synthesized aperture's beamwidth by filtering [1].

Since then, synthetic aperture techniques quickly gained the interest of many in the radar community because they provided the means for high resolution imaging without the need to build enormous antenna. By the 1970s, the first spaceborne synthetic aperture radar carried by NASA's SEASAT satellite had already returned data needed to form high resolution images of land, ocean and ice surfaces.

As the radar community explores the potential of this technique, scientists in the sonar community ponder over its applicability in the underwater environment. Although the fundamental concepts are the same, the unique characteristics of the underwater acoustic environment give rise to several additional problems. An obvious difference is the fact that acoustic waves used in the underwater environment travel at only a small fraction of the speed of electromagnetic waves in air. At a mere speed of 1500 ms^{-1}, there is a great constraint on the inter-ping time interval to avoid along-track and cross-track ambiguities. Consequently, the achievable mapping rate is relatively low. On top of that, there is the difficulty in achieving full phase coherence in all echo returns over a reasonably large synthetic aperture due mainly to the instability of a tow platform. This would degrade the quality of the processed image.

Since the early 90s, many techniques have been proposed to deal with these two major constraints: to reliably increase achievable mapping rate and to reduce phase coherence errors. This often introduces greater complexity to the system such as the addition of inertial navigational systems.

In this thesis, incoherent synthetic aperture processing techniques and potentials are studied in detail. In the past, P.D.Heering [31] and G.Shippey [33] had proposed this scheme as an alternative processing technique to coherent SAS, in which phase information are removed before along-track (azimuth) integration is performed, hence removing the reliance on phase coherence. A brief review is given in section 2.5. However, none has yet studied this scheme in analytical detail, nor presented supporting trials and results that can more vividly describe its potential in overcoming some of the persisting constraints in the field of SAS imaging. Novel concepts to exploit the potential robustness available to incoherent SAS processing schemes are studied and presented here, with comparisons and evaluations of the necessary design and implementation criteria.

1.2 Objectives

The aim of this work is to study and investigate the features, properties and design criteria of an incoherent SAS system with the view of establishing its realistic potential for applications in underwater imaging, as well as addressing some of the issues prevalent in the implementation of SAS imaging.

The key objectives set out for this project are as below:

- Garner an appreciation of the current challenges facing the implementation of SAS imaging, and to gather familiarity with the work that has been carried out in this area.
- Research and derive the technical properties of an incoherent SAS system; its key design parameters; and to make comparisons of its advantages and limitations with a coherent SAS system.

- Develop techniques necessary for, as well as investigate the issues arising from, the practical implementation of an incoherent SAS system under realistic operating assumptions and environment.
- Consider the potential of incoherent SAS processing, in the light of its technical properties, in achieving 3-D imaging capabilities and to put forth a practical model for such a system.
- Perform trials to verify the proposed model.

1.3 Thesis Organisation

In chapter 2, the theoretical concept of a synthetic aperture is presented. It is followed by a review of the major developments and evolution of SAS technology. The constraints and challenges that face this technology today are discussed. Methods for the processing of SAS data are presented with emphasis on time-domain techniques. Motion errors and compensation algorithms for SAS images are introduced. This is then followed by the introduction to, and argument for, incoherent SAS techniques, emphasizing its potential in underwater imaging. Chapter 3 presents the technical properties of an incoherent SAS system, such as achievable resolution, processing gain, absence of grating lobes and the concept of self-noise. The key parameters in the design of such a system are identified. The algorithm for the processing model is put forth and discussions are made on issues of computational complexity and processing time.

A novel algorithm is developed and presented in chapter 4, and named as the Fast Reduced-Elements Back-projection (FREB). At the expense of a lower signal to self-noise ratio, a two-fold benefit is obtainable. The processing time can be significantly reduced and the image fidelity improved. In chapter 5, a motion compensation technique designed especially for a time-domain incoherent SAS system is proposed. The algorithm is described in detail and results from simulations examining its characteristics and limitations are presented.

A sea-trial was carried out to give a more accurate picture of the potential of an incoherent SAS system in underwater imaging. The details of the trial are described, along with comparisons of the results with incoherent processing, incoherent processing with the FREB algorithm, and coherent processing. The case for a single transducer, multiple hydrophones array as a practical choice for synthesis of linear apertures is made and hence the need to accommodate bi-static arrangements of elements in the synthetic aperture. The final chapter goes on to extend the capability of incoherent SAS processing in the area of 3-D imaging with synthetic apertures beyond the conventional linear form. A novel and practical concept is presented here. Other than extending the incoherent processing model to take account of an arbitrary multi-static synthetic aperture, there are also the details of trials carried out to study the proposed approach along with some interesting results.

1.4 Statement of Originality

This section outlines the key new and original contributions made by this work in the area of synthetic aperture sonar imaging. They are set out as below:

- The identification of loci of range-ambiguity plot as an approach that enables a quick, simple and effective analysis of the point-target energy response corresponding to an incoherent synthetic aperture (chapter 3).
- The development of the FREB algorithm specifically designed for application to an incoherent SAS system aimed at reducing processing time and improving image fidelity (chapter 4).
- The proposal of a bulk motion compensation technique that is based upon the matching of the range curvature function of a relatively stronger reference target in order to estimate and compensate for motion errors (chapter 5).
- The evaluation of the potential and practical capability of incoherent SAS processing via the undertaking of a sea trial within a wholly realistic environment and operating constraint (chapter 6)

- Presenting the necessity, in realistic scenarios, for the application of an element-dependent matched weighting function to obtain improvement in the signal-to-self-noise ratio (chapter 6 and 7).
- The proposal of a novel concept for the practical implementation of incoherent SAS processing in 3-D imaging, along with detailed trials and results (chapter 7).

Chapter 2

Synthetic Aperture Sonar Background and Review

2.1 The Concept of Synthetic Aperture

In a real-aperture system (Fig.2.1), given a signal frequency (and thus wavelength λ), the achievable beamwidth, θ_b (in radians), is inversely proportional to the physical dimension, D_p, of the transmitter that is oblique to the beam angle. In sonar, to achieve an azimuth resolution of 1m at a range of 100m from the transducer requires a beamwidth of 0.01rad. With a 10kHz signal, it would require a physical transducer with the size of 15m. Deploying a large and expensive transducer, or transducer array, is prohibitive in terms of cost and risk. Another obvious weakness of a beamforming system is the dependency of azimuth resolution on the range from the transducer.

The idea of synthetic aperture is based on synthesizing the aperture of a large transducer by making multiple transmissions on a pre-specified path so that its returns can be processed to achieve a beam comparable, in terms of resolution, to that of a large transducer. This is due to the fact that a large transmitting element need not be physically continuous but can be composed instead of many smaller elements placed at an appropriate distance from each other to prevent grating lobes in the azimuth directions. Furthermore, it is not necessary for all elements to transmit simultaneously,

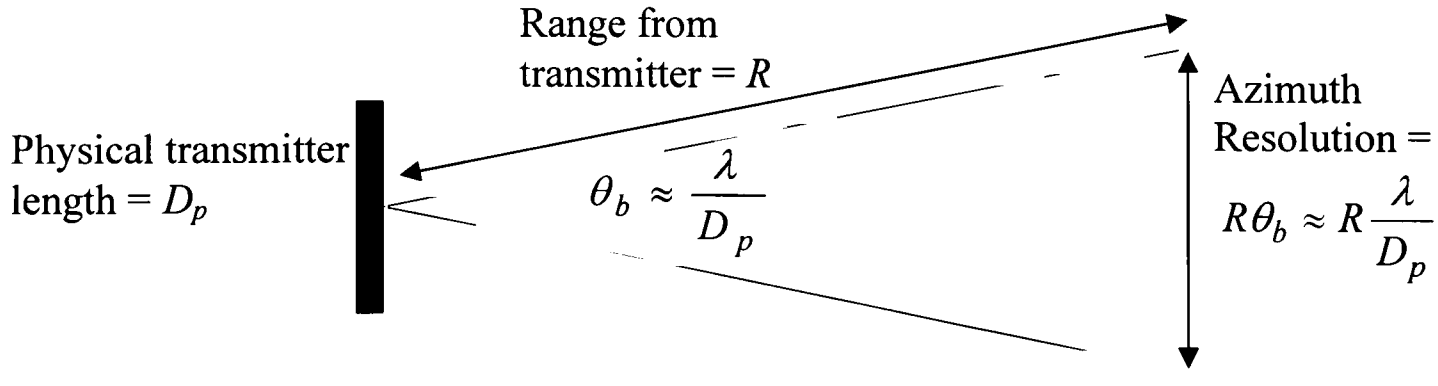


Figure 2.1: The azimuth resolution in a real-aperture system is inversely proportional to the physical length of the linear transmitter and varies with range.

but each can be activated in sequence as long as an orderly coherent phase relationship is maintained. Hence, a physically smaller transmitter can be carried aboard a moving platform with a constant-velocity of v, with pulses being transmitted periodically. In such a manner, the equivalent of a very long transmitting array with length D_s is synthesised from a number of smaller transmitting elements [1].

The synthetic aperture D_s generates a beam pattern with half-power beamwidth, θ_s, and its azimuth resolution, P_s, can be expressed as

$$P_s = R_0\theta_s = \frac{R_0\lambda}{D_s} \tag{2.1}$$

where R_0 is the range measured in the centre of the beam. From the geometry in Fig.2.2, the relationship between D_s and D_p can be found by:

$$\theta_b = \frac{D_s}{2R_0} = \frac{\lambda}{D_p} \tag{2.2}$$

Substituting this relationship into equation (2.1) gives

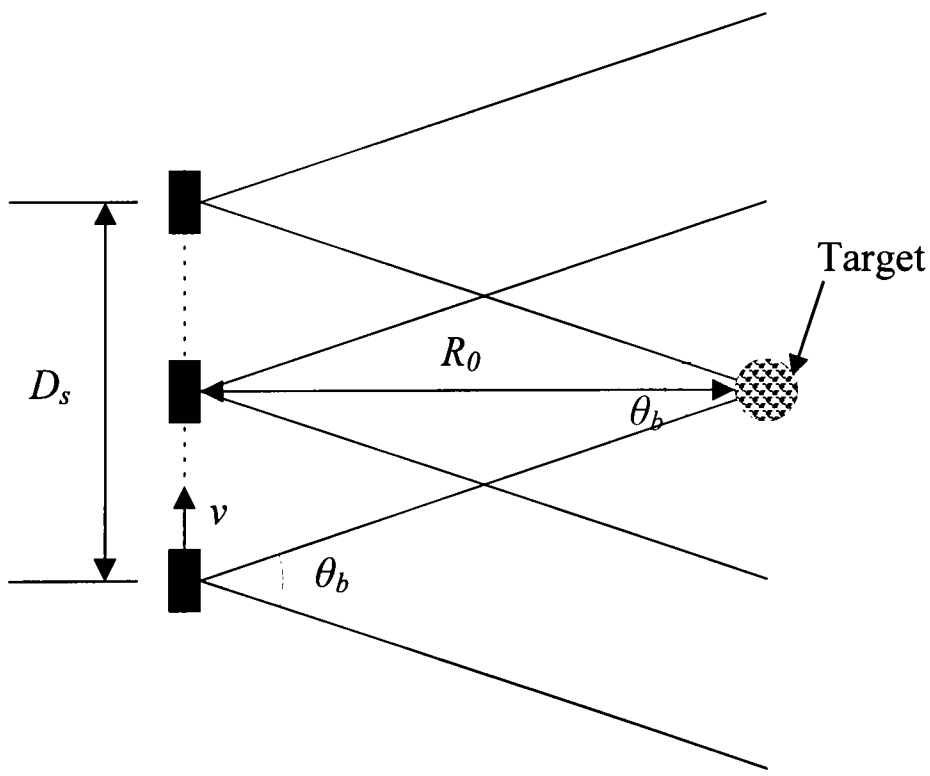


Figure 2.2: A transmitter moving at constant velocity v on a linear path and illuminating a target sequentially to form a synthetic aperture, D_s. The closest range from the synthetic aperture to the target is R_0.

$$P_s = \frac{R_0 \lambda}{2R_0 \lambda / D_p} = \frac{D_p}{2} \tag{2.3}$$

which is the well known expression that states that the azimuth resolution of a coherent synthetic aperture image is only dependent on and proportional to the physical size of the transmitter, as well as being independent of frequency and range [2].

Another advantage of using a synthetic array over a physical array is the freedom of array geometry and formations. The same system apparatus can be deployable under a greater number of circumstances because of its smaller physical size, thus offering increased flexibility and robustness.

There are, however, two basic constraints that need to be noted in utilising the synthetic aperture technique. They are imposed by the requirements of the pulse repetition frequency (PRF) of the transmitter to ensure that no ambiguities exist in either the along-track and cross-track directions of the moving platform. To avoid ambiguities in the along-track direction (spatial under-sampling) the seabed needs to be continuously covered by the synthesized beam in the along-track direction. So from equation (2.3), the first (lower) constraint is

$$PRF \geq \frac{2v}{D_p} \tag{2.4}$$

In [1], Tomiyasu presented four approaches to establish this constraint. The first approach considers a maximum phase shift of 2π-rad between two consecutive echoes, separated by the pulse repetition period, from a particular target. The second approach considers the requirement that the PRF must be greater than the maximum Doppler frequency (between pulses) in the echoes. The third approach is based on the condition that the number of discrete samples integrated in the along-track direction must exceed the along-track resolution cells across the sonar linear beamwidth. The fourth approach is based upon aligning the grating lobes of the synthesized beam pattern to the nulls of

the individual transmitter's response. In all cases the analysis arrived at the result in equation (2.4).

The PRF also needs to be low enough so that at any point in time, only one pulse exists in the range of interest, defined by the difference between R_{max} and R_{min}, where they are the maximum and minimum range respectively. Thus, adding this (upper) constraint to equation (2.4) produces

$$\frac{c}{2(R_{max} - R_{min})} \geq PRF \geq \frac{2v}{D_p} \tag{2.5}$$

where c is the speed of propagation of the pulse concerned.

Now, let the distance that the platform travels between two consecutive pulses, or the inter-ping spacing be D_i, it can be expressed as

$$D_i = \frac{v}{PRF} \tag{2.6}$$

Substituting it into equation (2.4) gives

$$D_i \leq \frac{D_p}{2} \tag{2.7}$$

which states that the inter-ping spacing must not be greater than one-half the physical length of the transmitter. This spatial sampling requirement is required to avoid along-track ambiguities as well as suppressing grating lobes from the synthesized beam pattern. The $D_p/2$ requirement, however, had proven to be insufficient in the suppression of grating lobes [3]. Gough and Hawkins [4] later reaffirmed this inadequacy. The confusion lies in the incorrect assumption that all the aliased energy is compressed (by along-track spatial compression) into the grating lobe peaks before the null of the real aperture pattern suppresses it. This interpretation is true for a real aperture array because all the elements are energized simultaneously, but not the case

in a synthetic aperture system. Hence they proposed a stricter spatial sampling requirement, where

$$D_i \leq \frac{D_p}{4}, \tag{2.8}$$

2.2 Synthetic Aperture Sonar (SAS) Developments

2.2.1 In the Beginning

In the light of the advantages and operating constraints discussed above, and the much slower speed of sound propagation in water compared to electromagnetic waves, one would not be greatly surprised that there exists a whole new set of implications in the utilisation of synthetic aperture techniques in an underwater environment. These had been the primary focus in the course of synthetic aperture sonar research.

The first SAS system developed for underwater imaging application that appeared in unclassified literature is the patent by Walsh in 1969 [5]. In his invention which utilizes the synthetic-aperture principle in a side-looking sonar intended for mapping the seabed, he stated that echoes observed from successive points along the path of a moving transducer can be correlated effectively to synthesize the beam pattern of a long array having an element at each of those points.

This is then followed by an experimental tank test system of the Tokyo Institute of Technology [6]. A steel wire with 4-mm diameter was imaged at an ultrasonic frequency of 1 MHz by a 9-mm diameter circular transducer. To reconstruct the image, the echo returns were phase-delayed independent of range, thus the processing of the synthetic aperture is considered to be unfocussed. The experimental result, shown in Fig.2.3 [6], illustrates that the along-track (azimuth) resolution of the reconstructed image is in good agreement to its theoretical hypothesis. Although the fundamental

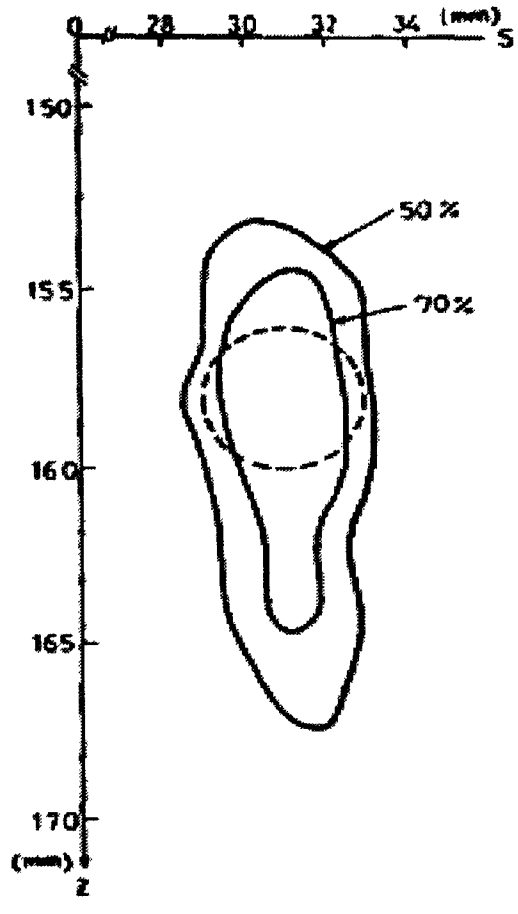


Figure 2.3: Experimental result from [6], showing the reconstructed SAS image of a cross section of the wire. S-axis represents the along-track direction while Z-axis represents the cross-track direction. The dotted line is the outline of the physical wire, and the locus of the reconstructed image at 70% and 50% of the peak energy amplitude were plotted.

principle of SAS had been proven experimentally, it is nevertheless an ultrasonic system conducted in a well-controlled environment.

2.2.2 Medium Instabilities?

In 1976, experiments had been undertaken by Williams to study the adverse effects of the ocean environment on the creation of an acoustic synthetic aperture [7]. The negative factors that were thought to be affecting the creation of an acoustic synthetic aperture in an ocean environment were essentially summarized into two governing factors: instabilities in the acoustic ray paths in the ocean due to medium inhomogeneities, and instabilities in the positional track of the transmitter-receiver platform. After conducting this experiment, one important conclusion was produced; the dominant limitation upon synthetic aperture encountered in the experiment was the transmitter tow-path irregularities, and no instabilities could be seen in the ocean ray paths in the presence of the tow irregularities. Following that, in 1982, Christoff, Loggins, and Pipkin [8] conducted an experiment to specifically study the effects of medium instabilities on a coherent SAS system. It was carried out in water that is

nominally 12m deep with ±0.6 m tidal variations. A bi-static 100 kHz system, securely mounted to avoid any platform instabilities, was used to measure the phase of echo returns over a period of time. The results, shown in Fig.2.4, led to the conclusion that the performance of a SAS system will not be measurably affected by temporal characteristics in the ocean environment, and even more so when the sonar operates in relatively shallow environment.

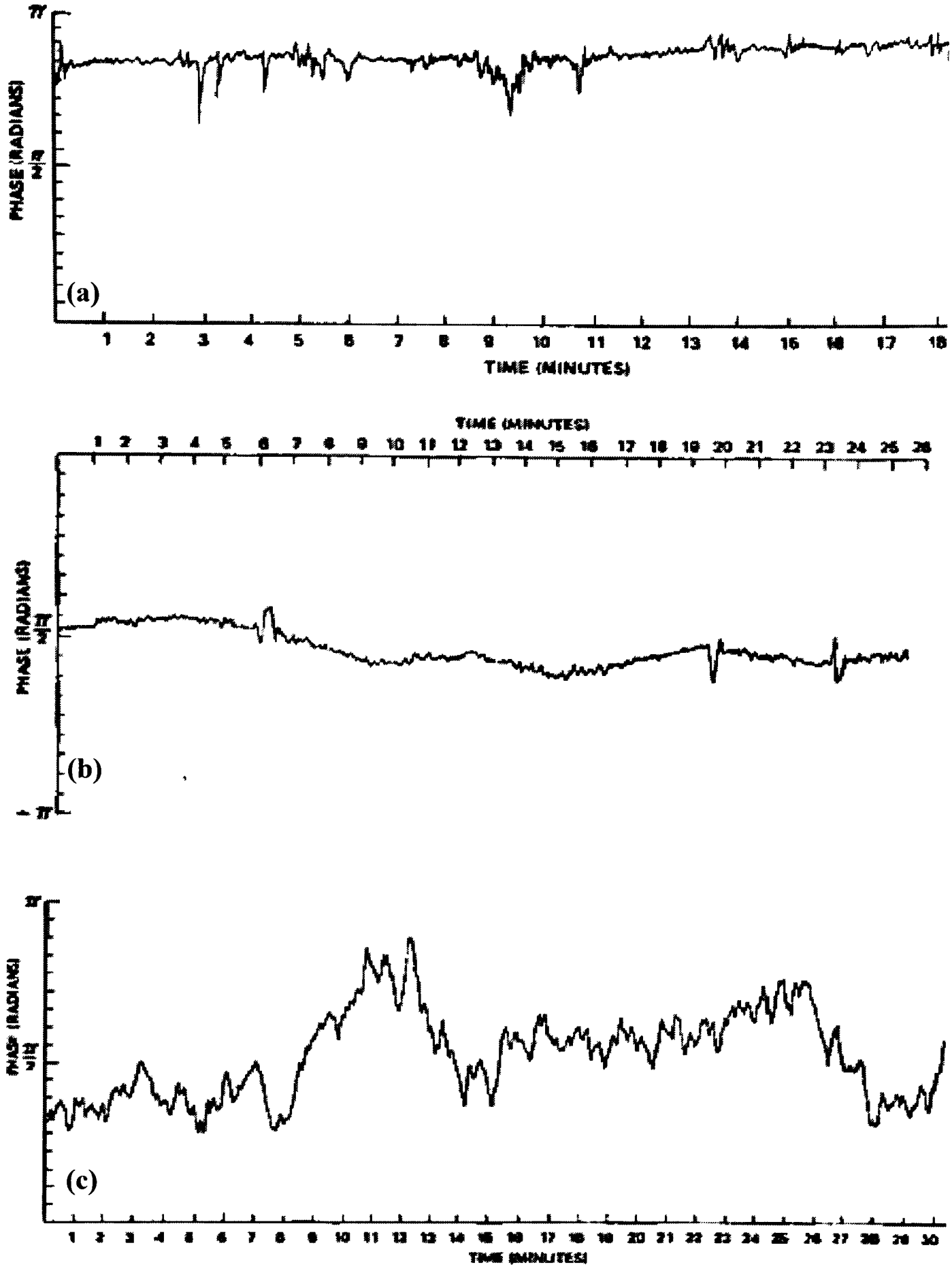


Figure 2.4: Results from the experiments performed in [8], plotted the phase of echo returns versus time under 3 conditions: (a) in the summer with sonar 4 m above seabed; (b) in the winter with sonar 4 m above seabed; (c) in the winter sonar 9 m above seabed.

Later in 1989, Gough and Hayes [71 conducted a similar experiment to study the temporal phase stability in the underwater environment but with a mono-static system and continuous-time frequency modulated (CTFM) signals (15-30 kHz), allowing an observation over a larger number of frequency bins. An air-filled sphere test target was deployed on the seafloor about 66m from the track on which the sonar slid. The conclusion reaffirms that the acoustic medium is stable for the forming of a coherent synthetic aperture, thus dispelling what was once thought to be the leading constraint in SAS applications.

2.2.3 Platform Instabilities

Now, there is only one major negative factor left, and that is the towed platform instabilities. There are two major issues stemming from this factor. They are limited coverage rate and image degradation due to the lack of coherence.

2.2.3.1 Coverage rate

One way to ensure platform stability is to tow it at a speed that provides stability given the platform hydrodynamic and tidal current profile. For example, an experiment conducted by Dinger and Goldstein [78] showed that, given ideal ocean conditions and tow mechanisms, RMS deviations of less than 1mrad is obtainable. The relationship between platform stability and tow speed is also shown in tests conducted in [79], where it was found that platform stability is increased by increasing tow speed into the range of 4 to 8 knots in mild sea conditions (seastate-0 to seastate-1). In SAS, the desired towing speed is, however, limited by the constraint on the PRF. In order satisfy the constraints in equation (2.5), increasing the tow speed requires an increase in the length of the physical aperture, or an increase in the PRF. Based upon equation (2.3), the first option degrades the along-track resolution of the system, while the second option reduces the coverage in the cross-track direction thus limiting the coverage, or the mapping rate of the system.

In order to overcome this limitation, several techniques have been suggested [9], and they fall into two categories; increasing the number of transducers, and under-sampling

in the along-track direction. The techniques that fall into the first category include multiple receive-apertures, multiple beams, multiple transmit frequencies and multiple pulses. The latter category involves using wide-bandwidth transmission and ambiguities suppression. They are not mutually exclusive, and some are more practically applicable than others.

The technique of multiple receive-apertures involves having a single transmitting element with many receiving elements in a linear arrangement parallel to the tow track of the platform [10]. The additional advantage of this is that the information from phase comparisons between pairs of hydrophones can be useful in estimating the deviation of the tow-platform from a straight path.

Multiple beams involves using multiple transmit beams to cover a larger area in the same timeframe. These beams can be of multiple frequencies and are usually separated in elevation (vertically) [10], thus extending the coverage in the cross-track direction. For proper operation, the altitude and height of the platform above the ocean bottom needs to be strictly maintained. On top of that, the task of combining the processed returns from adjacent beams greatly increases the processing load. These consequent complexities made this technique less favourable for increasing mapping rate in a practical situation. Multiple beams in the horizontal direction can also be applied [2].

The mapping rate can also be increased by using multiple pulses. This means that at any point in time, there will be more than one pulse in the propagation medium, but they need to be uniquely identifiable to avoid ambiguities. Coding techniques such as frequency modulation can be used to ensure that they are distinguishable from one another.

In the category of under-sampling in the along-track direction, the techniques involve wide bandwidth (low-Q pulses) transmissions and ambiguity suppression. For a synthetic aperture, the resultant beam pattern is determined by the synthetic beam pattern of the sampled apertures weighted by the two-way real beam pattern of a single real aperture. If the spacing between aperture samples exceeds the sampling

requirement of $D_p/4$, there will be a significant presence of grating lobes. The location of these grating lobes will be dependent on the frequency of the transmitted signal. Thus, by transmitting a wide bandwidth low-Q pulse, the energy from the grating lobes will smear into the background while the energy in the main-lobe integrates. The smeared energy will contribute to the self-noise of the processed image. The use of wideband signals for smearing energy in grating lobes in a spatially under-sampled SAS system was first suggested by de Heering in 1984 [11].

Among all the techniques listed above to increase the coverage rate of an SAS, multiple aperture technique [12]-[14] and the use of wideband signals [15]-[17] are the more practically feasible and attractive, thus finding their way into sea-trials and experimental systems.

2.2.3.2 Image degradation

The second effect stemming from platform instabilities is the degradation of image quality due to the lack of phase coherence in the integrated echoes. There are other sources that may contribute to the phase disturbance in echoes (hardware noise and medium instability), but motion-induced phase errors are typically the most significant contributor towards image quality degradation. The quality benchmark of a SAS image may vary depending on its application, but the sharpness and contrast of a processed SAS image are common quality-benchmarks in most application areas [13].

The basic SAS processing algorithm integrates echoes returning from a particular target based on the assumption that the path traversed by the platform is straight. Thus, when there are deviations of the platform from a linear path, there will be a mismatch of phase in the process of echoes integration. This mismatch causes the resolution to degrade, which in turn reduces the sharpness and cognitive quality of the image, where the cognitive quality is interpreted as how closely the image matches the real object. On top of that, the mismatch between the straight path assumed by the SAS processor and the real non-linear path will result in the occurrence of self-clutter or false targets which introduce ambiguities. Strong self-clutter in the image will cause the image to appear grainy or noisy, thus degrading its contrast.

So in order to minimise the image degradation due to platform instabilities, the deviations of the platform from a straight path need to be taken into account in the SAS processing algorithm. This process is known as motion compensation. To compensate for unwanted motions, they first need to be either tracked or extracted from the collected echoes. In coherent SAS processing, platform deviations need to be tracked to the accuracy of a fraction of the signal wavelength, typically $\lambda/4$ for a one-way path [1], in order to avoid any significant drop in image quality. Such a stringent requirement often increases the hardware cost and complexity of the system as a whole, and quite often poses a whole new set of operational problems. Thus, most efforts of current research have been to incorporate motion compensation ability into the SAS system so that platform deviations can be extracted from the SAS data itself. This method of motion compensation, where no external dedicated navigational system is added to the SAS hardware, is now commonly known as autofocussing. It is analogous to the autofocussing process in the optical field where a scene in the image is put into focus based on the parameters derived from the evaluation of the image itself.

2.3 Synthetic Aperture Sonar Processing

The processing of SAS data to form a reconstructed image has always been accomplished offline, or separated from the data collection process itself, due to the required computational load. Over the years, with the exponential increase of computational power especially in the past two decades, the time and financial cost related to the processing of SAS data are quickly diminishing.

The general steps involved in the coherent processing of SAS data are shown in Fig. 2.5. With each sonar ping, the data received on each channel are firstly sampled in time and stored, usually resulting in a 2-dimensional matrix with corresponding along-track (spatial) and time or cross-track (time or range) domains. The data matrix is then processed in both the cross-track direction and the along-track direction.

2.3.1 Cross-track Processing

Cross-track processing is in the range or time domain, and is equivalent to the traditional processing of target-ranging. The goal is to be able to locate targets accurately in range as well as to achieve the best resolution in the range domain.

Consider a signal *s(t)* being transmitted and reflected from a target, the returned signal, *r(t)*, will be an attenuated and delayed version of *s(t)*, such that

$$r(t) = A_r s(t + t_r) \tag{2.9}$$

where A_r is the range-dependent attenuation factor (which also accounts for target reflectivity) and t_r is the two-way time delay associated with the range of the target. If *s(t)* is a short pulse waveform, then *r(t)* will be usually be bandpass filtered to reduce the level of additive noise. Otherwise, if *r(t)* is a more complex pulse (e.g. linear frequency modulated chirp or linear period modulated) it will be correlated against *s(t)* to pulse-compress the returned signal, which is also known as matched filtering [18]. Since the experimental work carried out in this project mainly uses chirp signal, this method of processing will be used for purposes of discussion here. Such a process is often performed in the frequency domain. The FFT (Fast-Fourier Transform) is applied to *r(t)* and *s(t)* to generate *R(f)* and *S(f)* respectively, one of which is then multiplied with the complex conjugate of the other to obtain the processed signal. The inverse FFT is then applied to obtain the signal in the time domain:

$$\Gamma_{n_a}(t) = \int_{-\infty}^{\infty} R(f) \cdot S^*(f) \cdot e^{j2\pi ft}\, df \tag{2.10}$$

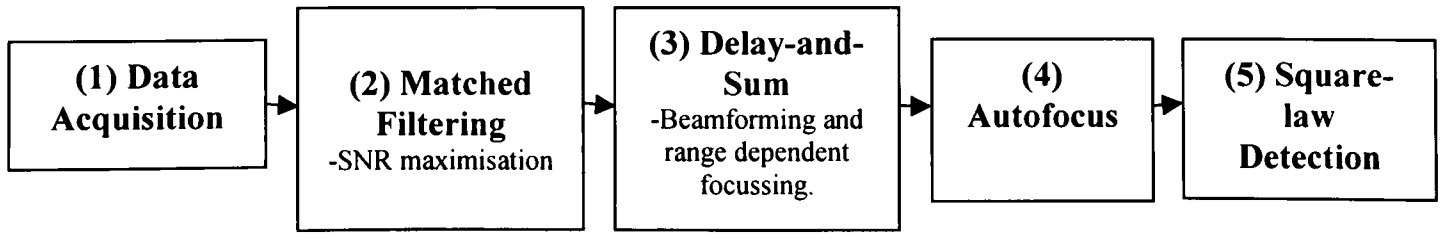
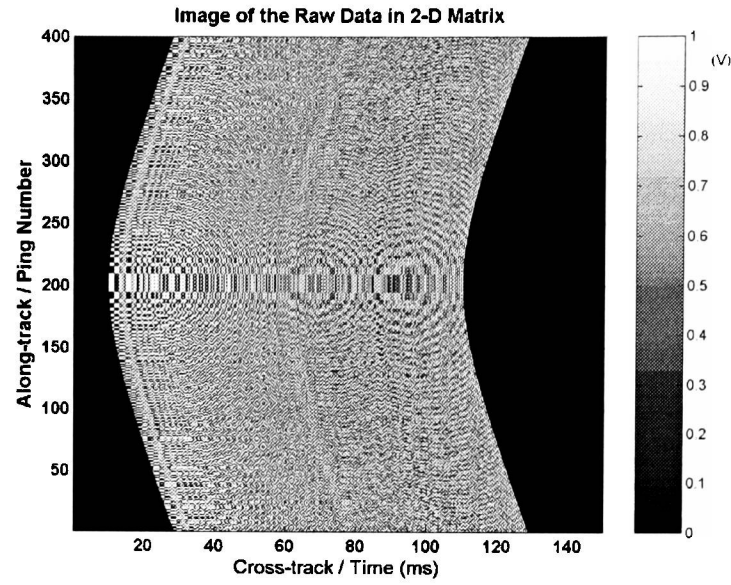


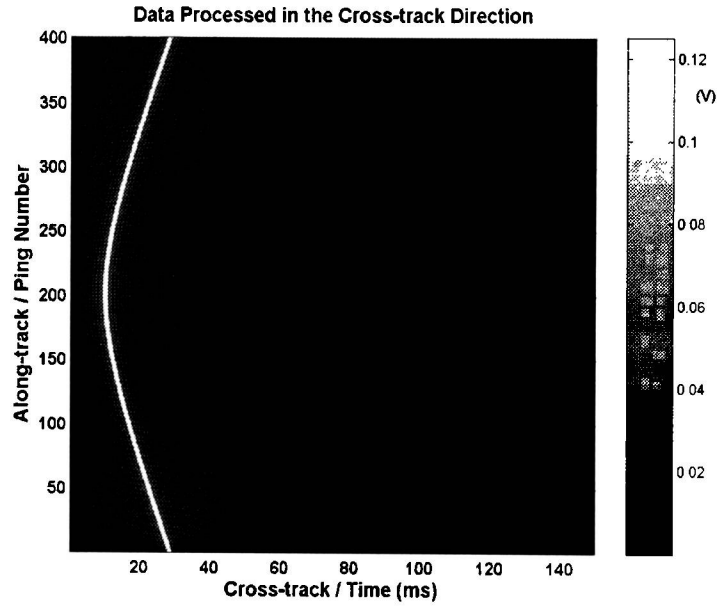
Figure 2.5: General steps involved in the coherent processing of SAS data.

where n_a is the index in the along-track direction. By this stage, the 2-dimensional image is at best a poor representation of the reflectivity characteristics of the target environment, with strong point targets appearing in a parabolic form across the along-track direction (Fig. 2.6(b)).

(a) *The raw data is collected by a pinging platform towed in the along-track direction. It is stored and represented in a 2-D matrix.*



(b) *The signal returns are processed in the cross-track direction, usually by matched filtering.*



(c) *The image is then processed in the along-track direction to reconstruct a high resolution image. It is a close-up view compared to the above images, as shown by the difference in scale.*

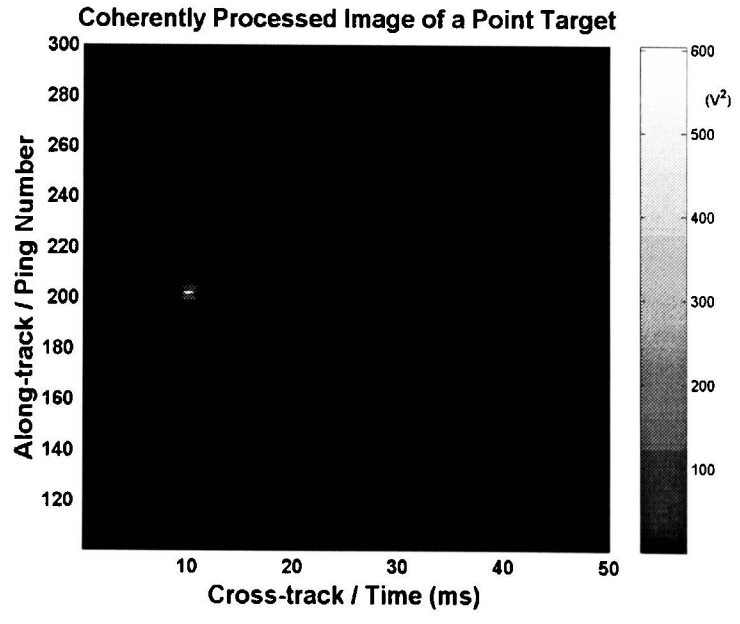


Figure 2.6: Image representation of cross-track and along-track processing, based on simulation of a point target.

2.3.2 Along-track Processing

The core part of SAS processing lies in the along-track processing of the data matrix. This is where most of the computational load will be spent to achieve a fine along-track resolution. To compress the signal in the along-track direction, the image needs to be beamformed such that the returns collected on every along-track position from a point target will be appropriately delayed and summed constructively. Thus for every pixel of interest on the image, its range from each along-track position will be used to determine the appropriate time delays for picking the samples to be summed.

The reconstructed image can then be expressed as:

$$I_{image}(n_a, n_r) = \sum_{n=1}^{N} w_n \cdot \Gamma_n(t - t_n(n_a, n_r)) \tag{2.11}$$

where $I_{image}(n_a, n_r)$ is the specific pixel of concern on the image to be reconstructed, n_a and n_r are the coordinates for the pixel concerned, in the along-track and cross-track directions respectively, and w_n accounts for amplitude shading and windowing in the along-track direction with N ping locations. A monostatic transmitter and receiver configuration is assumed here. The time delay t_n is the echo return time based on the range of the pixel (n_a, n_r) from each along-track position and is given by a hyperbolic equation:

$$t_n(n_a, n_r) = \sqrt{\frac{(n \cdot 2 \cdot v)^2}{(c \cdot PRF)^2} + (t_0)^2} \tag{2.12}$$

where t_0 is the return time-delay from the location (n_a, n_r) to the closest along-track position, a distance known also as the closest path of approach (CPA). To reconstruct the whole image, the process in (2.11) and (2.12) is repeated for all pixels in $Image(n_a, n_r)$. This simple model makes the assumption that inter-ping spacing is uniform, and that there is no spatial interpolation thus only one type of coordinates, (n_a, n_r) is used.

Such a model is known as the "time-domain back-projection" or the "coherent addition" algorithm where the image reconstruction process is performed pixel-by-pixel based on its range back-projected to the corresponding along-track positions. Its radar equivalence is called the "exact transfer function" algorithm [19] where a unique transfer function for each pixel is used to compress the 2-D image in the frequency domain. These algorithms, being analogous to a beamforming process with unique parameters for each pixel, are the most accurate image reconstruction method. The reason is that other than the necessary spatial interpolation needed in coordinate conversion, there are usually no other approximations. The trade-off, obviously, is that they are also the most computationally demanding and slow.

In the radar community, there are three other main synthetic aperture processing methods; the "range-doppler" algorithm [19], [20], [21], the "wavenumber" algorithm [21], [22] and the "chirp-scaling" algorithm [23]. These frequency-domain techniques are attractive due to their relatively smaller computational demand. However, adopting them to the processing of synthetic aperture sonar data is not appropriate [24]. These algorithms work well if the synthetic aperture is evenly sampled and linear, but any deviations from these conditions seriously degrade the quality of the image produced. There are motion compensation techniques to correct for such deviations, but they do not always work, especially in the situation where the transmitter and receiver beamwidth are very broad and the motion errors are very large. Also, approximations used in these algorithms often assume far-field imaging conditions as well as a signal bandwidth of relatively large Q-factor (narrowband). These assumptions are almost always true in radar imaging applications, but is not valid in the context of SAS imaging as broadband pulses (Q<10) are used. For example, in the sea trial in chapter 6, the hydrophone-receiver array is 24m long and the nearest range of interest is 20m. Hence, that is not a strong case for using far-field assumptions, as the Fresnel range, D_p^2/λ (where D_p is the size of the array and λ is the centre frequency) is of the order of 7.6km.

The notion of time-domain techniques being more appropriate is further reinforced by the use of time-domain back-projection technique in major SAS trials published in [15]

and [25] where the imaging is in the near-field. The SAS processing algorithms used in this project is thus based on time-domain techniques, and these will be detailed in Chapter 3.

2.4 Motion Estimation and Compensation

In the process of aperture synthesis, data are collected as the sonar moves along a pre-determined (usually linear) path. However, keeping the sonar platform on the desired path is rarely possible under realistic operating conditions. Such deviations are dependent on the sea-state (wind driven waves and internal ocean waves), hydrodynamics of the tow-body, and the coupling between the towing vessel and the towed-body. As an example, a heavy tow-platform towed in seastate-0 (very calm sea) at speed of $4ms^{-1}$, experienced sway motion in the order of a few centimetres [80]. Also, a U.S. submarine was found to roll by an average of 0.02rad while positioned 30m below a rough sea (seastate-5) [81].

Motion estimation and compensation is a process that attempts to approximate, to the best accuracy, any such unwanted deviations of the real path from the desired trajectory, so that they can be taken into account during synthetic aperture processing to avoid any motion-induced degradation of image quality. For a fully coherent system, the estimated deviations need to be accurate to the order of $\lambda/4$, such that for a narrowband 50 kHz system, the required accuracy is in the order of less than 1cm.

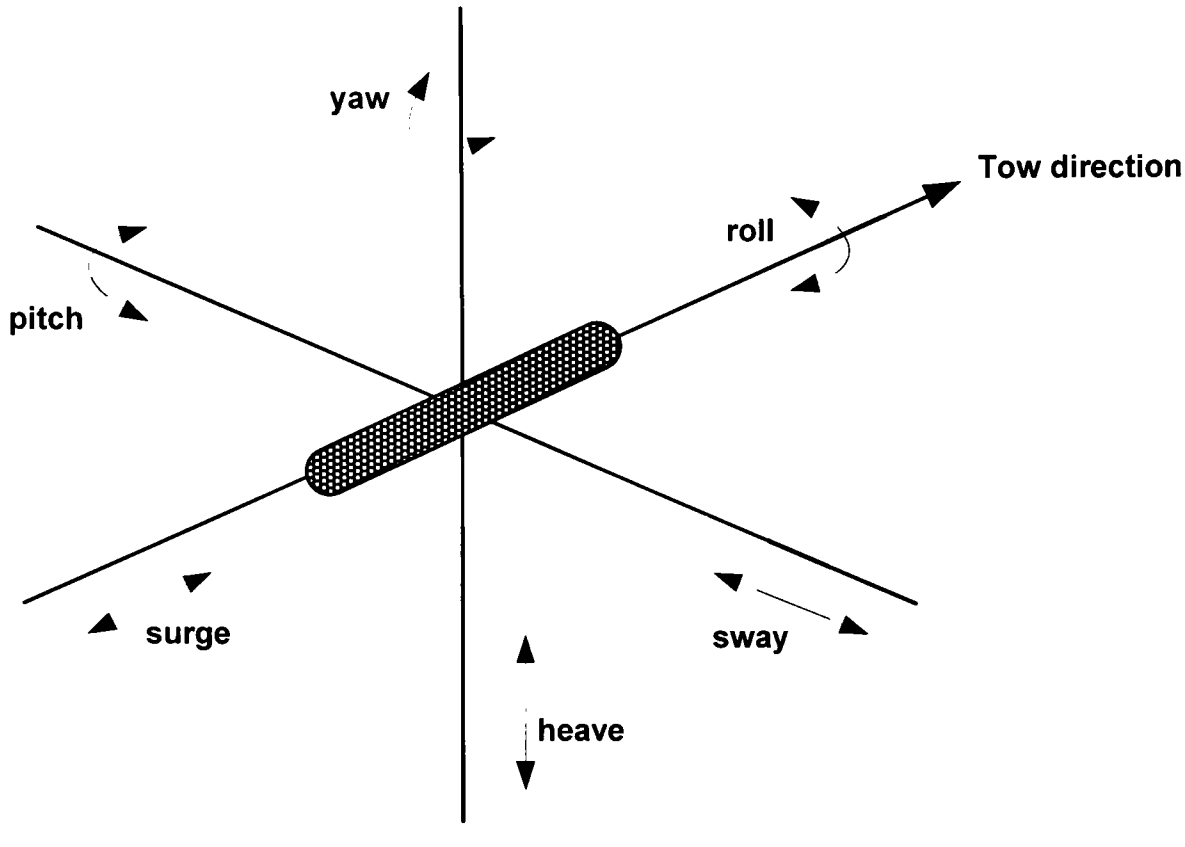


Figure 2.7: The types of path deviations experienced by a towed-platform.

For a linearly towed platform, there are six possible path deviations as illustrated in Fig. 2.7. Pitch, yaw and roll are rotational, whereas sway, surge and heave are translational. Rotational deviations mainly affect the beam position and thus only affect the echo amplitude, while the translational deviations affect the sampling of the aperture in the along-track position and will cause distortion in the processed image. Simulations performed in both [26] and [27] had shown that the main contributors toward image degradation are translational deviations, and that sway (translational) and rolling (rotational) are most commonly experienced by a towed array. They went further to show that, given the same amount of deviations, swaying is the most detrimental to the signal-to-noise ratio of the image. Fig. 2.8 shows the processed SAS images of a simulated point target without, and with, uniformly random motion errors, demonstrating the consequent blurring and degradation of the signal-to-noise ratio.

The dependence on specialised motion estimation hardware to compensate for path deviations is often impractical due to the unstable underwater environment and the

high degree of accuracy required, and may significantly increase the cost and complexity of the deployable system. The more attractive route has thus been to extract the trajectory information by the analysis of the data collected, possibly combined with modifications to the data collection process or hardware. Such a technique, also known as autofocus, works by maximising key parameters of the image itself.

There are four common motion estimation techniques based upon autofocus algorithms; contrast optimisation, phase gradient autofocus, multi-look registration and displaced phase-centres array (DPCA) [24],[27],[28]. They are briefly described below.

Contrast optimisation: The contrast of a highly structural part (i.e. with the presence of targets) of the image is chosen as a statistical measure of which to optimise. Relying on the fact that the significant cause of image blurring is due to the changes in along-track velocities, the along-track velocities for parts of the traversed path are estimated as the measure of contrast is maximised.

Phase gradient autofocus: This works by identifying strong targets in the distorted image as a function of range, and then approximating the best parabolic sensor-target range function by minimising the error of residual phase errors which are measured as the difference between the ideal (assumed situation without motion errors) along-track-range function and the actual registered along-track-range function of the strong target

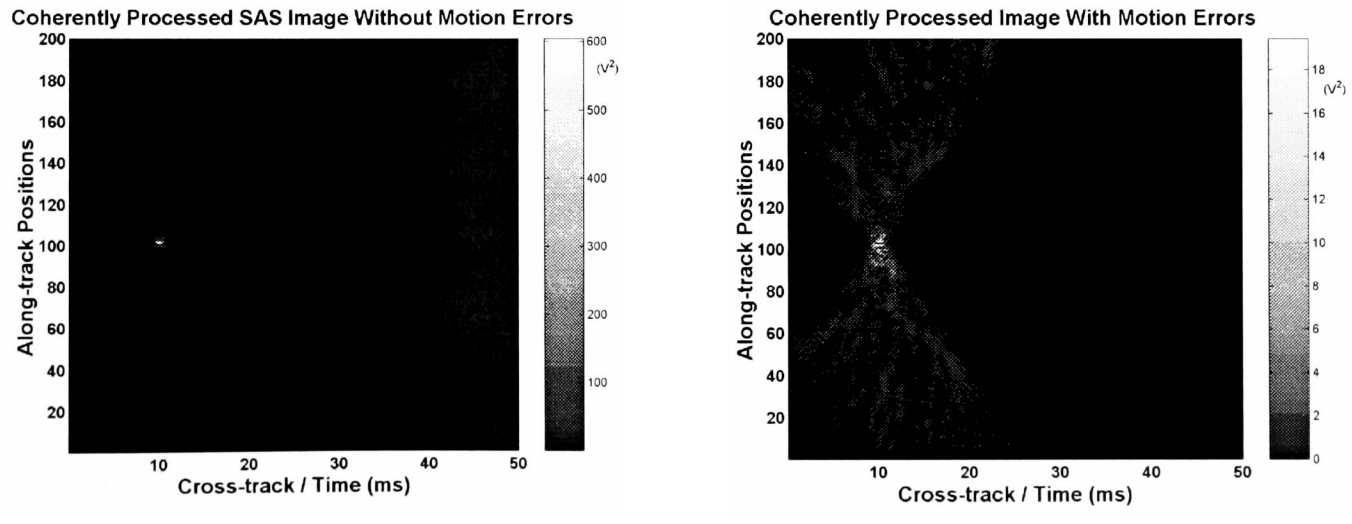


Figure 2.8: Blurring and defocusing effect, due to motion errors, in the coherently processed SAS image of a simulated point target. Images' contrasts are individually optimised. Peak-to-peak degradation is 15dB.

in the image.

Multi-look registration: By forming sub-apertures that overlap, strips of images can be formed to achieve a multi-look effect on a similar spot. Cross-correlations of similar "looks" can be performed to yield an estimate of the motion errors.

Displaced phase-centre array: This works by towing a long array of transducers and pinging in such a way that some channels on the array will closely overlap other channels on the array from the ping before. By cross-correlating the returns from the overlapping channels, the inter-ping motion errors can be estimated.

The above techniques each have their advantages and limitations. They have been shown to work on experimental SAS data which satisfies the requirement of the algorithms used [29],[30]. The concepts inherent in these techniques are used for the development of motion compensation technique used and applied in this project, which will be discussed further in chapter 5.

2.5 Brief Review of Incoherent Synthetic Aperture Processing

The concept of incoherent synthetic aperture processing denotes the absence of phase information in the reconstruction process of the synthetic aperture image. In incoherent synthetic aperture sonar processing, the phase information is removed by a square-law operation before along-track integration is performed (Fig. 2.9). The following integration operation thus effectively adds up the energy of the signal rather than coherently summing the complex forms of the signals. This method of processing is inferior to a fully coherent SAS processing in terms of the achievable along-track resolution. However, it is capable of addressing most of the challenges faced by a fully coherent SAS system.

The use of incoherent processing as an alternative, where phase information is removed, was first suggested by P.Heering in 1984 [31]. He derived that the along-track resolution of an incoherent SAS system is dependent on the bandwidth of the pulse and the dimension of the physical array, and that this resolution is poorer than in a coherent system. He suggested the use of broadband pulses (typically $Q<10$ in imaging sonar such that the bandwidth is 10% or more of the centre frequency) to optimise both the along-track and the cross-track resolution in incoherent SAS processing. D.J.Wingham [32] later suggested an incoherent approach to synthetic aperture radar data acquisition and processing with a square-law detector. The use of incoherent SAS processing as a possible alternative was also mentioned in [15] and [33], but only very briefly, showing that it involves the removal of phase information before the process of along-track integration, and that it can be exploited as an averaging tool to minimise distortions suffered in coherent SAS processing. The work done by V.Murino et al. [34] to investigate the incoherent approach to beamforming data from conventional 2-D arrays gave an interesting insight of its potential in array processing. In his conclusion, he suggested its application in SAS and predicted its main advantage of overcoming drawbacks and constraints associated with coherent SAS. A detailed study into the properties and advantages of incoherent SAS processing is carried out in Chapter 3.

The main factors that make an incoherent approach attractive can be summarised as below:

i) It is clear, by this stage, that obtaining returns with strong phase coherence over the long synthesized aperture is the greatest challenge inhibiting widespread application of SAS, and that this will continue to be the case for the foreseeable future of SAS. The utility of a fully coherent SAS system

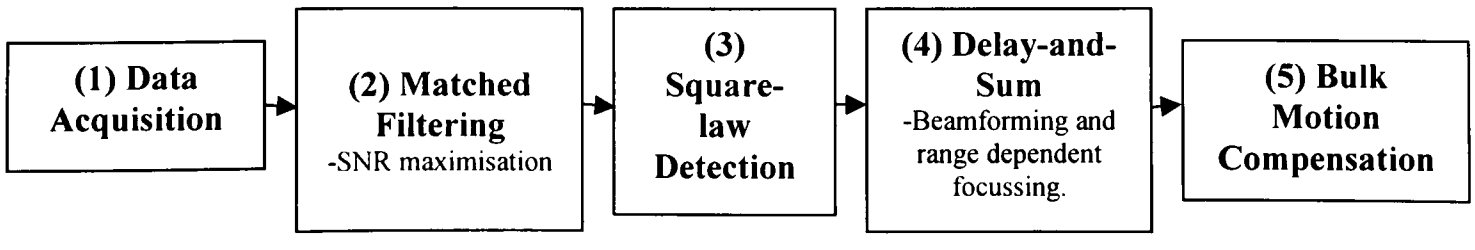


Figure 2.9: General steps involved in the incoherent processing of SAS data.

means that there are various strict constraints that must be satisfied in the imaging process, thus greatly reducing the robustness and flexibility in the time, cost and reliability of the hardware development and deployment process. The inevitable need for precise and accurate motion compensation techniques, which itself demands privileges that are usually not freely available in real circumstances, is a testament to the vulnerability of a fully coherent SAS system due to the lack of phase coherence.

ii) Secondly, there are application areas in underwater imaging application where the high resolution of a coherent SAS, if at all practically achievable, is not the top priority. In such cases where deployment time, cost and reliability are more important, the use of incoherent SAS may well be the better alternative.

iii) The use of incoherent processing addresses the major lingering challenges faced by a fully coherent SAS; slow mapping rate, strict along-track sampling requirement, inflexible element configuration in the aperture synthesis and the need for complex post-processing techniques.

2.6 Conclusion

The synthetic aperture technique is practically applicable in the underwater environment. The course of the development of synthetic aperture techniques in sonar applications have been outlined, and shown to be very much governed by the challenges that arise from applying this technique in underwater imaging. The theoretical background of synthetic aperture sonar processing along with motion compensation has been introduced.

The conclusions are that due to the nature of sound propagation, SAS suffers from a slow mapping rate and the difficulty in maintaining phase coherence throughout the whole synthesized aperture results in significant image degradation. The fluctuating platform trajectory calls for the need for accurate platform monitoring and motion compensation. This results in a much more complex system and imposes operating

constraints in realistic applications. Also, motion compensation methods that utilise autofocus algorithms rely heavily on criteria that are not easily satisfied under most operating circumstances. Due to these factors, incoherent SAS processing presents itself as a strong alternative for applying synthetic aperture principles to practical and robust sonar imaging.

Chapter 3

Incoherent Synthetic Aperture Sonar Processing

3.1 Introduction

Clearly, the limitations and its related setbacks suffered by a coherent SAS system raise questions of its reliability under non-ideal operating conditions. Incoherent SAS processing is a viable and promising alternative to a fully coherent SAS because it directly addresses some of the constraints present, and at the same time offers features that are otherwise unavailable.

This chapter investigates the incoherent approach applied in synthetic aperture sonar processing. The details of implementation are shown, and the technical properties of this technique are presented. Simulations are presented along the way for purposes of illustrations and comparisons. Discussions of the potential and limitation of this approach are made. All the simulations and analytical investigations in this chapter are performed using Matlab. Unless otherwise specified, they are based on two assumptions: monostatic configurations of transducers; and transducers' movements during pulse transmission and reception are negligible.

3.2 Phase Removal

In incoherent SAS processing, the phase information is removed before along-track integration, but only after cross-track processing. Cross-track processing is performed by a matched filter in the frequency domain for computational efficiency. A Hilbert transform is then applied, so that taking the inverse fast Fourier transform will give the analytical form of the cross-track processed signal in the time domain. Hence, phase information is usually preserved up to the stage of along-track integration.

The removal of phase information is performed by a modulus square operation [35], which is basically a multiplication of the received signal which has been processed in the cross-track domain, $\Gamma(t)$, by its complex conjugate, such that

$$P(t) = \Gamma(t) \cdot \Gamma^*(t) \tag{3.1}$$

to give the power of the signal $P(t)$. At this stage, the image becomes

$$I_{image}(n_a, n_r) = P_{n_a}(t_{n_r}) \tag{3.2}$$

which is a representation of the reflected energy density at locations corresponding to the pixels (n_a, n_r), where n_a and n_r are discrete positions in the along-track (azimuth) direction and cross-track (range) direction respectively.

3.3 Time-domain Back-projection

It has been established in section 2.3.2 that time-domain algorithms are more suitable for the along-track processing of SAS data. With an incoherent SAS approach, time-domain techniques are also the most suitable because the exact reconstruction algorithm can be used. This reduces the number of approximations being made, and hence avoids any unnecessary degradation of along-track resolution. Long computing time is a rapidly diminishing issue as the ratio of processing speed to cost continues to increase exponentially.

Consider a stationary point target located at coordinate (x_T, y_T) on a 2-D plane surveyed by a transducer (monostatic) towed linearly pinging at positions (x_0, y_n), where n is the index of along-track positions (Fig.3.1). Back-projection here implies the calculation of the range from the target to each ping position of the transducer in the along-track direction, such that

$$R_n = \sqrt{(x_T - x_0) + (y_T - y_n)} \tag{3.3}$$

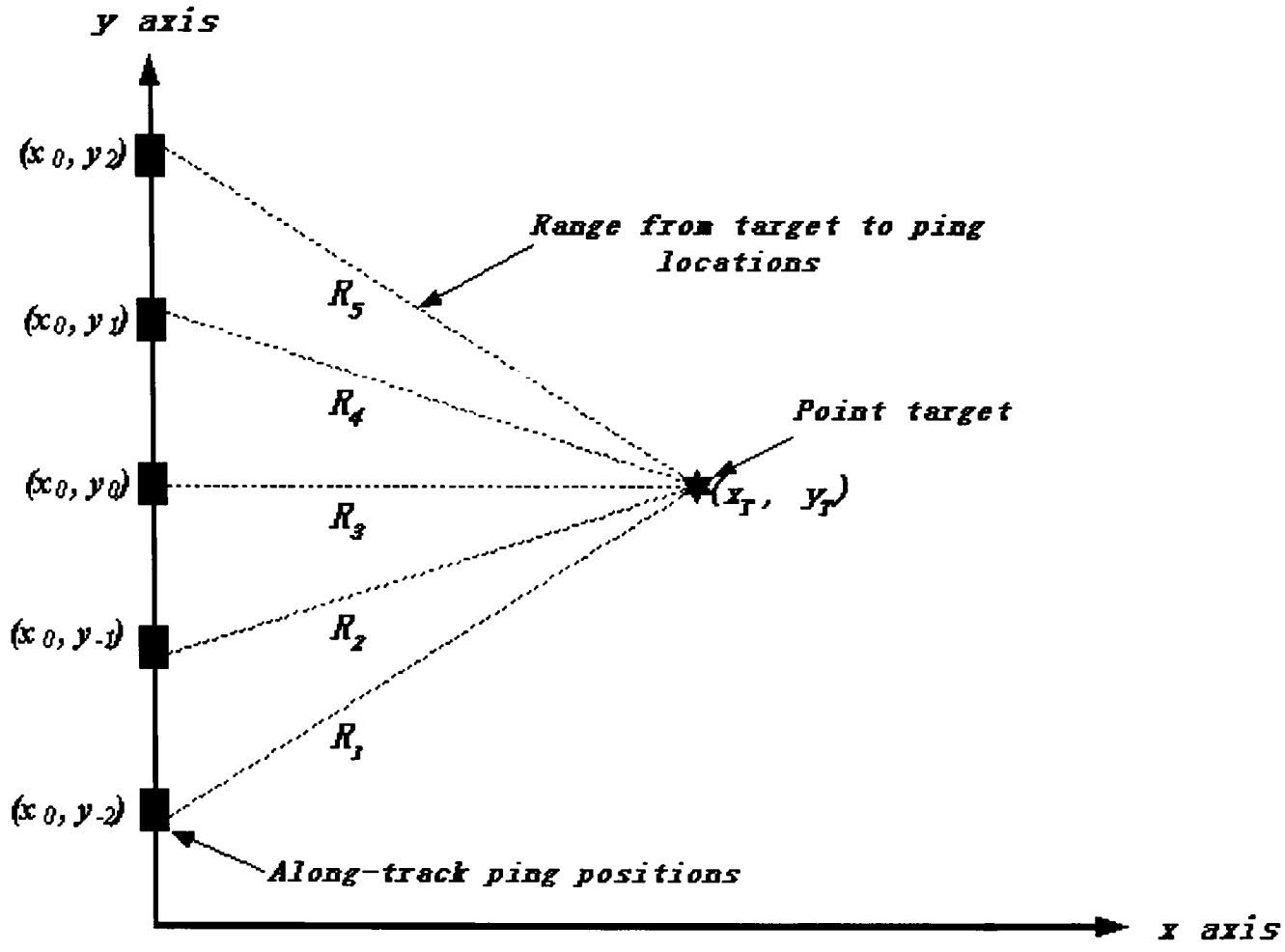


Figure 3.1: Range values from a point target to the ping positions on the along-track axis.

thus effectively back-projecting, in range, the point target's location to the synthesized aperture. R_n here is a set of range values corresponding, and unique, to the point target concerned. These are the exact ranges from the target to the ping positions.

This set of range values can be converted into the total propagation time of a transmitted pulse to and from the point target for each ping location. As such, a set of time-delays t_n is produced from the set of range values, R_n. The time-delays for the point target, if plotted against the along-track ping positions, will form a hyperbolic curve, and can also be called the range-curvature of the target. Based on equation (3.3), t_n can be expressed as:

$$t_n = \sqrt{\frac{(n \cdot 2 \cdot v)^2}{(c \cdot PRF)^2} + (t_0)^2} \tag{3.4}$$

where t_0 is the time-delay corresponding to the closest point of approach (CPA) of the target to the synthesized aperture. t_n is unique to the point target located at (x_T, y_T), and will be the set of time-delays used in order to integrate in the along-track direction to reconstruct the reflectivity at (x_T, y_T). The process of SAS image reconstruction is undertaken by performing such an operation for all other point of interest on the x-y plane.

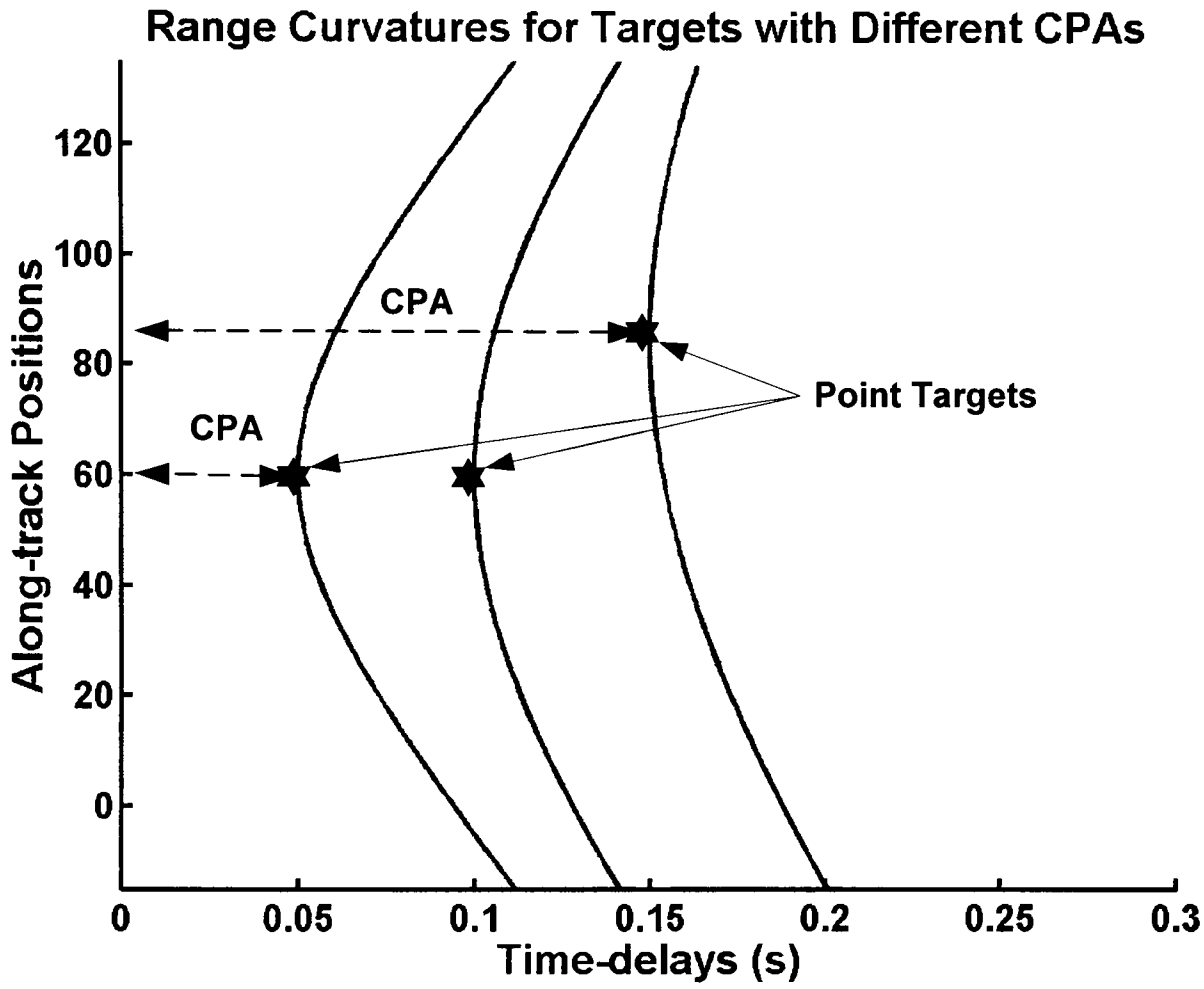


Figure 3.2: Time-delay or range curvatures unique to reflective points on the x-y plane.

As t_n is a function of t_0, a new set of time-delays is needed for each point of interest to be reconstructed (Fig. 3.2). This is the exact reconstruction algorithm, and is also known as a "fully focussed" SAS image reconstruction. The concept of depth of focus can be used to avoid re-estimating the time-delay function for every CPA. Targets with CPAs in the same depth of focus will share the same time-delay function. The larger the depth of focus, the greater will be the degradation of overall image quality due to the errors between the assumed and actual time-delay functions within the depth of

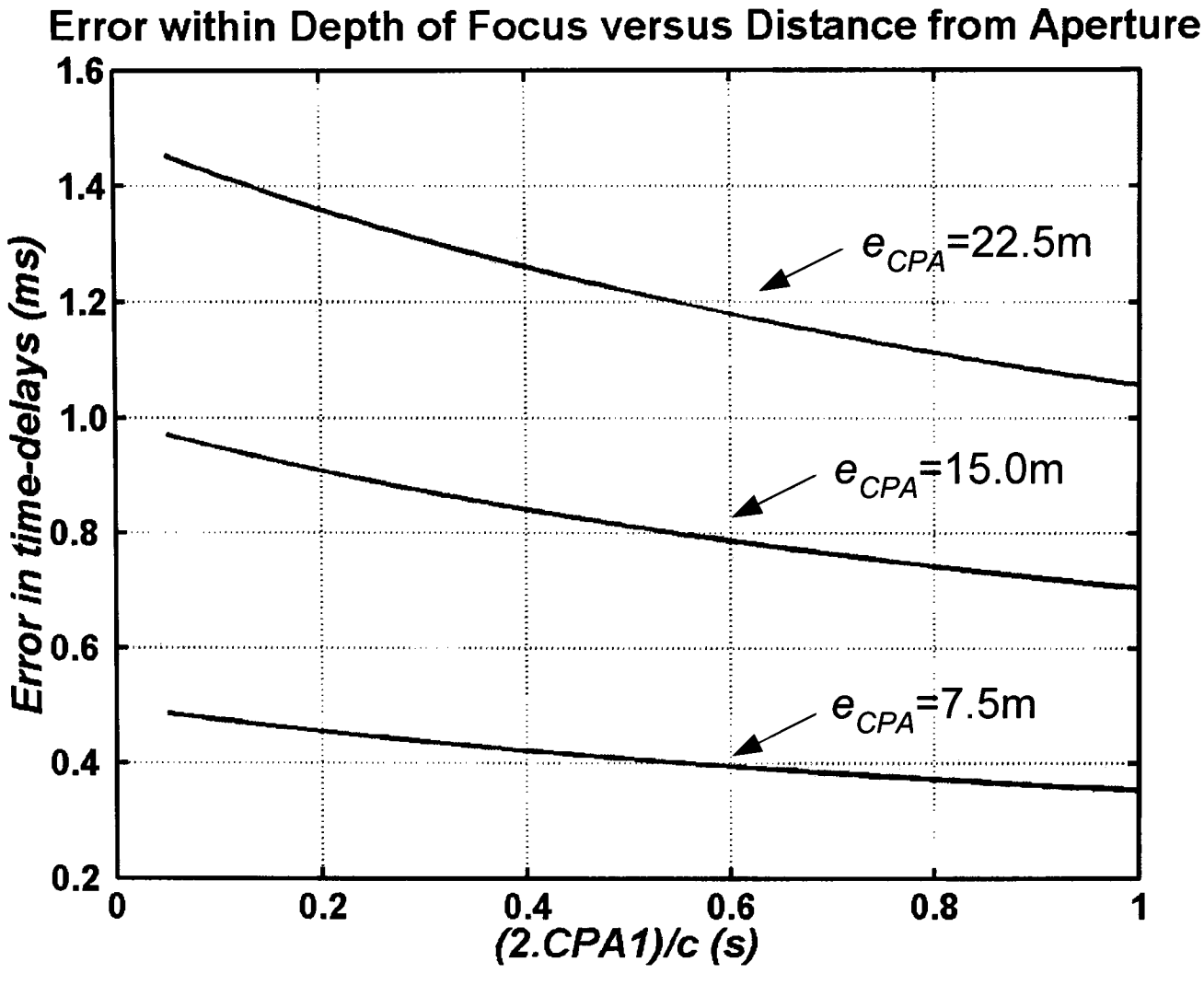


Figure 3.3: Plot of E_f versus *CPA1*, based on equation 3.6, showing that the error increases as a fixed depth of focus, e_{CPA}, approaches the synthesized aperture.

focus. One can tell by visual observation that this error increases as CPA decreases given the same depth of focus. This is due to the increasing gradient of the hyperbola as CPA decreases. Let this focussing error be defined by E_f such that

$$E_f = t_{n,CPA2} - t_{n,CPA1} \tag{3.5}$$

where $t_{n,CPA2}$ and $t_{n,CPA1}$ are the set of return time-delays for two reflective points with *CPA2* and *CPA1* respectively, and $t_{n,CPA} = 2.CPA/c$. Let $e_{CPA} = CPA2 - CPA1$, the focussing error can be expressed as:

$$E_f = \sqrt{1 + \frac{2 \cdot CPA1}{c} + \frac{e_{CPA}}{c}} - \sqrt{1 + \frac{2 \cdot CPA1}{c}} \tag{3.6}$$

which dictates that, with the same depth of focus, the maximum error due to the mismatch of time-delay curves increases as the depth of focus draws nearer to the synthetic aperture (Fig.3.3).

3.3.1 Coordinate mapping

To perform image reconstruction, it is convenient to have two separate matrices, I_{data} and I_{image}, to respectively represent the collected data and the result of along-track integration on the collected data. Based on the sampling criteria, the coordinates corresponding to any discrete samples on I_{data} can be known. However, this coordinate system may not always match the coordinate system in the desired form of I_{image}, in which case the necessary mapping function needs to be taken into account. One example will be the case when the reconstructed image, in the cross-track direction, needs to be represented with the coordinates of the seabed plane, rather than just the ranges from the synthesized aperture. Unless specified otherwise, this thesis assumes the same coordinates in both I_{image} and I_{data}.

3.3.2 Image reconstruction

The image reconstruction process uses the data in I_{data} to produce I_{image}, where I_{data} contains $Image(n_a,n_r)$ stated in (3.2). To reconstruct the SAS image, for each point on I_{image}, a sample will be chosen from each cross-track slice of I_{data} based on the back-projected ranges, and then summed to be the result, such that

$$I_{image}(n_a,n_r)=\sum_{n=1}^{N} I_{data}(n,n_d(n,n_a,n_r)) \tag{3.7}$$

where (n_a,n_r) is the coordinate of the point of interest on I_{image}, N the total number of pings in the synthesised aperture, n_d the sample delay which determines which sample on the n^{th} cross-track slice is selected for summation. The sample delay n_d is based upon the set of back-projected ranges:

$$n_d(n,n_a,n_r)=\frac{2\cdot f_s\cdot R_n(n_a,n_r)}{c} \tag{3.8}$$

where f_s is the sampling rate and R_n is the back-projected range function of the n^{th} element.

The process in equations (3.7) and (3.8) can also be expressed in terms of back-projected time-delays, as they are easily interchangeable with the monostatic transmitter-receiver assumption.

3.3.3 Two-way propagation distance in bi-static configuration

It is worth noting that the term *bi-static* and *multistatic* used in this project stresses on the fact that the transmitter and receivers are not strictly co-located in the proposed schemes, and is *not* a proposal for a deliberately separated transmitter/receiver system with a wide bi-static angle (angle between the transmitter and receiver as seen from the target at nearest range of interest) of $>30^{o}$ as seen in fully bi-static systems. This is clarified further below.

The term bi-static here refers to two specific situations in SAS imaging:

1) A towed SAS where the pulse is received at a different location than where it was transmitted. At 50m range, a typical imaging SAS towed at $1.5ms^{-1}$ would have moved by approximately 0.1m (in the along-track direction) from its original position when the return pulse is received. The bi-static angle is 0.1^{o}.

2) A single transducer/multiple sparsely spaced hydrophone array is used. In the sea-trial in chapter 6, the furthest hydrophone is 11.25m away from the boomer transmitter. At 30m range (the depth of the trial environment), the return path is approximately 2m longer, compared to the transmit path. The bi-static angle is 20.5^{o}.

The term multistatic is used to describe the proposed scheme in chapter 7, where there are 2 transmitters that correspond to other hydrophones attached onto the same laterally towed-array. With the proposed array dimension and element separation, the maximum bi-static angle is approximately 18.4^{o}.

Hence, because of the small bi-static angle, the scope of this work does not cover the technical properties for a fully bi-static system. It must be noted that properties of monostatic system such as along-track resolution and cross-track resolution no longer hold when the bi-static angle is large. In such cases, the interested reader is referred to [83,84] to gain an appreciation of the complexities involved in synthetic aperture systems with a wide bi-static angle ($\geq$~30° and $\leq$180°).

This work only stresses the need to take into account the difference of range between the outgoing and return signal path so that the range/time-delay curvature is matched optimally in the process of along-track integration.

The two-way path for a bi-static case, where the transmitters and receivers are not collocated, is not just $2R_n$. Rather, the total range of the two-way path R_T is now the sum of the range from the transmitter to the target, $R_{n,tx}$, with the range from the receiver to the target, $R_{n,rx}$. The two-way propagation delay is expressed as

$$n_d(n,n_a,n_r)=\frac{f_s\cdot(R_{n,tx}(n_a,n_r)+R_{n,rx}(n_a,n_r))}{c} \tag{3.9}$$

Hence, in the sea-trial case in chapter 6, the two-way path is 62m for the furthest hydrophone, and not 60m. Equation 3.9 replaces 3.8 for the calculation of total two-way range in the summation algorithm to take this into account. If this is not taken into consideration in the along-track integration of samples, then at the sampling rate of 51.2kHz, it results in an error of 68 range samples.

3.3.4 Interpolation

It is obvious from equations (3.7), (3.8) and (3.9) that there needs to be interpolation in the cross-track domain due to the fact that n_d is seldom a whole number, meaning that the required sample falls between two existing samples. Thus, interpolation is needed to provide a more accurate value for that sample. A linear interpolation between the two samples is believed to be sufficient. Alternatively, n_d can be rounded to a whole number, avoiding the need for interpolation, and its effect on image quality should be

minimal as long as the sampling interval in the cross-track direction is much smaller than the achievable resolution in that direction.

Interpolation can be used as a tool for reducing the memory requirement for image reconstruction. In order to keep the data matrix as small as possible, it can be down-sampled so that minimal memory is required for processing, and interpolation is employed during image reconstruction to estimate the removed samples.

3.3.5 Computational complexity

Let O be the complexity of the operation to obtain n_d as in (3.9), such that there are two hypotenuse calculations and an interpolation, the number of computational calculations to implement the process in (3.7) to reconstruct I_{image} with $N_a x N_r$ pixels is approximately $O.N_r.(N_a)^2$.

Making a mono-static assumption will reduce the complexity of O. The same happens when a depth of focus is introduced, where the same set of back-projected ranges and its corresponding delays are used for more than one point of interest. The reduction in computational complexity directly decreases the necessary computational time.

3.3.6 Processing gain

Coherent and incoherent processing yields a different processing gain given that the same number of along-track samples is used for aperture synthesis. For coherent processing, where the signals are summed vectorially [72(pp.70)], the processing gain in integrating N spatial samples from consecutive pings is [73(pp.25-26),74(pp.365)]:

$$G_c = 10 \cdot log(N) \tag{3.10}$$

expressed in dB. For example, for an active sonar that requires a signal-to-noise ratio (SNR) of 12dB in a single pulse (for probability of detection, PD, of 0.95 and probability of false alarm, PFA, of 10^{-3} [72]), integration of 100 coherent pulses will decrease the SNR requirement by 20dB to achieve the same level of PD and PFA.

If the pulses are summed incoherently (i.e. after square-law detection), the processing gain achievable is less than in coherent integration. This is treated as a loss in SNR relative to what would have been obtained in coherent integration, by Marcum [75]. This integration loss is a function of an incoherent integration efficiency that is less than 1 [73(pp.28)]. Defining this efficiency parameter as γ, the gain achievable in incoherent integration is:

$$G_i = 10 \cdot \gamma \cdot \log(N) \tag{3.11}$$

The incoherent integration efficiency, γ, is dependent on N, PD and PFA (and hence SNR) [Meyer Plots in 72]. By example, with PD of 0.95 and PFA of 10^{-6}, the Meyer Plots in [72] give an incoherent integration efficiency ranging from 80% for N=10, 72.5% for N=100, 68% for N=1000, dropping to 64% for N=10000. The target model used in this example is non-fluctuating.

Setting γ to be 50% such that the incoherent processing gain is 5log(N) is a conservative approximation, or for very large value of N. It is used in [76] and [77] as a simplistic and conservative approximation of incoherent processing gain, and with relation to SAS in [15(pp.86)]. When an incoherent processing gain of 5log(N) is used in this work for analytical purposes, it is worth noting that it is a conservative approximation, and in practise, incoherent processing gain in the region of 6log(N) to 7.5log(N) is realistic (N is usually within the region of 100 to 10000).

In cases where the trade-off in processing gain due to a lesser number of elements being integrated are discussed, a realistic processing gain (between 6log(N) to 7.5log(N)) is applied to give a more accurate representation of the loss in processing gain.

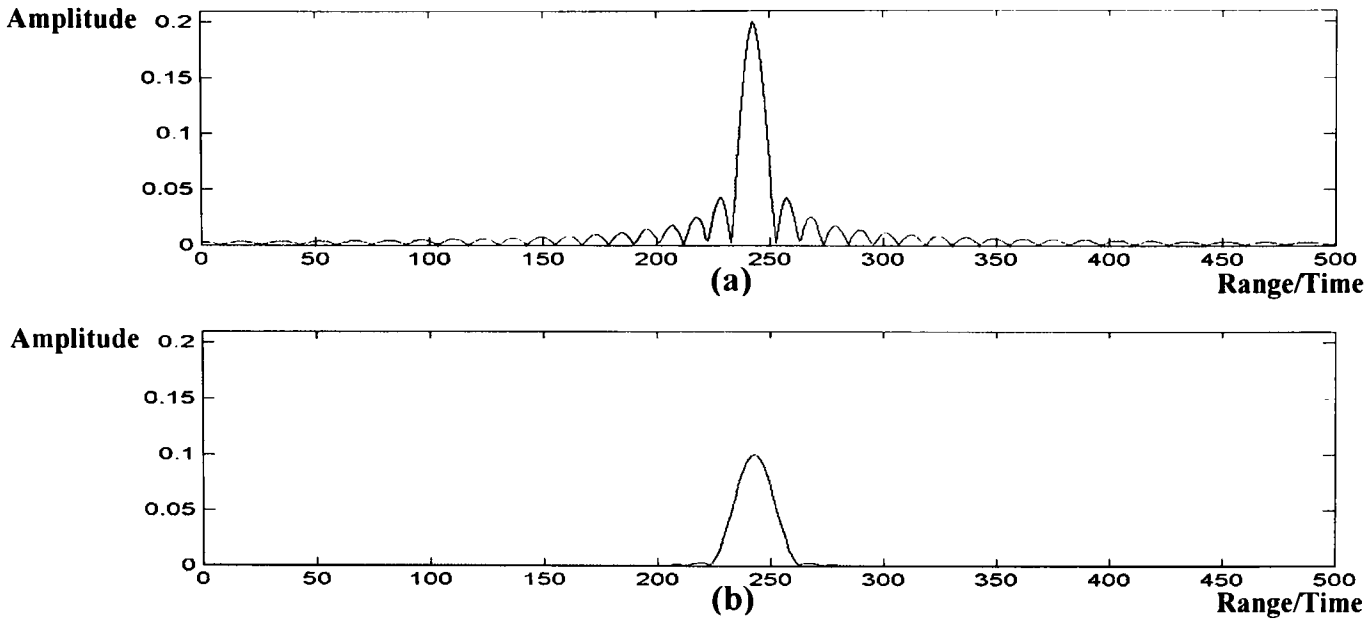


Figure 3.4: Matched filtered chirp pulse (a) without and (b) with Hanning window.

3.4 Pulse Design

Broadband pulses are used to obtain optimal cross-track resolution, and as shown in section 3.5, the along-track resolution as well in the case of incoherent processing. The transmitted signal used in this work is a linear frequency modulated (LFM) or "chirp" signal. It can be expressed as

$$s(t) = \cos(2\pi f_c t + \frac{\pi B t^2}{T}) \tag{3.12}$$

The Q-factor, f_c/B, is a good measure of the genuine degree of broadbandness, where f_c is the centre frequency and B the bandwidth of the pulse.

The use of windowing on the chirp pulses will reduce the level of range side-lobes on the matched-filtered pulses. However, because the effective bandwidth is reduced by windowing, the cross-track resolution becomes wider. This is shown in Fig 3.4.

In practical situations, unilateral weighting (where only the matched filter replica is weighted) is useful for maximising the power of transmission, such that the loss of

amplitude is offset by the much larger energy content of a non-weighted pulse transmission [36].

Where Doppler effects induced by the movements of transmitters and receivers *during* the process of transmission and receipt are detrimental to the gain of the matched-filter, the use of linear period-modulated (LPM) signals may be more appropriate [37],[38].

3.5 Along-track Resolution

The along-track resolution of an incoherent processing scheme can be derived from the geometry as shown in Fig.3.5. rx_a and rx_b are two transducer positions with beam angle θ_a, and r_0 is the closest path of approach to the target. The dotted lines are range-ambiguity curvatures with respect to the transducer positions, and they correspond to the matched-filtered responses from a point target marked '**x**'. The point target matched-filtered responses range from $-\Delta r$ to Δr.

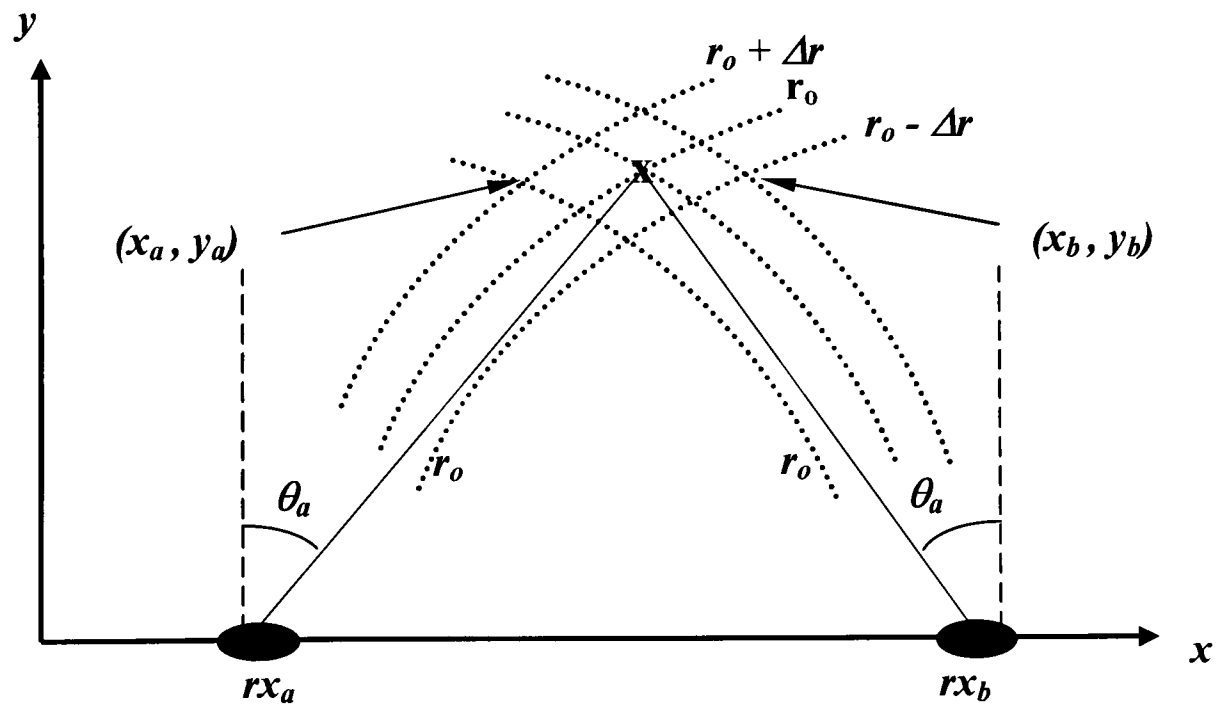


Figure 3.5: Geometry for the derivations of along-track resolution in incoherent processing.

The along-track resolution of the system is defined in terms of the correlation of the overlapping responses. This resolution is taken to be twice the along-track increment that causes the correlation to drop to half its peak value, considering only a cut along the along-track dimension of the azimuth-range ambiguity function [39]. Thus, the cross-track resolution, $P_r = 2.\Delta r$, and the along-track resolution, P_z, can be expressed as

$$P_z = x_b - x_a \tag{3.13}$$

With the assumptions that

$$x_b \gg x_a \text{ and } r_o \gg \Delta r/2 \tag{3.14}$$

which implies a long synthetic aperture length and a fine cross-track resolution. It can be shown that (Appendix A):

$$P_z = \frac{2\Delta r}{\sin\theta_a} \tag{3.15}$$

By considering the directional response of the transducers having a 3dB effective beamwidth [40],

$$\sin\theta_a = \frac{1.39\lambda}{\pi D_p} \tag{3.16}$$

Substituting (3.16) into (3.15) gives, with a conservative approximation,

$$P_z = \frac{4.5 \cdot \Delta r \cdot D_p}{\lambda} \cong \frac{3P_r D_p}{\lambda} \tag{3.17}$$

and for broadband pulses

$$P_z \cong 1.5QD_p \tag{3.18}$$

which is an important result in incoherent SAS processing. It shows that the use of broadband pulses is advantageous since the cross-track resolution influences the along-track resolution proportionally. It also shows that the wider is the beamwidth, the better the along-track resolution will be, and also implied that the along-track resolution improves as the synthetic aperture length covering the point of interest increases.

Simulations were used to confirm the results obtained. A point target 150m away is pinged by a chirp pulse with a Q-factor of 2.5. The along-track spacing is 3.33m.

The first simulation studies the dependence of the along-track resolution on θ_a. The along-track resolution is measured as the along-track spacing that corresponds to the half-level of the target response in the processed image, and it is computed for synthetic apertures of varying length to represent varying θ_a in (3.14). The cross-track resolution, P_r, is first established from the pulse-compressed signal to be 12.75m. Hence a plot based on (3.15) can be made and compared to what is obtained from the simulation. The results are shown in Fig. 3.6. When θ_a increases, the $x_b \gg x_a$ assumption becomes valid and thus the two theoretical plots converge. The simulation verifies the validity of equation (3.15) in terms of the dependence of the along-track resolution on the beam angle θ_a.

Such dependence of θ_a implies that the omni-directionality of the physical elements in the synthetic aperture is a desirable feature for finer along-track resolution. Besides that, one can also deduce that in the case of non omni-directionality, which is true under most circumstances, there will be a limit on the synthetic aperture length beyond which there is a smaller improvement in the along-track resolution. This synthetic aperture length depends on the CPA of the point of interest. It then follows that in order to achieve uniform along-track resolution at all ranges, a varying synthetic aperture length will be needed in the image reconstruction process.

The second simulation maintains θ_a constant (θ_a=1.15rad), but varies the Q-factor of the chirp pulse so that the cross-track resolution, P_r, of the matched-filtered output changes. The corresponding along-track resolutions are then measured and plotted. The results are shown in Fig. 3.7. As the cross-track resolution becomes finer, the validity of the assumption in (3.14) improves. Thus the theoretical plots at fine cross-track resolution converge. The simulation verifies the relationship between the along-track resolution and the cross-track resolution. It highlights the benefit of transmitting broadband pulses with typical Q-factor <1, where the cross-track resolution is fine, resulting in an improvement of the along-track resolution.

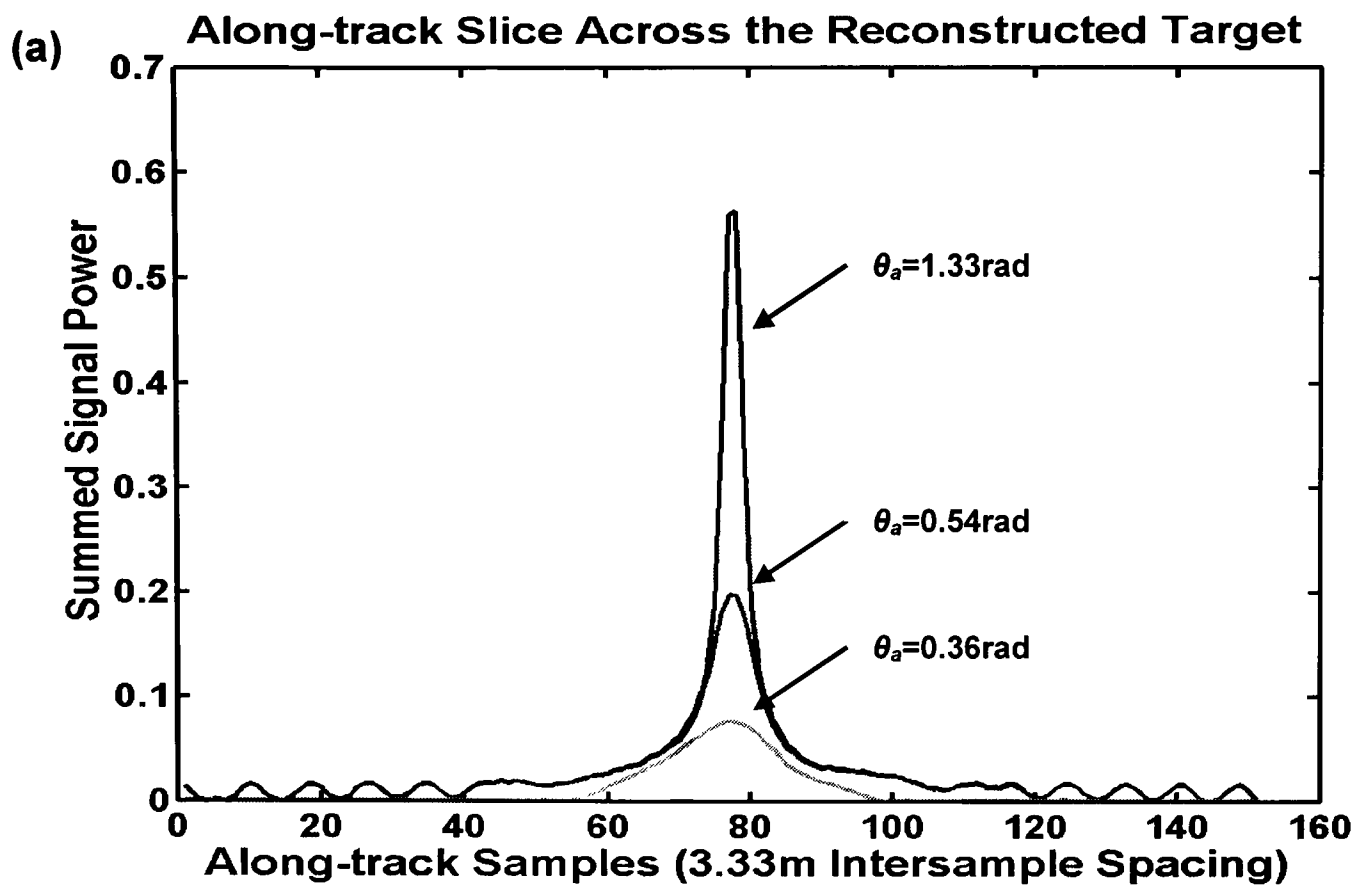


Figure 3.6: (a) The along-track slice shows the change in along-track resolution as θ_a changes. **(b)** The dependence of the along-track resolution on θ_a is shown by simulation and compared to the theoretical predictions.

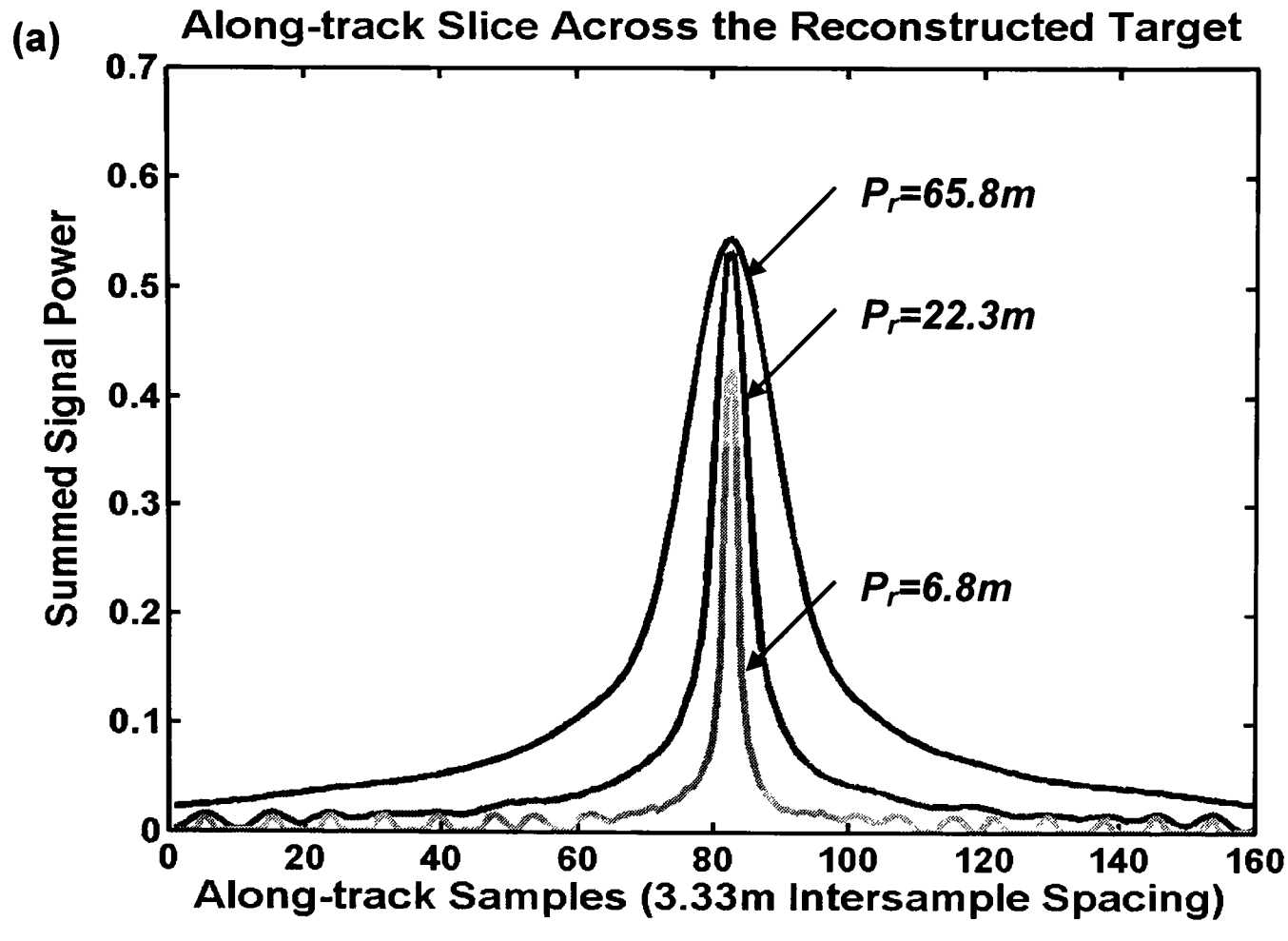


Figure 3.7: (a) The along-track slice shows the change in along-track resolution as P_r changes. **(b)** The dependence of the along-track resolution on P_r is shown by simulation and compared to the theoretical predictions.

3.6 Dynamic Focussing

Having established the relationship between the along-track resolution and the beam angle θ_b, it is clear that in order for the along-track resolution to be consistent over all cross-track ranges, it is necessary to have a variable synthetic aperture length for the different ranges. Such a requirement fulfils the relationship between the physical and synthetic beam, a relationship which produced equation (2.2). This equation underlines the linear dependence of the synthetic aperture length D_s, on the range between the target and the aperture, R_0. Fig. 3.8 illustrates this dependence.

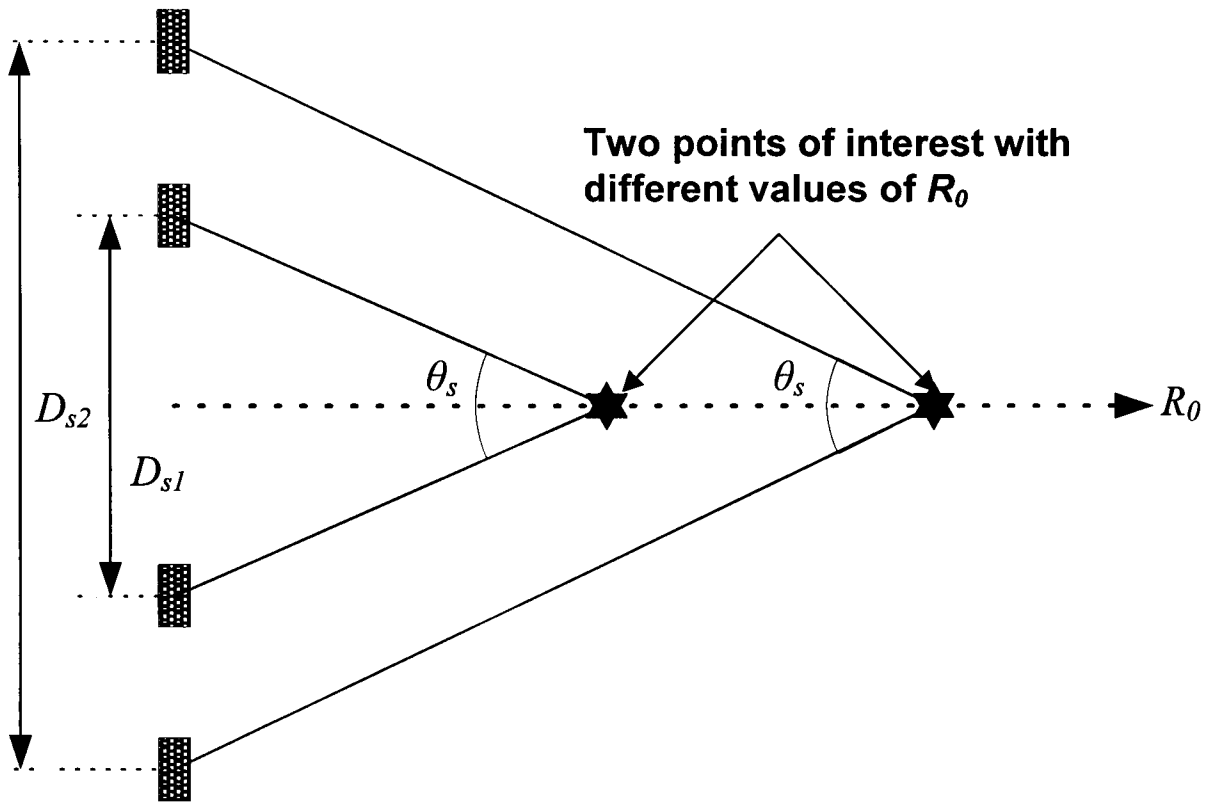


Figure 3.8: Dynamic focussing by varying the length of the synthetic aperture according to the range to the aperture, hence keeping θ_s and the along-track resolution constant.

In order to implement this, the synthetic aperture length used to focus a target with smaller R_0 may be shorter than it could have been, thus limiting its along-track resolution. In other words, the along-track resolution is capped by the level achievable at the farthest range of interest. Thus in practice, if achieving constant along-track resolution for all ranges is not paramount, it is not uncommon to use the largest

synthetic aperture available so that an optimal along-track resolution is always achieved albeit it degrading with increasing R_0.

3.7 Self-noise

One characteristic of images summed incoherently, due to the removal of phase, is the presence of self-noise or background-clutter surrounding the focussed point-target. It can be defined as the energy contained beyond the half-of-peak level perimeter surrounding the incoherently focussed image (Fig. 3.9). The pattern of distribution and the level of self-noise are both influential factors affecting the quality of the processed image. A low signal to self-noise ratio will increase the likelihood of targets with low reflectivity being masked by stronger targets nearby, as well as the appearance of false-targets contributed by the self-noise of adjacent strong targets.

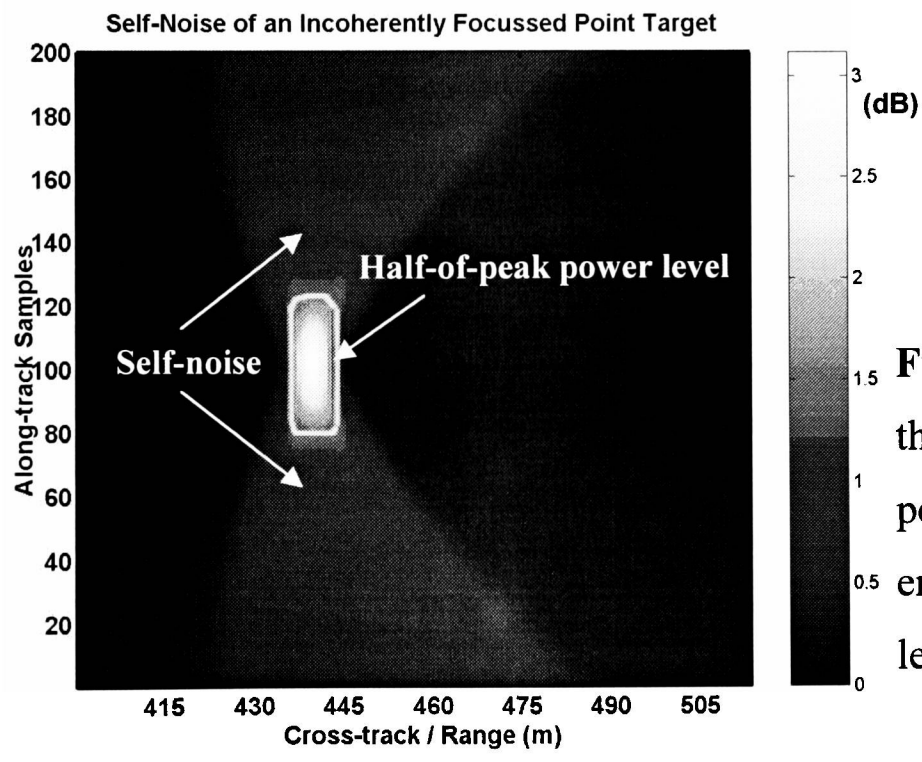


Figure 3.9: Self-noise around the incoherently focussed point-target, defined as the energy outside the half-of-peak level boundary.

The self-noise pattern can be managed by the selection of elements and the use of weighting functions in SAS processing. This fact is further exploited in Chapter 4.

3.8 Grating Lobes

In coherent processing, grating lobes appear when the inter-ping spacing exceeds $\lambda/2$, and this is especially evident when the pulses are narrowband. However, with incoherent processing, under-sampling in the along-track direction does not cause the appearance of grating lobes. Rather, it causes a reduction in the signal to self-noise level due to a lesser number of elements insonifying the same target. This is also true in the coherent case. In both cases, there is no reduction in the quality of along-track resolution. Along-track slices from the simulation results of the incoherent and coherent processing of uniformly under-sampled data are shown in Fig. 3.10.

In the case of incoherent processing, such a property provides the convenience of under-sampling in the along-track direction without the presence of grating lobes. The

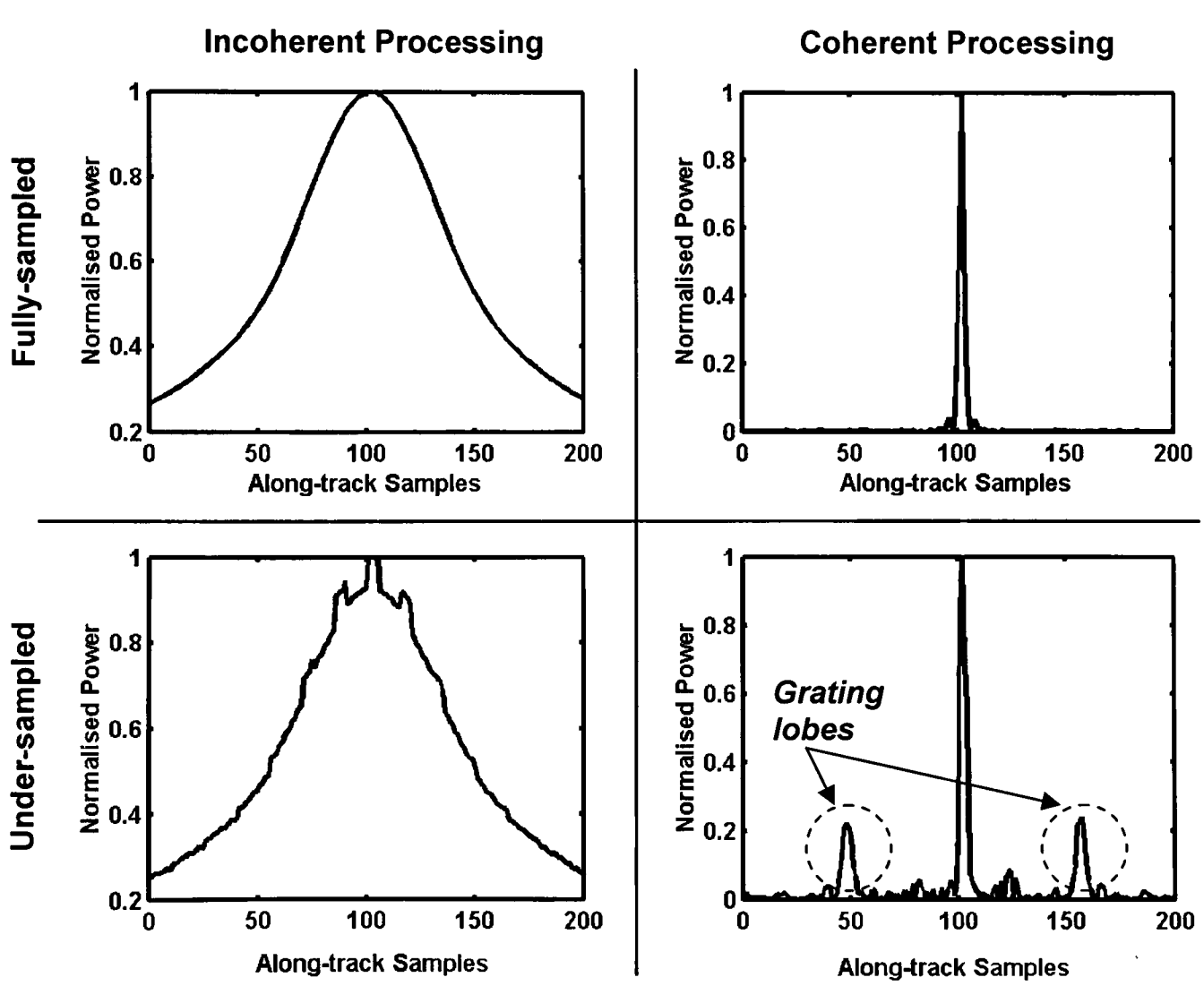


Figure 3.10: Along-track slices show that grating lobes appear when under-sampled data were processed coherently, but is absent in the incoherently processed image. The samples are uniformly spaced in both cases.

constraint in equation (2.4) governing coherent SAS processing is no longer valid, and the new lower constraint on *PRF* becomes

$$PRF \geq \frac{v}{P_z} = \frac{\lambda \cdot v}{3 \cdot P_r \cdot D_p} \tag{3.19}$$

The broader synthesized beam (lower along-track resolution) via incoherent processing, has relaxed the constraint on the *PRF*. Because P_z is bigger than P_s, v can be increased without violating the constraint. Thus with the same *PRF*, the tow speed, v, can now be increased to achieve a higher mapping rate. This increase in mapping rate, however, is at the expense of signal to self-noise ratio since less elements are available within the maximum length of the synthesized aperture. The limit of acceptable signal to self-noise ratio degradation, which varies depending on the target applications, must not be exceeded.

3.9 Tolerance to Motion Errors

Incoherent SAS processing does not demand a high level of precision in the knowledge of the actual along-track path compared to coherent SAS processing. It is thus more tolerant to unknown path deviations.

It is fair to assume that in coherent processing, even though minor unknown path deviations cause blurring to the image, it, nevertheless, still has a better sharpness than an incoherently processed image. However, this is only true if the intended target has a strong reflectivity in contrast to its background, and that the path deviations have zero mean value. The first condition may be met in some applications, but the latter is rarely fulfilled. This means that the path deviations will accumulate as the synthesized aperture gets longer, and consequently, the coherently processed image becomes severely grainy.

The incoherently processed image will also be blurred, but it retains the target's cognitive [60] properties far more satisfactorily with little graininess. There are two main reasons for this. Firstly, because coherent processing produces high resolution images, such that it has a fine synthetic beam, it is inevitable that the image appears "grainy" when there is mismatch between the estimated and the actual back-projected range-curvature function. Secondly, for the same reason that the gain of N samples added coherently is higher than the gain achievable if added incoherently, the fall in processing gain is far greater in coherent processing than in incoherent processing if there are any mismatch in range-curvature functions. Hence, the detection properties are better with incoherent processing despite a reduction in sharpness.

A simulation is run to illustrate the points made. Four equally reflective point-targets are simulated with path deviations generated from a uniformly random distribution with zero mean and a standard deviation of 0.9m.

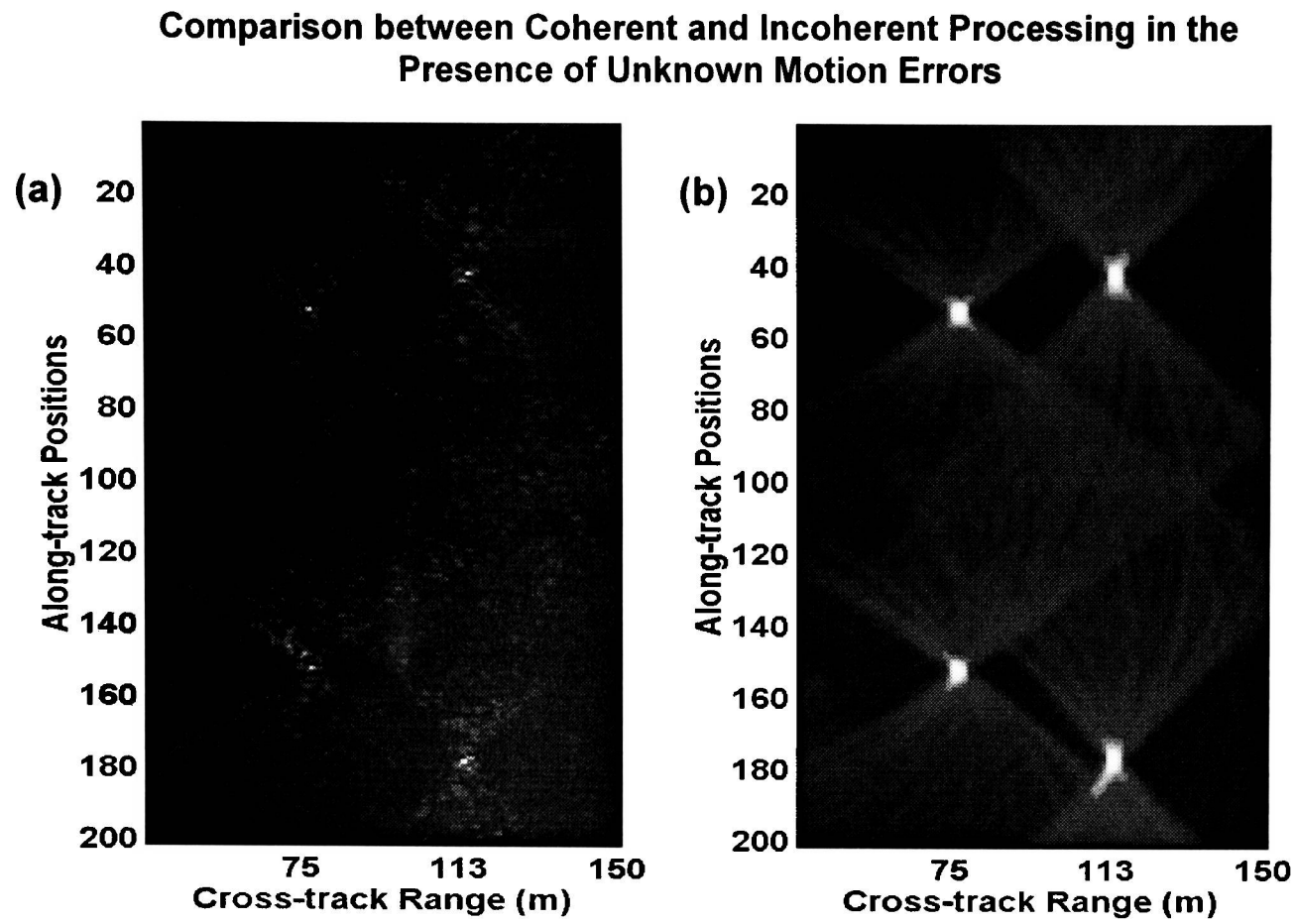


Figure 3.11: SAS image of 4 point targets processed (a) coherently and (b) incoherently with random unknown motion errors. The plots are normalised by its respective maximum, and represent the integrated energy in dB.

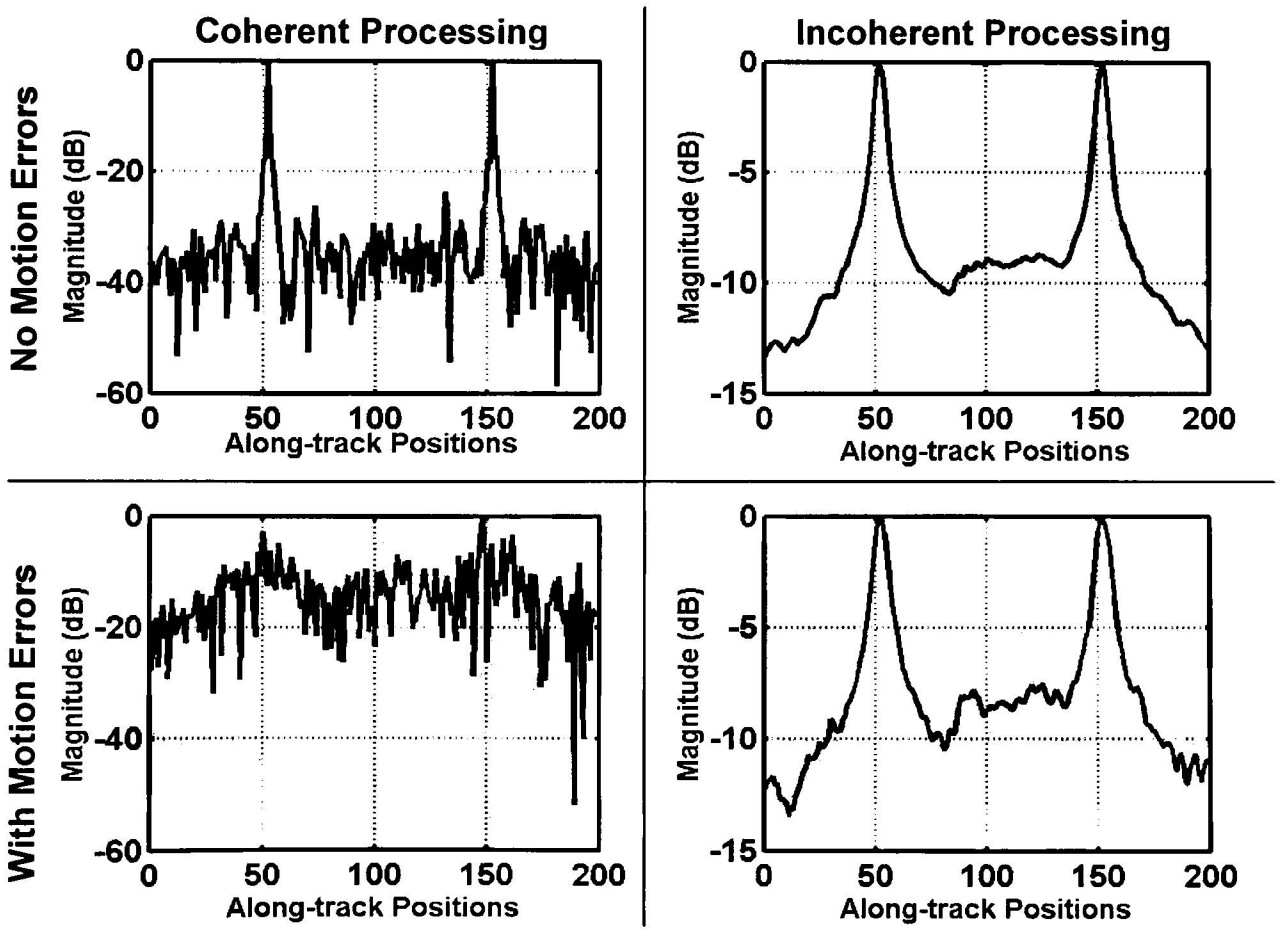


Figure 3.12: Along-track and cross-track slices showing the greater tolerance to random motion errors in incoherent processing. Note the difference in scale between the left and right plots.

Fig. 3.11 shows the images of the 4 point-targets processed coherently and incoherently. Grains are obvious on the coherently processed image and the point targets appear unfocussed and smeared, whereas on the incoherently processed image, the targets, although not as sharp, still have a relatively strong focus of energy with no appearance of grains. Slices of the images are taken along the along-track direction, cutting through the first two point targets, and compared to the corresponding slices from the processed images where no motion errors were introduced. These slices, in Fig. 3.12, show a more severe degradation in the processing gain of the coherently processed targets when there are random unknown motion errors. It is worth noting that the motion errors commonly experienced may not have a zero mean, in which case the unknown errors are cumulative and yield a more detrimental effect to the coherently processed image.

3.10 SAS Imaging Modes

There are two main imaging modes applicable in SAS imaging; stripmap and spotlight modes, terms originated from, and coined in, synthetic aperture radar [41].

Stripmap mode is the typical mode of imaging in survey and terrain mapping applications where large areas need to be covered. It is the imaging mode implemented throughout this work. In this mode the transducer's real beam faces the same direction, without any angular bias, for each and every ping, thus ensuring an even level of beam exposure across the swath of interest. Transducers with a wide beam are preferred so that a higher processing gain is obtainable via a longer synthesizable aperture.

Spotlight mode, on the other hand, involves steering the beam of the transducer towards a fixed spot on the scene for every ping. This is either in the form of mechanical steering, or electronic beam-steering with an array of transducers. This mode of operation is usually applied when a high resolution image is required of a specific, well-defined area. The raw data of a point target obtained in spotlight mode is similar to the raw data in stripmap mode with omni-directional transducers. This is due

to the fact that, ignoring acoustic absorption, the returns are equally strong across the whole synthesized aperture regardless of its length.

Most proposed SAS systems work in the stripmap imaging mode, however, in practice, omni-directional transducers that satisfy both the bandwidth and sensitivity requirements of the system are rarely available. In incoherent processing, the possibility of having a large inter-ping spacing suggests that it is not unusual to have a long synthesized aperture with few elements, where the limiting factor on the processing gain is the effective (3dB) beamwidth of the transducers. In this case, it is possible to have a longer synthesized aperture to improve the processing gain by including elements whose 3dB beam does not cover the point of interest. The condition for this is that the directional response of each individual element with respect to the point of interest must be taken into account in the SAS processing. This is done by introducing a weighting function into the image reconstruction algorithm in equation (3.7).

3.11 Weighting Function

In order to include elements whose 3dB beam does not cover the point of interest, it is necessary to introduce a weighting function in the image reconstruction algorithm. In order to obtain a maximum gain, the weighting function applied must match the directional response of the individual elements in the synthetic aperture. The argument for this is straight forward.

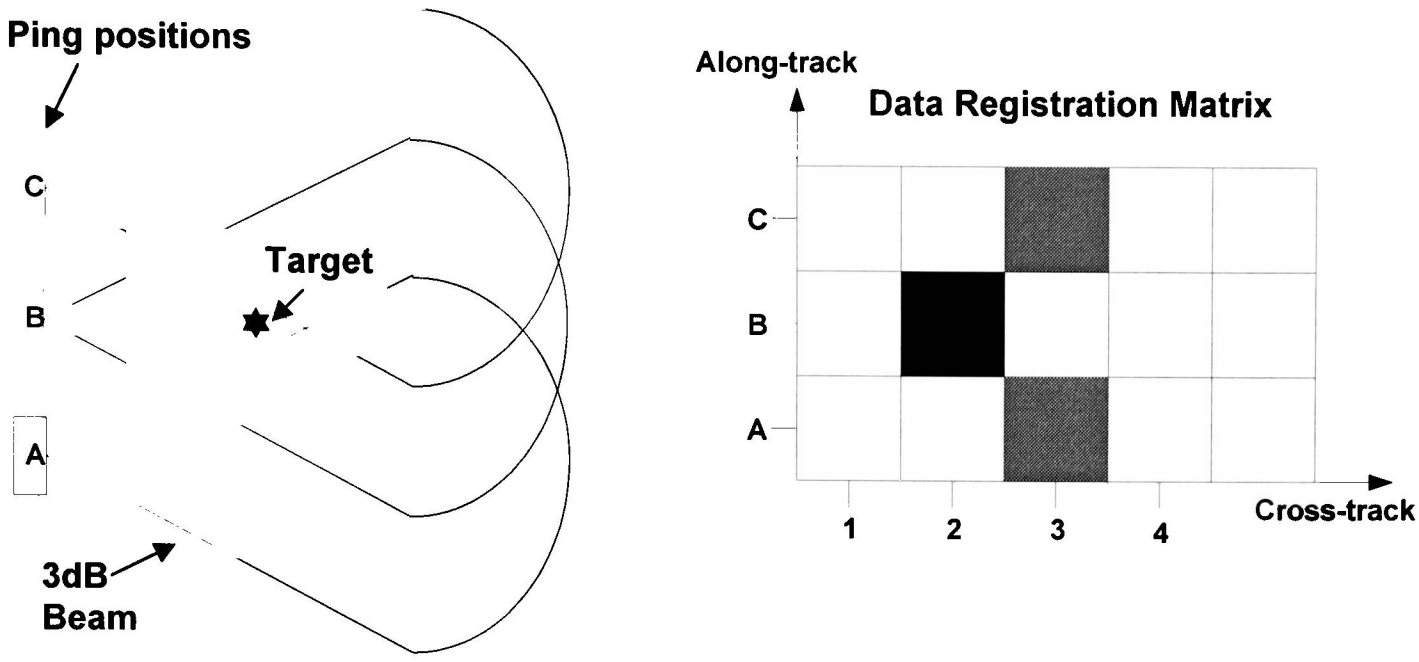


Figure 3.13: A target seen from three ping positions, with returns at different intensities recorded on the data registration matrix due to the directional response of the transducer.

Consider the scenario in Fig. 3.13, where there are three transducers' ping positions named as 'A', 'B' and 'C' surveying a target represented by the hexagonal shape. The target is within the 3dB beam of 'B' ping, but not for 'A' and 'C' pings. Thus, on the image registration matrix, the returns of the target detected by 'A' and 'C' is weaker than in 'B', as shown with a shade of grey versus black. Now, consider 'C' alone. For this single target, its return is recorded in pixel [C,3]. However, if there are other targets present, the energy in pixel [C,3] will represent the sum of the reflected energy from all the targets that lie on the same range-line of ambiguity. Based upon the directional response of the transducer, it can be deduced that the amount of contribution of each target along the range-line of ambiguity towards the energy in [C,3] depends on the angle of the targets with respect to the transducer. Hence, matching the weighting function with the directional response of the transducer is to acknowledge the fact that the targets along the range-line of ambiguity do not contribute equally to the total detected energy. By taking this into account, the error between the actual and the estimated energy distribution pattern is minimised, thus reducing the level of self-noise around the focussed target.

Equation 3.7 is thus modified to

$$I_{image}(n_a, n_r) = \sum_{n=1}^{N} w(n, n_a, n_r) \cdot I_{data}(n, n_d(n, n_a, n_r)) \tag{3.20}$$

where $w(n,n_a,n_r)$ is the weighting function applied across the synthetic aperture that corresponds to the point of interest at (n_a,n_r). The fact that the weighting function is also a function of n_a and n_r says that it is a function of the directional angle of the point of interest with respect to the element on the synthetic aperture.

Simulation results to compare the effect of using a matched weighting function are shown in Fig. 3.14. Three point targets are imaged with an element that has non-uniform directional response. The image processed with a matched weighting function has a significantly lower level of self noise. This may not be obvious on the processed images, but the plot of slices across targets in both directions showed that the self-noise level is up to 3dB lower in the cross-track domain if a matched weighting function is applied. In the along-track direction, however, there is a very small degradation. The real improvement is the reduction of the level and spread of self-noise in areas surrounding the focussed target. If more slices are taken at different angles instead of just strictly in the along-track or cross-track direction, it can be observed that this improvement is present for most directions around the target, albeit a slight degradation in the along-track direction alone. Hence, it produces a more contained, limited and even spread of self-noise around the target. Further results of this are shown in the tank trial results in chapter 7. This is true assuming that the signals are not noise-limited. Otherwise, the benefit is not justifiable in the light of the fact that an inverse, rather than matched, weighting function is usually optimal in a noise-limited scenario.

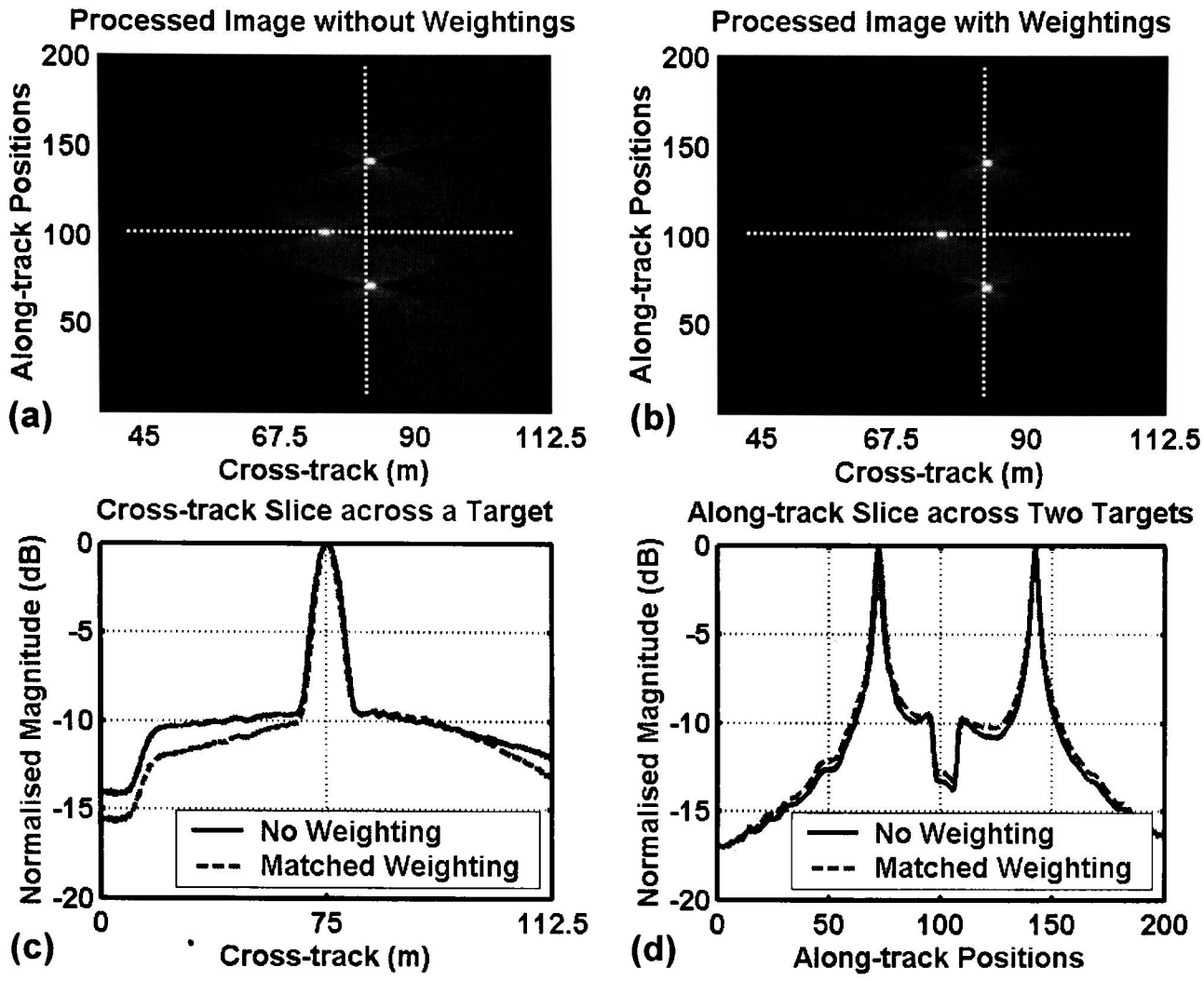


Figure 3.14: The image of 3 point targets processed (a) without weighting and (b) with weighting matched to the response of the transducer. For comparison, the slices in the (c) cross-track and (d) along-track direction over the targets as indicated by the dotted line over the processed image.

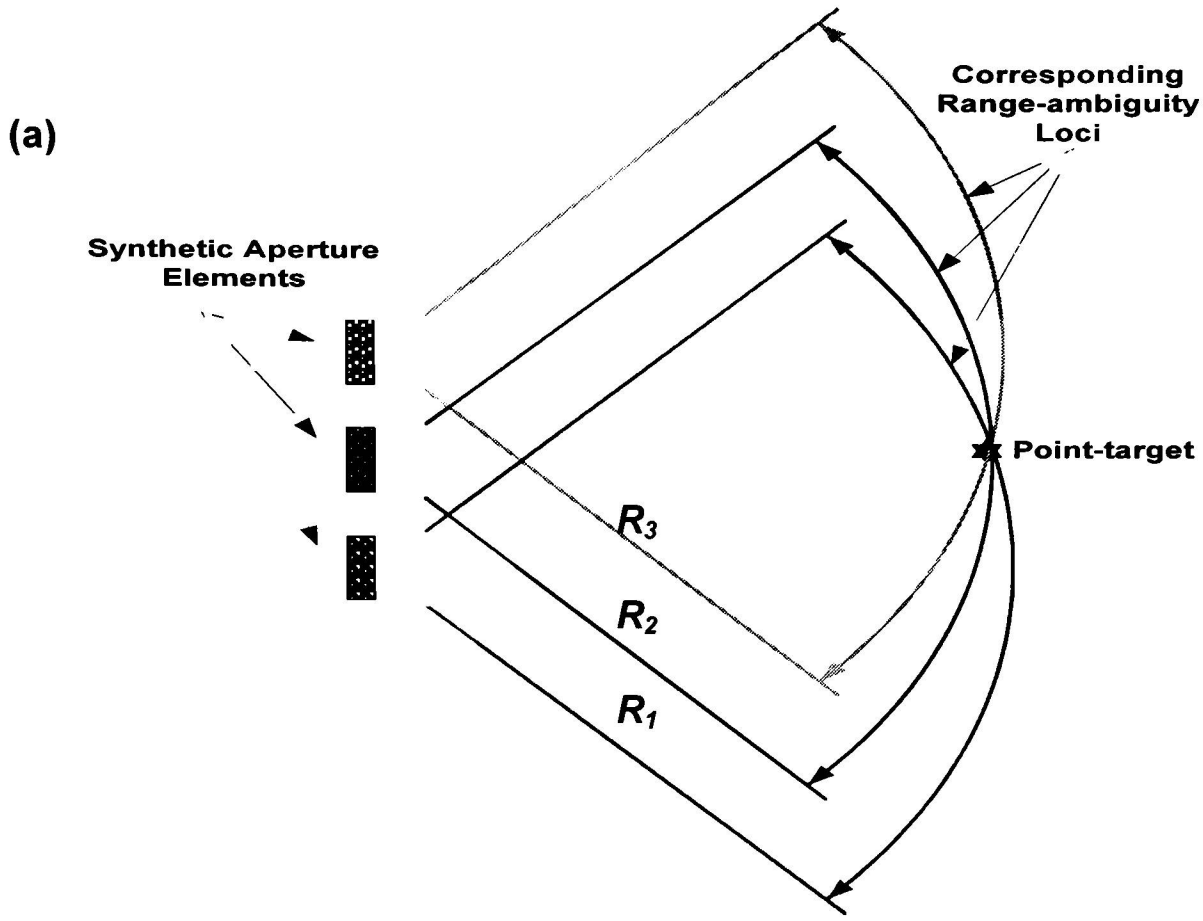
In the case where exactly the same synthetic aperture is used to focus all the points of interest, the final image will be non-uniformly weighted in the along-track direction. It can be avoided by using a different synthetic aperture for points at different positions in the along-track direction, such that the point of interest is always centred relative to the synthetic aperture. In another words, the initial value of n in the summation of equation (3.20) becomes a function n_a. This is practical because in many imaging situations, the synthetic aperture length used in processing is usually smaller than the overall length of the sonar towed path. Otherwise, the weighting in the final image can be removed by compensating it with a gain function. This, however, will increase the level of self-noise as well.

3.12 Point Target Energy Response

In order to study the effect of the synthetic aperture on the energy distribution pattern, it is necessary to have a scheme that enables an accurate representation of the energy distribution on and around a focussed point target, or the point target energy response. This scheme needs to be able to take into account the configuration of the synthetic aperture, the processing algorithm and the application of weighting function.

In this work, a range-ambiguity back-projection scheme is used. It is based upon the plot of range-ambiguity loci crossing on a point target (Fig. 3.15(a)). The distribution of the loci on and around the point target is the point target energy response of the synthetic aperture.

This is a simple yet powerful tool in the design process of an incoherent SAS system. It allows a quick and accurate estimate of the energy distribution pattern for a particular configuration or arrangements of elements in the synthetic aperture. Fig. 3.15(b) shows the point-target response plot for a uniform, monostatic, non-weighted synthetic aperture in two locations, both of which centred on the aperture and at a range of 80m and 100m respectively. The overlap of self-noise is highlighted. It shows how distributed energies from adjacent targets can contribute to an overall higher level of self-noise in the image.



Range-ambiguity Loci Over Two Point Targets

Figure 3.15: (a) The range-ambiguity loci of elements on a synthetic aperture towards a point target. (b) The point-target energy response of a uniform *2 m* inter-ping spacing synthetic aperture by plotting corresponding range-ambiguities loci.

Note that the scheme of merely plotting lines in Fig. 3.15(b) relies on the density of the lines to represent the intensity of the energy present, which is thus limited especially for purposes of analytical comparisons between two different synthetic aperture arrangements, or when the intensity of the lines vary such that the elements are directional. This scheme can be easily extended to address these concerns, and take into consideration the weighting function as well as a bi-static configuration of elements. An image can be used such that the lines are plotted as pixels on the image. In this way, points on the lines that overlap will have pixels with larger values. Fig. 3.16 illustrates this with the same synthetic aperture as the one used in Fig. 3.15(b).

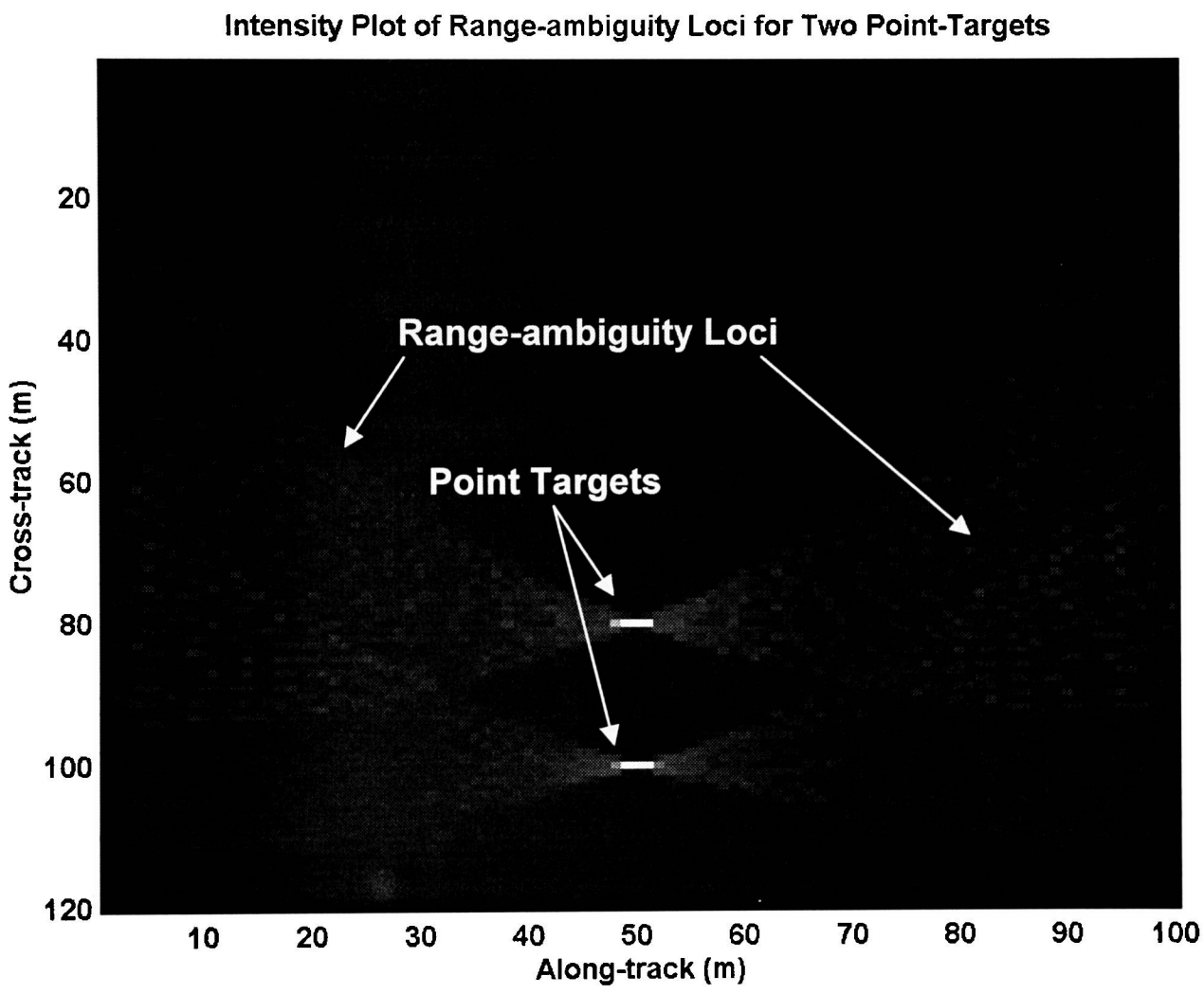


Figure 3.16: Intensity plot of range-ambiguity loci over two point targets, showing the point-target energy response of the synthetic aperture at the two locations.

This method allow one to predict, quickly and visually, the point-target energy response in the incoherent processing of a synthetic aperture with bi-static configuration of any form, and can be extended to predict the volumetric pattern of

point-target response in 3-dimension. This scheme is applied in the study of the algorithms presented in the later chapters.

3.13 Image Quality Benchmark

How does one compare the quality of an image processed with two different algorithms? There are some general criteria that a high quality image fulfils, like fine resolution, good contrast and strong signal to noise ratio. The first two influence the cognitive property of the image while the latter influences its detection property. The cognitive property of the image relates to its quality of recognition [60]. The detection property, though not completely distinct, relates to the probability of detecting a target in the presence of noise, reverberations or shadows of stronger nearby targets. Depending on the type of application, the property of which the quality benchmark is based upon and optimises may be different. The detection property is of priority in a mine-hunting application, whereas cognitive property is more important in the imaging of underwater archaeological sites.

In the context of incoherent SAS imaging, the resolution of the processed image is often difficult to quantify, especially if there are no available a priori knowledge of the target scene. The contrast of the image is a form of statistical measure, requiring no pre-determined knowledge of the target scene, and the simplest model being the standard deviation normalised by the mean of the image [27]. This differs from the standard definition of contrast in image processing, but rather focuses on the measure of structural content in the image. The measure of signal to noise ratio too, like resolution, requires the a priori knowledge of a target scene to give an accurate comparison.

Thus, a reliable way of comparing image quality is to take the measure of its contrast. It is worth noting that its accuracy in representing the overall image quality increases with the presence of structural content in the image. Such a comparison is usually done on the statistic of an individual, or a small group of slices, in the along-track direction

as most of the algorithms in question deal with the along-track processing of the SAS data. Let this quality benchmark be q, and measuring the contrast over individual along-track slices, n_r, will give

$$q_{n_r} = \frac{\sigma_{n_r}}{\mu_{n_r}} = \frac{\sqrt{\sum_{n=1}^{N} (I_{image}(n, n_r) - \mu_{n_r})^2 \Big/ N}}{\sum_{n=1}^{N} I_{image}(n, n_r) \Big/ N} \tag{3.22}$$

where σ and μ are the corresponding standard deviation and mean respectively, and N is the total number of along-track samples in the slice.

As an example of its implementation, this quality benchmark is tested on two incoherently processed point targets, one of which is (a) deliberately simulated perfectly and another which is (b) processed with a mismatched range-curvature function (Fig.3.17).

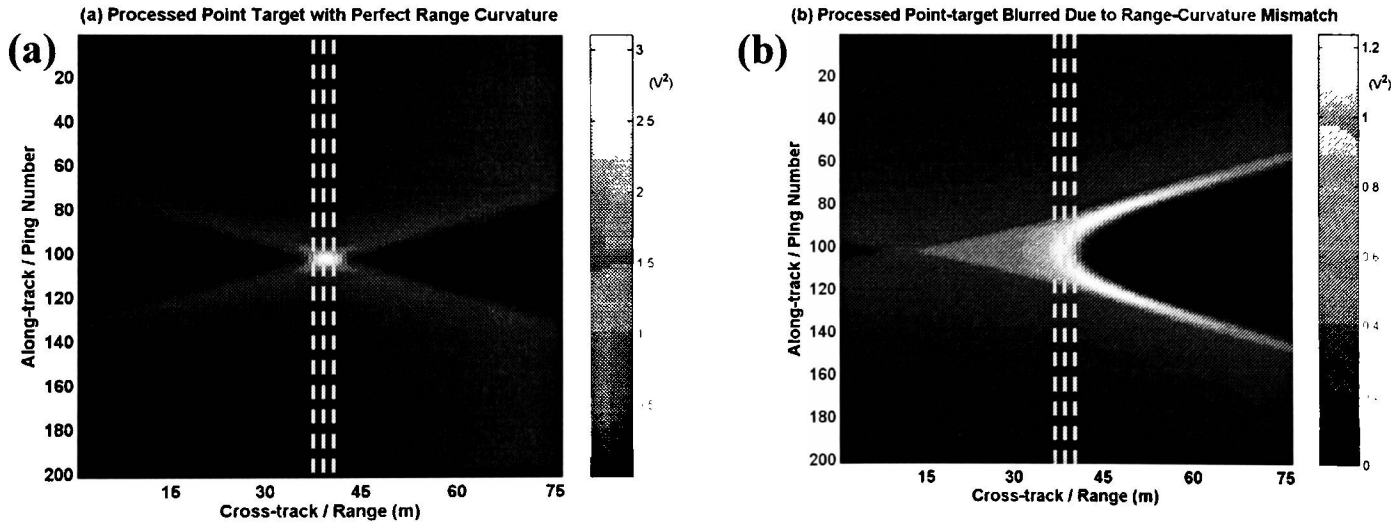


Figure 3.17: (a) Point target with processed with perfect range-curvature, and (b) point target processed with a deliberately mismatched range-curvature.

The dotted lines over the targets indicate the position of the along-track slices that are chosen for the calculation of q, and the three slices correspond to n_r (cross-track range) of 40m, 41m and 42m. They are chosen because they are within an area influenced by

the presence of a target. The standard deviation is calculated for values along the dotted lines and divided by its mean, and the results are as such:

	n_r = 40m	n_r = 41m	n_r = 42m
Image (a)	q_{nr} = 1.59	q_{nr} = 1.75	q_{nr} = 1.77
Image (b)	q_{nr} = 1.34	q_{nr} = 1.35	q_{nr} = 1.30

The higher value of q_{nr} indicates a stronger structural presence in the along-track slice at n_r. The mismatch in range curvature had caused q to drop in image (b).

3.14 Design Considerations in Incoherent SAS Imaging

It is obvious from the discussions in this chapter that there are many parameters that influence the outcome of the incoherent imaging process. The consideration for the design parameters should start with the definition of the quality that is most desirable, one of which the design of the system would seek to optimise. This is then offset by limited resources related to the cost and availability of transducers, survey time, processing time and the system's complexity.

In order to have an incoherent imaging system that optimises the image quality, one important factor is the consideration of how many pings per point of interest are needed first, which is based upon the required signal to self-noise ratio. Then, by setting a requirement for the along-track resolution and cross-track resolution, the bandwidth of the transmitted pulse can be decided. The along-track resolution can be easily constrained by the use of highly directional elements, especially if bandwidth is scarce. The inter-ping spacing, which determines the coverage rate of the system, is often limited by the needed number of effective pings per point of interest when given the beamwidth of the physical elements. The coverage rate can be increased at the expense of signal to self-noise ratio and along-track resolution.

An alternative approach would be to set the needed coverage or mapping rate first. Given the beamwidth or directionality of the element, the effective pings per point of

interest can be known. Setting the bandwidth of the transmitted pulse, and thus the cross-track resolution, will give the achievable along-track resolution. The signal to self-noise ratio can be estimated from the available effective pings per point of interest. It can be increased at the expense of mapping rate.

Hence, the overall design paradigm encapsulates the balance between the achievable signals to self-noise ratio plus along track resolution, and the achievable mapping rate, where their mutual effect reduces as the beamwidth of the individual elements increases. Having fixed the point of balance between these two factors, the along-track resolution can be further increased via the increase in cross-track resolution. Weightings need to be applied in cases where the elements are highly directional and yet many elements are needed in the process of incoherent summation.

As a design example, a 50kHz imaging system with bandwidth of 20kHz (Q=2.5) is considered. Given that 100 pings are needed per point of interest (to achieve gain of approximately 13dB), the range of interest is 20m-150m, and that 3 transducers with beamwidth of 1.05rads (60degrees) are available, the transducers can be built as an array and their maximum separation can be calculated (Fig. 3.18).

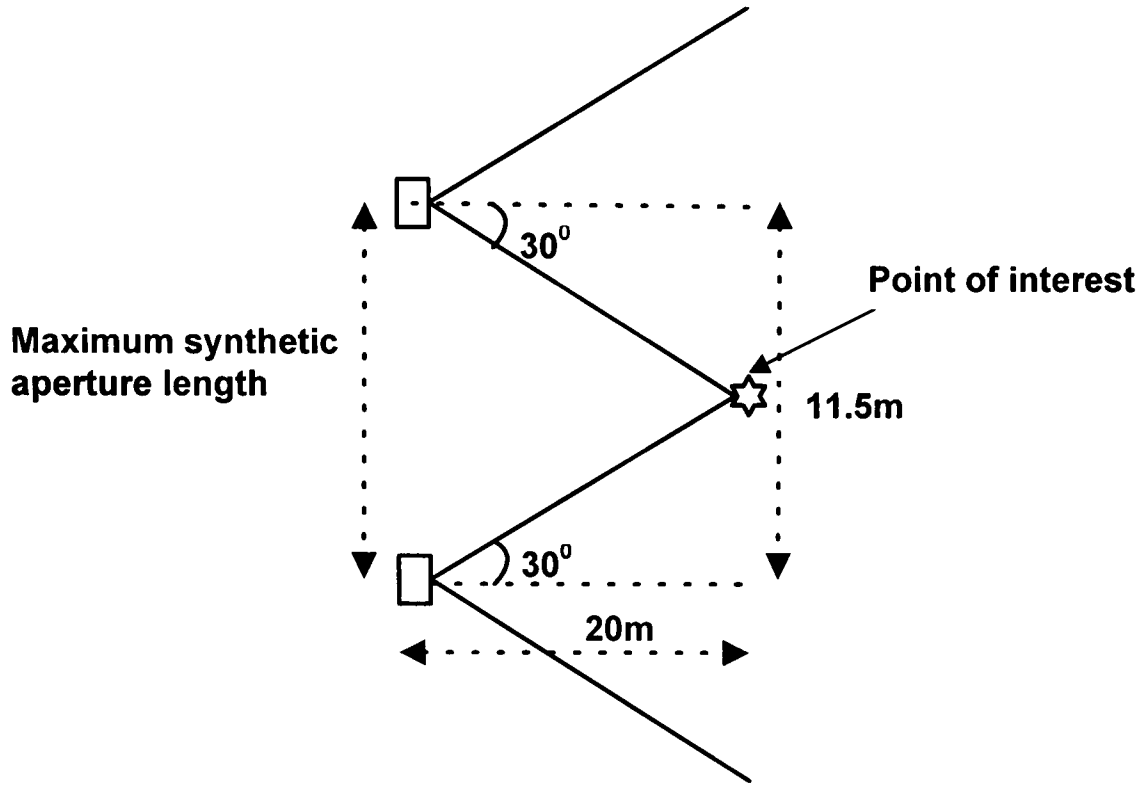


Figure 3.18: Maximum synthetic aperture length limited by the beamwidth of the transducer and the minimum range of interest.

The maximum synthetic aperture length is found to be 11.5m, and hence to meet the requirement of 100 pings per point of interest (such that N=100 in along-track integration), the maximum *inter-element* spacing of the transducer is 11.5/100=0.12m. Because there are 3 transducers the maximum *inter-ping* spacing is 3x0.12=0.36m. The upper limit of PRF (as set by the cross-track range of interest) is $1500ms^{-1}/(2x130m) = 5.8Hz$. For the lower PRF limit, choosing a PRF of 5Hz gives a maximum achievable tow speed of $1.13ms^{-1}$. Setting a tow-speed of $1ms^{-1}$ will then give an inter-ping spacing of 0.23m, and this is acceptable because it does not exceed the maximum inter-ping spacing of 0.36m. The 3 transducers should then be attached 0.08m apart onto the tow platform. The mapping rate in this case is $130m^2s^{-1}$. The cross-track resolution and along-track resolution is 0.08m and 0.24m respectively.

Designing a coherent system with the same available hardware and complexity, while satisfying the $\lambda/2$ constraint (a bigger constraint than the required N in coherent cases), and pushing the PRF to 5.5Hz, will only provide a maximum tow speed of $0.08ms^{-1}$, and a mapping rate of $10.4m^2s^{-1}$. The along-track resolution, however, is 0.02m.

The computational speed for incoherent processing is at least two times faster than for coherent processing, given the use of the same time-domain algorithm. However, where the system needs to process information close to real-time, the computational requirements still prove to be too demanding. Where shorter processing time is a primary requirement, along-track resolution and signal to self-noise ratio can be traded off by using a smaller number of elements in processing, as well as by the implementation of a depth of focus such that the same range back-projection function is used for points of interests in more than one range.

3.15 Core Advantages and Disadvantages of Incoherent SAS Processing

Having established the key properties of incoherent SAS processing, it is clear that there are some key advantages in incoherent processing in terms of overcoming the limitations present in coherent SAS imaging, and these are summarised against the background of the necessary trade-offs.

The first *advantage* is the allowance of sparse sampling in the along-track without the occurrence of grating lobes. One sparse sampling scenario is to keep the synthetic aperture length constant while reducing the number of elements, and the other is to keep the number of elements constant while increasing the synthetic aperture length. Sparse sampling can be implemented to the convenience of the surveying process, such as to have a higher mapping rate, shorter survey time, and smaller hardware requirement. It can also be implemented just before the process of incoherent summation on readily available dataset meant for coherent processing by using only selected samples, thus reducing the processing time needed especially if a quick and crude image is needed. The *price* paid because of the lesser number of elements is a loss of SNR by approximately $6\log(N)$ to $7\log(N)$. This trade-off is illustrated in Fig. 3.19, based on typical N (total number of integration samples) of 100, 1000 and 10000.

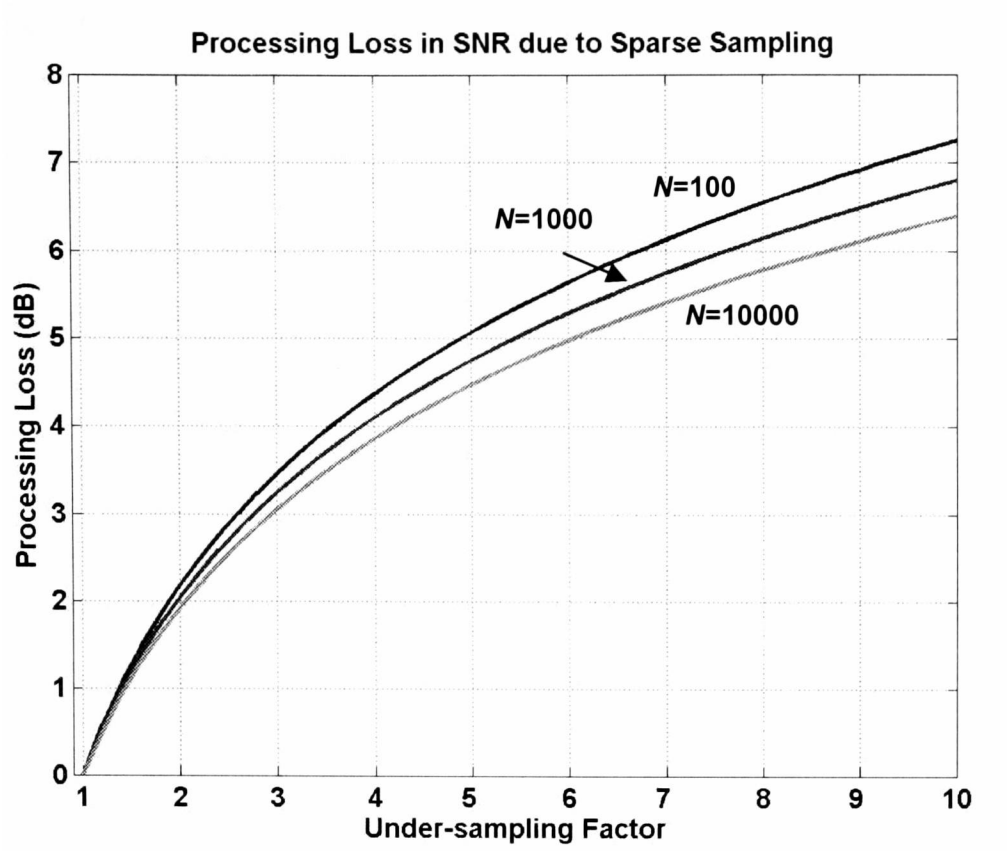


Figure 3.19: Loss in SNR due to sparse sampling, as a function of an under-sampling factor. This under-sampling factor is just a dividing factor for N, such that 1 means that there are no under-sampling, and 2 means that the number of samples is reduced by half.

The absence of grating lobes means that the arrangement of elements in the synthetic aperture does not have to be linear, nor do they have to be uniformly spaced or symmetrically shaped. This provides a greater degree of freedom in the surveying process, as well as the prospect for a more flexible imaging approach. The synthetic aperture can be practically extended to be 2-dimensional, or even 3-dimensional, which potentially produces images with better cognitive properties. This helps overcome the limitation in traditional imaging with linear array in the "side-scan" manner which suffers from shadows and the lack of accurate object-height representation.

The second highlight of this technique is its tolerance to motion errors. Given the same set of motion errors, the net effect of image degradation is much less in an incoherently processed image. In cases where motion compensation is needed, the motion estimations need only be accurate in the order of half the compressed pulse length, whereas an accuracy of the order of $\lambda/2$ is required for coherent dataset. This greatly increases the robustness of an incoherent SAS system.

By example, for a 50kHz system (assuming Q=2.5), the motion error tolerance is of the order of ±0.015m for a coherent system, whereas for an incoherent system, the tolerance is of the order of ±0.04m. It must be noted here that as the bandwidth of the signals are increased to improve the cross-track/range resolution of the system, the compressed pulse length becomes smaller and hence the tolerance also decreases. If the Q factor is now 1.5 instead of 2.5, the tolerance will drop to ±0.023m. A simulation showing its tolerance is shown in section 3.9.

One crucial *disadvantage* of using an incoherent SAS system is the inferior along-track resolution. This can be evaluated by comparing the expression of the along-track resolution of a coherent SAS (equation 2.3) and an incoherent SAS (equation 3.17). The comparison of along-track resolution for typical SAS imaging systems is shown in Fig. 3.20.

	Coherent SAS	Incoherent SAS
	$P_s = \frac{D_p}{2}$	$P_z \cong \frac{3P_r D_p}{\lambda}$
25kHz system, Q=5, θ_b=1.05rad	P_s = 0.030m	P_z = 0.23m
50kHz system, Q=5, θ_b=1.05rad	P_s = 0.014m	P_z = 0.42m
50kHz system, Q=2.5, θ_b=1.05rad	P_s = 0.014m	P_z = 0.21m

Figure 3.20: Comparison of along-track resolution between coherent and incoherent SAS, where P_s is for coherent SAS , P_z is for incoherent SAS, and θ_b is the transducer's beamwidth.

With incoherent SAS system, remote SAS imaging is more feasible with autonomous unmanned vehicles (AUV) without a great deal of increase in system and processing complexity. A recent experiment of the viability of coherent SAS imaging by an AUV done in [42] has indicated that the top challenge lies in the obtaining of accurate trajectory information, hence requiring the overlapping of looks between pings and the introduction of targets of opportunity. With incoherent processing, remote SAS imaging is far more feasible, and in good sea conditions (sea-state-0 to sea-state-1),

motion compensation is not needed at all as long as the AUV's trajectory is inherently straight.

3.16 Conclusion

A time domain incoherent processing technique is presented, which encourages the use of broadband pulses, in order to gain improvement in along-track resolution. The technical properties of incoherent SAS imaging have been established with comparisons to coherent processing. The key differences are the achievable along-track resolution, the absence of grating lobes, the tolerance to motion errors and the characteristics of the processed image.

The concept of signal to self-noise ratio is introduced to enable the analysis of the effect of the self-noise level, and the self-noise energy distribution pattern, on the image quality. Two image quality benchmarks, based upon the image's detection properties and cognitive properties, are defined as the signal to self-noise level and the contrast of the image respectively.

The main driving parameters in the design of incoherent SAS are identified. The optimisation of mapping rate stands against the optimisation of signal to self-noise ratio and along-track resolution. Wide bandwidth and beamwidth of the transducers are factors that allow one to improve the achievable along-track resolution.

Finally, the core advantages of incoherent processing are compared against the trade offs being made, and that forms the basis and foundation on which the research works presented in the following chapters are based upon.

Chapter 4

Fast Reduced-Elements Back-projection

4.1 Introduction

Although frequency domain methods are computationally more efficient, time domain techniques are more flexible and appropriate for the processing of SAS data. In this chapter, a newly developed time-domain technique [43], which exploits the fact that sparse sampling is applicable to the incoherent processing of SAS data, is presented and its application is discussed. It is called the Fast Reduced-Elements Back-projection (FREB) method, based upon its core principle of using a reduced number of elements in the process of incoherent summation.

The fundamental principle of the FREB technique is similar to the time domain incoherent processing technique presented in chapter 3, thus it retains the flexibility inherent to time domain inversion techniques such as accommodating a non-linear synthetic aperture shape and non-equispaced elements. This technique achieves a two-fold objective: significantly reducing processing time, and optimising the pattern of self-noise energy distribution around and on the target. The first objective enables a quick production of a SAS image, while the latter improves the fidelity of the image.

The principle and underpinning of the FREB technique is then presented and discussed. Examples and simulation results are presented to give a clear idea of the benefit derived from the use of this technique. The performance criteria for this technique are identified and its limitations are also discussed.

4.2 Fast Reduced-Elements Back-projection (FREB)

The original motivation for the development of this technique was not solely based upon the aim of reducing processing time. A large part of it was actually driven by the intention to seek ways to analyse and optimise the distribution of self-noise around a point target. From the analysis of the point target energy response via the plot of range-ambiguity loci crossings, it has been observed that in a widely implemented linear and equispaced synthetic aperture, the self-noise energy mainly concentrates on both sides of the point target facing both ends in the along-track direction. Such a lack of symmetries in the energy distribution of the point-target energy response will result in the degradation of image fidelity. The non-even distribution and overlap of self-noise may produce artefacts with only some arrangements of point-scatterers. Therefore if the signal to self-noise ratio is low, a non-uniform occurrence of artefacts degrade the cognitive property of targets in the final image.

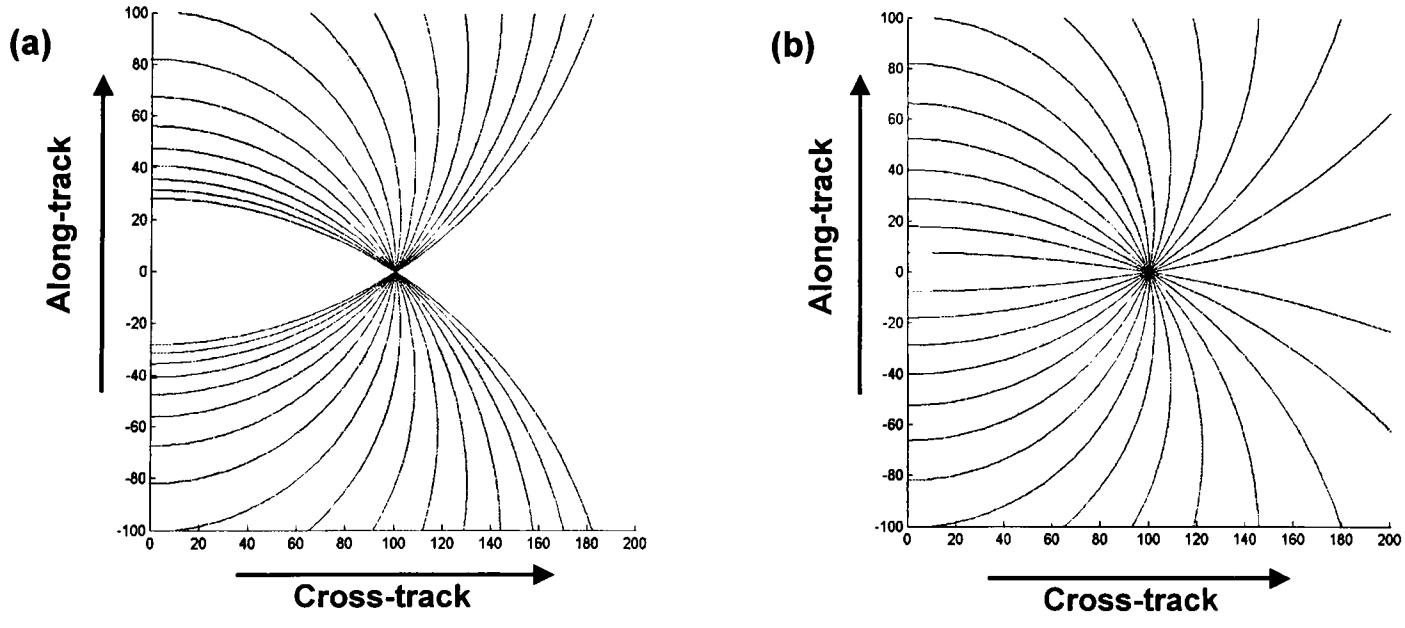


Figure 4.1: (a) Conventional non-uniform pattern compared to (b) uniform spread of range-ambiguity loci.

4.2.1 The principle

The ideal distribution pattern is one where the self-noise energy is uniformly distributed around the point target. By plotting this scenario (Fig. 4.1), it can be observed that such a distribution pattern is achieved by the uniform angular spacing between the loci of range-ambiguities at the crossings of the point target.

Each locus corresponds to an element on the synthetic aperture, and its orientation around the target is related to the position of the element with respect to the point target. This means that the arrangement of elements in the synthetic aperture directly affects the distribution pattern of the loci around the target. Based upon this fact, the task then is to find the element arrangements in the synthetic aperture that will produce a uniform, or close to uniform, angular spacing between loci.

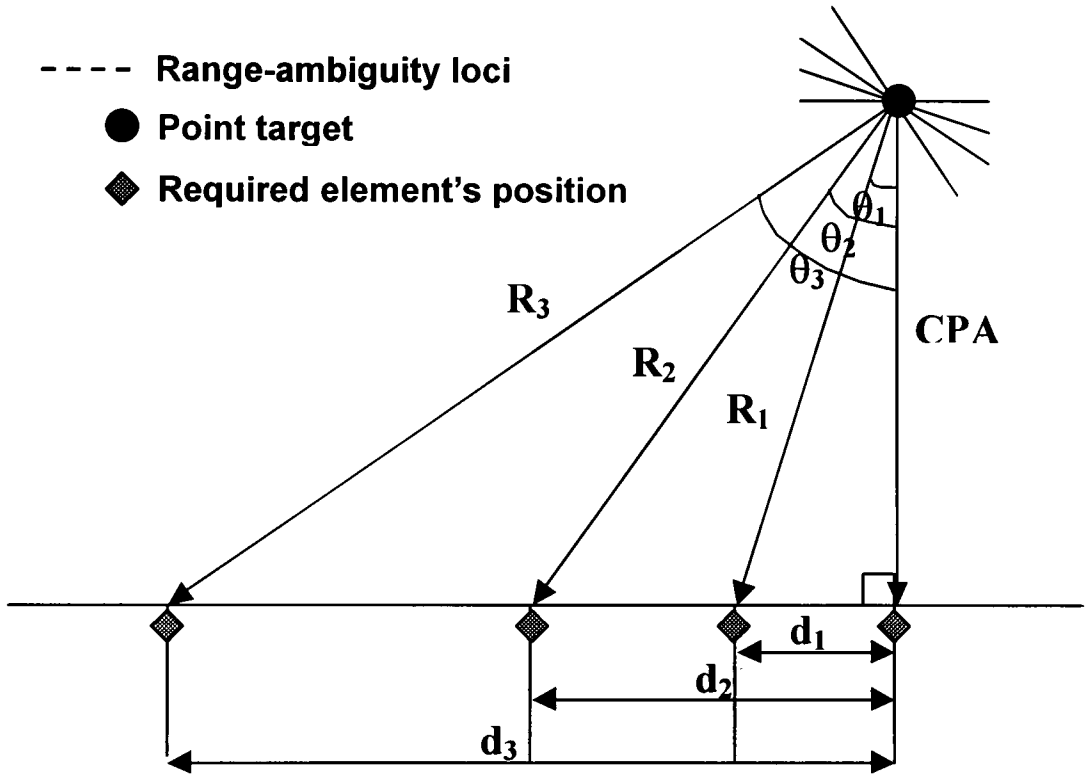


Figure 4.2: Geometry of element position with respect to a point target for a uniform angular spacing of loci.

The geometry for such a scenario is shown in Fig. 4.2. Now, in order to greatly simplify the mathematical evaluation, each range-ambiguity locus is assumed to be the tangent of the locus which is located at the crossing with the point target. In this case, the plot of radius from the locus crossing with the point target to the corresponding

element is perpendicular to the locus's tangent. As such, the angle between two locus tangents crossing on the point target is equal to the angle between their corresponding plots of radius to the elements. Hence, in order to achieve a uniform angular spacing, the conditions that need to be satisfied are $\theta_2=2\theta_1$ and $\theta_3=3\theta_1$, meaning

$$\theta_n = n\theta_1 \tag{4.1}$$

where n is an integer multiple of θ_1. Expressing d_n with relation to θ_n and CPA (or R_0) gives

$$d_n = CPA \cdot \tan(\theta_n) \tag{4.2}$$

Satisfying the condition of equation (4.1) in equation (4.2) produces

$$d_n = CPA \cdot \tan(n\theta_1) \tag{4.3}$$

stating the set of element positions, d_n, which gives a uniform angular spacing of loci at the crossings. These positions are relative distances to the element that has a CPA range to the point-target.

The relationship between d_n and n means that the inter-element spacing will increase in a non-linear fashion. For a given maximum length of synthetic aperture, the elements that are needed under this scheme will be far less compared to the case of uniform inter-element spacing. The reduction in the necessary number of elements, coupled with the benefit of making even the spread of self-noise energy around the target, gave this scheme its name of Fast Reduced-Element Back-projection (FREB).

4.2.2 The application

By dictating the relative distances of other elements relative to the element with CPA, the necessary arrangement of elements in the synthetic aperture is defined. The case of sparse sampling here is in the selection of elements that make up the synthetic aperture, and not in the actual along-track spatial sampling during the process of imaging or

surveying. The implication here, for the implementation of the FREB scheme, is that it is better if the along-track spatial samples are uniformly spaced. They, however, do not need to satisfy the classical constraint of along-track sampling requirement for coherent SAS. Nevertheless, it should be noted that a high along-track sampling rate will improve the accuracy of the positions of the selected elements. This also means that this scheme is very well suited for implementation in the incoherent processing of SAS data originally surveyed for coherent processing.

Different points in the image will have a different corresponding CPA element, thus requiring a selection of different set of elements in the synthetic aperture, even though the set of inter-element spacing is still the same. θ_l is determined by the selection d_l, and this is usually the smallest inter-element along-track spacing of the raw data. The application of this scheme modifies the image reconstruction algorithm to:

$$I_{image}(n_a, n_r) = \sum_{n=[n_a \pm d_n]_n}^{N} w(n, n_a, n_r) \cdot I_{data}(n, n_d(n, n_a, n_r)) \tag{4.4}$$

in which the $[\ ]_n$ symbol denotes an operation of rounding to the closest valid n position, so that the next, closest, available element to the position specified by $n_a \pm d_n$ is selected for summation.

4.3 Analysis of FREB

This section presents the analysis of the benefits gained from using this scheme in terms of improvements in the self-noise energy pattern and the required computational time. The trade off in signal-to-noise ratio in this scheme, due to the use of a smaller number of elements in the process of summation, and its implications are discussed.

4.3.1 Improvement of self-noise energy pattern

The improvement in self-noise energy pattern can be shown by a comparison between the final images produced with conventional uniform element spacing back-projection and with the FREB scheme. A point target simulation is performed.

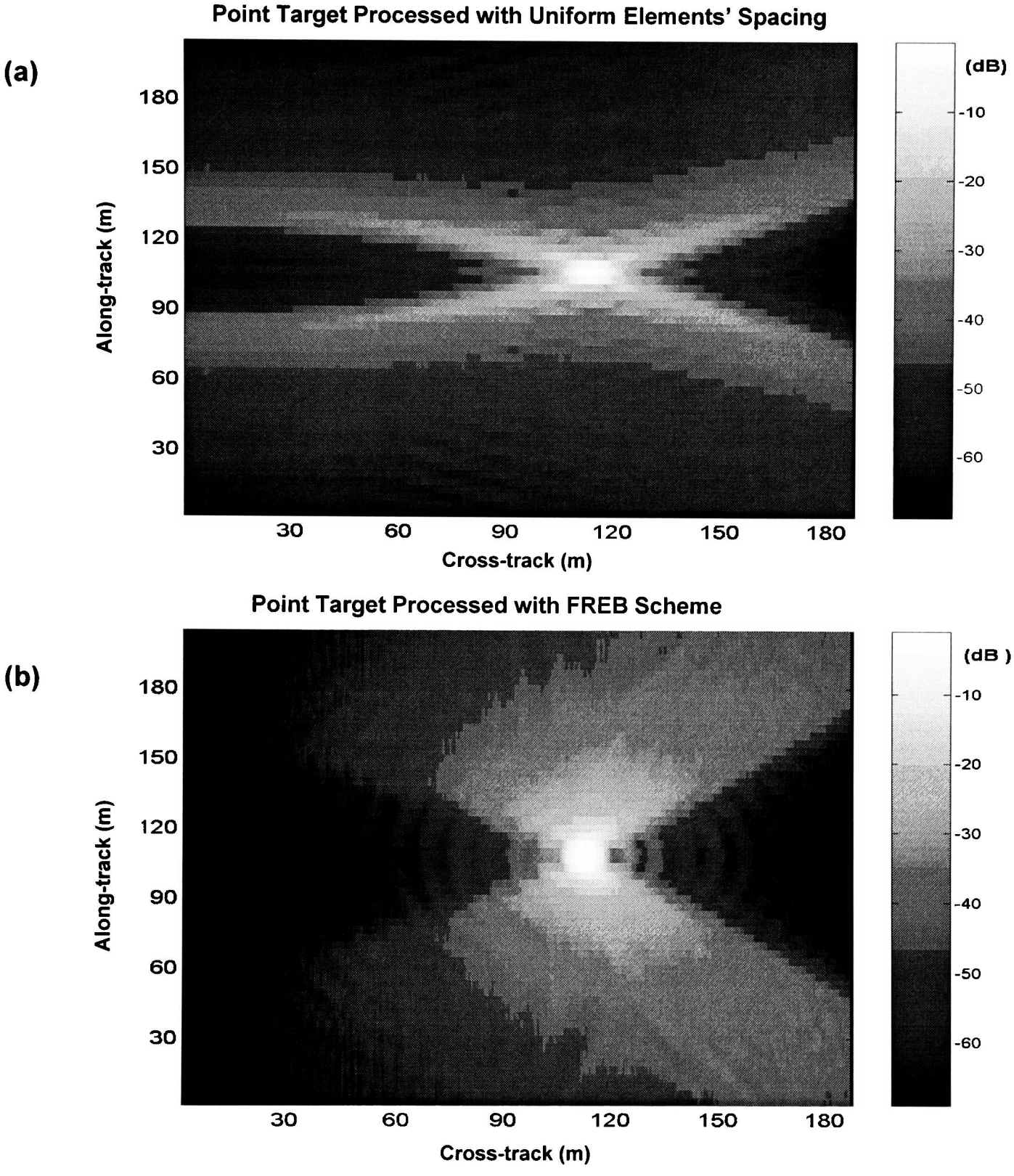


Figure 4.3: A more uniform pattern of self-noise energy distribution resulting from the use of FREB scheme.

It can be seen that there are streaks of far-reaching energy in Fig. 4.3(a), but in Fig. 4.3(b), the energy is more uniformly distributed around the target and there are no persistent streaks of energy escaping the target.

A simulation with 4 point targets coupled with a closer inspection showed that it is not a case of all gain without loss. The images processed incoherently with conventional equal elements' spacing and with FREB scheme (equal loci-spacing) are shown in Fig. 4.4.

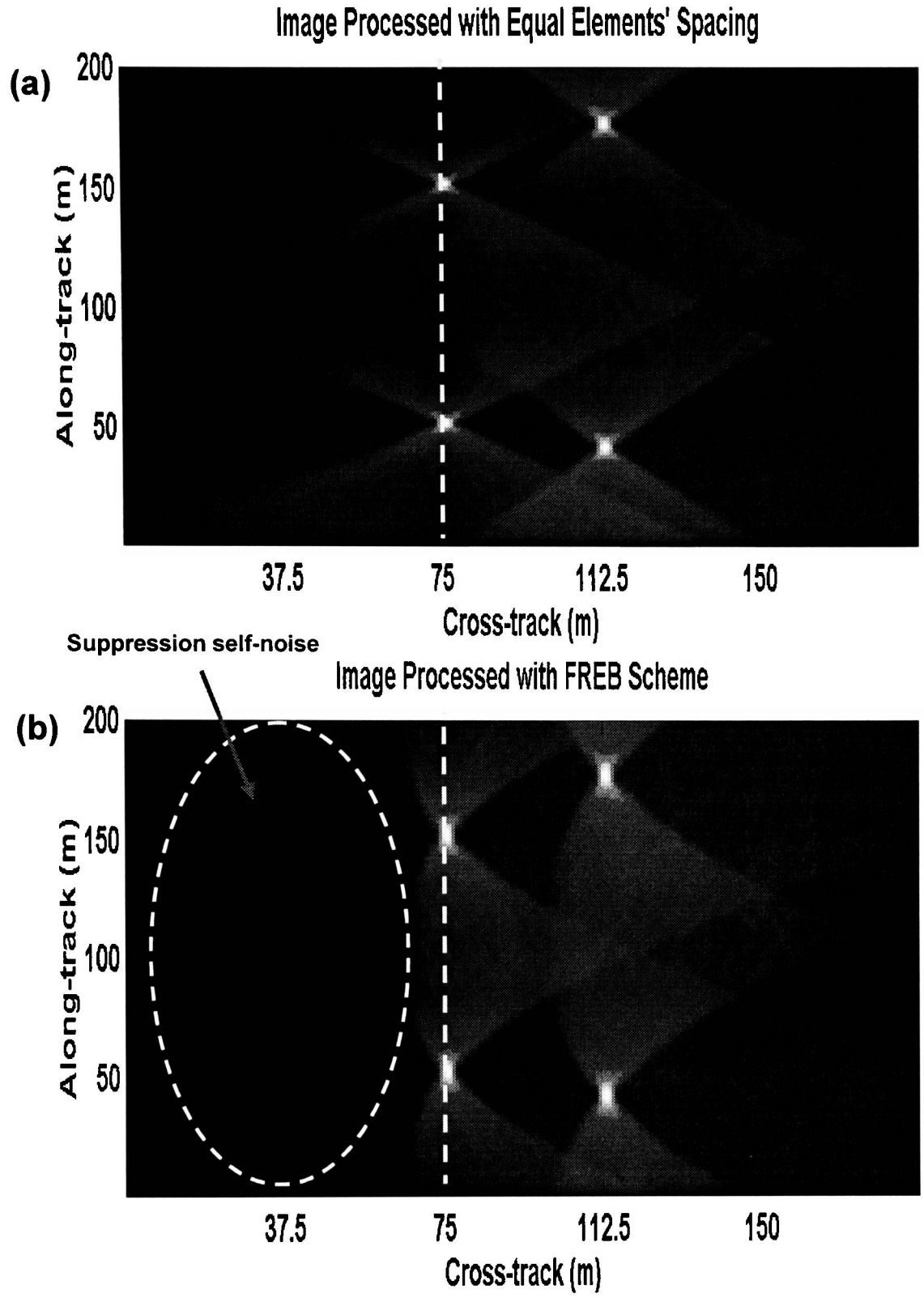


Figure 4.4: 4 point targets processed incoherently with (a) equal elements' spacing and (b) FREB scheme.

A slice in the along-track direction across the first two targets is taken from each image for comparisons in Fig. 4.5.

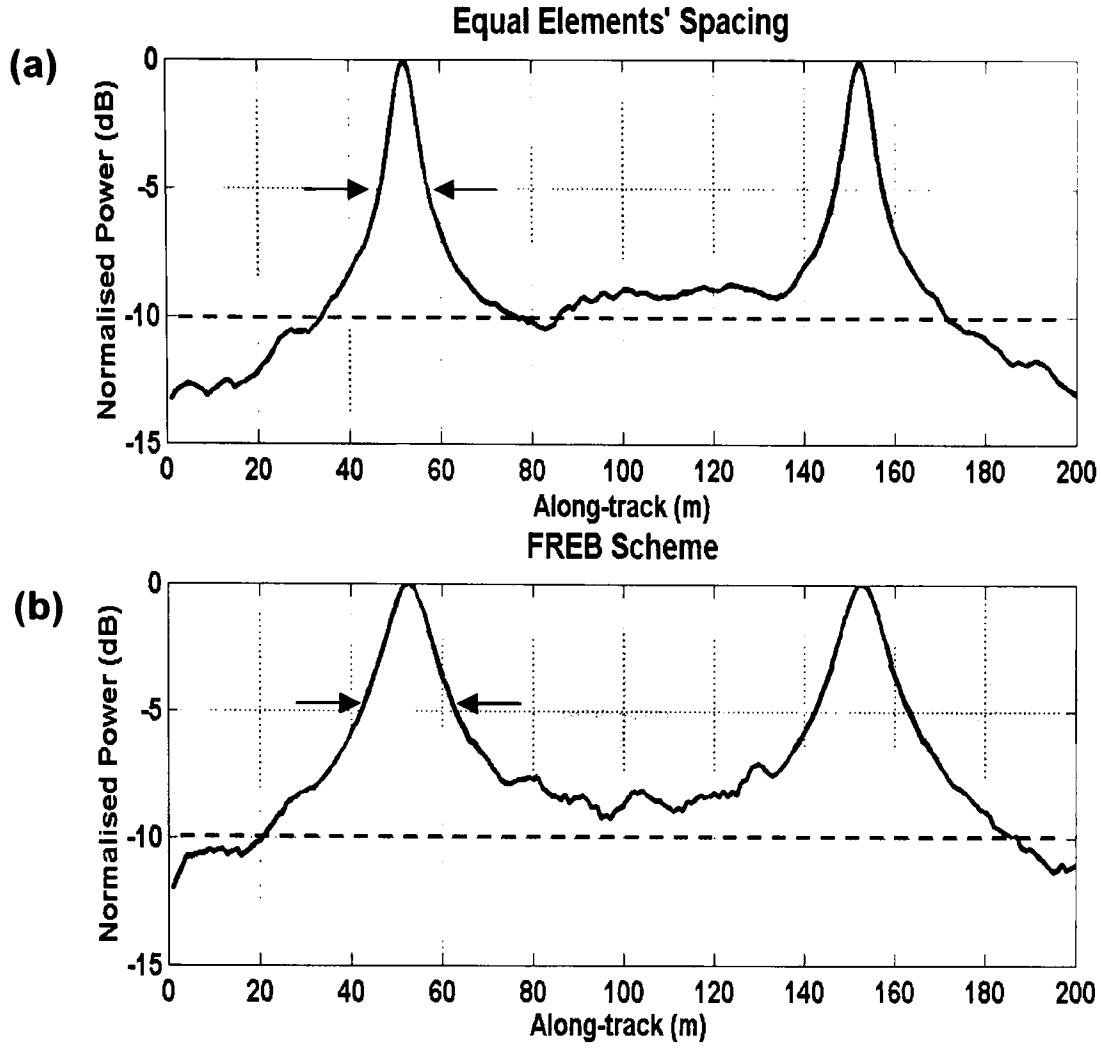


Figure 4.5: Along-track slice across two point targets processed with (a) equal elements' spacing and (b) FREB scheme.

This simulation has reduced the number of summation per pixel from 200 to 137. Due to the smaller number of elements integrated, the noise floor level has increased by an average of about 1.5dB. This is higher than a realistic prediction of a processing loss of $7.25\log_{10}(200/137)=1.2$dB, because the simulation is based upon a simplistic model with very high probability of detection ($PD=0.999$) and low probability of false alarm ($PFA=10^{-10}$). This degradation causes the overlapping of self-noise to be more prominent compared to real-targets.

Another trade-off that can be observed is the broadening of the main-lobe by a factor of approximately 2 (as indicated by the arrows in Fig. 4.5), which relates to the degradation of along-track resolution. This broadening of the main-lobe comes from the higher self-noise level in the along-track direction, which is a trade-off from the suppression of self-noise in other regions (Fig. 4.4). A shorter synthetic aperture length

also contributes to the degradation of along-track resolution. Due to the fact that d_n increases non-linearly and is *not* always a round multiple of d_1, the synthetic aperture length is usually shorter that what it would have been in the case of normal incoherent processing with all available elements.

On the one hand, the scattering of self-noise energy is clearly better contained, but on the other hand, the signal to self-noise ratio has degraded. Other than the quantifiable degradation in signal to self-noise ratio, it is not a straightforward case in the attempt to determine the exact loss or gain in image quality via the use of point-target energy response analysis alone. Nevertheless, it is technically fair to conclude that there is a substantial suppression of self-noise spatially, and that this has been achieved with a degradation in signal to self-noise ratio and along-track resolution.

4.3.2 Reduction of processing time

The core benefit of using FREB scheme is the reduction of computational complexity, and hence the needed processing time. This is obvious from the fact that lesser elements are involved in the incoherent summation process. As shown in section 3.3.5, the computational complexity for a conventional bi-static incoherent processing can be expressed as $O.N_r.(N_a)^2$. Let the total number of elements used in the synthetic aperture be N_i, the computational complexity, CC becomes

$$CC = O \cdot N_r \cdot N_a \cdot N_i \tag{4.5}$$

In order to compare the reduction in processing time, the numbers of elements used in incoherent summation in both cases need to be known. In the conventional incoherent processing where all the elements are used, $N_{i,c}$ is quite straightforwardly

$$N_{i,c} = \frac{D_s}{d_1} \tag{4.6}$$

In the conventional case, d_1 is fixed as the inter-element spacing, and consequently angle θ_1 decreases as the CPA grows. And by definition of Fig. 4.2, d_n is always equals to $n.d_1$.

As for the FREB scheme, equation (4.3) is used to obtain an expression for the number of elements used. With the point of interest centred on the synthetic aperture,

$$\frac{D_s}{2} = CPA \cdot \tan(n\theta_1) \tag{4.7}$$

Hence n, derived from equation (4.7), is the number of elements on one side of the synthetic aperture, excluding the element corresponding to the CPA of the point of interest. $N_{i,FREB}$, the number of elements in a synthetic aperture in FREB scheme, is twice the n found from equation (4.7) plus the element corresponding to the CPA, and is thus expressed as:

$$N_{i,FREB} = \left[2 \cdot \frac{\tan^{-1}\left(\frac{D_s}{2 \cdot CPA}\right)}{\theta_1} \right]_N + 1 \tag{4.8}$$

where $[\ ]_N$ denotes the operation of rounding to the closest smaller whole number. $N_{i,FREB}$ decreases with the choice of greater θ_1. However, as the CPA increases, such that targets further away are being focussed, $N_{i,FREB}$ also decreases. Hence, in order to have a consistent processing gain for targets along all the cross-track ranges, it is necessary to decrease θ_1 as the CPA increases. Since θ_1 is related to d_1, it can only be decreased accordingly with relation to the multiples of the inter-element spacing.

Consider a case where the inter-element spacing is 0.5m and D_s is set to be 30m. To illustrate such a relationship, a plot, of $N_{i,FREB}$ versus the parameters of CPA, and multiples of the θ_1 that corresponds to the inter-element spacing, is shown in Fig. 4.6.

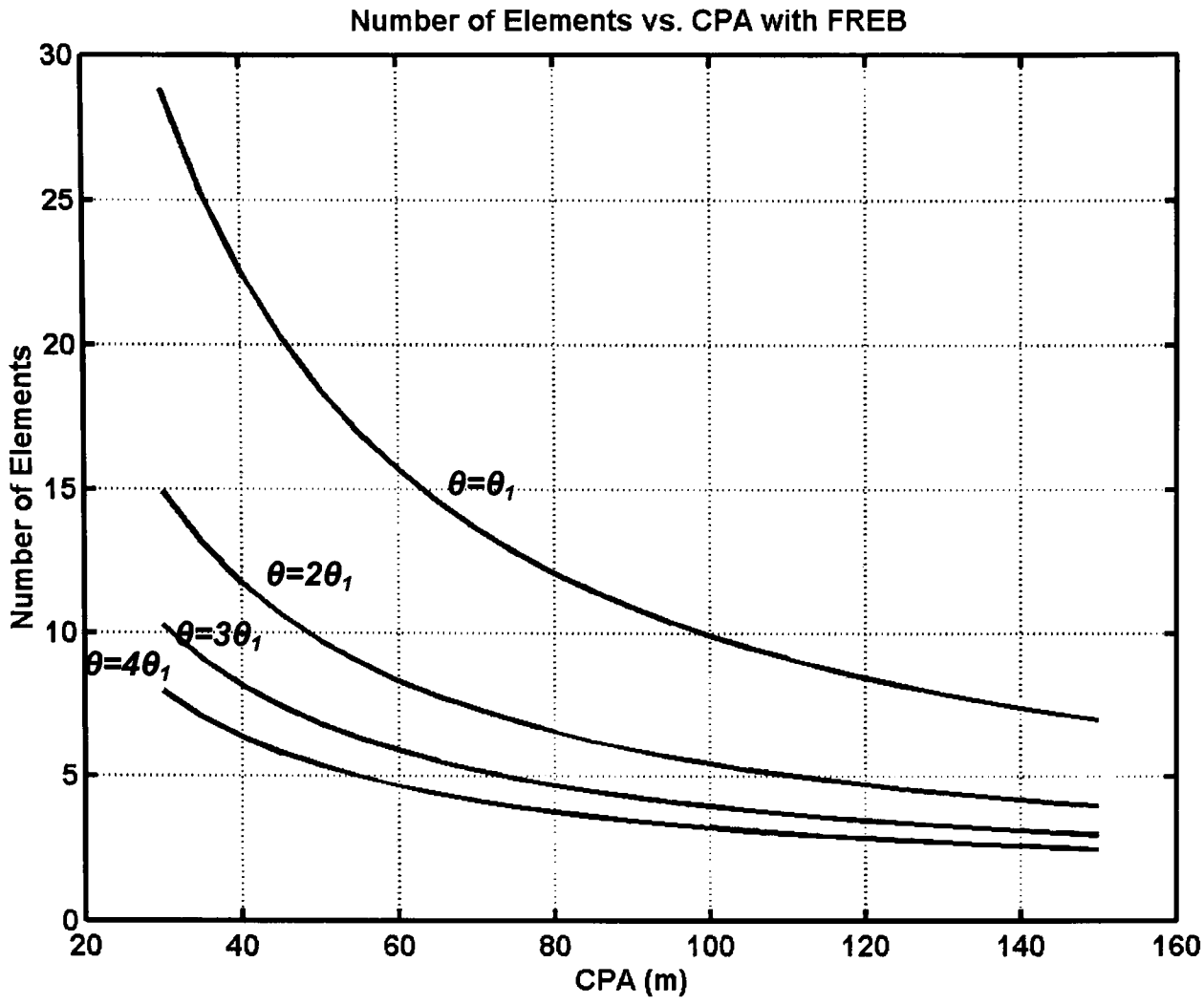


Figure 4.6: Plot of $N_{i,FREB}$ versus CPA and the inter-loci angular spacing being the multiples of θ_1, with an inter-element spacing of 0.5m and D_s of 30m.

To gauge the reduction of computational complexity from the application of FREB scheme, an improvement factor, IF, is introduced and expressed as

$$IF = \frac{N_{i,FREB}}{N_{i,c}} \tag{4.9}$$

The smaller the fraction of IF, the greater is the reduction in computation time. An improvement factor of 0.5 would mean a reduction of the computation time by half. Fig. 4.7 shows the plot of IF versus CPA with varying multiples of θ_1. Inter-element spacing is 0.5m and D_s is 30m.

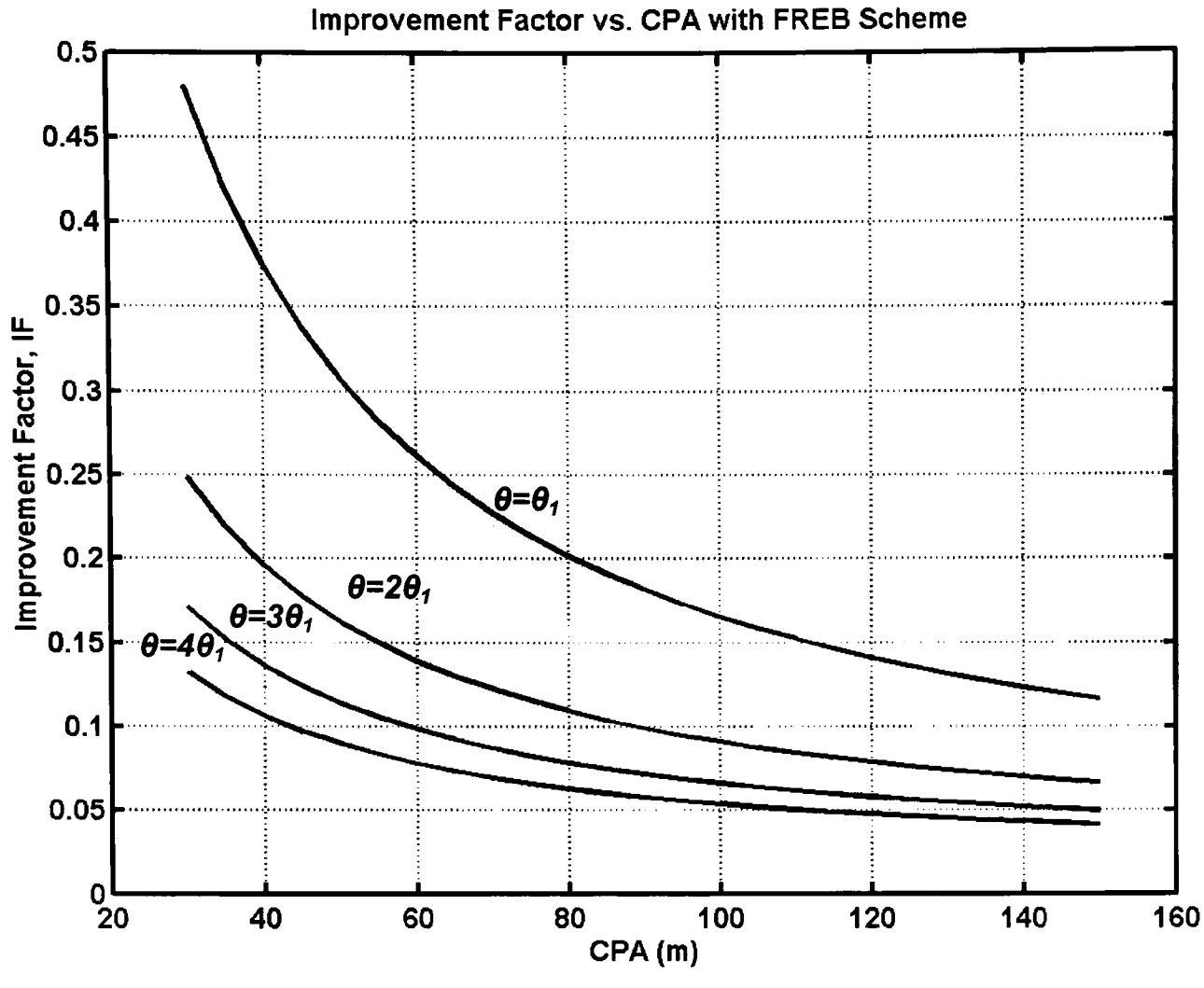


Figure 4.7: Plot of *IF* versus *CPA* and the inter-loci angular spacing being the multiples of θ_1, with an inter-element spacing of 0.5m and D_s of 30m.

The most influential parameter in the improvement factor's relationship is the value of the loci's angular spacing. This directly depends on the along-track inter-element spacing, because the angle θ is usually chosen to correspond to the d_1 that is equal to a whole multiple of the along-track inter-element spacing.

4.4 Implications of FREB

The application of FREB strongly depends on the survey's inter-element spacing and arrangements. It requires that the survey's inter-element spacing be uniform. If this is not the case, reduction in processing time can still be achieved since lesser elements are used in integration, but the resultant self-noise energy distribution may not be as evenly distributed and well contained.

This technique is especially useful to process, in a short time, survey data that was meant for coherent processing. It fits well into a scenario where incoherent processing is used as an initial processing tool to identify areas of interest in an otherwise large area of surveyed data. The highlighted areas can be processed with more complex and time-consuming coherent processing techniques in a later stage to extract more detailed information or to provide images of higher resolution.

In cases where the synthetic aperture is non-linear or extends beyond one dimension, for example a planar synthetic aperture, the FREB scheme is also easily applicable so long as the elements are approximately uniformly-spaced within the same dimension. If the elements are not similarly uniform in both the planar dimensions, then the total number of elements will be treated differently for each planar dimension, and so will the *IF*. The computational complexity can thus be expressed as

$$CC_{planar} = O \cdot N_r \cdot (N_{a1})^2 \cdot (N_{a2})^2 \cdot (IF_{a1}) \cdot (IF_{a2}) \tag{4.10}$$

4.5 Conclusion

The use of the range-ambiguity loci crossings plot has proven to be the quickest and simplest method for predicting and representing the point-target energy response of a synthetic aperture, with any form and shape, in incoherent processing. Albeit being slightly empirical, it is accurate and technically justified. Such a technique led to the revelation that the pattern of energy distribution is directly related to the arrangements of the elements in the synthetic aperture, having assumed that their weightings are uniform. It was then found that the best arrangement would be one of which the range-ambiguity loci are equally distant from each other angularly, hence giving the most uniform and contained spread of self-noise energy. Practically, however, this leads to a reduction in processing gain because the maximum limit of D_s meant that it is inevitable that a smaller number of elements are used as compared to a conventional case.

More importantly, it has been shown that the FREB scheme provides a viable way of speeding up the time-domain incoherent back-projection algorithm. Although a smaller number of elements are used in summation, it is still the best possible arrangement of elements as far as the self-noise energy pattern is concerned. The reduction in computational time is mainly decided by the choice of d_1, which is in terms of the multiples of the basic inter-element spacing.

The discussion made here had conveniently assumed that the strength of all the loci is uniform, such that all the echoes have the same strength irrespective of their angle of arrival. This, however, is only true if the chosen synthetic aperture length had been strictly constrained by the effective beamwidth of the individual elements, which may not always be the case in practice. Hence, in such cases, a uniform angular spacing between the loci is only optimal for elements that are able to cover the target within its effective beamwidth. For elements that do not cover the target within its effective beam, its loci, which have smaller intensity, may well need to be denser to achieve a similarly uniform distribution. The solution to this requirement can be found with the point-target energy response analysis incorporating loci with variable intensity, which was introduced in section 3.12. Nevertheless, it is worth noting that the difference is usually too small to justify the additional complexities, and hence the processing time, in taking this into account.

The FREB scheme can be extended to synthetic apertures that are 2-dimensional. It is also applicable to data that are meant for coherent processing. The practical use of this scheme and its realistic contributions to the reduction in computational time for incoherent processing are presented in chapters 6 and 7.

Chapter 5

A Correlation-Based Bulk Motion Compensation Algorithm

5.1 Introduction

Motion compensation can come in two forms, one where navigational aids are used to provide information on the path deviations, and one where path deviations are extracted from the SAS survey data itself. This chapter deals with a motion compensation algorithm that is based upon the extraction of path error information from the SAS data itself.

In incoherent processing, there is no need to know, and correct for, the path deviations to the same precision as in coherent processing. Rather, what is needed is just an algorithm to estimate, coarsely, the obvious motion errors in the trajectory that will reduce the incoherent processing gain of the target, and compensate for it. By example of a 100kHz imaging system with Q=4, the motion error needs to be compensated to the accuracy of ±0.06m (a fraction of its pulse compressed length), rather than to the accuracy of ±0.0075m (a fraction of its wavelength). Hence, the term of "bulk" motion compensation.

The preceding factor is better appreciated if considered in the light that in relatively calm sea conditions (seastate-0 to seastate-2), the motion deviations (translational motion) experienced by a towed platform has a root-mean-square in the region of a few to tens of centimetres (1-50cm), and increases with rougher sea conditions. Checketts had carried out a study into the performance degradation of a SAS imaging system due to time-varying towed-array orientation and trajectory [26,82], where more detailed information can be obtained.

This chapter presents a correlation-based bulk motion compensation algorithm with new approach; range-curvature fitting and optimisation. The concept of correlation processing to estimate total deviations between pings is not new [46,47]. Also in [48], Callow et al described a noncoherent autofocus technique for single-receiver broad-band synthetic aperture sonar imagery which is based on ping-to-ping phase correlation. However, the motion estimation approach based upon fitting the best range-curvature is novel in SAS processing. It does not make far-field assumptions; does not require the need for phase preservations (incoherent); and operates in the time-domain (suitable for broadband pulses). One condition, though, must be met for its implementation, and that is the presence of a relatively strong target, either a naturally or a deliberately planted target.

5.2 Motion Errors

Consider the case of a linear synthetic aperture operating in a monostatic mode. In an ideal situation where there are no motion errors, the pulse-compressed returns of a target will appear as a hyperbolic curve which expresses the range curvature or the time-delay curve of the target with respect to the elements in the synthetic aperture. When motion errors are introduced, this curve will deteriorate from its ideal shape. The model of the scenario where unknown path deviations occur between pings is shown in Fig. 5.1.

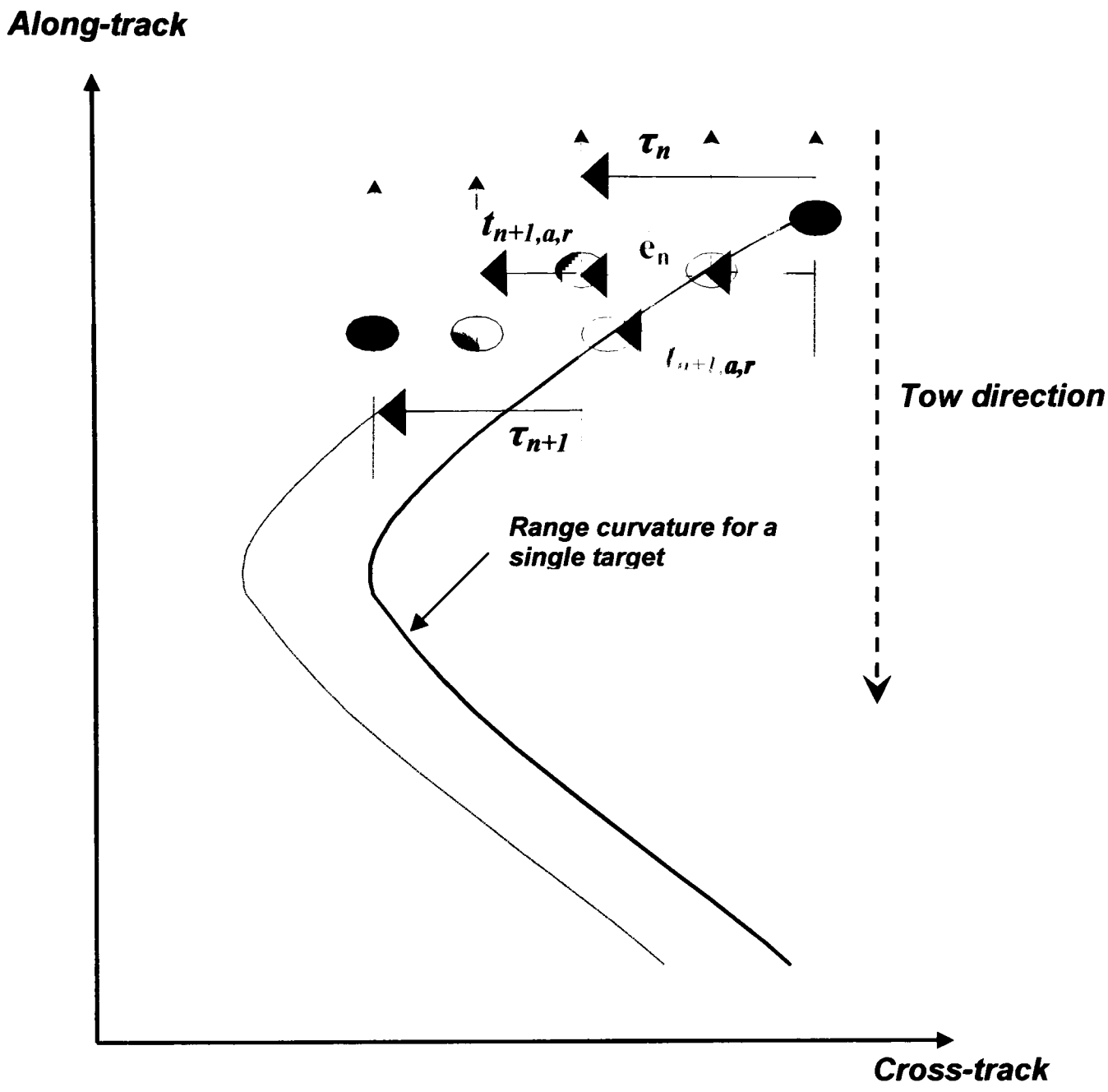


Figure 5.1: The geometry of the deviations of ping returns from the ideal range-curvature. The ellipses represent the pulse-compressed range curvature formed by a point target.

In the diagram, the blue-coloured spots represent the ideal positions of the peaks of the compressed pulses, forming a hyperbolic curve expressed with the function in equation (3.4). The red-coloured spots represent the positions of the same corresponding peaks but with unknown path deviations. Let the tow direction be from the top towards the bottom of the diagram, where the top-most blue spot corresponds with the initial platform position. On the arrival of the next ping, instead of being at the location of the second blue spot from the top, the peak appears at the location of the first red-spot due to path deviations. The difference in time-delay with the ping before it will be the sum of the inter-ping time-delay as expressed in equation in (3.4) with the unknown path deviations. The variables are defined as such:

τ_n is the total deviation between the n^{th} and the $(n\text{-}1)^{th}$ ping, or more generally the ping-to-ping deviation.

$t_{n,a,r}$ is the natural inter-ping time-delay that comes from the different range from the target to different elements in the synthetic aperture (equation (3.4)), between the n^{th} and the $(n\text{-}1)^{th}$ ping, for a target at the range of r and along-track position of a with respect to the image.

e_n is the gross error or path deviation that needs to be corrected for the n^{th} ping.

By this,

$$e_1 = \tau_1 - t_{1,a,r} \tag{5.1}$$

for the first pair of adjacent pings. Extending this to consider the other adjacent pings (from the top to bottom), it can be seen from the diagram in Fig. 5.1 that the third ping position (second red-spot) is contributed by the natural time-delay, plus the path deviation in the third ping, plus the path deviation from the previous, second ping. Hence, the relationship of the path deviations can be shown to be

$$e_{n+1} = e_n + \tau_{n+1} - t_{n+1,a,r} \tag{5.2}$$

where n begins with the first ping from the top. The path deviations are inherently accumulative as n progresses from ping to ping.

5.3 The Principle

From equation (5.2) it can be seen that, if $t_{n+1,a,r}$ is accurately known, then the path deviations will be known and easily compensated. However, a and r are not known apriori. Since $t_{n+1,a,r}$ will be dependent and unique for different a and r, the task then is to find the best estimate of a and r so that the best estimate function of $t_{n+1,a,r}$ can be obtained. Let the estimated values of a and r be ae and re respectively. This gives

$$e_{n+1} = e_n + \tau_{n+1} - t_{n+1,ae,re} - e_{t(n+1)} \tag{5.3}$$

where $n \geq 0$, $e_0 = 0$, and e_t is the estimation error such that

$$e_{t(n+1)} = t_{n+1,a,r} - t_{n+1,ae,re} \tag{5.4}$$

The term that can be readily found is $\tau_{n+1} - t_{n+1,ae,re}$, which is the difference between the total inter-ping time-delay obtained by detecting the peaks of cross-correlations, and the natural inter-ping time-delay based on the estimated time-delay function. Let this term be called td_{n+1}, substituting it into and rearranging the terms in equation (5.3) gives

$$td_{n+1} = e_{n+1} - e_n + e_{t(n+1)} \tag{5.5}$$

and can also be expressed as

$$td_{n+1} + td_n = e_{n+1} + e_{t(n)} + e_{t(n+1)} \tag{5.6}$$

In both equations (5.5) and (5.6), the variables on the left can be found. Minimising these will minimise the unknown errors - path deviations and time-delay function estimation errors - on the right of the equation. But which equation is the optimal choice?

The process of minimisation involves a root-mean-square (RMS) operation on all the values of the variables on the left corresponding to all the values of *n*. This is repeated for all estimates of *ae* and *re*. The estimates that give the least RMS are chosen.

Now, consider a simplified example where there are only 4 pings.

Case 1: For equation (5.5),

$td_4 = e_4 - e_3 + e_{t(4)}$ for $n=3$

$td_3 = e_3 - e_2 + e_{t(3)}$ for $n=2$

$td_2 = e_2 - e_1 + e_{t(2)}$ for $n=1$

$td_1 = e_1 + e_{t(1)}$ for $n=0$

The RMS operation is performed on the values td_4, td_3, td_2 and td_1 for each *ae* or *re*.

Case 2: For equation (5.6),

$td_4 + td_3 + td_2 + td_1 = e_4 + e_{t(4)} + e_{t(3)} + e_{t(2)} + e_{t(1)}$ for $n=3$

$td_3 + td_2 + td_1 = e_3 + e_{t(3)} + e_{t(2)} + e_{t(1)}$ for $n=2$

$td_2 + td_1 = e_2 + e_{t(2)} + e_{t(1)}$ for $n=1$

$td_1 = e_1 + e_{t(1)}$ for $n=0$

The RMS operation is performed on the values td_4, $2.td_3$, $3.td_2$ and $4.td_1$ for each *ae* or *re*.

The better the RMS result in representing the time function estimation error $e_{t(n)}$, the more accurate will the minimum value of the RMS, over all estimates of *ae* and *re*, represent the optimal estimate for *ae* and *re*. It can be seen that in case 1, the path deviations e_n averages out while $e_{t(n)}$ add up. In case 2, the path deviations add up and the $e_{t(n)}$ also add up, in multiples depending on *n*. Case 2 is seemingly more optimal

because of the stronger presence of $e_{t(n)}$ compared to e_n, but this is only true if e_n over all n has a relatively small mean, in which case it is expected to give more accurate estimates than case 1. As for case 1, although it is slightly less sensitive to changes in $e_{t(n)}$ as compared to case 2, it is nevertheless more resilient to path deviations that have inherent mean values. Note that the motion errors themselves may be random or normally distributed, but the inter-ping path deviations e_n are cumulative by definition. Hence, it is always likely that there will be a significant mean of e_n over n. However, using e_n's statistical properties to define the performance boundaries of both cases is not necessary for this algorithm because there is no way of knowing a priori what e_n will be.

A simulation-based experiment is performed to obtain a comparison between the estimation criteria in case 1 and case 2. The motion errors are simulated to be uniformly random for each ping *relative to its previous ping*. It is worth noting that there is not a straightforward way to model the path errors as they are influenced by more than one time-varying factor [26]. It is reasonable that a Gaussian distribution may closely represent these errors. For 'control' purposes, this experiment was repeated with inter-ping errors from Gaussian distribution and the results also suggested Case 1 to be a better estimator.

A point target is located at a point with along-track location a, and cross-track location r. A set of uniformly random numbers are generated within the range of -0.5 to 0.5, and scaled to give a set of random time-delays that represent motion errors with a standard deviation of 0.56 m in each direction (towards and away from the aperture). These delays are accumulated as n progresses such that the deviations are cumulative, and then added onto the corresponding n^{th} ping. The value of re is set to be the same as the actual value, r, and thus remain constant. The optimal ae is found by choosing, from all possible values of a, the one corresponding to the lowest value of RMS. Based upon the criteria set out in case 1 and case 2, one set of RMS values is obtained for each case, thus each giving its result of the optimal ae. Both ae are used to estimate the path deviations, and they are then compared to the actual set path errors introduced. The differences between the estimated path difference and the actual introduced path

errors over all n are then calculated, and its root-mean-square calculated. This whole process is then repeated for a point-target at different along-track location within the span of the synthetic aperture. The results are shown in Fig. 5.2.

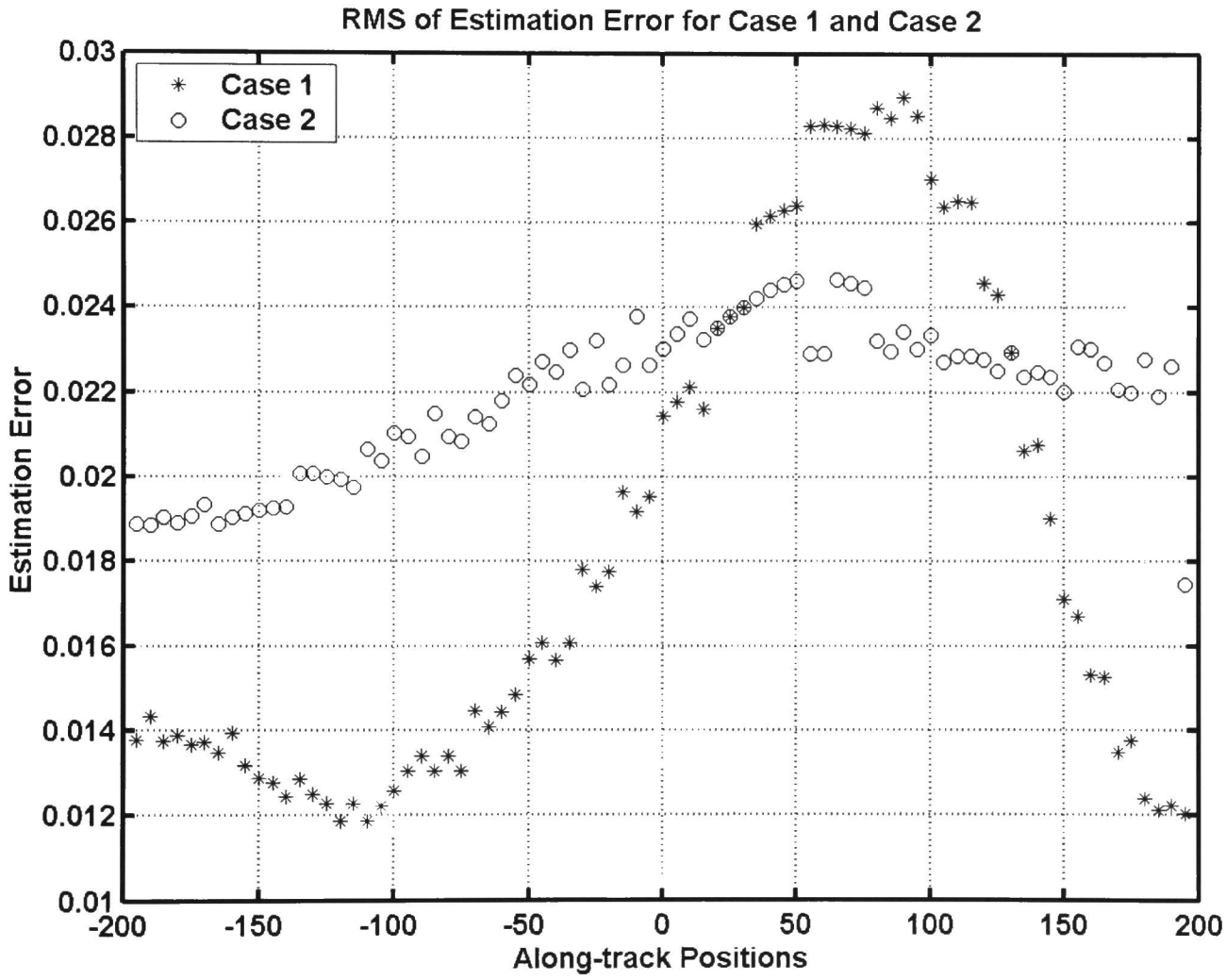


Figure 5.2: Estimation errors for targets at different along-track position with estimation criteria in Case 1 and Case 2 are compared.

It is clear that the estimation criteria set out in case 1 has out-performed that in case 2 for most of the target's along-track positions. To ensure that this result is consistent, this experiment is repeated with 10 different sets of uniformly random numbers that have the similar degree of standard deviation. Results in Fig. 5.3 show that case 1 is a more accurate estimation than case 2.

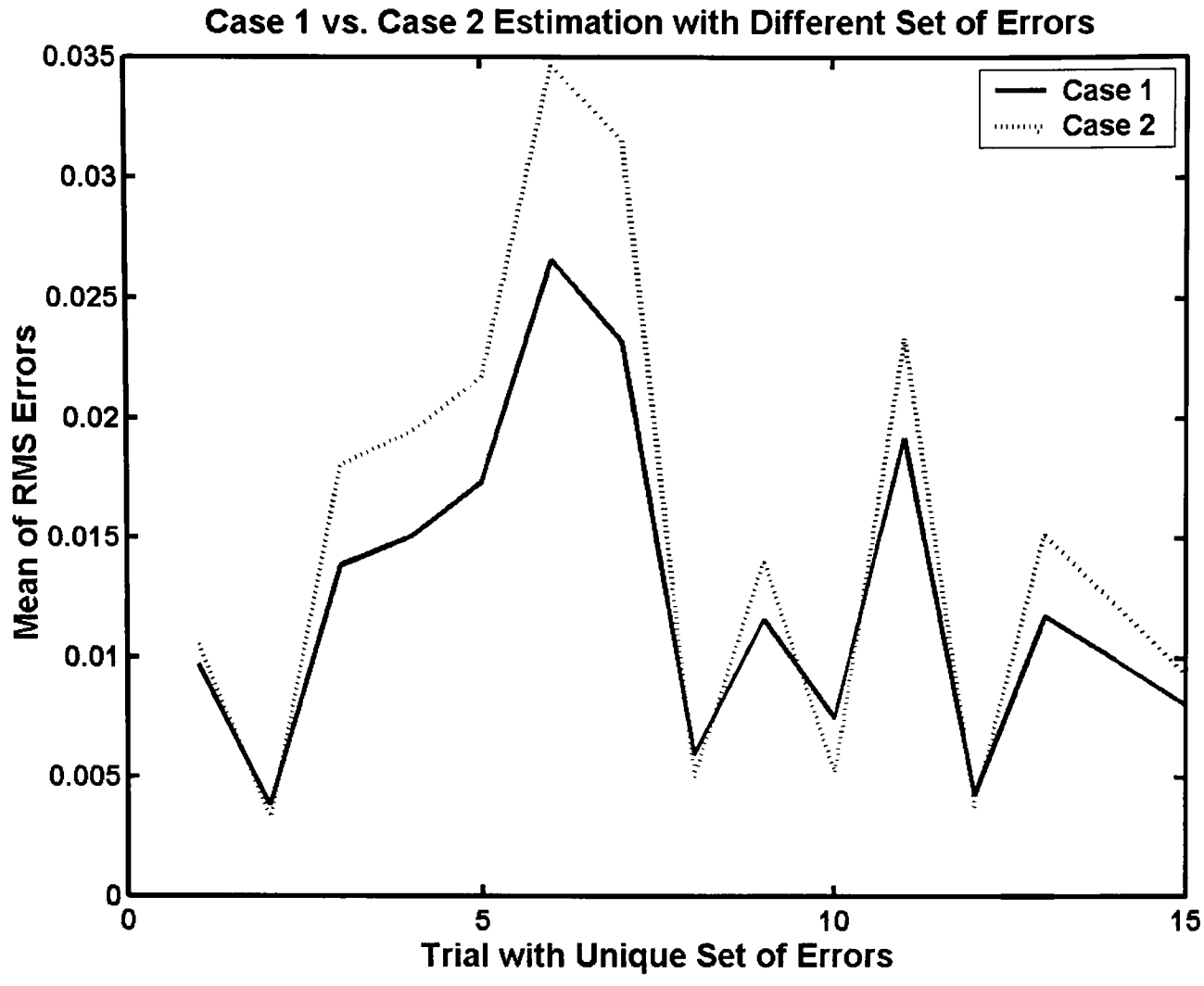


Figure 5.3: Comparison of the estimation accuracy between the criteria in case 1 and case 2, using 15 different sets of random errors but with the same degree of standard deviation.

The estimation performance Case 1 and Case 2 can be seen to be closely correlated due to the fact that both estimation criteria are based upon the same errors of e_n and $e_{t(n)}$. As seen in the example set out earlier, the difference between these two criteria lies on the *cumulative* (over n) presence of $e_{t(n)}$ in Case 2 but not in Case 1.

5.4 The Estimation Algorithm

The goal, as laid out in section 5.3, is to find the *ae* and *re* that best match the ideal (had there been no path deviations at all) *a* and *r*. The qualities of *ae* and *re* are determined by the RMS algorithm set out in case 1 and case 2.

In a practical situation, the image is first processed without motion compensation. The location of the relatively stronger target chosen as the anchor target, although usually appears to be very blurred and faint on the image, provides an excellent initial estimate for both *ae* and *re*. Also, based upon the blurred image, the number of *ae* and *re* that needs to be estimated is reduced. The algorithm is described by the flow chart in Fig. 5.4. Inter-ping cross-correlations would have been performed and the inter-ping time-delays, τ_n, stored before the execution of this algorithm. When the final *ae* and *re* have been obtained, they are used in equation 5.2 to obtain e_n for all n, and then motion compensation is performed by introducing time-delays of $-e_n$ into the corresponding n^{th} pings.

In cases where there are no confident initial estimates, $re_{initial}$ will be set to be the location of the peak of the anchor target, on the cross-track range axis, of the first along-track return. $re_{initial}$ can then be set to be re_{max}, because if the anchor target is located within the image, its CPA will never be larger than the distance of any of its pulse-compressed peaks. The values from ae_{min} to ae_{max} need to include all the possible along-track positions.

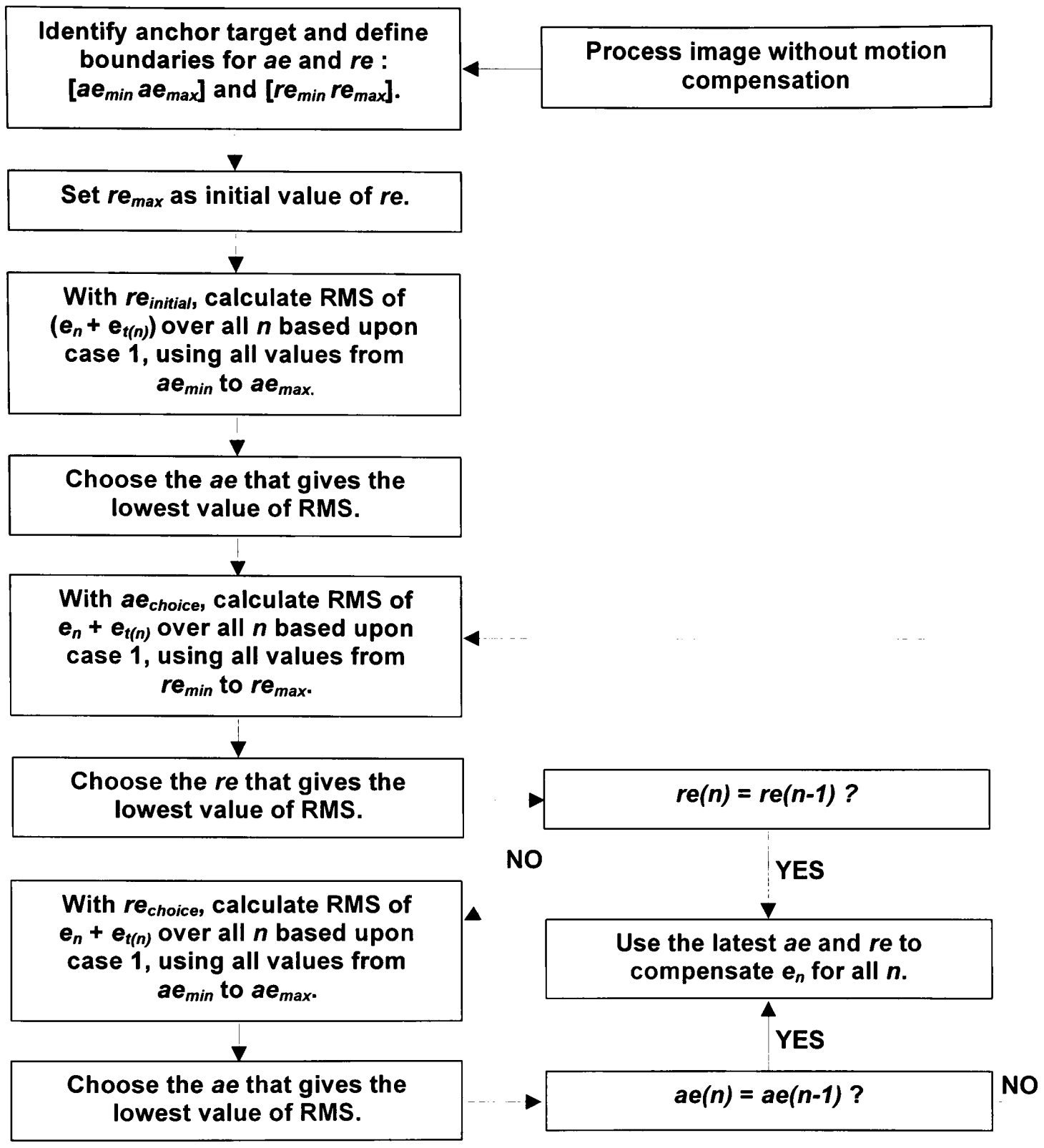


Figure 5.4: Algorithm for searching the best match of *ae* and *re*.

5.5 Simulation Example and Results

A simulation is carried out with 4 point-targets placed on an image, one of which has a 1.5 times larger magnitude than the others, and is meant to be the anchor target. A set of path deviations with a standard deviation of 0.55m for each direction (towards and away from the aperture) was used. They are then turned into cumulative errors for each ping, and added onto the target returns (Fig. 5.5(a)). The returns are pulse compressed, and then inter-ping cross-correlations are carried out over all n to extract the inter-ping deviations.

The image is first processed without motion compensation (Fig. 5.5(b)). Based on the selected anchor target,

$re_{intital} = 100$ m

$ae_{min} = 195$ m

$ae_{max} = 250$ m

The algorithm shown in Fig. 5.4 is then applied, starting with the initial value $re_{initial}$.

The first estimation for along-track position is

$ae_1 = 220$ m.

This is then used to obtain a new estimate of re, with

$re_{min} = 85$ m

$re_{max} = 100$ m

The best estimation is obtained by choosing the value of re that has the least RMS error based upon the criteria in case 1, giving

$re_1 = 100$ m

and since $re_1 = re_{\text{initial}}$, the estimation algorithm stops with the final estimated values of

$ae = 220$ m

$re = 100$ m.

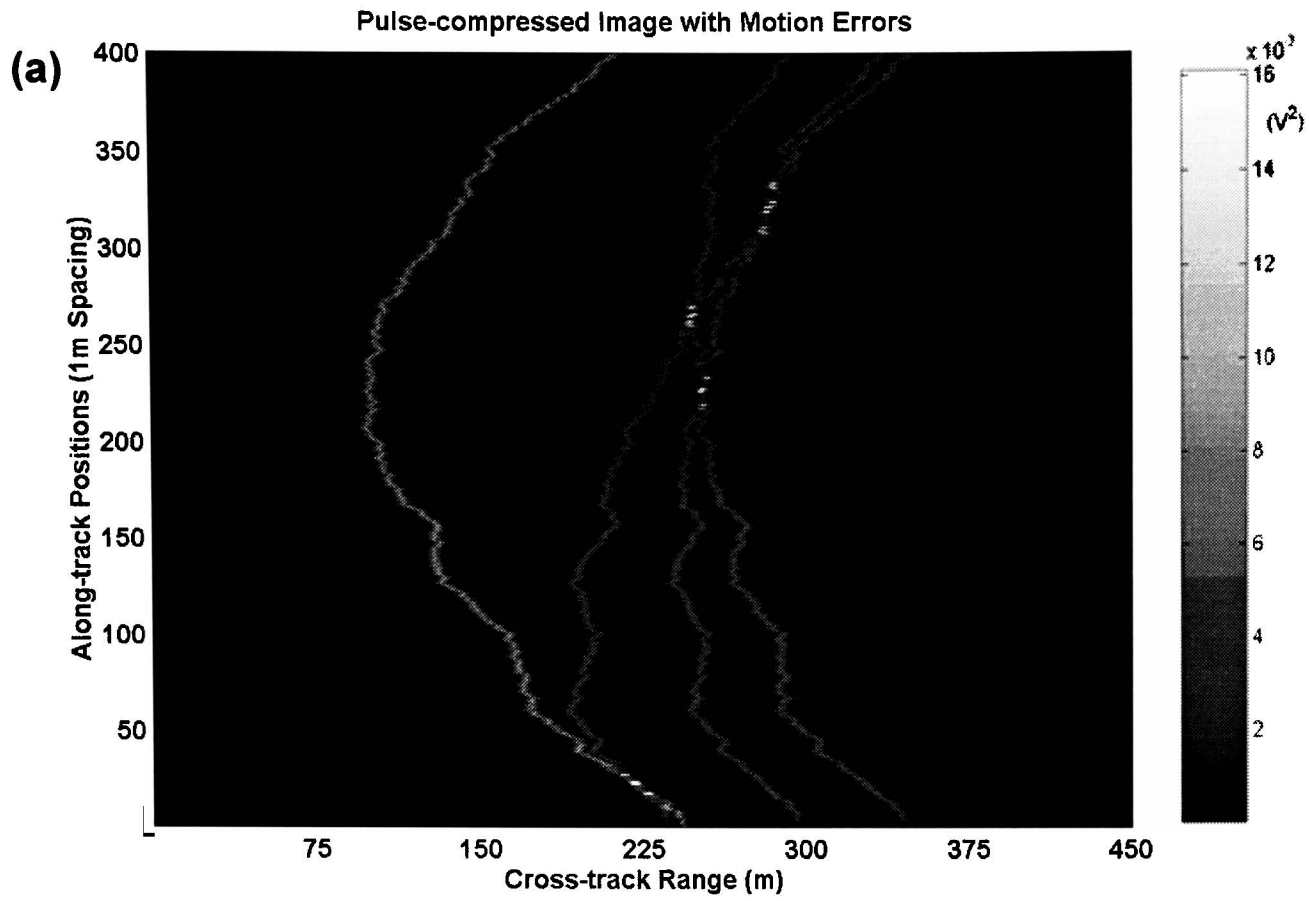


Figure 5.5: Simulation of 4 point targets **(a)** in the pulse-compressed with uncompensated errors, and **(b)** processed SAS image with uncompensated errors.

With the final estimates, the path deviations that need to be compensated, e_n, are calculated and motion compensation is accomplished by introducing delays of $-e_n$ to the corresponding n^{th} ping. The unprocessed image that has been motion compensated is shown in Fig. 5.6(a). The image is then processed to produce the SAS image in Fig. 5.6(b).

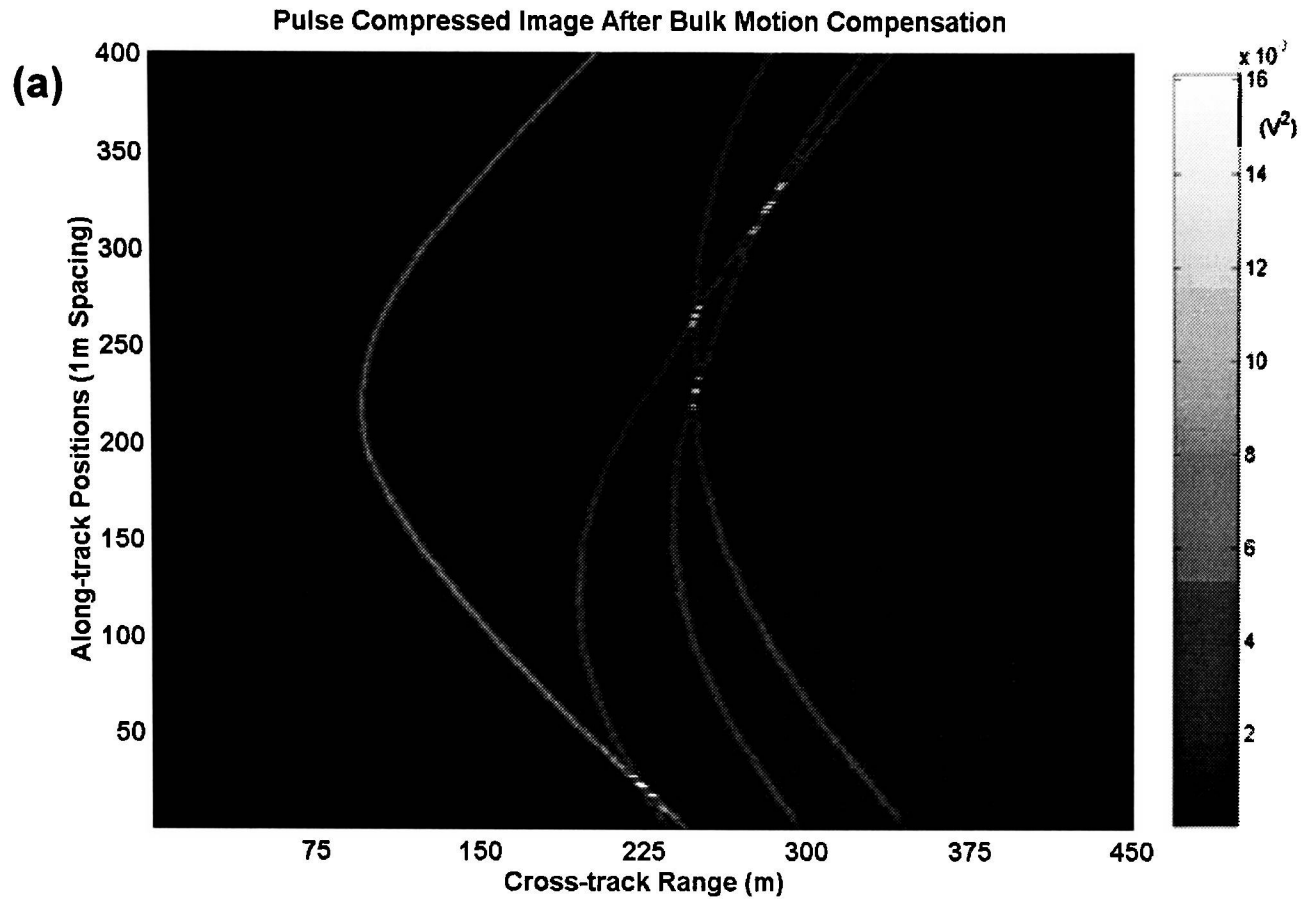


Figure 5.6: (a) Pulse-compressed image after motion compensation, and **(b)** the SAS processed image produced from the motion compensated returns.

The actual values for *a* and *r* are 230 m and 75 m respectively. From the results shown, it can be seen that although the estimated values of *ae* and *re* were not spot on, there are nevertheless improvements to the final image. The targets appear sharper and the

signal-to-self-noise ratio is clearly higher. The estimated cumulative path deviations at each n in comparison to the actual introduced deviations are shown in Fig. 5.7.

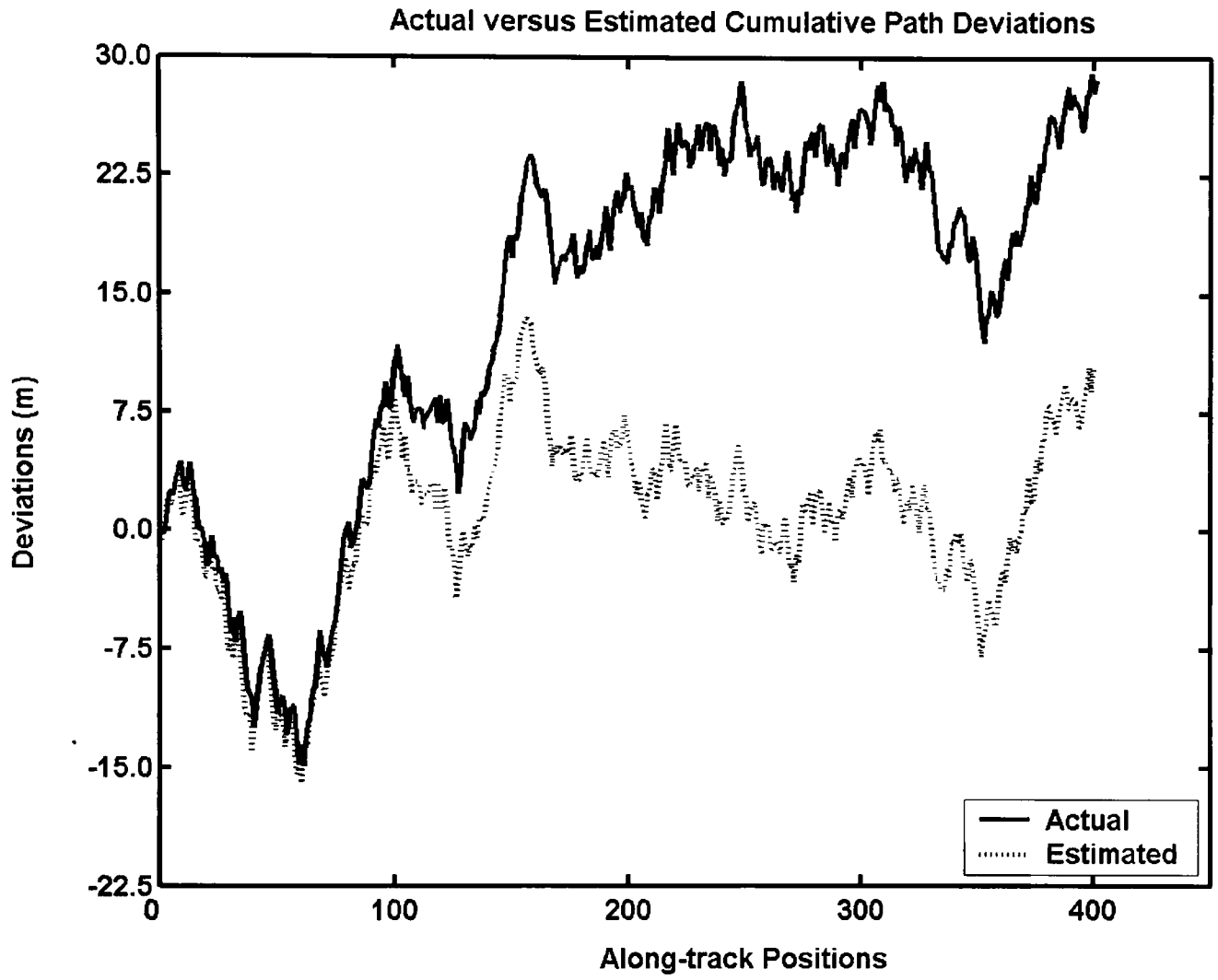


Figure 5.7: The estimated deviations in comparison to the actual set of introduced deviations. These are the cumulative path deviations, e_n.

5.6 Discussion

The simulation carried out in section 5.5 had demonstrated that this method can yield an improvement to the SAS processed image, even if the random errors are relatively large. The final locations of the focussed targets may not coincide with the locations of the actual target especially if the estimation errors are significant, a trade off necessary for improved sharpness and signal-to-self-noise ratio.

The accuracy of the estimation algorithm improves as the standard deviation of the random errors reduces. This is confirmed with further simulation-based experiments carried out. Two measures are used; the RMS of the error between the estimated and the actual path deviations, and the difference between the actual along-track position of the anchor target, *a*, and the final estimated position *ae*. These measures are plotted against a magnitude dampening factor which, by way of a simple division, decreases the standard deviation of the path deviations. The results are shown in Fig. 5.8.

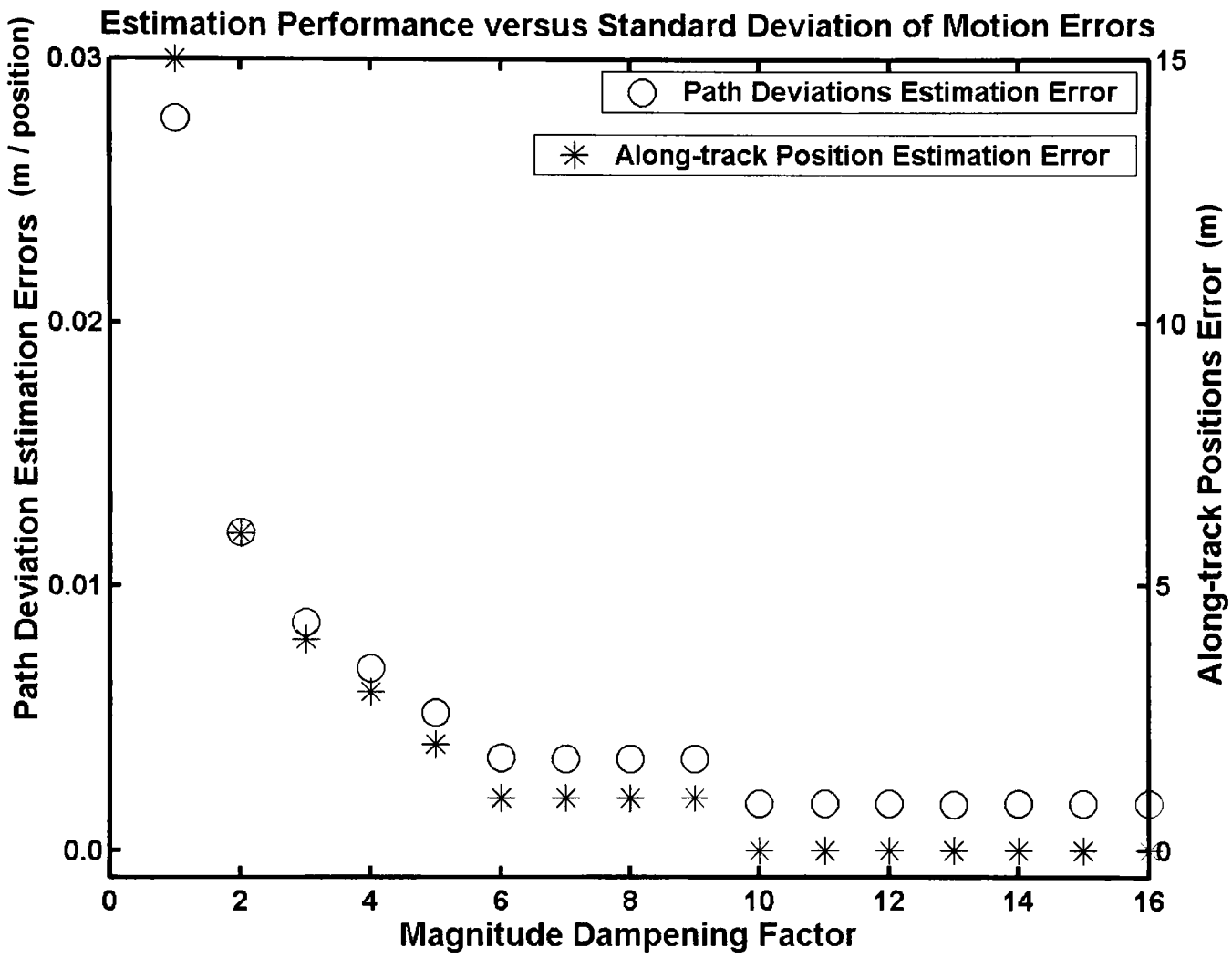


Figure 5.8: Accuracy of the estimation algorithm increases as the standard deviation of the path errors decreases.

If the path deviations are small enough where the image processed without motion compensation is sufficiently sharp, this algorithm will not be necessary. The improvement to the final image would have been too small, and any residual estimation error may cause more blurring to the targets instead.

The accuracy of this method also depends greatly on how accurately the inter-ping cross-correlations extract the inter-ping deviations with respect to the anchor target. If there are strong targets nearby with enough energy to mask the returns of the anchor target over an along-track section, the inter-ping cross-correlations for that section may not accurately represent the inter-ping deviations for the anchor target, but rather, the stronger targets nearby. If the stronger energies are well separated in range from the anchor target's returns, the cross-correlations can be limited to twice the length of the anchor target's pulse length, thus alienating spurious peaks produced from the stronger energies.

This method uses the set of path deviations estimated from the anchor target to correct for all targets at all cross-track ranges. Thus, any targets that need to be motion compensated must fall under the coverage of the anchor target. Since the omni-directionality of the transducers is often limited in practise, more than one anchor targets may well be necessary for long or different synthetic apertures.

5.7 Conclusion

In incoherent SAS processing, the image quality is more resilient to unknown tow-platform's movements. However, in cases where these movements are larger than the compressed pulse length or when the platform trajectory itself is not straight (i.e. circular or has sharp turns), bulk motion compensation is needed to improve the fidelity of the image.

The time-domain technique presented in this chapter is based upon the concept of finding the best fit of range or time-delay curvature, to the range-curvature of a pre-determined anchor target, which the range-curvature is a function of the positions of the synthetic aperture elements with respect to the anchor target. This is underpinned by the fact that for any point in space in the image, its parabolic range-curvature function is unique and is distinguishable only by the along-track and cross-track

coordinates of that point. Thus the estimation algorithm looks for the best estimate of these coordinates by minimising the RMS of the error from the mismatch of the fits.

Results from simulations have shown this algorithm producing tangible improvements to the sharpness and the signal-to-self-noise ratio of point targets on the image. Such improvements directly depend on the accuracy of the inter-ping cross-correlations in extracting the inter-ping deviations of the anchor target. As an example, for a single stationary target, its compressed pulse return will have slightly different time-delays between the first and second ping. This difference in time-delay is found by cross-correlating the returns of the first ping with the return of the second ping. Over the length of the synthetic aperture, there may be other returns that are stronger than the 'reference' target, hence affecting the accuracy of the cross-correlation procedure in extracting the inter-ping time-delays.

The primary limitation of this technique is its inevitable necessity for an anchor target, the availability of which can either be based upon opportunity, or the deliberate introduction of one (or more if necessary) to the survey scene.

Chapter 6

Sea Trials of a Bi-static, Time-Domain, Incoherent Synthetic Aperture Sonar

6.1 Introduction

This chapter presents the results of a sea survey over the Aeolian Sky wreck obtained with the incoherent SAS processing scheme. Particular emphasis is put on the transducer-hydrophones orientation, the implementation of bi-static (maximum bi-static angle of the towed-array is 20.5°) time domain processing, processing time, and application of the FREB algorithm.

The purpose of the trial is to demonstrate the robustness and practicality of the incoherent SAS scheme, as well as the implementation of the FREB scheme to real data. A realistic comparison is made between the robustness of incoherent and coherent SAS processing. The relevant issues and techniques laid out in the previous chapters are put into application in the processing of the data from this sea trial.

6.2 The Aeolian Sky Wreck

The Aeolian Sky sank in the English Channel on the 4th Nov, 1979 when it was in tow after a collision. Now lying on its portside, it spans a size of 149m x 22m on the seabed, in waters with a maximum depth of 30m, along with most of its cargo of steel pipes and vehicle chassis. There are many large steel pipes and a few vehicles that once were part of its cargo now lying around the wreck. A recent dive to the wreck revealed that part of the hull in the middle of the wreck has collapsed. Its location on GPS is (50 30.55N, 02 08.33W) [49].

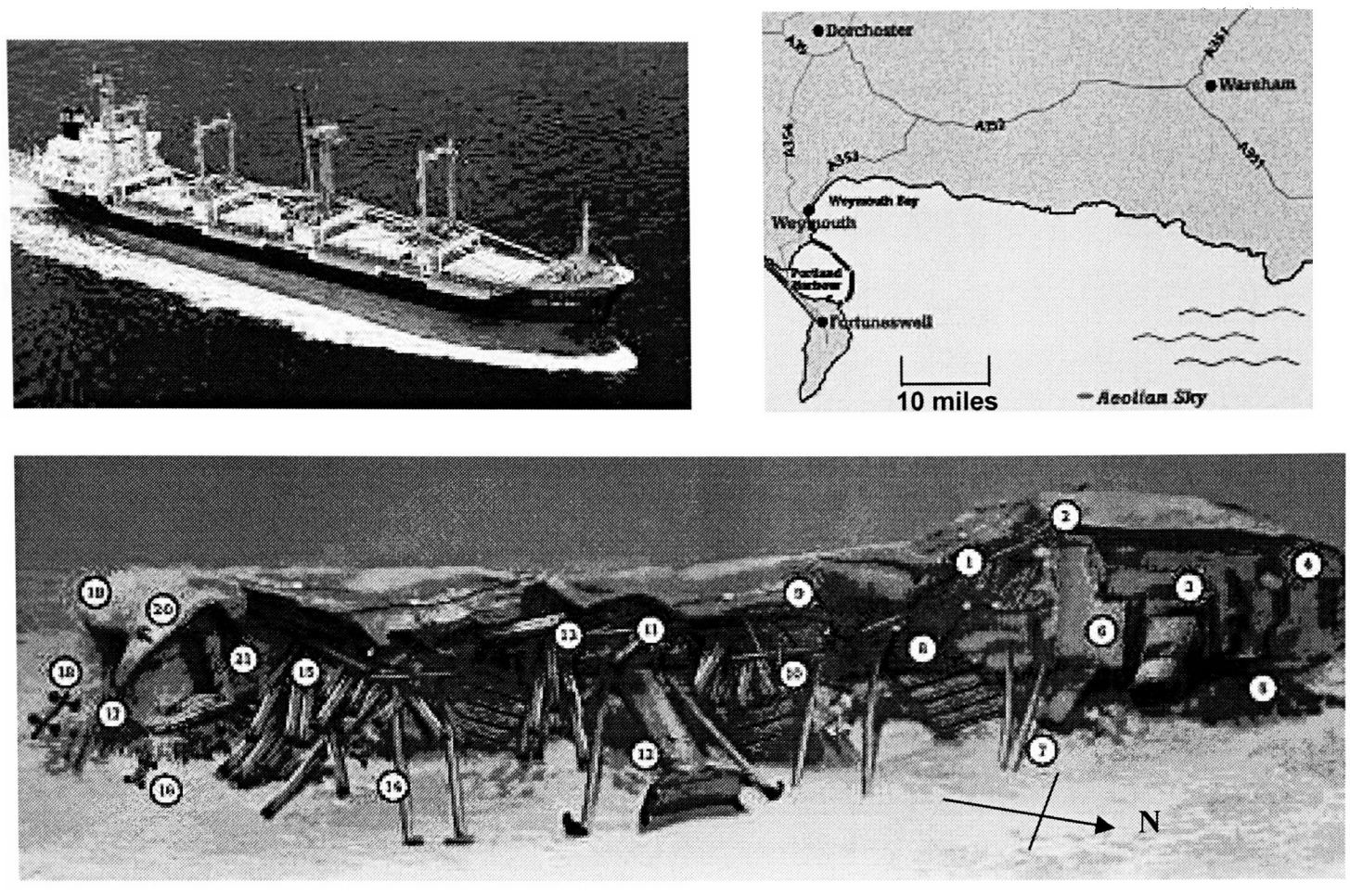


Figure 6.1: The Aeolian Sky freighter (top-left) [49], the location of the wreck off the coast of Dorset, UK (top-right) [49], and a sketch of the wreck by John Liddiard which was produced after his dive to the wreck in 2000. (bottom) [50]. The numberings on the wreck's sketch does not bear any significance to this trial.

6.3 The Survey

The survey was carried out by a team at QinetiQ (Winfrith), UK, in January 2001. A boat was used to tow a 32-channel linear array of hydrophones. The hydrophones are 0.75m apart. Transmission pulses were produced from a GeoPulse boomer system, which produces low-frequency wideband pulses from 1 to 5 kHz. The boomer is attached to centre of the array. The pulse repetition frequency is 0.6 Hz, giving an inter-ping interval of 1.7s. The receive window's time duration is 200 ms, and the received signals are sampled at 51.2 kHz.

The vessel travelled at an average speed of 3.4 ms^{-1} during the survey. One run over the survey area took less than 4 minutes. A Global Positioning System on board the vessel was used to record its position in 2 seconds intervals, but it was not

synchronised in any way to the transmission and not referenced to the location of the towed array. It merely provided information of the actual path of the vessel with respect to the Aeolian Sky wreck, which is useful to define the boundaries of the area of interest when processing the image, as well as to confirm the appearance and orientation of the wreck in the final SAS image.

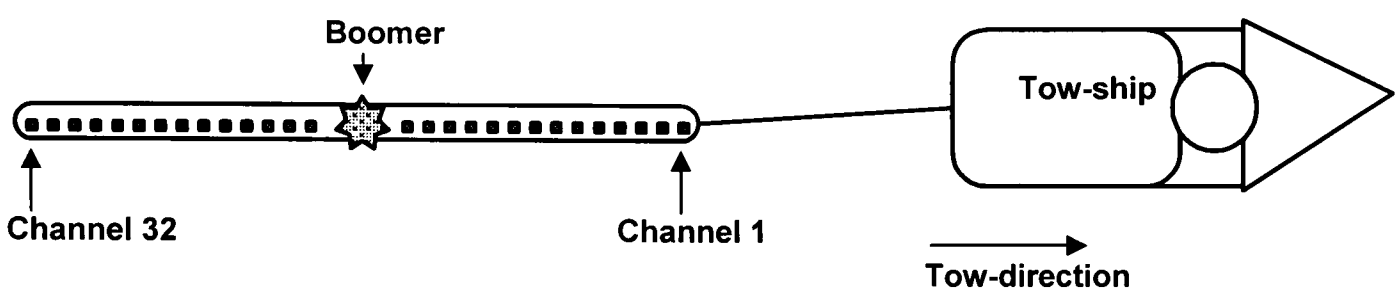


Figure 6.2: Top-view of the orientation of the boomer and the hydrophones on the towed array with respect to the tow direction.

Fig. 6.2 illustrates the orientation of the boomer and the hydrophones on the array with respect to the direction of tow. Data were recorded simultaneously from channel 1 to channel 32 for each ping that is sent from the boomer. Fig. 6.3 shows the received signals from the 32 hydrophones, indicating that the location of the boomer is at the centre of the array.

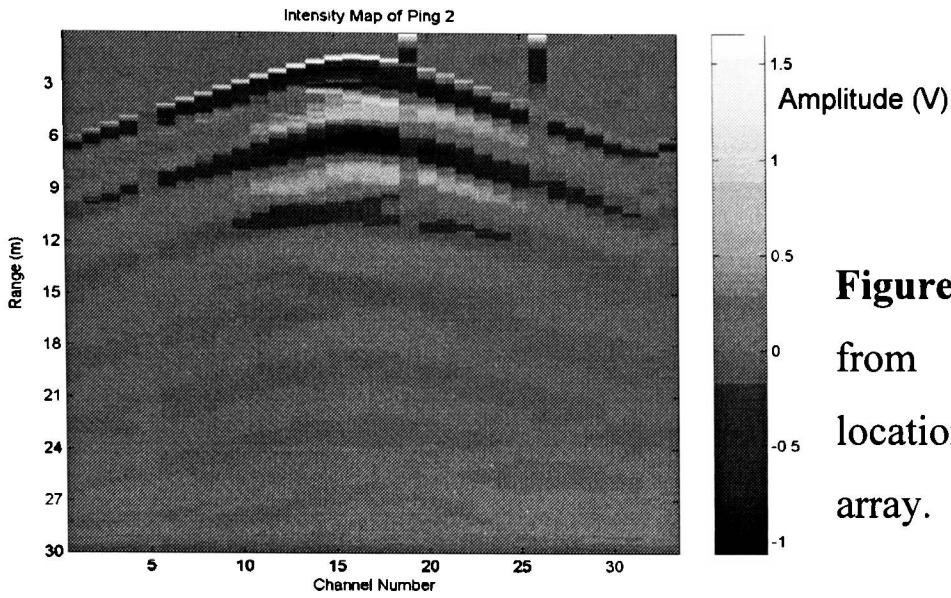


Figure 6.3: Received signals from Ping-2 indicating the location of the boomer on the array.

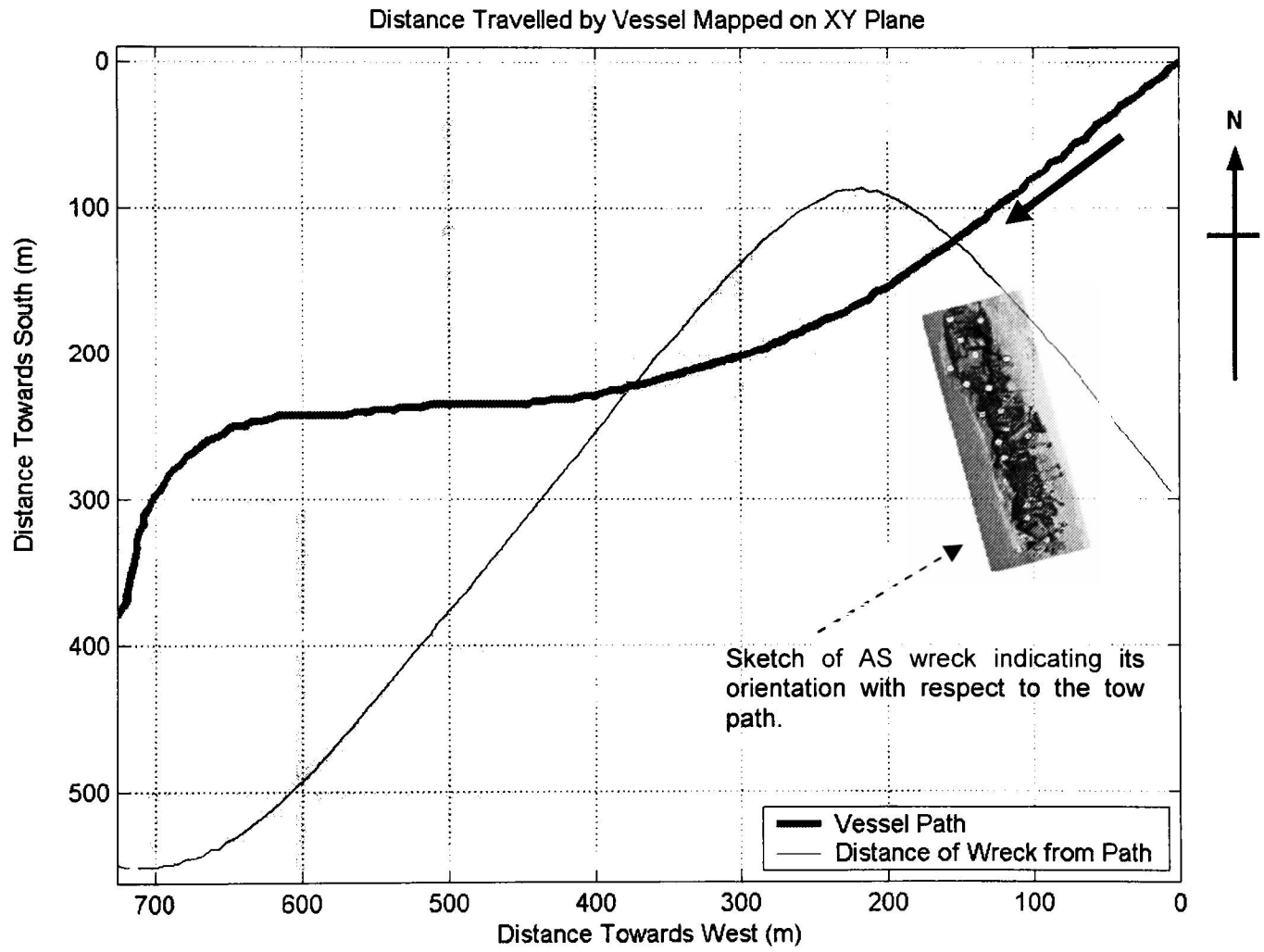


Figure 6.4: The path of the tow vessel with respect to the wreck. The thicker line is the path itself, while the thinner line represents the distance of the vessel from the wreck corresponding to each point on the path.

The route taken by the vessel is extracted from the GPS data recorded by the vessel, and is shown in Fig. 6.4. A scaled image of the wreck's sketch is included in the plot to show its orientation and location with respect to the vessel's survey route.

6.4 Synthetic Aperture Processing

6.4.1 Raw Image Formation

With the available survey information, it is known that the towed-array moves forward by 5.7 m between each ping. The arrangement of the receive elements with respect to the next ping is shown in Fig. 6.5.

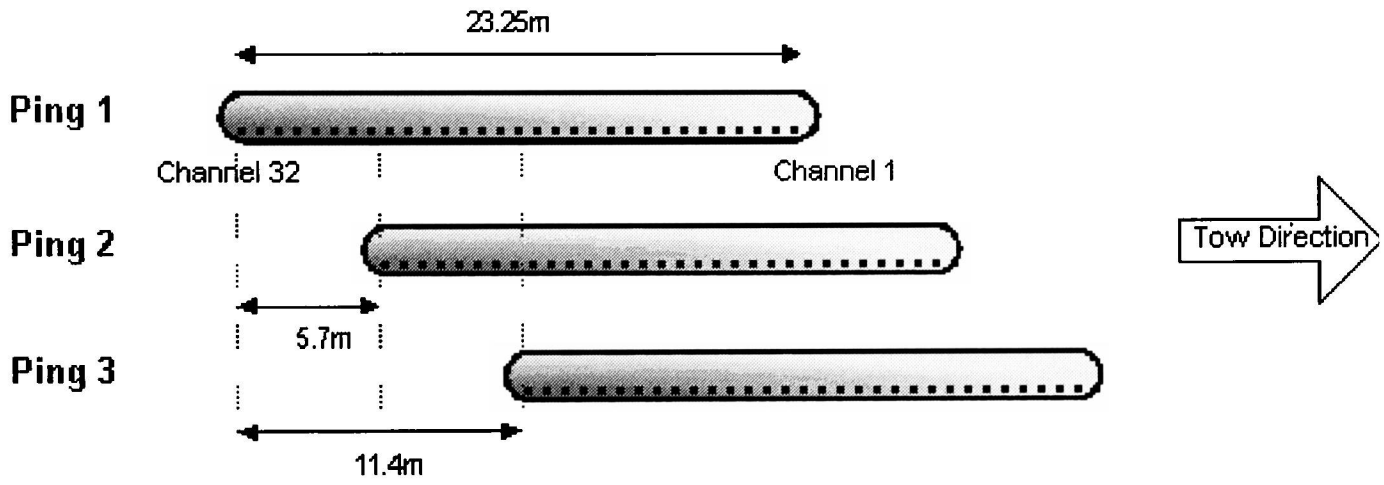


Figure 6.5: Inter-ping arrangement of hydrophone elements on the towed-array.

The first step is to build the raw data image. From the inter-ping arrangement of the hydrophones, up to 4 unique raw data images of the wreck scene can be built.

Raw Image 1: *$Ping_{n_odd}$ (channel 32 – channel 16)* linked to *$Ping_{n_odd+2}$ (channel 32 – channel 16)* and so on.
Raw Image 2: *$Ping_{n_odd}$ (channel 16 – channel 1)* linked to *$Ping_{n_odd+2}$ (channel 16 – channel 1)* and so on.
Raw Image 3: *$Ping_{n_even}$ (channel 32 – channel 16)* linked to *$Ping_{n_even+2}$ (channel 32 – channel 16)* and so on.

Raw Image 4: $Ping_{n_even}$ *(channel 16 – channel 1)* linked to $Ping_{n_even+2}$ *(channel 16 – channel 1)* and so on.

As an example, for raw image 1, if n starts with 1, then the image will start with the data from channel 32 to channel 16 of $Ping_1$ and then followed by channel 32 to channel 16 of $Ping_3$, skipping $Ping_2$. The arrangement in raw image 1 is chosen for the construction of the raw image to be processed. The arrangements in raw image 2 and 4, where channels 1 to 16 are involved, were not chosen because some channels were affected by hardware glitches. The spacing between channel 1 and 2 and between channel 3 and 4 were not the same with the rest due to wiring errors. Also, channel 6 and channel 13 were not synchronised with the other channels.

Since the survey covers quite a large area with respect to the wreck itself, only selected pings were used for raw image formation. Only pings with timestamps that correspond to the timestamps of the GPS within the desired area (Fig. 6.4) were selected. The *raw* data image being formed is shown in Fig. 6.6.

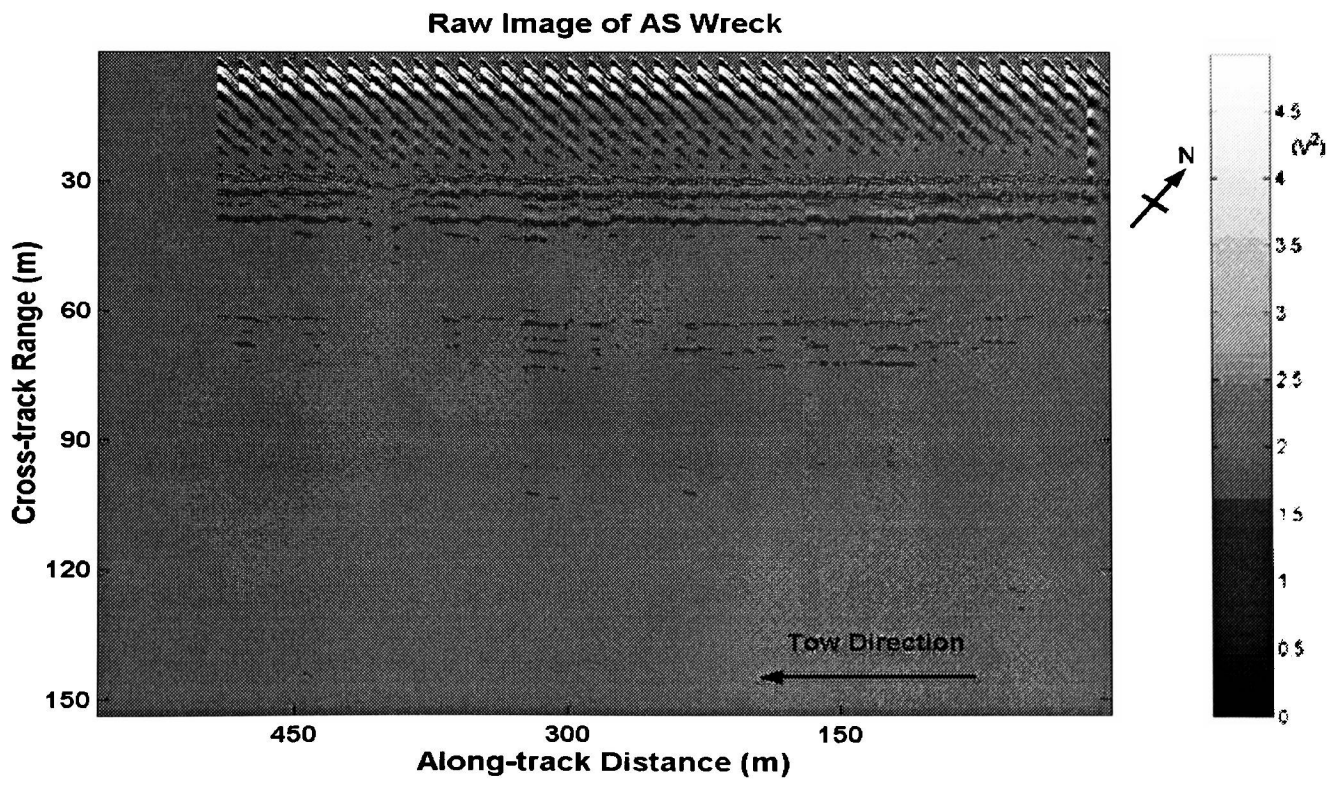


Figure 6.6: Raw data image from the Aeolian Sky wreck survey.

6.4.2 Cross-track Processing

The transmitted pulses in this trial were not frequency modulated, and thus pulse compression by matched filtering is not possible. Instead, the returns were band-pass filtered to extract the signals within the desired frequency bins. The power spectral density of the returns from one of the pings, shown in Fig. 6.7, showed that most of the energy lies in the lower frequency band. To avoid severe multi-paths from surface and seabed reverberation, a higher frequency bin is desirable. Based upon the spectrum, the frequency bin of 20-22 kHz was chosen as it has the highest frequencies with sufficiently strong energy. At lower frequencies, especially below 10 kHz, the reflections from the sea bottom are too strong and would mask the echoes from the wreck.

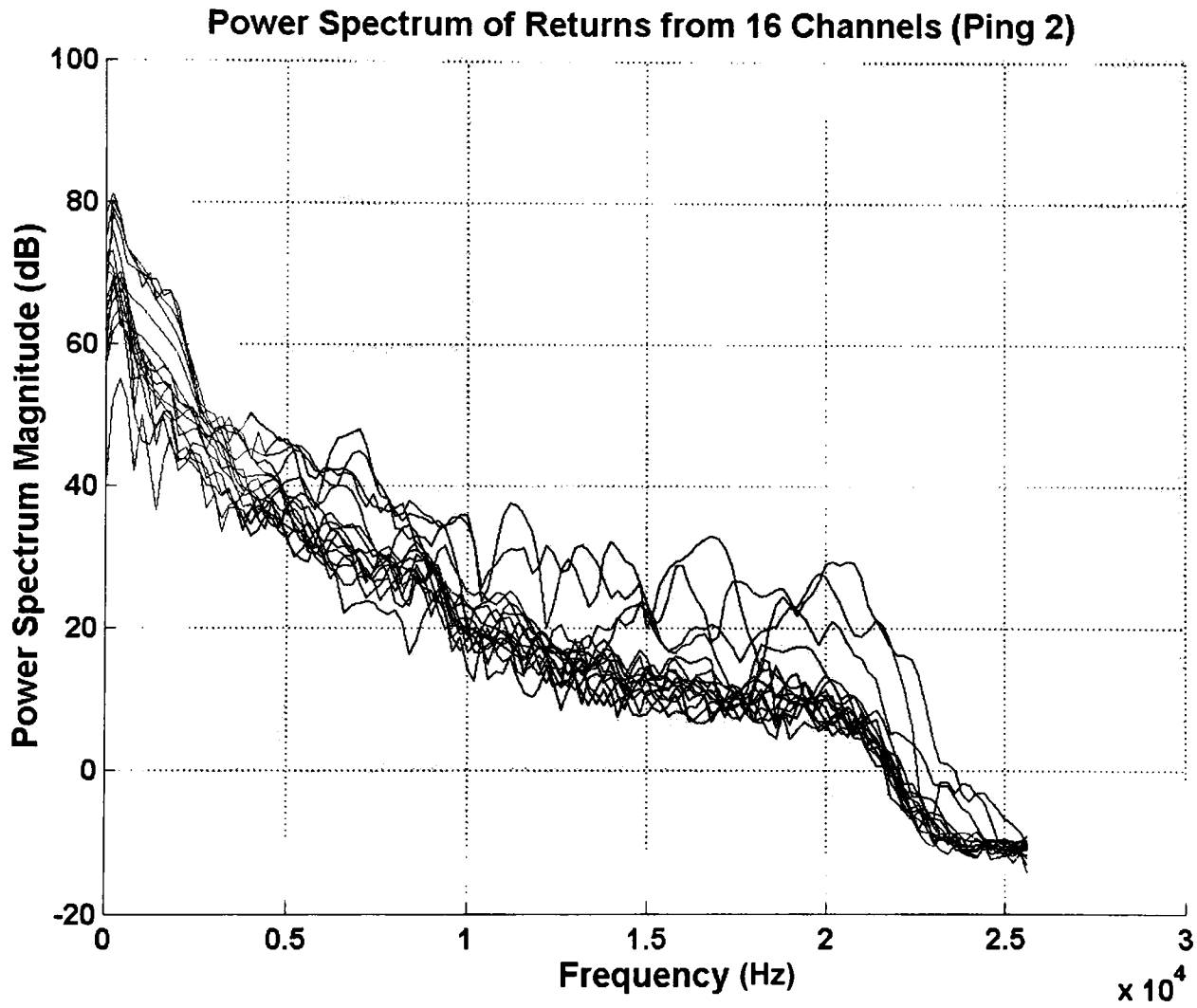


Figure 6.7: Spectra of the returns from 16 channels of Ping 2, showing that the highest usable frequencies are just below 22 kHz.

The returns were then filtered by a 20-22 kHz finite impulse response band-pass filter. The resulting power spectral densities are shown in Fig. 6.8.

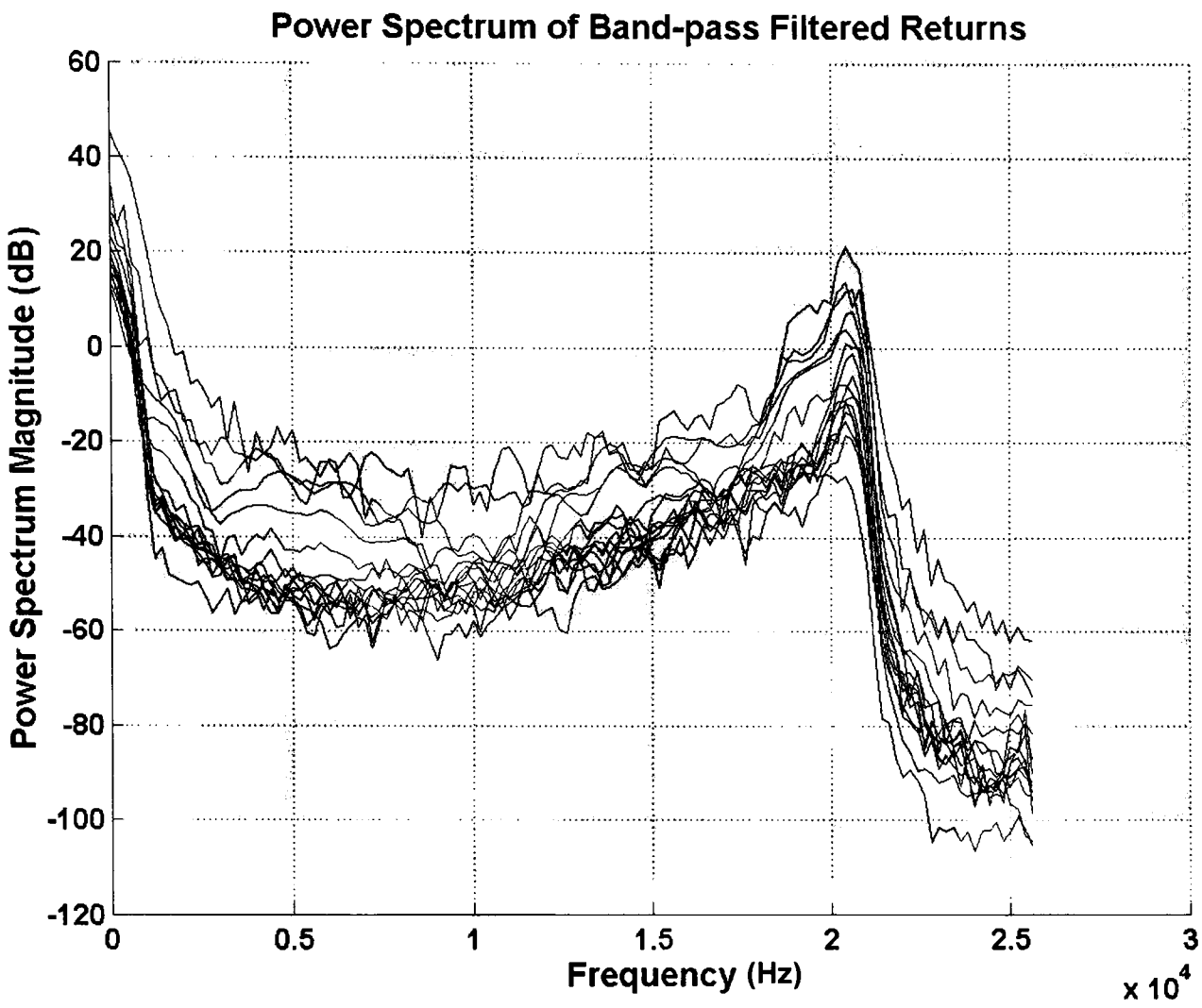


Figure 6.8: Power spectral density of the returns after passing through a 20-22 kHz band-pass filter.

Having performed the filtering operation, a Hilbert Transform is applied so that the signals are in an analytical form. This also facilitates the later coherent processing of the raw image to obtain a coherent SAS image for comparison.

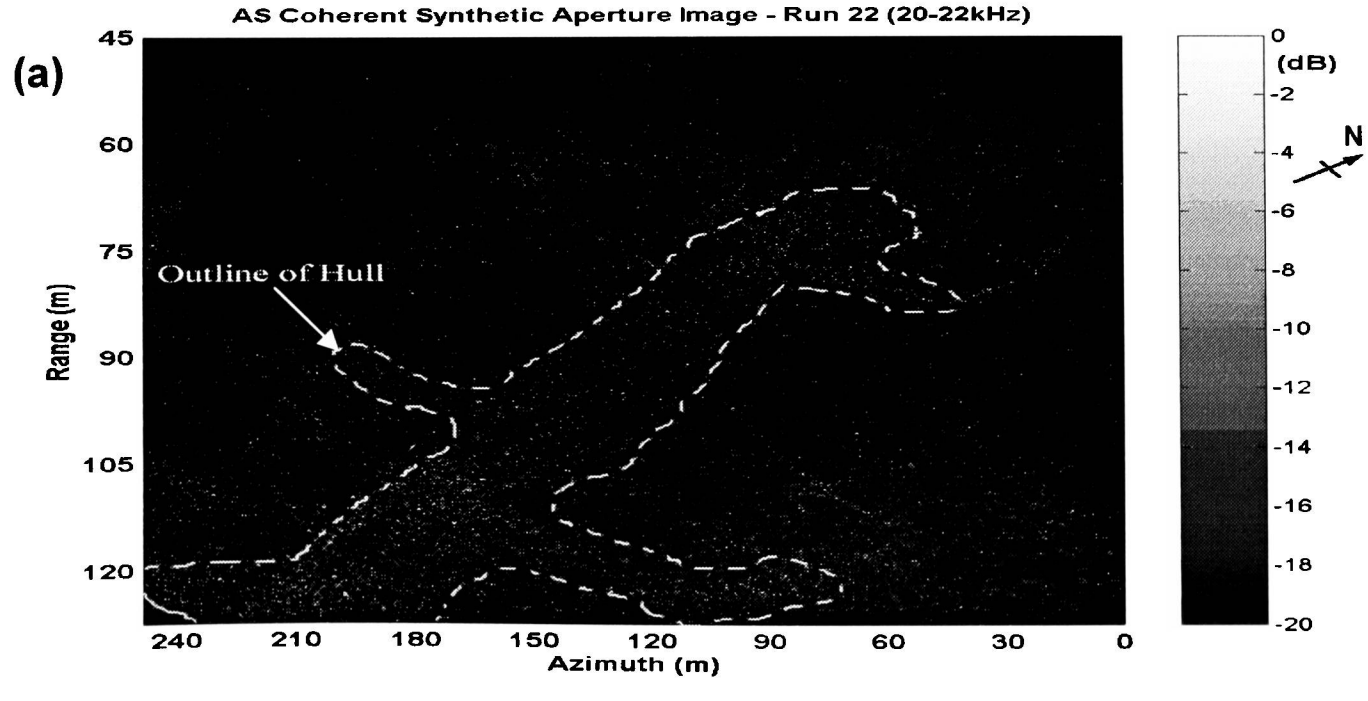
6.4.3 Along-track Processing

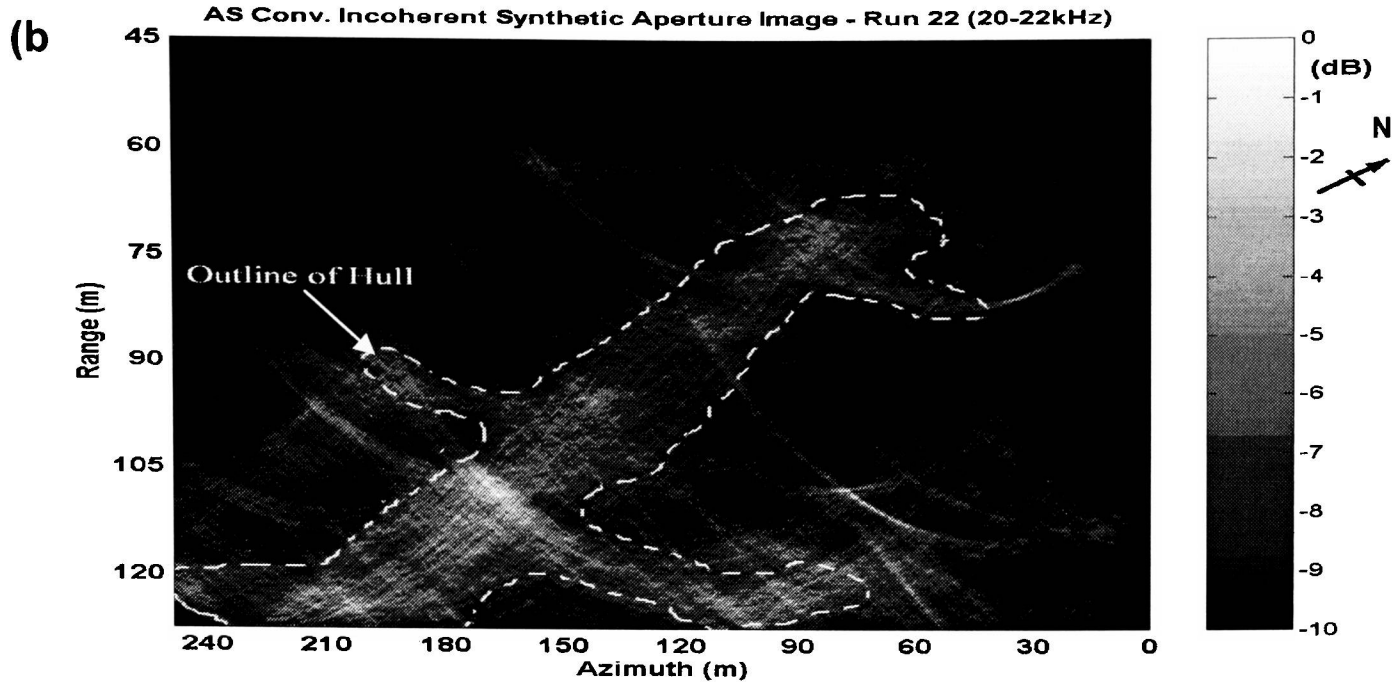
The next step is the removal of phase. This is done by multiplying the signals with their complex conjugates, thus giving the power representation of the reflected acoustic energy at a given time. The incoherent SAS algorithm in equations (3.7) and (3.8) is then applied. Monostatic assumptions were made here, but will be removed later in this chapter.

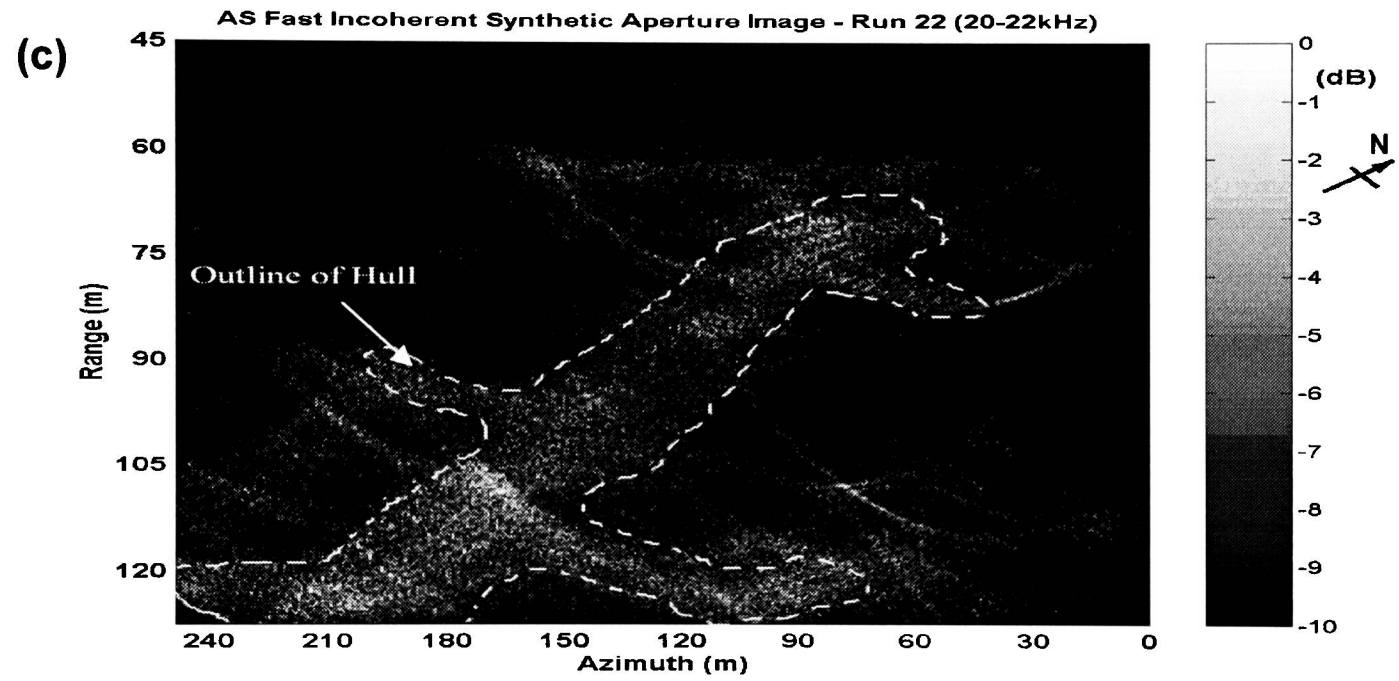
The characteristics of the hydrophones such as the resonant bandwidth and the exact directional response were not known, but they are treated as omni-directional. Hence, weighting functions were not applied on the synthetic aperture in the process of incoherent summation. The synthetic aperture length was set at 75 m, or 101 elements. After the processing, time-varying gain was applied in the cross-track direction to compensate for energy loss due to acoustic absorption.

An image formed via coherent summation was produced to give a comparison of the achievable image quality between coherent and incoherent methods, under a practical environment, and in this case, with no privileges of complex hardware systems, experimental pre-runs, accurate navigational aids or motion compensation algorithms.

The FREB scheme laid out in chapter 4 is also applied here to show its practicality of implementation, as well as its contribution to the reduction of processing time and its effect on the image quality. The images are shown in Figure 6.9. All the images have been hard-detected (with a fixed threshold and normalised to the image's maximum) at half-power level to improve the dynamic range of the images' contrast. They were then normalised by their respective maximum or peak values to make them easier to compare visually.







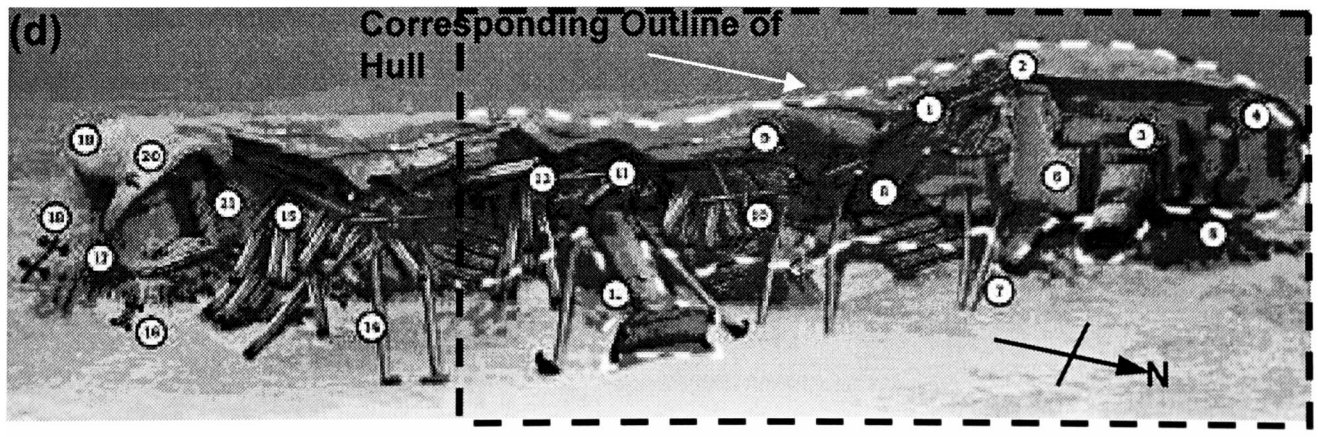


Figure 6.9: Final SAS images of the Aeolian Sky Wreck with (a) coherent processing, (b) conventional incoherent processing, (c) incoherent processing with FREB, and (d) the corresponding outline of the hull showing the part being imaged.

6.4.4 Analysis of Results

From the results shown in Fig. 6.9, it can be seen that the image processed incoherently yields a structurally identifiable representation of the first half of the Aeolian Sky wreck. Self-noise is largely hidden by the process of hard-detection as the processing gain is sufficiently high due to the use of a high number of elements in the synthetic aperture. Much of the blurring in the images comes from the uncompensated motion errors of the towed array. However, the incoherent SAS method had proven itself to be resilient towards these errors, which were incurred under real operating circumstances, to give a visually fit image of the wreck.

The coherently processed image, on the other hand, is very blurred and grainy and cannot produce any figure with strong structural features. This is mainly due to acute lack of phase coherence as no motion compensation was applied, as well as the under-sampling in the along-track axis. The theoretical requirement of the along-track spacing in this case is 0.038 m (based on 20 kHz frequency), thus the raw data were actually 20 times under-sampled.

The image processed incoherently, but with the FREB algorithm, saw a reduction in the processing gain, as a smaller number of elements was used in incoherent summation. The wreck appears slightly grainy, but there is no loss of structural features compared to the image processed with the conventional incoherent SAS method. The 'overflowing' effect from self noise is less severe than in the conventional method, thus the structural features of the wreck appear sharper. The processing time recorded with the FREB algorithm is 1279 seconds, while the conventional incoherent method took 2823 seconds. A time-saving of more than a factor of 2 was made. The coherent method took a processing time of 5382 seconds.

The processing times recorded are based on processing performed entirely in the Matlab environment, hence the generally long time needed. The processing algorithms were later implemented in C, which is more efficient in handling loops and provides

quicker access to large matrices. The FREB algorithm implemented in C consumed only 162 seconds of processing time on a 1.2 GHz central processing unit.

6.5 Bi-static Processing

The requirement for a single-transmitter, multiple-receiver array configuration is paramount for increasing the mapping rate of a synthetic aperture sonar (SAS) at a reasonable economic and complexity cost, without compromising imaging performance [13,27]. There are other promising methods like continuous transmission frequency modulated (CTFM) signals [51,52], but they are more computationally intensive and complex, and may suffer from Doppler effects during transmission due to the continuous transmission. Thus, the single transmitter multiple receiver array has been increasingly adopted [14,42,53] in SAS applications in recent years, and is also the choice of array configuration in this survey. In coherent SAS imaging, the data are usually pre-processed, by interpolation and range dependent phase compensation, to create imaginary mono-static transmit/receive elements such that their round trip delay time would be equivalent to that of a corresponding element in a bi-static configuration. This decreases computational load in the subsequent mono-static synthetic aperture processing. However, one loses the ability to apply amplitude weightings based on the direction of wave departure from the transmit element and the direction of arrival to each of the individual receive elements with regard to a particular pixel to be processed.

The results in section 6.4.4 are based upon the assumption that the boomer and the hydrophones are co-located. But in actuality, since the boomer is located in the middle of the array, there is only one boomer location that corresponds to every 16 elements on the raw image. Applying bi-static processing, hence removing the assumption that the boomer and hydrophones are co-located, will remove the range back-projection errors resulting from such an assumption. It then allow the investigation into whether, with time-domain incoherent SAS processing and the use of single transmitter multiple receiver array, there is any significant gain in image quality from the investment of additional computational effort and time needed for bi-static processing.

The incoherent bi-static SAS processing is performed based upon the principles of summing the ranges to the transducer and hydrophones to obtain the two-way propagation range (equations 3.7 and 3.9), and hence the time-delay. The implementation of this to the data obtained in this sea trial is illustrated in Fig. 6.10.

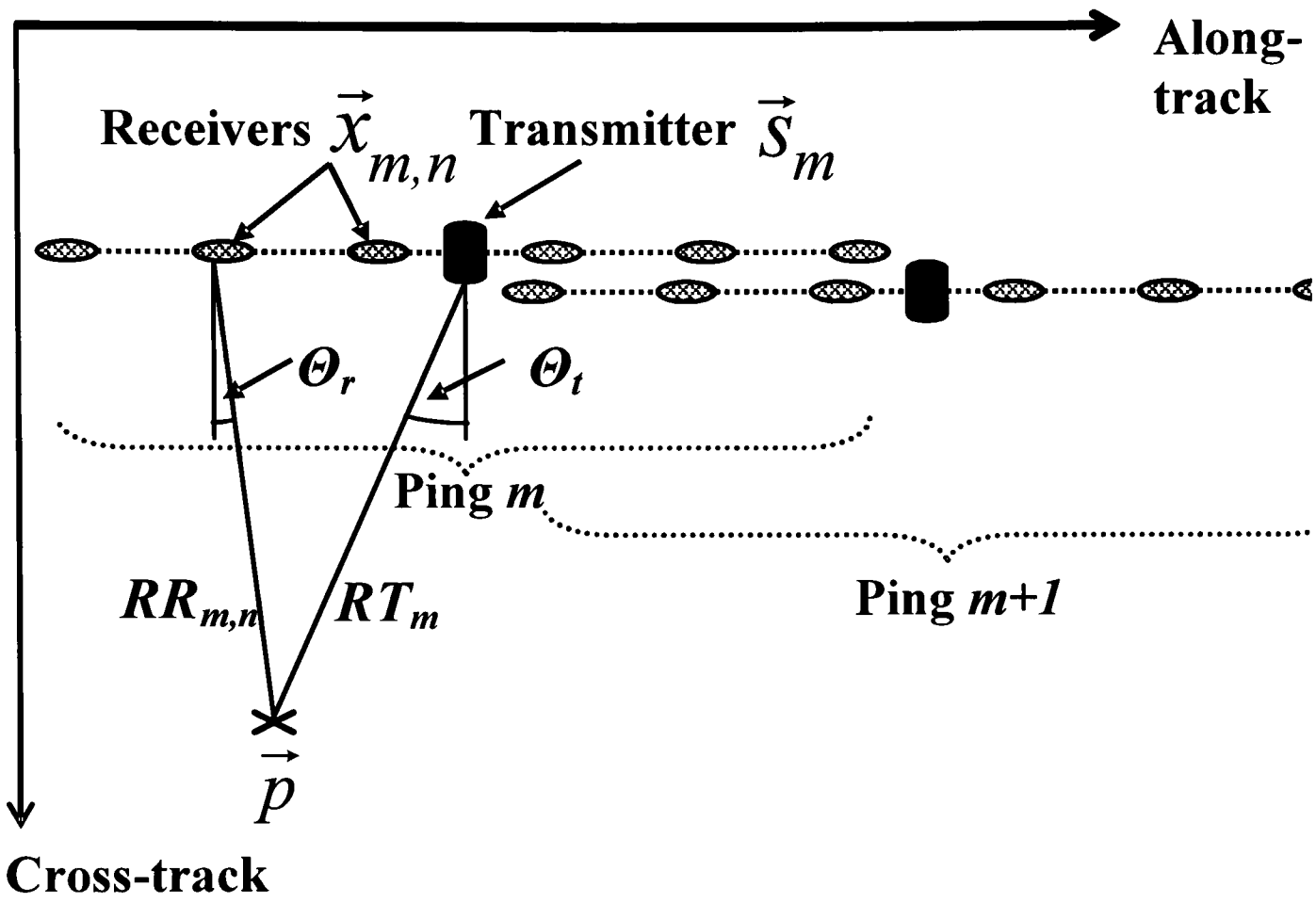


Figure 6.10: An illustration of the bi-static configuration by which the incoherent SAS processing on the sea trial data is performed. To avoid cluttering, only 6 receive hydrophones were drawn for every boomer ping location, despite the fact that there are 32 receive elements in the array.

Based upon Fig 6.10, $\vec{x}_{m,n}$ and $\vec{s}_m$ are the positional vectors of the n^{th} receiver and the m^{th} transmitter location respectively, and the pixel concerned lies at $\vec{p}$. The total time-delay is the sum of the propagation times from the transmitter and from the receiver to the pixel:

$$t_d = \frac{RR_{m,n} + RT_m}{c} \tag{6.1}$$

Expressing the time-delay as sample-delay and $RR_{m,n}$ and RT_m as dot products gives:

$$n_d(\vec{p},\vec{x},\vec{s}) = f_s \cdot \frac{\vec{p}\cdot\vec{x}_{m,n} + \vec{p}\cdot\vec{s}_m}{c} \tag{6.2}$$

and thus

$$I_{image}(\vec{p}) = \sum_{m=1,n=1}^{M,N} w_{p,m,n} \cdot I_{data}(n, n_d(\vec{p},\vec{x},\vec{s})) \tag{6.3}$$

where M is the number of transmissions and N is the number of receive elements in the physical array. The raw data was built with 'raw image 1' arrangement as described in section 6.4.1. For every ping, there are 16 receive elements that correspond to each transmit element position. Hence in the summation, m is incremented by 1 whenever n approaches 16, and then n is reset to 1 for the incremented value of m. The weighting factor $w_{p,m,n}$ can now be a function of the angles θ_r and θ_t which can be derived from the positional vectors $\vec{p}$, $\vec{x}_{m,n}$ and $\vec{s}_m$, thus allowing a weighting factor to be applied such that it takes account of the directional response of the individual transmit and receive elements.

The image obtained from applying bi-static processing produced a measurable increase in contrast. Also, a careful inspection reveals that the sharpness of the structural features of the wreck had improved. These are shown in the results presented in Fig. 6.11. The contrast is measured for each along-track slice over all the cross-track ranges, such that for each slice, the standard deviation divided by the mean is calculated to give the normalised contrast for that slice. As seen from Fig. 6.11, there is an improvement of about 13.3% at shorter ranges of 45m to 75m, and at longer ranges/CPA of 90m to 135m, the improvement falls to about 3.3% only. The improvement comes from the fact that the differences between the outgoing and return path of pulses are taken into account, hence giving a better match to the actual range-curvature function in the processing. Due to the relatively small bi-static angle in this

case (20.5°), the difference in the two-way return path becomes less significant as the range increases. This is analogous to a far-field assumption, where wave-front can be assumed to be flat if the range to the source is much larger than the array length. In this case, as the range increases, the difference (error from monostatic assumption in the calculation of the range curvature) becomes less significant, and hence the improvement that can be gained decreases from 13.3% to 3.3%.

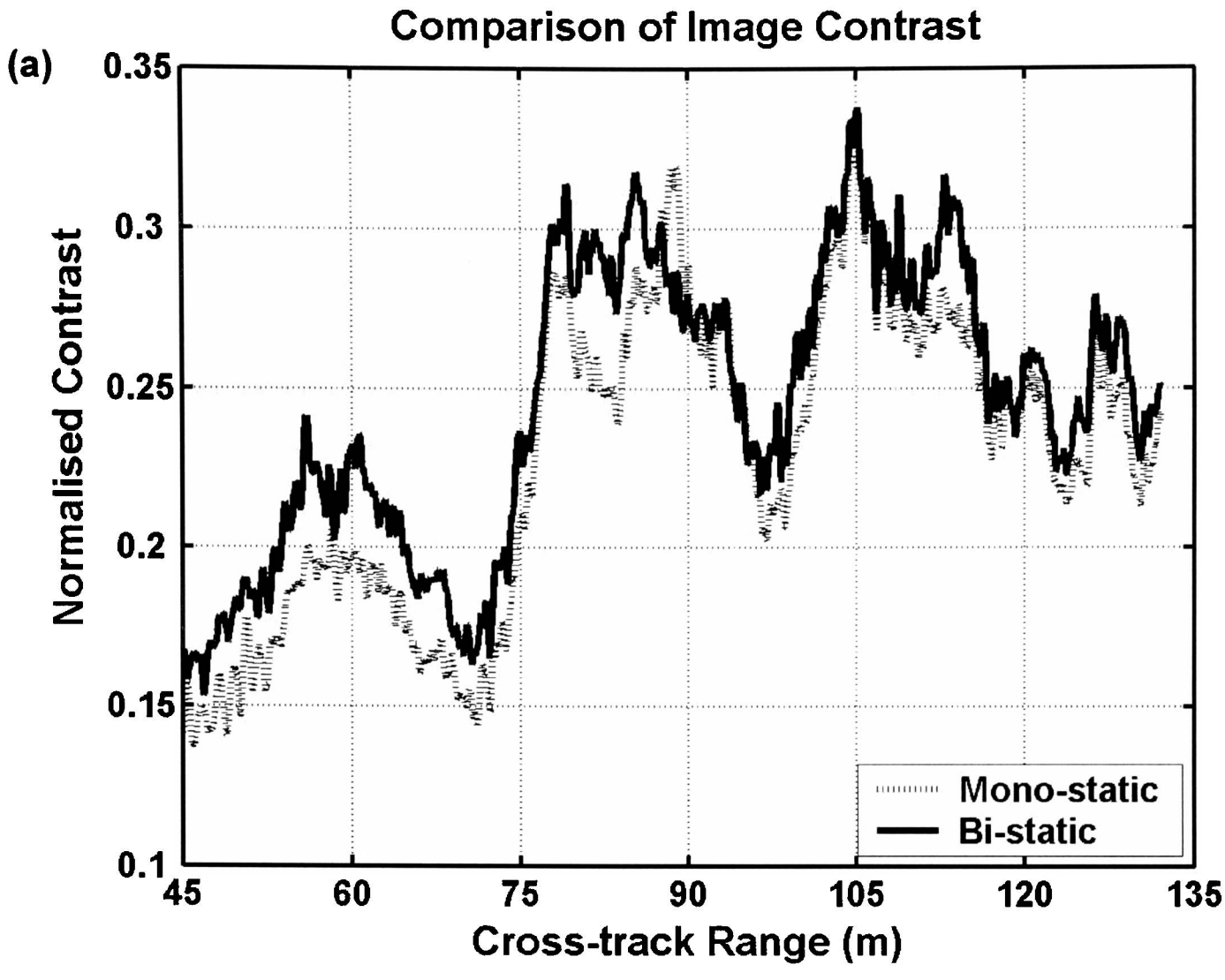


Figure 6.11: (a) Improvement in the image contrast with bi-static processing, measured on each along-track slice over all the cross-track ranges. (b) The incoherent SAS image processed with bi-static processing, where the structural features of the wreck are visibly sharper.

The comparison was repeated, but with a synthetic aperture length that is deliberately reduced by half. The results showed a negligible gain in image contrast from the removal of bi-static assumption. Hence, if there is any predominant factor that reduces the signal-to-self-noise ratio, such as severe motion errors, the improvement in image contrast from the removing of the mono-static assumption will reduce in significance. This is because, as the blurring caused by the other factors increases, the figure in the image becomes less structural, hence the use of contrast as a benchmark no longer yield reliable results.

6.6 Conclusion

The results from the sea survey of the Aeolian Sky wreck is the first and the strongest testimony yet of the feasibility of an incoherent, time-domain SAS system operated with a towed single transmitter, multiple receiver array.

There are a few important characteristics in this survey that highlight the robustness of this system. Firstly, no motion compensation had been applied; no additional hardware was required to obtain accurate navigational data of the towed array. Despite this fact, the processing of the data had yielded a recognisable image of the wreck. Should bulk compensation be necessary, motion errors can be extracted by correlating the overlapping elements between adjacent pings.

Secondly, the survey was accomplished in a fairly short time. The application of incoherent SAS processing allowed for a wider spacing between hydrophones. This coupled with the use of a single boomer, multiple hydrophone array configurations allowed for a successful survey with an acceptable mapping rate, using relatively low-cost hardware that demands little system preparation time. It is not unreasonable to conclude that had there been a broadband, high power, high frequency transmitter, the images would have been much sharper and crisp.

Thirdly, the implementation of full bi-static processing to match a bi-static array arrangement is necessary to obtain an optimal quality in the image. Also, such a processing scheme enables the application of a weighting function that matches both the directional response of the transmitter and the receiver (which may differ in a bi-static case) based on their respective angles to the location cell concerned.

Utilising a "nested array" approach, such that the second half of the elements on the array overlaps spatially with the first half from the previous ping, had increased the system's data acquisition reliability. Despite 2 channels not functioning properly and another 2 channels wired incorrectly, there were still adequate data available to form the raw data image without having to drop any along-track spatial elements. If all the channels had been working reliably, then up to 4 distinct raw images of the wreck could have been formed, individually processed and then summed in the end to give maximum processing gain.

Chapter 7

Incoherent Synthetic Aperture Sonar 3-D Imaging with 2-D Synthetic Aperture

7.1 Introduction

Applications of synthetic aperture imaging techniques in the underwater environment are usually, thus far, confined to the deployment and synthesis of linear arrays. Incoherent SAS processing, though inferior in resolution, is not limited by the usual constraints of conventional coherent SAS, and thus presents new opportunities for robust imaging systems. Apertures of arbitrary shapes can be synthesized depending on the nature and requirement of the target application and environment. Based upon this concept, a 3-dimensional SAS imaging technique utilizing the synthesis of 2-D apertures is presented here. The aspect of array set-up combined with the method of aperture synthesis is novel.

This chapter begins with the discussion on non-linear synthetic aperture, and then goes on to consider the implementation of two forms of synthetic apertures that are beyond the conventional linear form. One of them is a uniformly spaced planar synthetic aperture in mono-static mode and the other is a less hardware-demanding multi-look synthetic aperture working in multi-static mode. The core of the presentation lies in the results obtained from the experimental trials undertaken based on these two designs. Given that other factors like transducer trajectory and medium instabilities can be controlled, issues like applying unique transmitter and receiver weighting functions and the effect of the synthetic apertures' geometries on the point-target energy response can be studied more accurately.

Stemming from these 3-D approaches, several new issues like image registration and representation; impacts on object visualisation; and normalisation methods are being investigated and discussed. There is no doubt that the processing time needed to carry out such schemes is much greater compared to a linear synthetic aperture, but this is

not the prime consideration in this chapter as these schemes are underpinned by a valid assumption that computational speed to cost ratio will continue to increase exponentially in the future.

7.2 Beyond Linear Synthetic Aperture

In the previous chapters, it has been established that an incoherent SAS system is not constrained by the limiting factors present in a coherent system. The fact that the along-track sparse sampling is practically applicable, and that the incoherent SAS processing is relatively more resilient to motion errors, mean that the synthesis of an aperture need not be constrained to the conventional linear form. Extending the synthetic aperture beyond the linear form opens up a whole new arena of possibilities in underwater imaging. This line of thought is not new. Many in the SAR community had in the recent years undertaken trials that attempt to synthesise apertures beyond the linear form; where the synthetic aperture is planar [54], multi-pass SAR where several apertures are synthesised at different grazing angles [55], and via two synthetic apertures making coherent stereo collection [56]. Among the SAS community, multi-aspect SAS [57,58] and interferometric SAS [27] are both significant examples of attempts to expand the boundaries of linear synthetic aperture with the goal of extracting more visual and analytic information from the target scene.

The primary advantage of having a synthetic aperture beyond the linear shape is to be able to achieve an imaging capability past the current ability of 2-dimensional azimuth-range visual imaging and representation. The phenomenon of shadows and blind spots [59] which are ever so common in images produced from strictly linear arrays can be reduced. Targets can be visualised and represented more accurately in three dimensions. Metamorphosis of targets can be identified in greater detail and comparisons are more easily made. Successful implementation of 3-D imaging will also prove useful for automatic object recognition systems in underwater applications. A very comprehensive and attentive analysis and discussion on the issues, potential, present constraints and promising techniques in the field of 3-dimensional image

generation and processing in underwater acoustics was presented recently by V.Murino [60]. The use of planar arrays, physical and until recently synthetic, are not uncommon among the ultrasonic community where acoustic imaging is applied extensively for biomedical purposes and in the field of non-destructive testing. There have been a number of proposals from this field with regard to the synthesis of planar arrays. They mainly attempt to synthesise coherently, with as small number of elements as possible without causing a significant beam-pattern deterioration or presence of grating lobes, a sparsely sampled, aperiodic, planar synthetic array [61,62,63]. However, the environment and the condition under which they operate differ significantly from that in underwater applications, hence rendering the direct adaptation of these methods prohibitive. Nevertheless, a fundamental concept underpinning these methods was observed: the beam-pattern can be optimised by using unique weightings on each element, either individually, or combined with the appropriate choice of element positioning such that the elements on the planar synthetic array are positioned to produce an optimal beam-pattern. The same is applicable in the synthesis of apertures for incoherent SAS imaging.

The concept of synthesising 2-D apertures with incoherent SAS processing is straightforward. It had been established in the previous chapters that the synthetic aperture can, theoretically and upon satisfying performance parameters, be in any shape or form. As long as the relative positions of the elements are known to the accuracy of a fraction of a pulse length, one can compute as before, for a particular point to be focussed, the total propagation range corresponding to all the elements in the synthetic aperture. The positional vectors of the elements in the synthetic aperture will however need to be represented in the 3-D domain. Depending on the shape and form of the synthetic aperture, the point-target energy response will vary and this is an area that will be explored further in this chapter.

7.3 Mono-static 2-D Synthetic Aperture

7.3.1 Concept and Simulation

In the first attempt to study the potential of an incoherent SAS system for robust 3-D imaging, a simulation of a mono-static uniformly-spaced planar synthetic aperture is carried out. This concept is illustrated in Fig. 7.1.

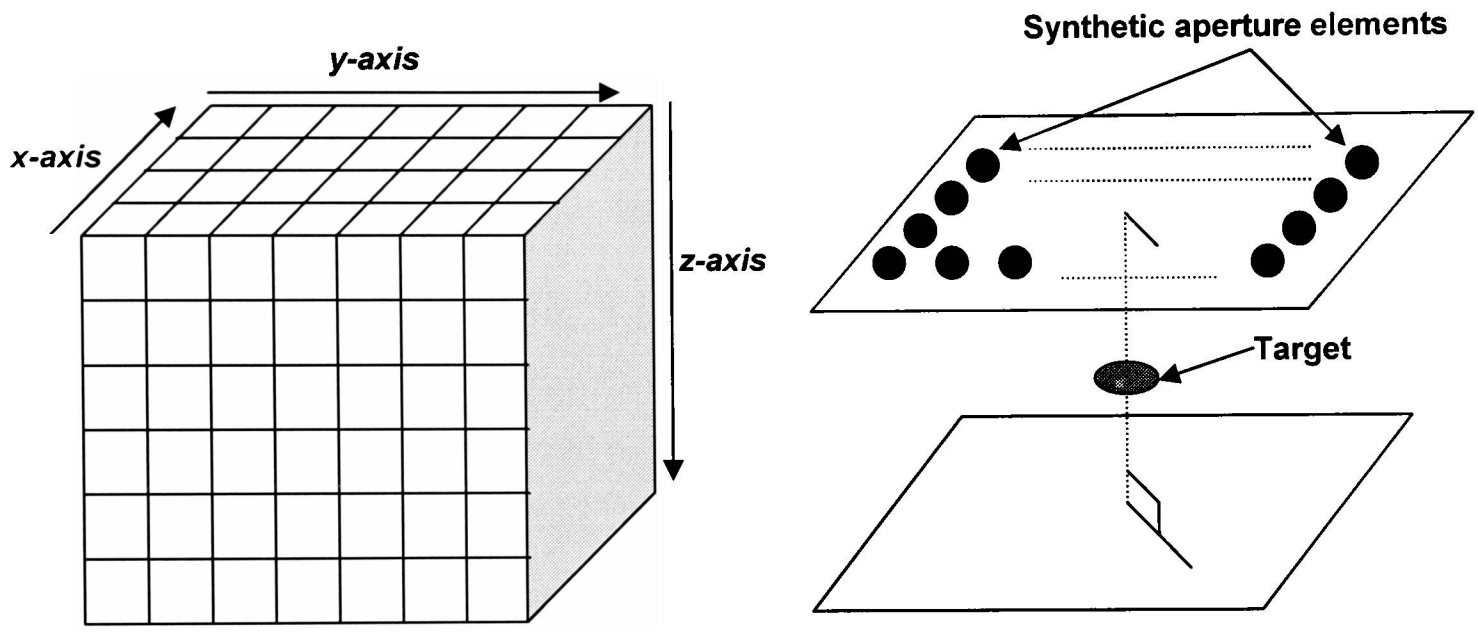


Figure 7.1: Axes of a 3-D matrix (*left*) and the planar arrangement of transducer elements forming a 2-D synthetic aperture with respect to the volumetric survey scene (*right*).

A 3-D data matrix was formed with chirp pulses reflected off a simulated point target. The chirp pulses are simulated to be transmitted from a single element (as represented by a black round spot in Fig. 7.1) and repeated with at the next position until the whole planar aperture is formed. The chirp pulse has a Q-factor of 2.5. The returns are appropriately delayed based upon the range between the corresponding synthetic aperture elements and the point target. The process of summation is a modified version of equations (3.7) and (3.8) such that the 3-D coordinates are used. Instead of using (n_a, n_r), where a and r represented along-track and cross-track range respectively, the coordinates in this 3-D case shall be changed to x-y-z axis as illustrated in Fig. 7.1. The

z axis can be read as the height from the bottom, while the x and y axes are perpendicular to the z axis. Hence, the equations now become

$$I_{image}(n_x, n_y, n_z) = \sum_{m=1}^{M} \sum_{n=1}^{N} I_{data}(m, n, n_d(m, n, n_x, n_y, n_z)) \tag{7.1}$$

where (n_x,n_y,n_z) is the current point in the 3-D volume on which focussing is performed, and n_d is the sample delay from the current point of interest to the corresponding synthetic aperture element (which is within a 2-D planar arrangements) denoted by (m,n). The sample delay is thus expressed as

$$n_d(m, n, n_m, n_n, n_p) = \frac{2 \cdot f_s \cdot R_{m,n}(n_x, n_y, n_z)}{c} \tag{7.2}$$

where the range function R is a 3-D vector dot product between the location of the (n_x, n_y, n_z) point of interest and the location of the (m,n) synthetic aperture element.

In the simulation, two point-targets were introduced, and slices along the x-y plane at the location of the point targets are observed before and after incoherent SAS processing. The results from the simulation, shown in Fig. 7.2, verified the accuracy of the processing laid out in equations (7.1) and (7.2). Based upon this principle, a hardware trial was carried out in a laboratory water tank.

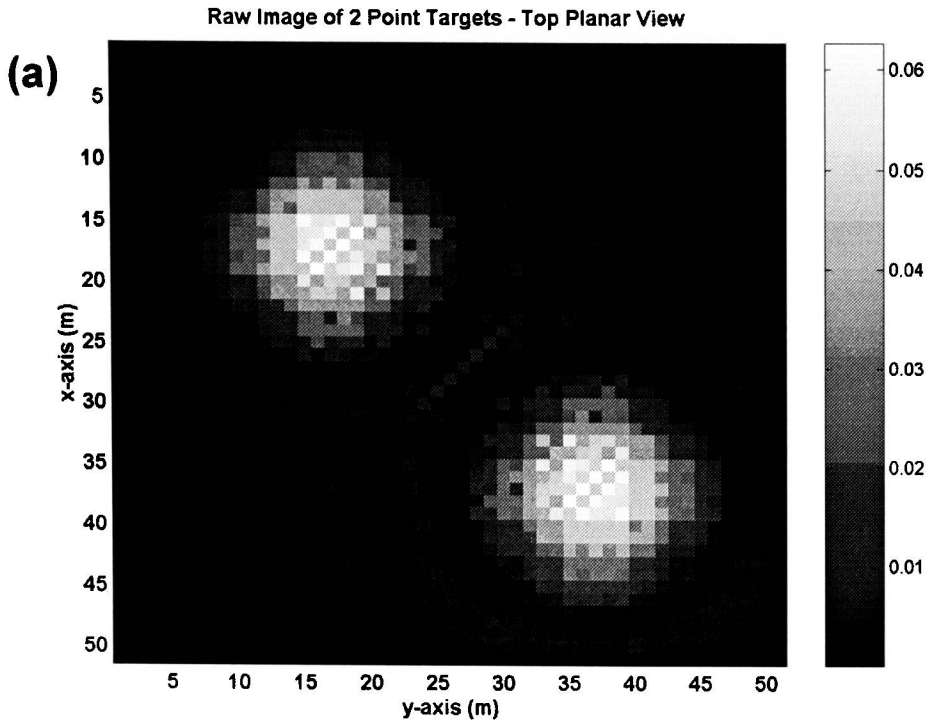


Figure 7.2: Slices of the *x-y* plane across the *z* axis at the location of the 2 point targets (a) from the raw image, and (b) from the processed image.

7.3.2 Laboratory Tank Trial

The trial, as illustrated in Fig. 7.3, is conducted in a water tank with the dimension of 1.5m width, 1.5m length and 1.5m depth. A tungsten carbide ball, 2cm in diameter, is hung by a very thin string 20cm below the water surface. Two identical transducers with resonant frequency of 500kHz were used, operating in transmit and receive modes respectively. The transducers were guided by a X-Y movement table.

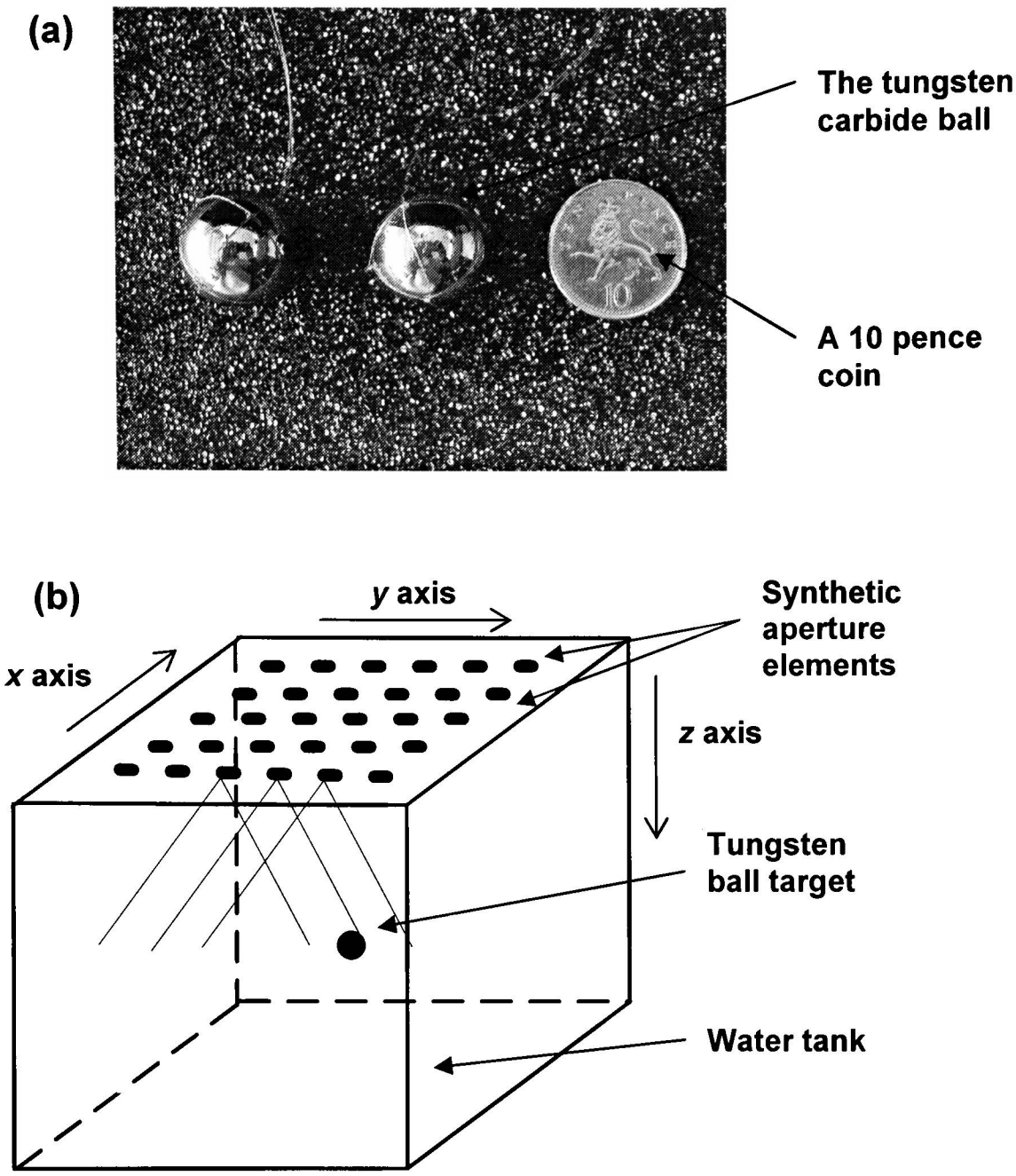


Figure 7.3: (a) Photo of the tungsten carbide ball used in this trial, and (b) an illustration of the water tank trial, with a ball target suspended in water, and the synthetic aperture elements facing the bottom of the tank.

A total of 75 readings were taken in each direction of the *x*-*y* plane, thus forming a 75x75 elements planar synthetic aperture. The transmitted signal was a chirp pulse with a bandwidth of 200kHz, centred on 500kHz and shaped by a Hanning window. The pulse duration was 0.1s. The inter-ping spacing was 0.5cm while the sampling rate was 2MHz on both the transmitting and receiving channels. The receive channel was synchronised with the transmit channel to avoid range ambiguity in the *z* axis. The transducers remained stationary during pulse transmission and reception.

The incoherent SAS processing was performed with a script written in C language, and took approximately 133 minutes on a 1.2 GHz CPU. Since the processed data was in a 3-D matrix, the results are represented as a -3dB layer plot of the data, which was normalised by the largest value of the focussed target. This means that at just below 0dB, the tungsten ball would appear as a tiny dot, and at -1dB it would grow into a larger 3-D circle, simply due to the fact that the summed energy is usually strongest at the centre of a focussed target and decreases outwards. The result is shown in Fig. 7.4.

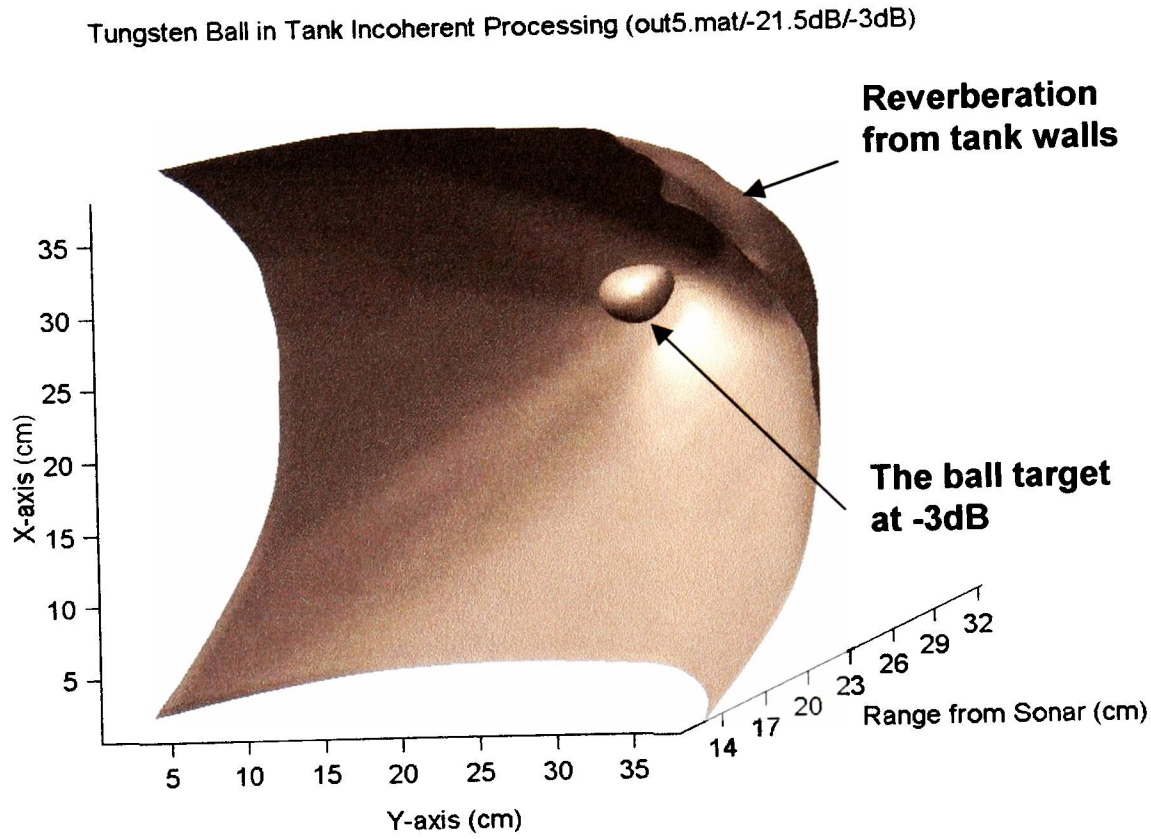


Figure 7.4: -3dB layer plot of the focussed tungsten carbide ball, seen as the rounded object at the centre, and the large layer at the back that comes from the reverberation off the tank walls.

Before discussing on the results, it is worth noting that the along-track resolution is now 2-D and is parallel to the *x*-*y* plane. Since the synthetic aperture elements are facing the bottom of the tank such that its look angle is normal to the *x*-*y* plane, the range resolution is the resolution in the *z* axis. Based upon the result, at -3dB, the 3-D object representing the tungsten carbide ball has a dimension of approximately 4 x 5 x

1 cm with respect to the $x-y-z$ axis. This is not far from the theoretical prediction of the achievable resolution in incoherent SAS processing. Based on equation (3.17) and the theoretical range resolution of 0.4cm, the along-track resolution is 6 cm. Note that this theoretical approximation is a conservative one. Hence, in terms of resolution, the processed image came out as good as the theoretical predictions.

As for the shape, an essential attribute in the cognitive properties of SAS images, comparisons cannot be made here. However, based on the fact that the point-target energy response of an incoherent SAS has a -3dB layer that is almost ellipsoidal, one can assume that objects with sharp corners, such as a cube, would have its corners rounded, and may appear circular if the cube itself is small compared to the along-track resolution. The disparity between along-track and cross-track range resolution in incoherent SAS processing, such that the along-track resolution is always lower than the cross-track range resolution, meant that there is likely to be distortions in the representation of the actual objects, especially objects with dimensions that are small relative to the along-track resolution yet large relative to the cross-track resolution.

Nevertheless, the result of this initial tank trial is a strong indication of the potential of incoherent SAS in underwater 3-D imaging. It is worth noting that, based upon the centre frequency of 500kHz, the synthetic aperture elements in this trial were 3 times "spatially under-sampled" as far as the inter-element spacing constraint of a coherent SAS is concerned. Synthesising a 2-D mono-static synthetic aperture for coherent SAS processing would be too technically demanding, at least for the foreseeable future. As a result such a survey would require an unacceptable level of time and costs, not to mention the compounded motion compensation problem. Hence, it is strongly anticipated that incoherent SAS processing is a more viable approach towards synthesising a 2-D aperture for 3-D imaging compared to coherent SAS processing schemes.

This trial was repeated with two identical ball targets, to show that the self-noise is sufficiently subdued and that no false targets are present in the processed image. The result is shown in Fig. 7.5. The trial was also conducted with the two ball targets

placed closely to each other (5cm separation), approaching its along-track resolution, and the two targets were seen to merge.

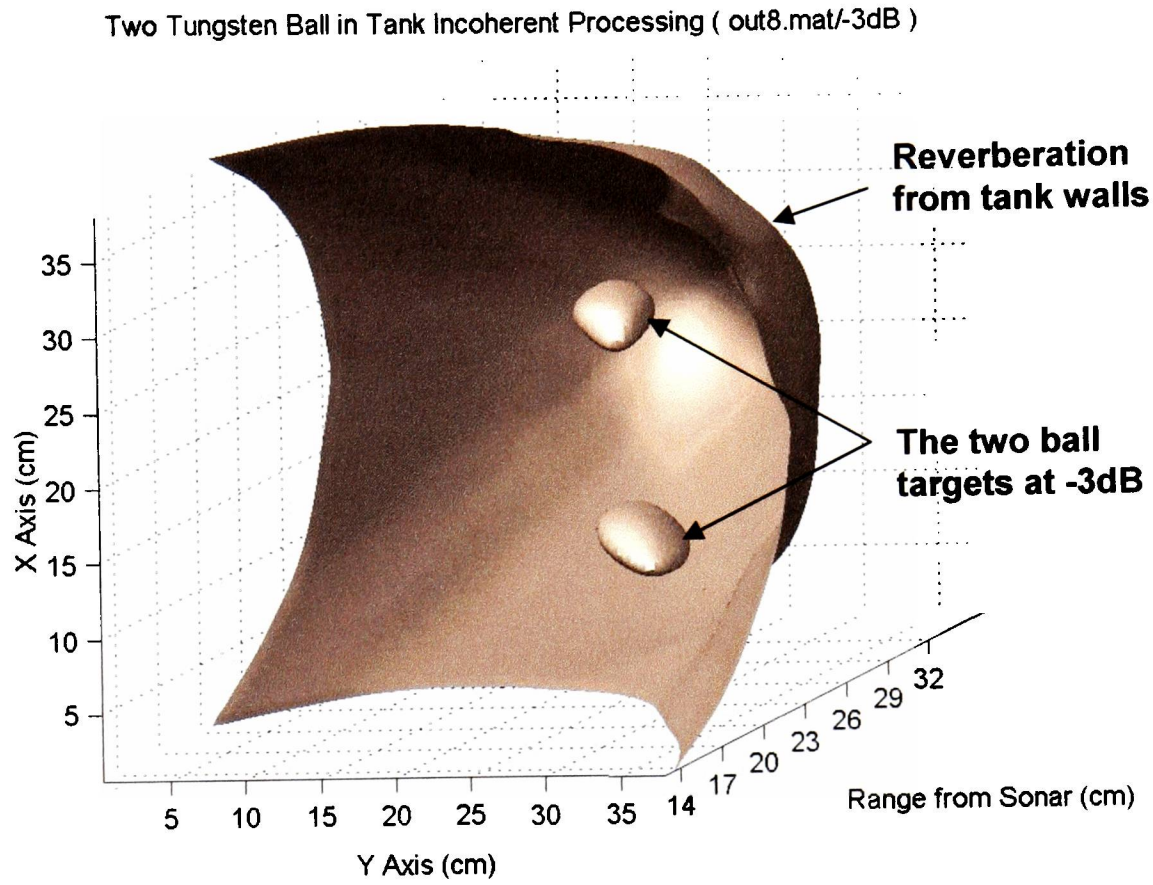


Figure 7.5: 3-D Layer plot at -3dB of the two tungsten carbide ball targets suspended in mid-water, with the reverberation from the tank walls in the background.

7.3.3 FREB Algorithm with 2-D Monostatic Synthetic Aperture

The FREB algorithm is tested here. By setting the initial spacing to be twice the original inter-element spacing, it managed to produce a reduction of computation time by around 70%. The result is shown in Fig. 7.6. It can be seen that the top tungsten ball has a wider dimension compared to the one in Fig. 7.5 due to the degradation in the signal to self-noise ratio. The lower tungsten ball is smaller in dimension because the -3dB layer plot was based upon, and normalised to, the upper tungsten ball, and the lower tungsten ball had a lower summed energy. This is due to the approximations made in the choice of elements that are inherent to the FREB scheme. Hence it should not be misinterpreted as an improvement in resolution. The tank reverberation is also

nearer to the two targets because of the lower processing gain as a result of summing a smaller number of elements.

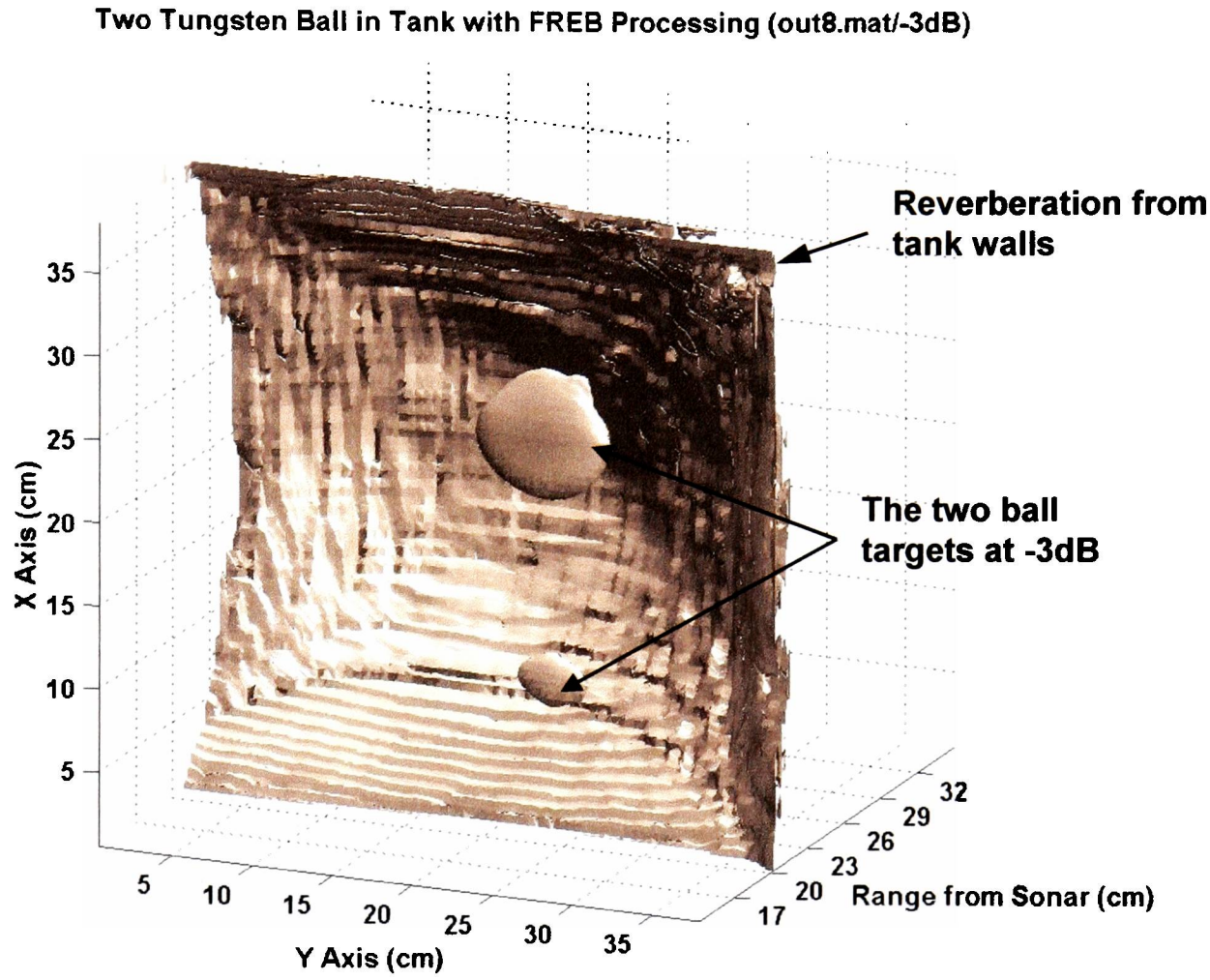


Figure 7.6: 3-D layer plot at -3dB of the two tungsten carbide ball targets suspended in mid-water, processed with the FREB algorithm, providing a 70% reduction in computation time.

7.4: 3-D Image representation

7.4.1 The Issue of Dynamic Detection

In section 7.3, the processed 3-D data was represented by drawing, in 3-D space, continuous layers that correspond to -3dB level in the data, which was normalised by the maximum value from the target of interest. However, such a method may not be directly implemented in practical underwater imaging applications, especially in the mapping of large scenes that contain targets with varying reflectivity. Normalising the entire 3-D data by a fixed maximum value actually forces the detection criteria to have only one reference for every point in the 3-D space. As a result, the detection criteria's sensitivity is fixed. In cases where there are a few very strong targets, the threshold of detection may be too high for the rest of the scene. This poses a major problem in the accurate representation of the 3-D data and in the correct reconstruction of the imaged scene, because weaker targets will easily be missed, encapsulated or masked. Hence, what was needed is a detection process that normalises the strength of a target based upon its local environment rather than the whole scene, enabling a different threshold to be set in different areas in the scene.

7.4.2 Moving Averaging-Window CFAR Detector

A promising approach is the application of a moving averaging-window constant false-alarm rate (CFAR) detector [64]. This concept was initially brought forth in radar so that adaptive thresholds can be applied during the detection of targets in the range domain [65]. The same principle can be applied in SAS images, whether 2-dimensional or 3-dimensional. The moving averaging window and the test window will need to be modified to take into account the number of dimensions the data has, such that a 2-dimensional and a 3-dimensional window is required for a 2-D and 3-D SAS image respectively.

The probability of false alarm, PFA, for a Gaussian distribution is expressed as [66]:

$$PFA = 0.5\left[1 - erf\left(\frac{r - 2BT{\sigma_{nse}}^2}{\sqrt{8BT{\sigma_{nse}}^4}}\right)\right] \tag{7.3}$$

where r is the threshold, B the bandwidth, T the sampling time interval, ${\sigma_{nse}}^2$ is the average noise power and *erf(x)* is the error function of x defined as:

$$erf(x) = \left(\frac{2}{\sqrt{\pi}}\right)\int_0^x \exp\left(-t^2\right)dt \tag{7.4}$$

By setting *PFA* constant and solving for x in *erf(x)*, the threshold value r can be expressed as

$$r = x\sqrt{4 \cdot (2BT) \cdot {\sigma_{nse}}^4} + 2BT \cdot {\sigma_{nse}}^2 \tag{7.5}$$

Being a function of ${\sigma_{nse}}^2$, which is estimated by the moving averaging window, the threshold r is adaptively varied to maintain a constant false-alarm rate. The value or average of values in the test window is compared against this threshold to decide whether meaningful targets are present within the test window. The application of such a scheme is illustrated in Fig. 7.7, in which a 2-D window is shown.

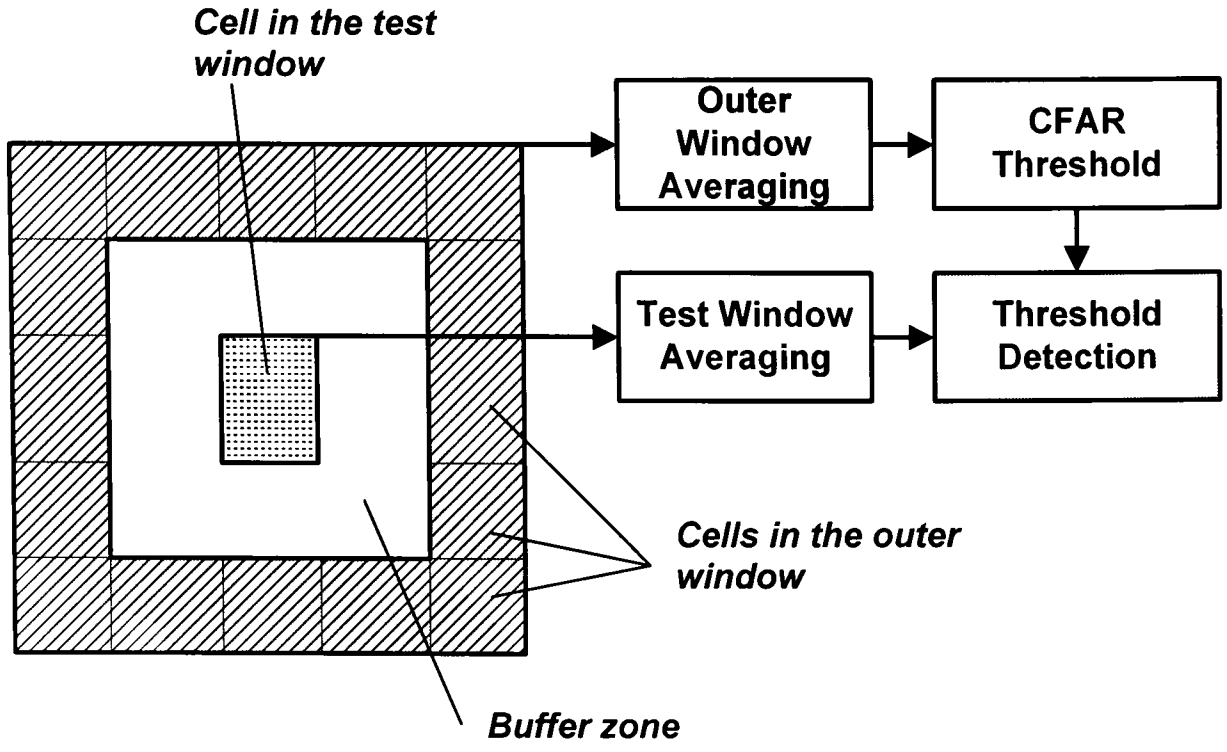


Figure 7.7: A 2-D moving averaging-window CFAR detector with split windows.

If there is more than one value in the test-window, they are first averaged, and then tested against the threshold value which is produced based on the average value obtained from the cells in the outer window. The purpose of a buffer zone between the test window and the outer window is to avoid the overflowing of energy from the test-window into the outer window. This is also a good precaution when the optimal shape of the test window is not known.

It is obvious that such a scheme has plenty of room for customisation. When the window is 2-D or 3-D, the performance of the detection can be affected by the dimensions and shape of the test window, buffer zone and the outer window. The optimal dimensions and shape are predictably a function of the point-target energy response, the spatial density of targets with strong relative contrasts, and the dynamic range of the energy within which all the possible targets of interest lie. Weighting coefficients can be applied in either or both the averaging processes, then these coefficients can be modified adaptively by the higher ordered statistics of the values in the respective windows. This area has been well expounded in the published literatures, in particular [67-70], and interested readers are referred to them.

7.4.3 Normalisation of Incoherent SAS Images

For purposes of application in incoherent SAS images, simulation results (an example of which is shown in Fig. 7.8) show that uniformly weighted rectangular windows (whether in 2-D or in 3-D) are sufficient in most cases, as long as the dimension and shape of the test-window is matched to, or should not exceed twice the dimension of, the theoretical resolution cell. If the test window is larger than twice the dimension of the theoretical resolution cell, it will result in unnecessary degradation in resolution. A theoretical resolution cell is the cell with dimensions defined by the theoretical resolution of the imaging system in the respective dimensions. The buffer zone must at least have the width, in all directions, of the test-window. The size of the outer-window can be estimated based upon the spread of the self-noise in the point-target energy response.

Such a detection scheme leads to a loss of resolution in the detected image, especially when the test-window is large compared to the theoretical resolution cell. It is an inevitable price to pay to ensure that weaker targets are not missed and can be represented as meaningfully as possible.

Soft-detection, which records the amount by which the threshold level was exceeded, is usually a better method compared to a hard yes-no detection because it preserves the variation of reflectivity among the targets. Hard yes-no detection here means that if the average in the test window is above the threshold, then a 1 is given and a 0 otherwise. Hence, a black-white image is seen in Fig. 7.8 for hard-detection. As for soft detection, if the average in the test window exceed the threshold by $10V^2$ then a 10 is recorded and 0 otherwise. For the next pixel if the average exceeds by $15V^2$ then a 15 is recorded and 0 otherwise, and so on.

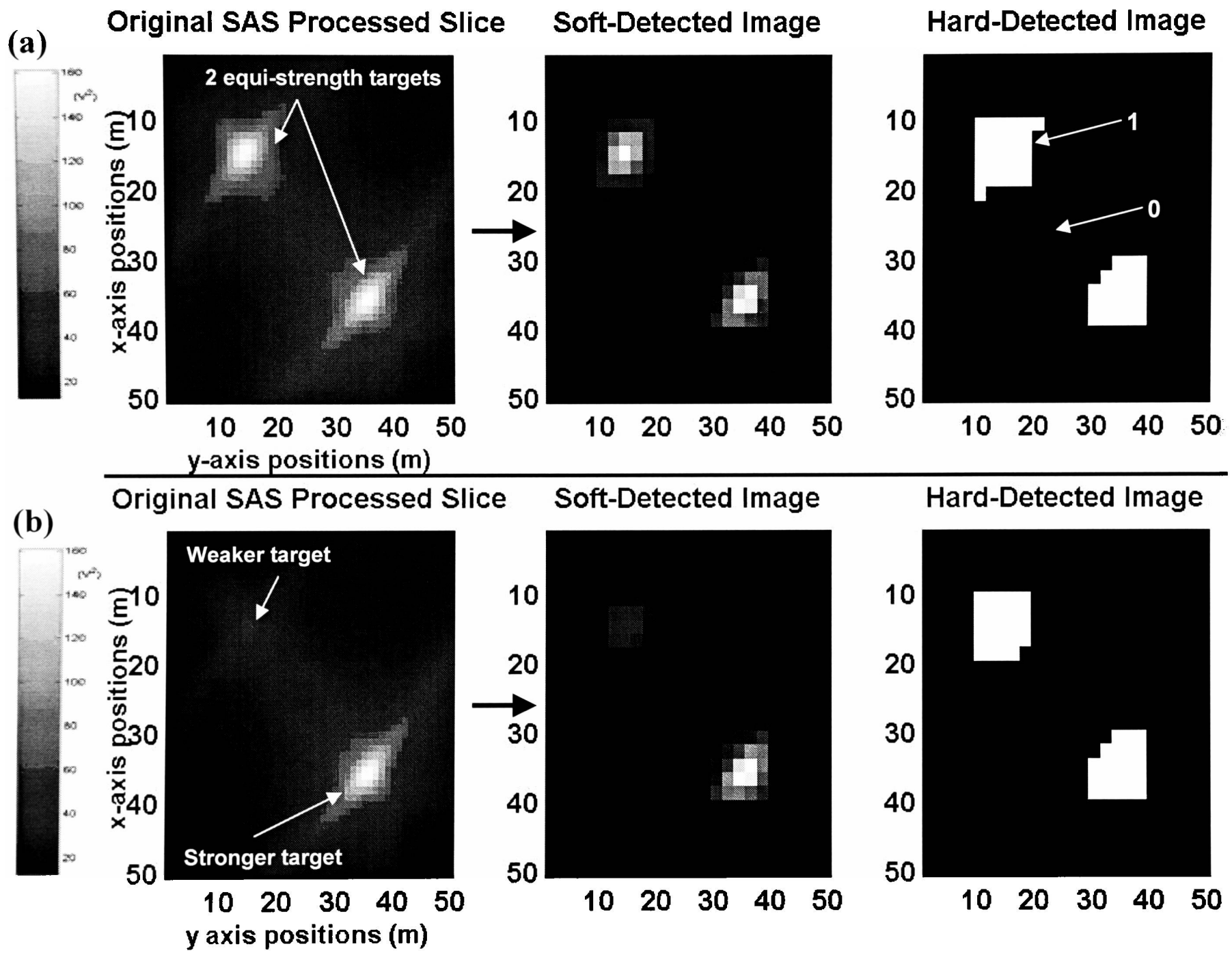


Figure 7.8: Results of normalising by using a 2-D moving averaging-window CFAR detector on slices of the *x-y* plane across two targets that are (a) equal in strength and (b) one target only half as strong as the other target. Soft detection records the level that the threshold was exceeded, while hard detection only makes a yes-no decision.

In some circumstances, the averaging-windows need to be modified to produce images that meet the requirement or the purpose of the imaging application. In seabed topography for example, a common application of underwater imaging, the processed 3-D data obtained need not be detected by a 3-D averaging-window. Instead, a one dimensional averaging-window can be implemented in the z axis to detect the position of the seabed in terms of its depth from the sea surface. The 3-D data can then be represented as a 2-D map that presents the height of the seabed corresponding to each point on the map. Such a map is superior to that produced by a linear synthetic aperture because the number of shadow or blind spots is greatly reduced, revealing features that would otherwise be hidden.

The implementation of this moving window-averaging CFAR detector scheme as described here is straightforward in terms of the design of the averaging-window and the calculation of threshold. It requires relatively shorter processing time when compared to other more complex approaches.

7.5 Multi-static 2-D Synthetic Aperture

7.5.1 A Practical Concept

The tank trial presented in section 7.3 had established the viability of synthesising a 2-D aperture for 3-D imaging with the implementation of incoherent SAS processing. However, for most realistic purposes, synthesising a 2-D aperture is likely to be prohibitive in terms of the required cost and time. Synthesising a fully monostatic 2-D aperture with a small number of physical transducers will take a long time to cover a large area. On the other hand, using a large array of physical transducers to cover a large area quickly is too costly considering the large number of transducers required. Hence, a reasonable compromise would be the use of a few transducers with a larger number of hydrophones, since hydrophone elements are relatively much cheaper than broadband high-frequency transducers. Such a configuration, where the ratio of transmitters to receivers is high, is already common in linear synthetic aperture systems (section 6.5).

A novel and practical 2-D synthetic aperture with a multi-static configuration is presented in this section. It is based upon two transducers operating with a linear array of hydrophones. One transducer is located at each end of the linear array, and the array is traversed in the direction that is perpendicular to itself. The orientation of the transducers (and their beams) is slanted such that there is a grazing angle with respect to the seabed. All the hydrophones face the seabed such that their broadsides are perpendicular to the seabed's plane. This is illustrated in Fig. 7.9.

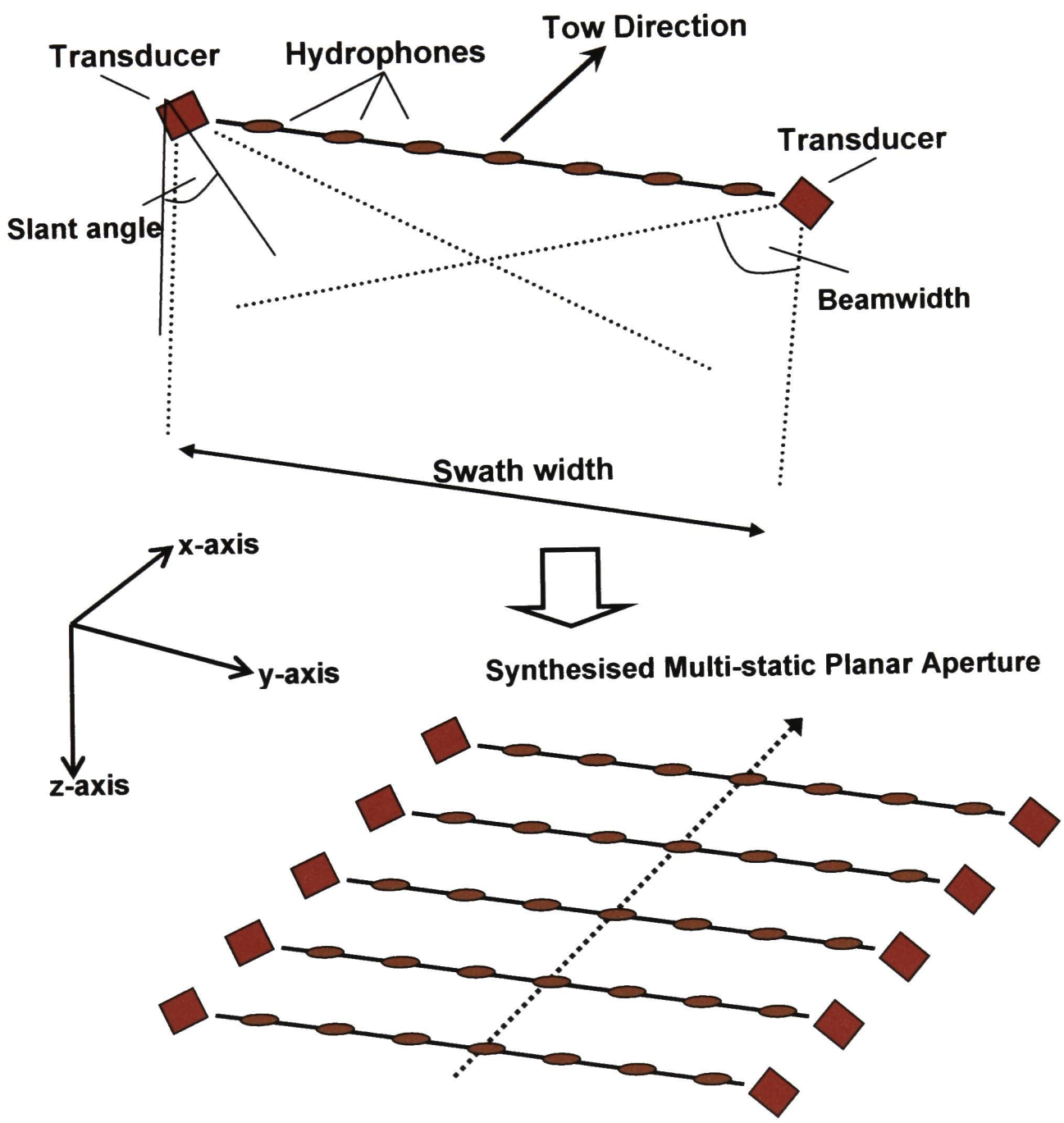


Figure 7.9: A practical multi-static planar synthetic aperture.

Given that both the transducers (on the left and on the right of the array) have a beamwidth of at least 1.05rad (60°), and if the minimum seabed depth is 10m, the array can span a length of 17m. However to keep the bi-static angle smaller, and to minimise instability in towing, the length should be kept to about 15m. The number of hydrophones in between the transducers can be set to 14 with 1m spacing. More hydrophones can be used should it be needed in SNR considerations. The slant angle (refer to Fig. 7.9) of the transducers are set to be half its beamwidth, hence 0.53rad and -0.53rad respectively in this case.

The two transducers should transmit pulses simultaneously to maximise mapping rate. However, it is better for the chirp pulses from each transducer to have different frequency bands so that two distinct raw maps can be used in the processing. If the same pulse is transmitted from both the transducers, then the hydrophones in the centre of the array will receive a bias of higher energy.

Before presenting the tank trial results for this concept, the issues of point-target energy response and multistatic weightings for a multi-static planar synthetic aperture are first discussed.

7.5.2 Point-target Energy Response of a Multi-static Planar Synthetic Aperture

By the reference to point target energy response, the concern here is mainly on the pattern of self-noise distribution around the point-target. As justified in chapter 3 and 4, the fidelity of an incoherent SAS image is largely dependent, and influenced by, the distribution of self-noise in the point-target energy response. The point-target energy response of a synthetic aperture is directly related to the spatial arrangement of its constituent elements. In cases where the configuration of the elements is multi-static, this is even more the case, because the point-target energy response can differ greatly from the one with a monostatic configuration given the same shape and dimension of the synthetic aperture.

In this proposed arrangement, a transducer is placed on each end of the array as this is the best arrangement possible in producing an acceptable point-target energy response with only two transducers. The self-noise of the point-target energy response is distributed more evenly because the transducers are symmetrical in the axis parallel to the array. On top of that, by having a transducer on each side, shadowed areas, which are present due to the respective grazing angles of the transducers (0.53rad or 30^{o}) with respect to the seabed, can be mutually insonified.

A key issue affecting the self-noise distribution, in incoherent SAS processing, is the presence of any non-symmetry in the geometry of the transducers or hydrophones in the synthetic aperture, especially in a multi-static case. The axis in which the elements are not symmetrical will suffer irregularities in its self-noise distribution, and it is likely to affect the imaging performance in that axis. In this case, if a transducer is present on only one end of the linear array, then non-symmetry occurs in the axis that is parallel to the linear array. Let it be the y axis (x-y axes are both parallel to the planar synthetic aperture), and analysis of the point-target energy response is undertaken in the domain of y axis versus the cross-track range axis (z axis). This analysis is performed with the same technique applied in section 3.12, which is based upon the plot of range loci crossings over a point-target, but modified to accommodate a multi-static configuration. In Fig. 7.10, the point-target energy response of the synthetic apertures are shown, one with a transducer on only one end of the array, and the other with a transducer on both ends of the array. In the same figure, the imaging responses of a straight line (represented by grouped point-targets), which can be a flat bottom in a real environment, are shown. They illustrate the adverse effect of an uneven point-target energy response towards the imaging of objects.

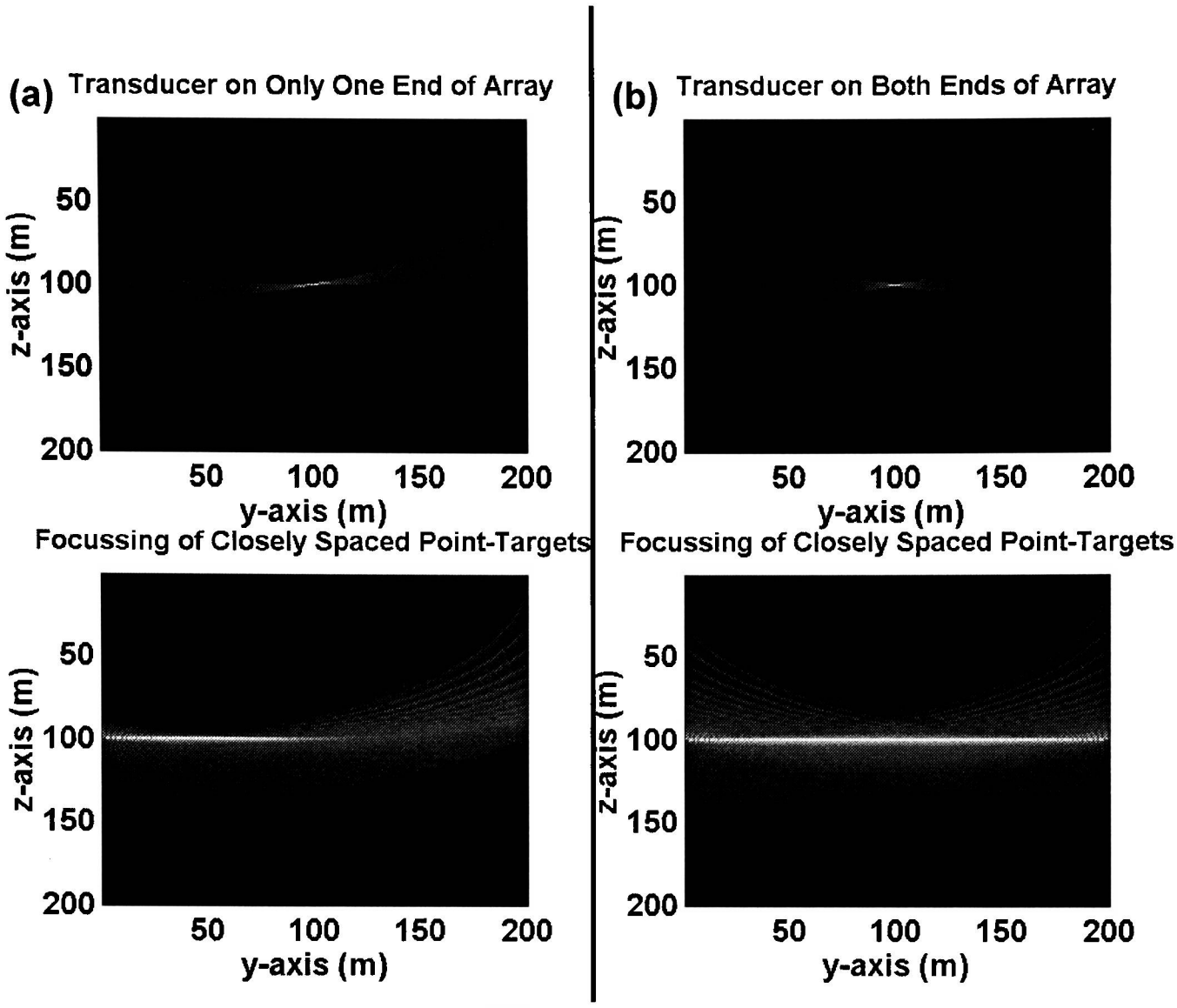


Figure 7.10: The point-target energy response of the synthetic aperture synthesised with (a) a transducer on only the left end of the linear array and (b) a transducer on each end of the linear array. The plot is in the domain of z axis, which is the equivalent of cross-track range or depth, versus the y axis, which is parallel to the linear array. Their corresponding performances in imaging a line of point-targets are also shown.

By inspection, it can be seen in Fig. 7.10(a) that the image of the linearly arranged point-targets suffers from distortion towards the right side. The point-targets in that region were masked by strong, overlapped self-noise. As a result, subsequent detection process will fail to detect any targets in that region. On the other hand, in Fig. 7.10(b), where there is a transducer on both ends of the array, the self-noise of the point-target energy response has a more spatially balanced distribution, hence producing a better image of the linearly arranged point-targets.

7.5.3 Applying Multi-Static Weightings

In section 3.11, the case for matching the weighting function to the directional response of the synthetic aperture elements individually had been made for a monostatic case. In cases where the directional response of the elements is available, and is non-uniform over the region of the beam used in aperture synthesis, applying a weighting coefficient that is matched to the normalised directional response in the process of incoherent summation will improve the signal to self-noise ratio. The same principle applies in a bi-static case, and a multi-static case can be treated as the multiple of a bi-static case.

The weighting function applied in the process of incoherent SAS processing in equation (3.20) shall be modified to

$$w(n) = w_T(\vec{s}_T(n), \vec{p}) \cdot w_R(\vec{s}_R(n), \vec{p}) \tag{7.6}$$

in order to take account of the difference in directional response between the transducer (transmitting element) and hydrophones (receiving elements). w_T and w_R are the weighting functions corresponding to the transducer and hydrophones respectively. Vectors are employed to represent locations in the 3-D space conveniently. $\vec{s}_T(n)$ and $\vec{s}_R(n)$ are the directional vectors of the transducer and hydrophone locations respectively that correspond to the n^{th} summation index, while $\vec{p}$ is the directional vector of the pixel being focussed. These directional vectors are based on a common origin.

An example scenario is shown in Fig. 7.11 with an n^{th} transmit element and a pixel being focussed. The weighting coefficient is determined from the weighting function by the value of θ_T, which is the angle between, and evaluated by the dot product of, the vectors $(\vec{p} - \vec{s}_T(n))$ and $\vec{r}_T(n)$. The vector $\vec{r}_T(n)$ is the orientation vector for the n^{th} transmit element, and is perpendicular to the acoustic resonating surface of the element concerned.

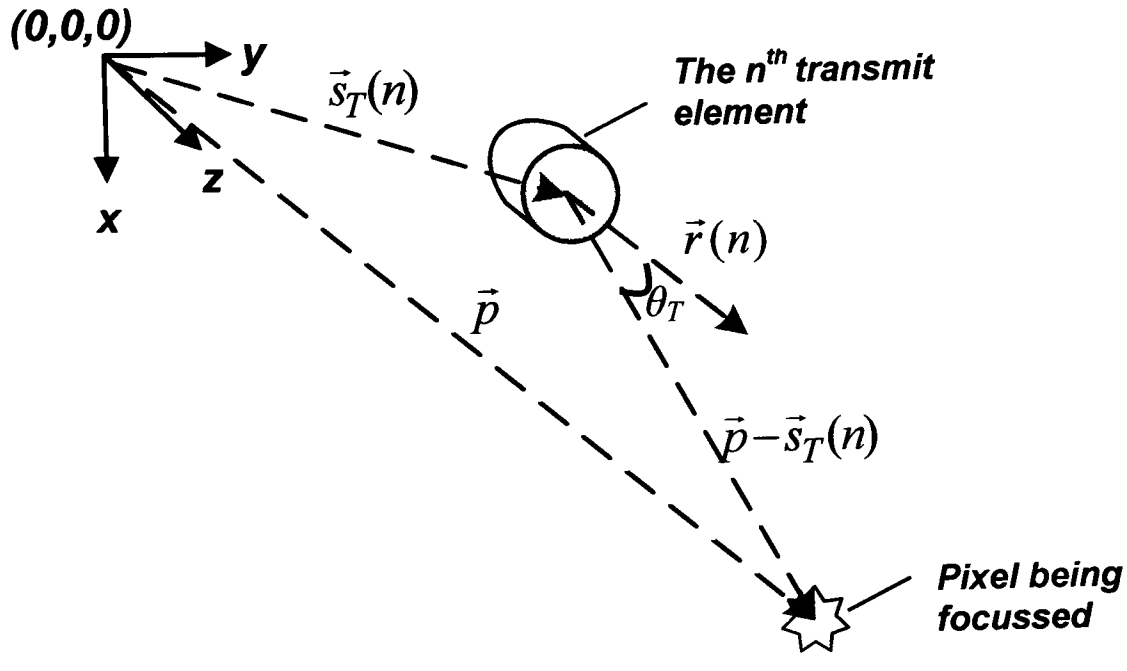


Figure 7.11: Using directional vectors to determine the observation angle, from the n^{th} transmit element, of the pixel being focussed in 3-D space.

Utilising such a scheme allows the use of individual weighting functions on each element during the process of summation, while being able to accommodate synthetic apertures that are beyond the linear shape, as well as a multi-static arrangement of elements.

More importantly, it is an invaluable design tool for an incoherent SAS system, when incorporated into the range-loci plotting as detailed in section 3.12, to predict the influence on the point-target energy response by the choice of hydrophones or transducers with various directional responses. Furthermore, such a weighting scheme can effectively match or compensate, depending on necessity, irregularities experienced by the pulses during the course of propagation in the medium, as long as these can be modelled by spatial or angular functions with respect to the elements.

The additional computation time incurred, mainly by the derivation of the observation angles, will be significant. However, it is envisaged that in a practical system utilising the concept laid out in section 7.5.1, there would be many hydrophones that are likely to be fairly omni-directional, and two or four medium-frequency transducers that are directional. In the attempt to maximise the coverage of the transducers, the aperture

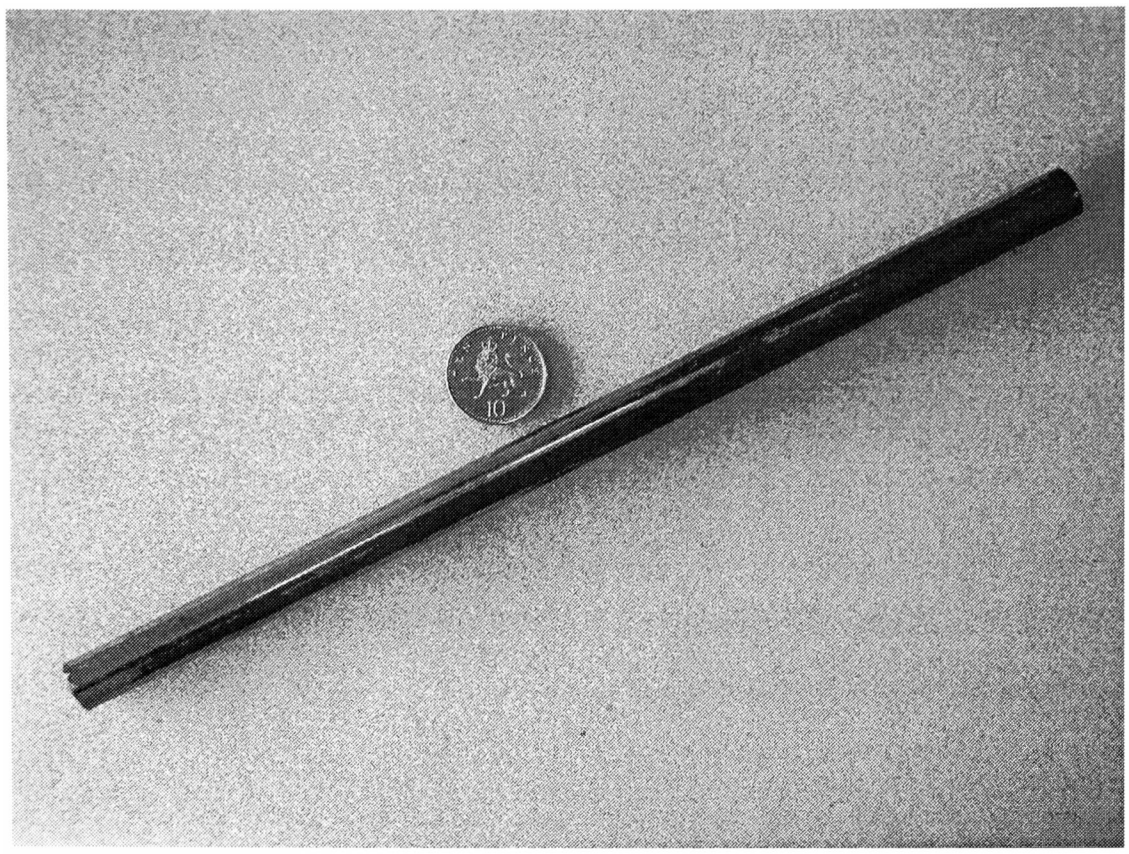
synthesis for a pixel may involve transducer elements that are beyond their angular range of uniform directional response. Hence, the application of matched weightings is only needed for the transducer elements, reducing by half the number of calculations that would be needed should there be matched weighting for the hydrophone elements as well. A further reduction in the additional computation time can be achieved by using the same template of angles, derived for all the pixels at a particular range, over a span of ranges.

7.5.4 Laboratory Tank Trial

This section details the tank trial of a multi-static 2-D synthetic aperture based upon the proposed concept. The purpose of this trial is to test the practicality of the proposed multi-static synthetic aperture in incoherent SAS processing and to gain a crude insight of its ability to resolve objects in 3-D. A secondary objective was to demonstrate the improvement in image quality with the use of element-dependent matched weighting functions.

The tank and the data acquisition system used in this trial were the same as those used in the first tank trial on the planar mono-static synthetic aperture. The target in this trial is a hollow metal rod that is 20cm long and 1cm thick, as shown in Fig. 7.12(a). This allows for a visual evaluation on the ability of this system in resolving the shape of an object in 3-D space. The rod is suspended in mid-water by a very thin nylon string that yields negligible acoustic reflectivity. This is shown in Fig. 7.12(b), where the reflection of the X-Y table set-up overhead the tank can be seen.

(a)



(b)

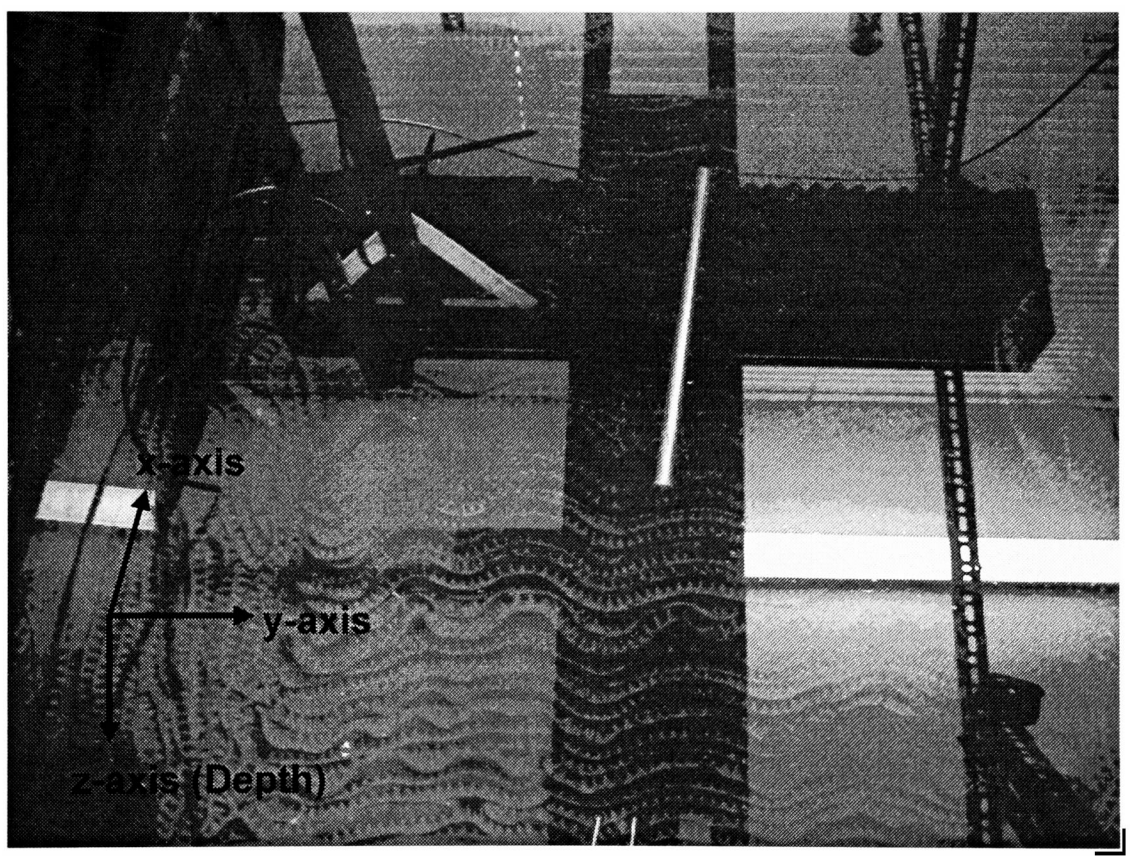
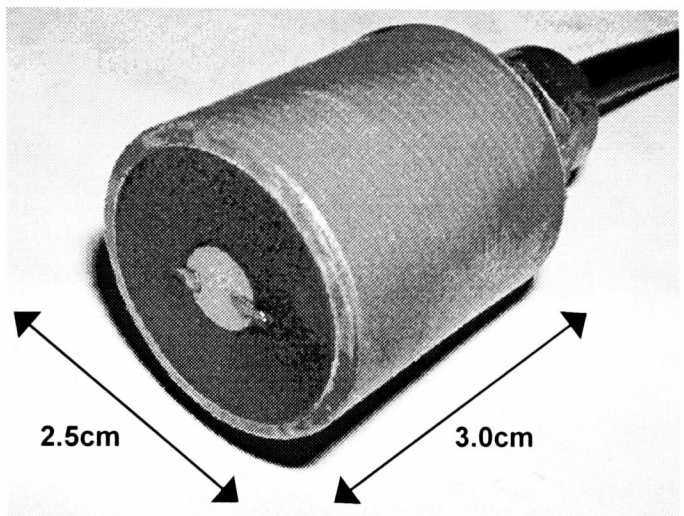


Figure 7.12: (a) The metal rod used as a target in this tank trial, and (b) the rod suspended in mid-water in the tank, with the reflection of the X-Y table set up overhead the tank.

Two piezo-ceramic transducers were built in the laboratory to replace the transducers used in the first tank trial. This is due to the fact that the original transducers have rectangular ceramics and hence their beamwidth and directional response in the x axis is not the same as in the y axis. The newly built transducers use circular ceramics and have a resonant frequency of 250kHz. Fig. 7.13 shows the new transducer and its estimated two-way directional response. The directional response is fairly similar in both the x and y axes.



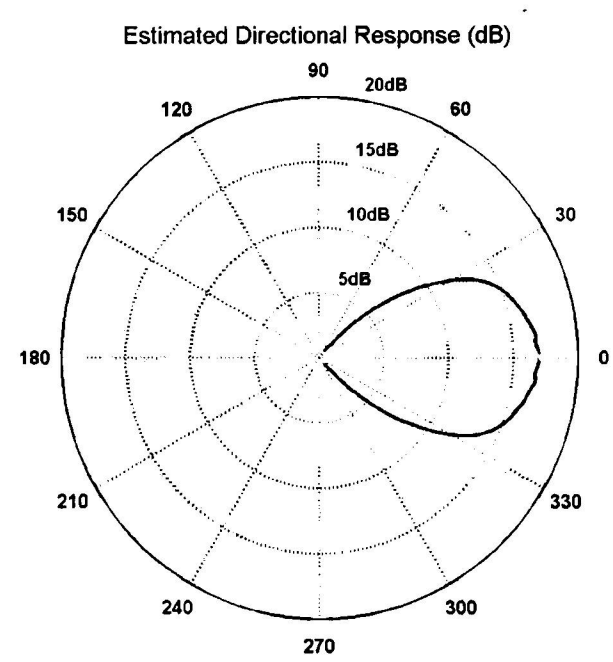


Figure 7.13: The transducer ($Q \cong 3.1$) built for this tank trial and its two-way directional response estimated in dB. The beam response is circularly symmetrical.

One of the transducers operates in transmitting mode and the other in receiving mode, hence the receiver here is not omni-directional. The trial was carried out in two stages; the first stage was positioning the transmitting transducer on the left of the tank and moving the receiving transducer in the y axis after each ping, and then both transducers are moved forward in the x axis before the receiving transducer is moved in the y axis again. The second stage was to repeat the whole process with the transmitting transducer on the right of the tank. This produces two sets of raw data, one from the left transducer and the other from the right transducer. In an actual system, two transmitting transducers are needed to avoid having to repeat the survey, which also

means that pulses need to be frequency coded to avoid interference so that two distinct sets of raw data can be obtained.

A total of 84 readings were taken in each direction of the *x-y* plane, thus forming an 84x84 element planar synthetic aperture of receiving elements, with the transmitting elements on either side of the plane arranged linearly along the *x* axis. The transmitted pulse was a chirp pulse with a bandwidth of 100 kHz centred on 250 kHz and shaded by a Hanning window. The pulse duration was 0.1s. The inter-ping spacing was 0.5cm while the sampling rate was 1MHz on both the transmitting and receiving channels. Both the channels were synchronised and the transducers remained stationary during pulse transmission and reception.

The incoherent SAS processing was performed on the 2 raw data sets separately, corresponding to the left and the right transducer respectively. The two sets of processed data were then summed together to produce the final result. The individual sets of data may need to be normalised if their respective gains are significantly different. This could simply be done by choosing a block of data where there is a strong presence of targets, and by comparing their mean values, a normalising factor can be calculated. Such comparison and subsequent normalisation must be made after time-varying gains have been appropriately applied.

Fig. 7.14 shows the image of the rod from the processing of data from the left transducer only, with no matched weighting, illustrating the effect of the spatially unbalanced point-target energy response on the final image. The image of the rod is distorted upwards of the tank (Fig. 7.14(b)) and this is in-line with the analysis shown in Fig. 7.10. The results of processing and summing both sets of data, without the application of matched weighting are shown in Fig. 7.15, whereas Fig. 7.16 shows the results from the same set of data processed with the application of matched weighting to the individual elements.

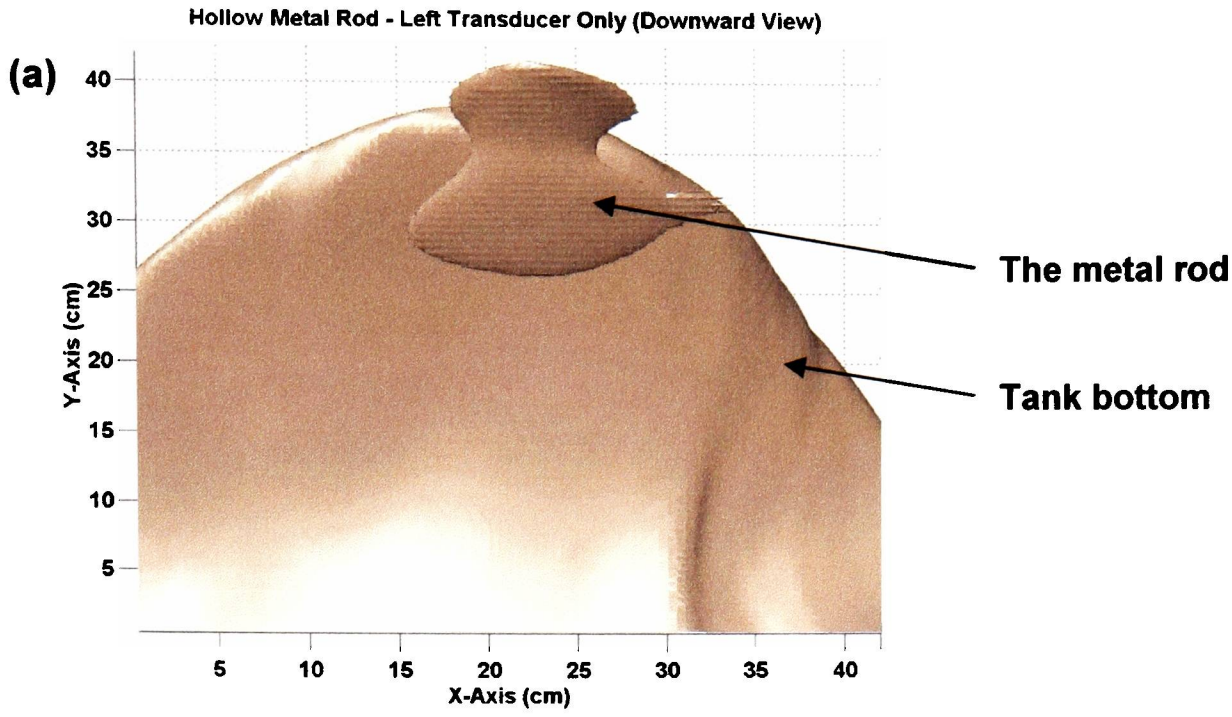


Figure 7.14: 3-D plots (at 3-dB level) of the rod in mid-water, processed with the raw data from the left transducer only. (a) The downward view to the tank, (b) the sideway view and (c) a slanting view.

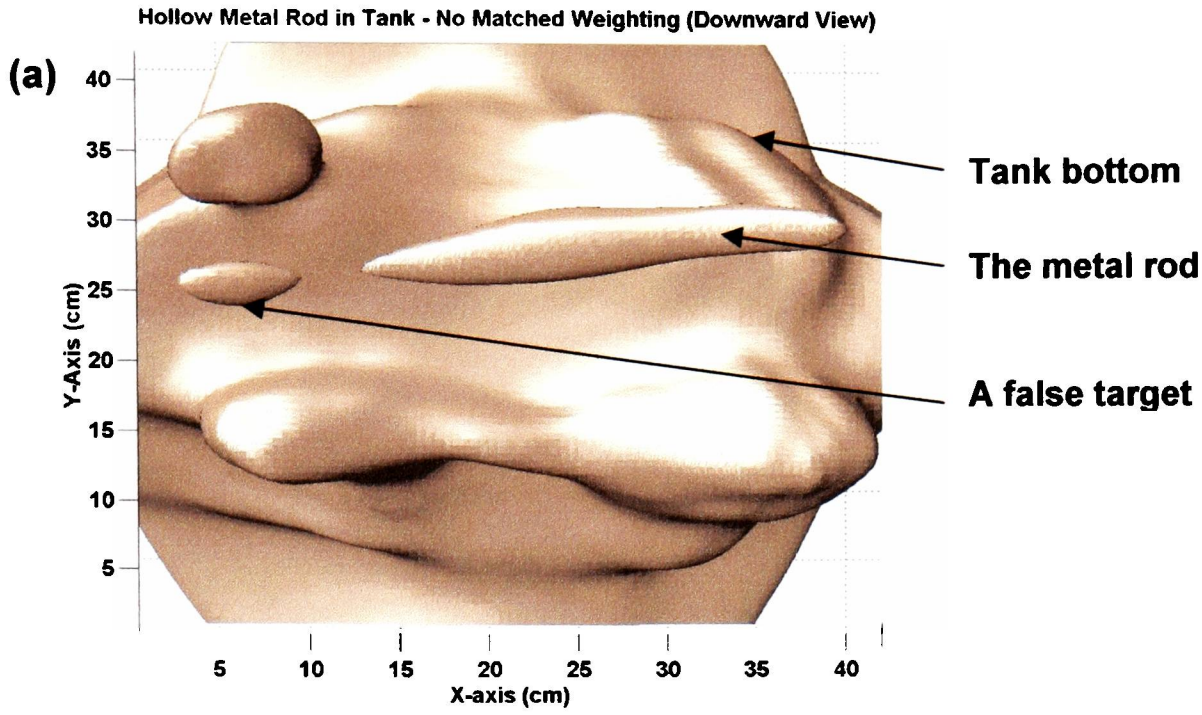


Figure 7.15: 3-D plots (at 3-dB level) of the rod in mid-water, processed with no matched weighting. (a) The downward view to the tank, (b) the sideway view and (c) a slanting view.

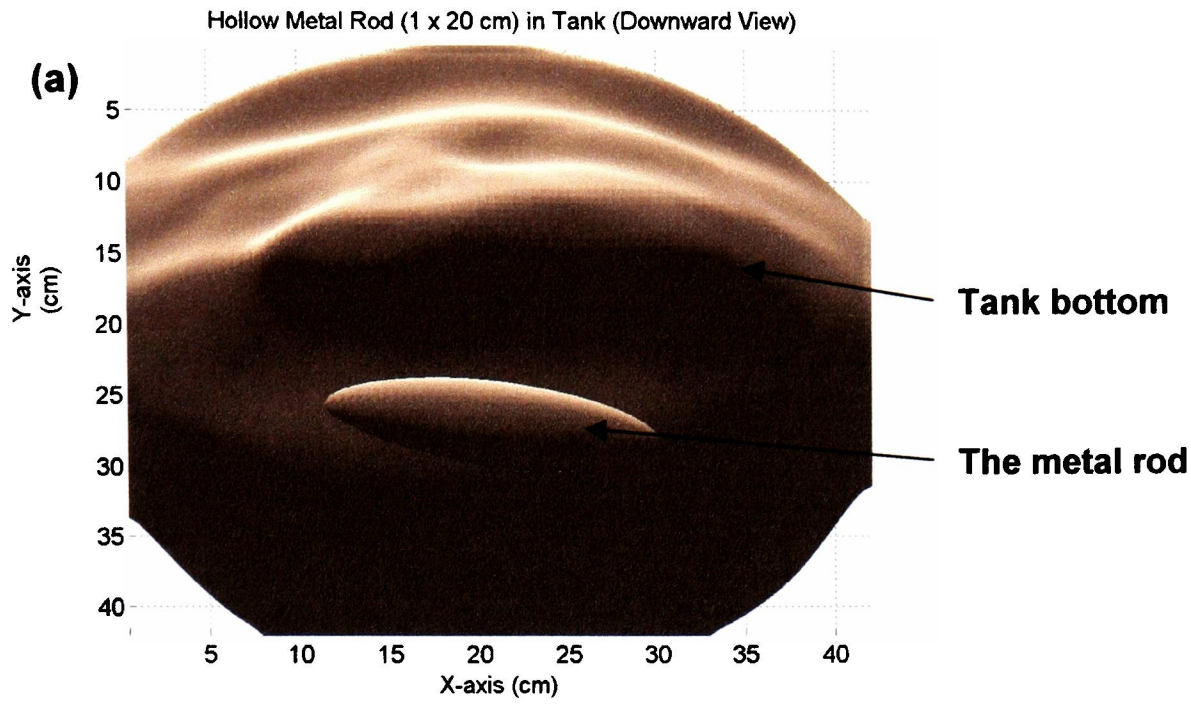


Figure 7.16: 3-D plots (at 3-dB level) of the rod in mid-water, processed with the application of element-dependent weighting. (a) The downward view to the tank, (b) the sideway view and (c) a slanting view.

7.5.5 Analysis of Results

From Fig. 7.14, it can be seen that the unbalanced point-target energy response of the synthetic aperture with only one transducer on the left of the hydrophone elements had caused the image of the rod and even the tank bottom reverberation to appear bending upwards towards the surface of the water. This is clearly seen in the sideway view of the 3-D image.

In Fig. 7.15, where both the data from the left and right transducers are summed, but without the application of matched weighting, it can be seen that the shape and location of the target and the tank reverberation are more spatially aligned with the actual objects. However, one false target has appeared. This is mainly due to the self-noise coming in from angles that are not appropriately shaded by the element-dependent matched weighting, plus contribution from the tank wall reverberations. The total processing time required was approximately 620 minutes with a 1.2GHz CPU. This is due to the fact that the arrangement of the synthetic aperture is multi-static and hence the range to transmitter and the range to receiver need to be calculated separately. Also, the set of data from the left and right transducers are individually processed.

In Fig. 7.16, element-dependent matched weighting is applied. The false target is no longer present, and the shape of the rod is clearly more symmetrical. The image of the tank bottom is relatively smoother and flatter, which more accurately represents its actual form. The orientation of the rod in mid-water, having a small angle to the x axis, is also clearly represented in the image. The image is not as thin as the actual rod because the systems along-track resolution (in the x-y plane) is not as fine as the rod's width, hence being under the influence of the point-target energy response the image becomes slightly rounded along the length of the rod. The total processing time required was approximately 4320 minutes with a 1.2 GHz CPU. The need to calculate the observation angle, with respect to the pixel of interest, of each element involved in summation caused this significant increase in processing time.

Notice that the results in Fig. 7.15 and 7.16 did not suffer a strong presence of the reverberation from the tank walls on all four sides compared to the results in the

monostatic trial. This is mainly due to the orientation of the transmitting transducer being slanted at an angle as shown in the concept diagram in Fig. 7.9, thus confining the survey swath within the edges of the tank bottom.

7.6 Conclusion

There are a number of benefits in synthesising apertures that are beyond one dimension. Synthesising 2-D apertures with incoherent SAS processing enables the production of 3-D images, the reduction of shadow zones and the possibility to post-process the data in a particular dimension of interest.

The viability of synthesising apertures beyond the traditional linear form with incoherent SAS processing has been successfully demonstrated, along with its application in the imaging and representation of objects in 3-D. The results from trials performed with a monostatic, planar synthetic aperture with sparsely arranged elements gave positive indications of its potential. To tackle the need for a variable threshold detection scheme, the moving averaging-window CFAR detection technique was presented.

A novel, practical and cost-effective imaging approach has been proposed based upon the characteristics and techniques available to incoherent SAS processing. This is underpinned by the deployment of a linear physical array of sparsely spaced hydrophones with one transducer on each end, and towed in a traverse direction to synthesise a multi-static planar aperture. The application of element-dependent matched weighting functions was extended to accommodate this approach. Tank trial of this approach gave results that match its point-target energy response predicted in simulation. The results also show a clear improvement in the suppression of self-noise by the application of element-dependent matched weighting.

In a multi-static case, computation time required for the processing of data from 2-D apertures is significantly longer, making it necessary for most of the processing to be carried out offline.

Chapter 8

Conclusions and Further Work

8.1 Key Conclusions

This work has been fundamentally divided into three parts. The first part is the study into the nature and characteristics of incoherent SAS processing. Time domain techniques are more suited for incoherent SAS processing because exact reconstruction algorithm can be applied and approximations can be kept to a minimal level. The exact reconstruction algorithm, where the exact two-way range from each synthetic aperture element to the pixel under reconstruction is calculated, is described. The model for image reconstruction in the time-domain is presented and its processing gain and required computation time is estimated.

The distinctive characteristics of incoherent SAS imaging had been studied in greater detail and its impact on the design requirement of such a system has been discussed. The key areas are the absence of grating lobes independently of the elements' spacing and arrangement; strong resilience to motion errors; reduced processing complexity; greater system design flexibility; and better robustness during practical application.

Two crucial concepts that bear unique relevance to incoherent SAS processing are presented. The first is the concept of point-target energy response of an incoherent synthetic aperture, the equivalent of a point spread function in coherent imaging. This can be obtained by plotting the loci of range-ambiguity, for each element on the synthetic aperture, such that it crosses the location of the point of interest. The width of these loci will depend on the cross-track range resolution. The intensity at any point on the loci represents the directional response of the element at the corresponding angle to the point. The plot effectively produces a spatial representation of the energy distribution as back-projected to the synthetic aperture given a point target source. The second concept is the signal to self-noise ratio. Due to the fact that incoherent SAS relies only on the intensity of the pulse returns to resolve targets, there is always a strong presence of background energy around a point of

focussed energy. The ratio of the focussed energy to the average background energy is referred to as the signal to self-noise ratio. Both these concepts played an important role in the development of techniques in this work, and served as a reliable evaluation tool of the nature and performance of a synthetic aperture with arbitrary form and arrangement.

Key parameters of this technique were derived: along-track resolution and its dependent factors, processing gain and optimal element-dependent matched weighting function. The along-track resolution is linearly dependent upon the cross-track range resolution, hence making wideband pulses a desirable feature. The processing gain in incoherent processing is half the number of decibels compared with the case for coherent processing. This also means that the reduction in processing gain is less in incoherent processing given the same reduction of the number of elements involved in the summation. It was also argued that the optimal weighting function for the element is one which matches the element's directional response. Applying such a function to each element individually during processing is necessary when the directional responses of the transmitting and receiving elements differ and where the arrangements of elements in the synthetic aperture is bi-static or multi-static. These theoretical predictions were verified with simulations.

The second fundamental part of this work encompasses the development of techniques that deal with issues arising from the practical implementation of an incoherent SAS system. The FREB algorithm was developed with the issues of reducing processing time and achieving an optimal point-target energy pattern in mind. By looking at the relationship between the spatial arrangement of the elements in the synthetic aperture and the distribution of the range-ambiguity loci around a point-target, it was found that spreading the angular spacing between the loci decreases the intensity of the self-noise. It also produces a more uniform self-noise distribution around the point-target. In addition, the scheme required a lesser number of elements to be included in the summation process, hence reducing the required computation time. The trade off in this technique is a lower processing gain. There exists the flexibility, in this scheme, to adjust the level of savings in computation time in order to meet the minimum requirement of signal to self-noise ratio in a particular application.

Although incoherent SAS processing is much more resilient to motion errors, some situations still call for the need of motion compensation to remove errors in the estimation of the path travelled by the physical array. Considering the fact that this motion error only need to be accurate to the order of a fraction of the pulse length, a bulk motion estimation and compensation method, based upon the range curvatures of target returns and the cross correlations of adjacent pings, is presented. This technique relies on the presence of a relatively strong reference target, and by minimising the root mean square errors in the estimated range curvature of the target across the synthetic aperture, the path errors are estimated and can then be compensated for targets in all other ranges. The main advantages of this technique are the short computational time required and that it yields a good degree of accuracy given the presence of a strong reference target.

The third and final fundamental part of this work is the practical verification and implementation of the theoretical studies and investigations that were carried out within the first two parts. A sea survey of the Aeolian Sky wreck was conducted with a towed linear array of 32 hydrophones and a boomer. This sea trial demonstrates, for the first time, the results achievable with incoherent SAS processing schemes under an unconstrained and realistic operating environment. The inter-element spacing exceeds the traditional constraint in coherent systems by a factor of 5 and no motion compensation was applied, yet the image produced was still recognisable. On the other hand, the image produced by coherent integration was severely tainted by graininess which completely buried the structure of the wreck. The FREB scheme was employed and the obtained image was comparably as good, if not better, and yet the processing time was reduced by half. Further improvement in contrast was obtained by accommodating the bi-static arrangement of the synthetic aperture at the expense of increased processing time.

In order to achieve the final aim of this project, work was carried out to study the potential of synthesising 2-D synthetic apertures with incoherent SAS processing to give 3-D imaging capability. Simulation results gave positive indications and hence hardware trials were undertaken. Trials were carried out for a monostatic planar synthetic aperture, and then a new and practical multi-static synthetic aperture was put

forth and tested in the trials. The proposed multi-static synthetic aperture yields an excellent cost-benefit compromise while achieving 3-D imaging capability with little increase in hardware and processing complexity. An issue that stemmed from the trials is the detection and representation of targets in 3-D, and was addressed with the use of an adaptive-threshold detection scheme, and, depending on the form of the final image desired, a dimension-specific normalisation. Element-dependent matched weighting was applied and produced an image with relatively superior fidelity.

In summary, this work had achieved the primary goal to study and investigate the realistic potential of the application of incoherent SAS processing in underwater imaging, and more specifically in dealing with the lingering issues of slow mapping rate and image quality degradation from path motion errors that are strongly associated with coherent SAS imaging systems. Further to this, the two prevalent negative concepts, with regard to incoherent SAS processing, that some arrangement of targets in the image scene can cause the appearance of "artefacts" or what is referred to in this work as the false targets that are built by the contributions of self-noise, as well as the large computation time required by this inherently time-domain technique, has been effectively dealt with by the development of the FREB scheme. A practical autofocus motion compensation scheme was also developed to compensate for bulk motion errors should it be necessary. The use of off-the-shelf and economical inertial navigational aids is also a viable alternative as the requirement for positional accuracy is much less demanding than in the case of coherent SAS imaging. The sea survey of the Aeolian Sky wreck gave a strongly positive indication, and comparison, of the capability and robustness of an incoherent SAS system in dealing with the customary issues in SAS imaging under realistic operating assumptions and environment. Finally, the tank trials carried out had verified the theoretical hypothesis of the ability, with incoherent SAS processing, in implementing a synthetic aperture of arbitrary shape and the production of 3-D volumetric images.

No doubt the along-track resolution of the images is inferior to what is theoretically achievable with coherent SAS systems. However, given the work and results established in this project, and, given that any of the following condition is true in the requirements of a particular application; a less rigorous resolution capability; quick and economical system deployment and reconfiguration; low system complexity; or

high operating robustness; the consideration and the choice to implement an incoherent processing SAS scheme in the underwater imaging application may not be an unwise one.

8.2 Further Work

There are two crucial areas that stem from this research which deserve further investigation. The first is the issue of detection and image representation. To date, there are relatively few studies into optimal methods in image representation and visualisation of processed SAS data. It is envisaged that techniques available to the SAR community are good references, but care has to be taken in adapting them especially for images from incoherent SAS, due to the nature of the point-target energy response being a strong function of the elements' arrangement and spatial distribution in the synthetic aperture. The adaptive-threshold detection method presented in this work had, in simulation, produced results that made it a recommendable option. It is stated, in this work, that the optimal shape of the window is one which matches the form of the point-target energy response. However, more work is required in the design of the split averaging window to explore the relationship between the shape and elements' arrangement of the synthetic aperture and the optimal shape and dimension of both the inner and outer averaging window. Following that, an estimation of the degradation in detection performance, measured by its faithfulness in producing an accurate visual representation of the real object, can be made as a function of the accuracy of the shape of the averaging window. This then allows the cost function of the detection performance in terms of the required processing time and complexity to be obtained, and hence provides a choice of recommendable averaging schemes that are specifically catered to some commonly applied forms of synthetic aperture configurations.

The second area that is worthy of further investigation is the practical issues surrounding the synthesis of a 3-D synthetic aperture. It has been established that synthesising a 3-D volumetric aperture is theoretically promising, but no specific trials on it had been performed. The concept proposed here is not one of which two

planar synthetic apertures are displaced from each other in depth to form a 3-D synthetic aperture. Rather, it is anticipated to take the form of an encapsulating envelope around the target scene or volume. This may be carried out by one or more autonomous underwater vehicles (AUV). Additional navigational aids can be installed on board the AUV to give positioning information of the AUV with respect to each ping, hence allowing the synthesis of an arbitrary 3-D synthetic aperture which surrounds, to the best possible extent, its target scene.

References

[1] K.Tomiyasu, "Tutorial review of synthetic-aperture radar (SAR) with applications to imaging of the ocean surface," *Proceedings of the IEEE*, vol. 66, no. 5, pp. 563-583, May 1978.

[2] L.J.Cutrona, "Comparison of sonar system performance achievable using synthetic aperture techniques with the performance achievable by more conventional means," *Journal of the Acoustical Society of America*, vol. 58, no. 2, pp. 336-348, Aug 1975.

[3] P.T.Gough and D.W.Hawkins, "Imaging algorithms for a strip-map synthetic aperture sonar: minimising the effects of aperture errors and aperture undersampling," *IEEE J. Oceanic Eng.*, vol. 22, no. 1, pp. 27-39, Jan 1997.

[4] K.D.Rolt and H.Schmidt, "Azimuthal ambiguities in synthetic aperture sonar and synthetic aperture radar imagery," *IEEE Journal of Oceanic Engineering*, vol. 17, no. 1, pp. 73-79, Jan. 1992.

[5] G.M.Walsh, "Acoustic mapping apparatus," *Journal of the Acoustical Society of America*, vol. 47, no. 5, pp. 1205, Dec 1969, Review of U.S. Patent 3,484,737.

[6] T.Sato, M.Ueda, and S.Fukuda, "Synthetic aperture sonar," *Journal of the Acoustical Society of America*, vol. 54, no. 3, pp. 799-802, 1973.

[7] R.E.Williams, "Creating an acoustic synthetic aperture in the ocean," *Journal of the Acoustical Society of America*, vol. 60, no. 1, pp. 60-73, July 1976.

[8] J.T.Christoff, C.D.Loggins, and E.L.Pipkin, "Measurements of the temporal phase stability of the medium," *Journal of the Acoustical Society of America*, vol. 71, no. 6, pp. 1606-1607, June 1982.

[9] P.T.Gough and D.W Hawkins, "A short history of synthetic aperture sonar", *Proc. IEEE Int. Geoscience & Remote Sens. Symp.,* Paper BB1002, Seattle, USA, pp. 618-620, July 1998.

[10] H.E.Lee, "Extension of synthetic aperture radar (SAR) to underwater applications," *IEEE Journal of Oceanic Engineering*, vol. OE-4, pp. 60-63, Apr. 1979.

[11] P. Heering, "Alternative schemes in synthetic aperture sonar processing," *IEEE Journal of Oceanic Engineering,* vol. 9, no. 4, pp. 277-280, Oct. 1984.

[12] B.L.Douglas and H.Lee, "Synthetic aperture active sonar imaging," *IEEE International Conference on Acoustics, Speech, and Signal Processing, ICASSP-92*, vol. 3, pp. 37-40, Mar. 1992.

[13] D.Billon, F.Le Clerc and L.Hue, "Detection and imaging performance of a synthetic aperture sonar," *OCEANS '93 Proceedings*, vol. 1, pp. I132-I137, Oct. 1993.

[14] B.L.Douglas and H.Lee, "Synthetic-aperture sonar imaging with a multiple-element receiver array," *IEEE International Conference on Acoustics, Speech, and Signal Processing, ICASSP-93, vol. 5*, pp. 445-448, Apr. 1993.

[15] M.P.Hayes and P.T.Gough, "Broadband synthetic aperture sonar," *IEEE Journal of Oceanic Engineering*, vol. 17, no. 1, pp. 80-94, Jan. 1992.

[16] J.Chatillon, A.E.Adams, M.A.Lawlor and M.E.Zakharia, "SAMI: A low-frequency prototype for mapping and imaging of the seabed by means of synthetic aperture," *IEEE Journal of Oceanic Engineering,* vol. 24, no. 1, pp.4-15, Jan. 1999.

[17] M.A.Lawlor, A.E.Adams, O.R.Hinton, V.S.Riyait and B.Sharif, "Methods for increasing the azimuth resolution and mapping rate of a synthetic aperture sonar," *Proceedings of OCEANS '94*, vol. 3, pp. 565-570, Sept. 1994.

[18] G.L.Turin, "An introduction to matched filters," *IRE Transactions on Information Theory*, vol. 6, pp. 311-329, June 1960.

[19] C.Y.Chang, M.Y.Lin, and J.C.Curlander, "SAR processing based on the exact two-dimensional transfer function," *International Geo-Science Remote Sensing Symposium*, vol.1, pp. 355-359, 1992.

[20] M.Y.Jin and C.Wu, "A SAR correlation algorithm which accommodates large range migration," *IEEE Transactions on Geo-Science Remote Sensing*, vol. GRS-22, pp. 592-597, Nov. 1984.

[21] R.Bamler, "A comparison of range-Doppler and wavenumber domain SAR focusing algorithms," *IEEE Transactions on Geo-Science Remote Sensing*, vol. 30, pp. 706-713, July 1992.

[22] C.Cafforio, C.Pratti and F.Rocca, "SAR data focussing using seismic migration techniques," *IEEE Transaction on Aerospace and Electronic Systems*, vol. 27, pp. 194-207, Mar. 1991.

[23] R.K.Raney, H.Runge, R.Bamler, I.G.Cumming and F.H.Wong, "Precision SAR processing using chirp scaling," *IEEE Transaction on Geo-Science and Remote Sensing*, vol. 32, no. 4, pp. 786-799, July 1994.

[24] S.M.Banks, "Studies in high resolution synthetic aperture sonar," *PhD Thesis – University College London, UK,* Sept. 2002.

[25] J.Chatillon, M.E.Bouhier and M.E.Zakharia, "Synthetic Aperture Sonar for Seabed Imaging: Relative Merits of Narrow-Band and Wide-Band Approaches," *IEEE Journal of Oceanic Engineering*, vol. 17, no. 1, pp. 95-105, Jan. 1992.

[26] D.G.Checketts, "Performance degradation of a synthetic aperture sonar imaging system due to a time varying towed-array orientation and trajectory," *PhD Thesis – University of Birmingham, UK,* Sept 1987.

[27] H.D.Griffiths, T.A.Rafik, Z.Meng, C.F.N.Cowan, H.Shafeeu and D.K.Anthony, "Interferometric synthetic aperture sonar for high resolution 3-D mapping of the seabed," *IEE Proceedings on Radar, Sonar and Navigation*, vol. 144, No. 2, pp. 96-103, Apr. 1997.

[28] A.P.Blake, "Autofocus techniques: multilook registration and contrast optimisation – a comparison," *RSRE memorandum 4626*, Ministry of Defense, RSRE Malvern, UK, Sept 1995.

[29] D.Marx, M.Nelson, E.Chang, W.Gillespie, A.Putney, K.Warman, "An introduction to synthetic aperture sonar," *Proceedings of the 10th IEEE Workshop on Statistical Signal and Array Processing*, pp. 717-721, Aug. 2000.

[30] B.D.Huxtable, E.M.Geyer, "Motion compensation feasibility for high resolution synthetic aperture sonar," Proceedings of OCEANS '93, vol. 1, pp. I125-I131, Oct. 1993.

[31] P.D.Heering, "Alternate Schemes in Synthetic Aperture Sonar Processing," *IEEE Journal of Oceanic Engineering*, vol. OE-9, No. 4, pp. 277-280, Oct. 1984.

[32] D.J.Wingham, "Square-law detected synthetic aperture radar," *IEE Electronics Letter*, vol. 24, no. 7, pp.419-421, Mar. 1998.

[33] G.Shippey and T.Nordkvist, "Phased array acoustic imaging in ground co-ordinates, with extension to synthetic aperture processing," *IEE Proceedings of Radar, Sonar and Navigation*, vol. 143, no. 3, pp. 131-139, June 1986.

[34] V.Murino, C.S.Regazzoni, A.Trucco and G.Vernazza, "A noncoherent correlation technique and focused beamforming for ultrasonic underwater imaging: a comparative analysis," *IEEE Transactions on Ultrasonics, Ferroelectrics, and Frequency Control*, vol. 41, no. 5, pp. 621-630, Sept. 1994.

[35] M.Fink, R. Mallart and F.Cancre, "The random phase transducer: a new technique for incoherent processing – basic principles and theory," *IEEE Transactions on Ultrasonics, Ferroelectrics, and Frequency Control*, vol. 37, No. 2, Mar. 1990.

[36] P.Atkins and T.Collins, "Signal processing and sonar system design", *Continuing Education Course in Underwater Acoustic and Sonar Systems*, School of Electronic and Electrical Engineering, University of Birmingham, UK, April 2001.

[37] J.J.Kroszczynski, "Pulse compression by means of linear-period modulation," *Proceedings of the IEEE*, vol. 57, pp.1260-1266, 1969.

[38] T.Collins and P.Atkins, "Non-linear frequency modulation chirps for active sonar," *IEE Proceedings of Radar, Sonar and Navigation*, vol. 146, Issue 6, pp. 312-316, Dec 1999.

[39] J.M.F.Moura and A.B.Baggeroer, "Passive systems theory with narrow-band and linear constraints: Part 1 – spatial diversity," *IEEE Journal of Oceanic Engineering*, vol. OE-3, no. 1, pp. 5-13, 1978.

[40] A.D.Waite, "Sonar for practising engineers", 2nd Edition, *Thomson Marconi Sonar Limited*, 1998.

[41] M.Soumekh, "Synthetic aperture radar signal processing with Matlab algorithms", *Wiley & Sons Publications: New York, US*, 1999.

[42] K.D.LePage and H.Schmidt, "Bistatic synthetic aperture imaging of proud and buried targets from an AUV", *IEEE Journal of Oceanic Engineering*, vol. 27, no. 3, pp. 471-483, July 2002.

[43] K.Y.Foo, P.Atkins and T.Collins, "Robust underwater imaging with fast broadband incoherent synthetic aperture sonar", *IEEE Proceedings of ICASSP-03*, vol. 5, pp. v17-v20, Apr. 2003.

[44] L.M.H.Ulander, H.Hellsten, and G.Stenstrom, "Synthetic-aperture radar processing using fast factorised backprojection", *EUSAR 2000 3rd European Conference on Synthetic Aperture Radar*, pp. 753–756, May 2000.

[45] S. M.Banks and A.Bellettini, "The application of fast factorised back-projection to synthetic aperture sonar", Technical Report IN-686, SACLANT Undersea Research Centre, La Spezia, Italy, August 2001.

[46] M.Gindre, C.Lebeault and F.Rieuneau, "Ultrasonic imaging using correlation techniques: computer simulations and experimental results," *Acoutical Imaging,* vol. 17, New York:Plenum, 1988.

[47] K.A.Johnson, M.P.Hayes and P.T.Gough, "A method for estimating the sub-wavelength sway of a sonar towfish," *IEEE Journal of Oceanic Engineering,* vol. 20, no. 4, Oct. 1995.

[48] H.J.Callow, M.P.Hayes, and P.T.Gough, "Noncoherent autofocus of single-receiver broad-band synthetic aperture sonar imagery," *IEEE Conference and Exhibition on OCEANS 2001,* vol. 1, pp. 157-162, Nov. 2001.

[49] Divernet – Diver Magazine, "Wreck Tour 27 – the Aeolian Sky - May 2001," *Diver Magazine Online*, http://www.divernet.com/wrecks/wtour270501.htm, May 2001.

[50] J.Liddiard, "The wreck of the Aeolian Sky," *John Liddiard Underwater,* http://www.liddiard.demon.co.uk/photoix/asky/index.htm, Jan 2002.

[51] P.T.Gough, A.de Roos, and M.J.Cusdin, "Continuous transmission FM sonar with one octave bandwidth and no blind time," *IEEE Proceedings*, vol. 131, part F, pp. 270-274, 1984.

[52] P.T.Gough, "A synthetic aperture sonar system capable of operating at high speed and in turbulent media," *IEEE Journal of Oceanic Engineering,* vol. oe-11, no. 2, Apr. 1986.

[53] H.J.Callow, M.P.Hayes, and P.T.Gough, "Wavenumber domain reconstruction of SAR/SAS imagery using single transmitter and multiple-receiver geometry," *IEE Electronic Letters*, vol.38, no.7, 28th March 2002, pp. 336.

[54] B.R.Mahafza and M.Sajjadi, "Three dimensional SAR imaging using linear array in transverse motion," *IEEE Transaction on Aerospace and Electronic System,* vol. 32, issue 1, Jan. 1996.

[55] J.Homer, I.D.Longstaff, Z.She and D.Gray, "High resolution 3-D imaging via multi-pass SAR," *IEE Proceedings on Radar, Sonar and Navigation*, vol. 149, no. 1, Feb. 2002.

[56] C.V.Jakowatz, D.E.Wahl and P.A.Thompson, "Three-dimensional SAR imaging using cross-track coherent stereo collections," *Conference Record of the 31st Asilomar Conference on Signals, Systems and Computers,* vol. 2, Nov 1997.

[57] J.E.Fernandez and J.T.Christoff, "Multi-aspect synthetic aperture sonar," *IEEE Conference and Exhibition on OCEANS 2000,* vol. 1. pp. 177-180, Sept. 2000.

[58] D.A.Cook, J.T,Christoff and J.E.Fernandez, "Broadbeam multi-aspect synthetic aperture sonar," *IEEE Conference and Exhibition on OCEANS 2001*, vol. 1, pp. 188-192, Nov. 2001.

[59] P.N.Denbigh, "Signal processing strategies for a bathymetric Sidescan Sonar," *IEEE Journal of Oceanic Engineering*, vol. 19, no. 3, pp. 382-390, July 1994.

[60] V.Murino and A.Trucco, "Three-dimensional image generation and processing in underwater acoustic vision," *Proceedings of the IEEE*, vol. 88, no. 12, pp. 1903-1948, Dec. 2000.

[61] A.Trucco, E.Omodei and P.Repetto, "Synthesis of sparse planar arrays," *IEE Electronic Letters*, vol. 33, no. 22, pp. 1834-1835, 23rd Oct. 1997.

[62] L.J.Busse, "Three-dimensional imaging using a frequency-domain synthetic aperture focussing technique," *IEEE Transactions on Ultrasonics, Ferroelectrics, and Frequency Control,* vol. 39, no. 2, pp. 174-179, Mar. 1992.

[63] A.Yamani, "Three-dimensional imaging using a new synthetic aperture focussing technique," *IEEE Transactions on Ultrasonics, Ferroelectrics, and Frequency Control,* vol. 44, no. 4, pp. 943-947, July 1997.

[64] M.I.Skolnik, "Introduction to radar systems," *McGraw-Hill International Book Company*, 2nd edition, pp.388-395, 1983.

[65] H.M.Finn and R.S.Johnson, "Adaptive detection mode with threshold control as a function of spatially sampled clutter-level estimates," *RCA Review*, pp. 414-464, Sept, 1968.

[66] P.R.Atkins and T.Collins, "Signal Processing and Sonar Systems", *University of Birmingham Continuing Education Course in Underwater Acoustics and Sonar Systems,* Course Book 2, pp. 20.1-20.23.

[67] H.You, G.Jian, P.Yingning and L.Dajin, "A new CFAR detector based on ordered statistics and cell averaging," *Proceedings of the CIE International Conference of Radar 1996*, pp. 106-108, Oct. 1996.

[68] H.You and G.Jian, "A new CFAR detector with greatest of selection," *IEEE Record on the International Radar Conference 1995,* pp. 589-591, May 1995.

[69] L.A.Prastitis and S.D.Himonas, "A CFAR detector using a data discrimination algorithm," *IEEE Proceedings of the National Radar Conference 1991,* pp. 117-121, Mar 1991.

[70] P.P.Ghandi and S.A.Kassam, "Optimality of the cell averaging CFAR detector," *IEEE Transactions on Information Theory,* vol. 40, no. 4, pp. 1226-1228, Jul. 1994.

[71] P.T.Gough and M.P.Hayes, "Test results using a prototype synthetic aperture sonar," *Journal of Acoustical Society of America,* vol. 86, no. 6, pp. 2328-2333, Dec. 1989.

[72] F.E.Nathanson, "Radar Design Principles," *McGraw-Hill Book Company, New York, US*, 1969.

[73] D.P.Meyer and H.A.Mayer, "Radar Target Detection, Handbook of Theory and Practice," *Academic Press, New York and London,* 1973.

[74] W.A.Holm and J.D.Echard, "FFT signal processing for non-coherent radar systems," *IEEE Proceedings of ICASSP '82,* vol. 7, pp.363-366, May 1982.

[75] J.I.Marcum, "A statistical theory of target detection by pulsed radar"," *IEEE Transactions on Information Theory,* vol. 6, issue 2, pp.59-267, Apr 1960.

[76] R.A.Wagstaff, "Use of amplitude without phase angle to achieve pseudo-coherent processing gain," *Journal of Acoustical Society of America,* vol. 112, issue 5, pp. 2422, Nov 2002.

[77] F.Daum, "Super noncoherent integration," *Record of the IEEE National Radar Conference '94,* pp 123-128, Mar 1994.

[78] R.Dinger and J.Goldstein, "Motion stability measurements of a submersible towed extremely low frequency receiving platform," *Proceedings of the IEEE*, OE-3, pp. 62-67, 1978.

[79] Somers, Carson, Revie, Edge, Barrow and Andrews, "GLORIA II – An improved long-range side-scan sonar," *Oceanology International*, 1978.

[80] D.A.Chapman, "A study of the ship induced roll-yaw motion of a heavy towed fish," *Ocean Engineering*, vol. 11, no. 6, pp. 627-654, 1984.
[81] B.Kinsman, "Wind waves and their generation and propagation on the ocean surface," *Prentice-hall Inc.*, Englewood Cliffs, N.J., 1965.

[82] D.G.Checketts and B.V.Smith, "Analysis of the effects of platform motion errors upon synthetic aperture sonar," *Proceesings of the Institute of Acoustics*, vol. 8, part 3, 1986.

[83] M.Cherniakov, "Space-surface bistatic synthetic aperture radar – prospective and problems," *RADAR 2002*, pp. 22-25, 15-17 Oct 2002.

[84] M.Lowe, "Algorithms for high resolution bistatic SAR," *RADAR 2002*, pp. 512-515, 15-17 Oct 2002.

Appendix A

Along-track Resolution of an Incoherent Synthetic Aperture

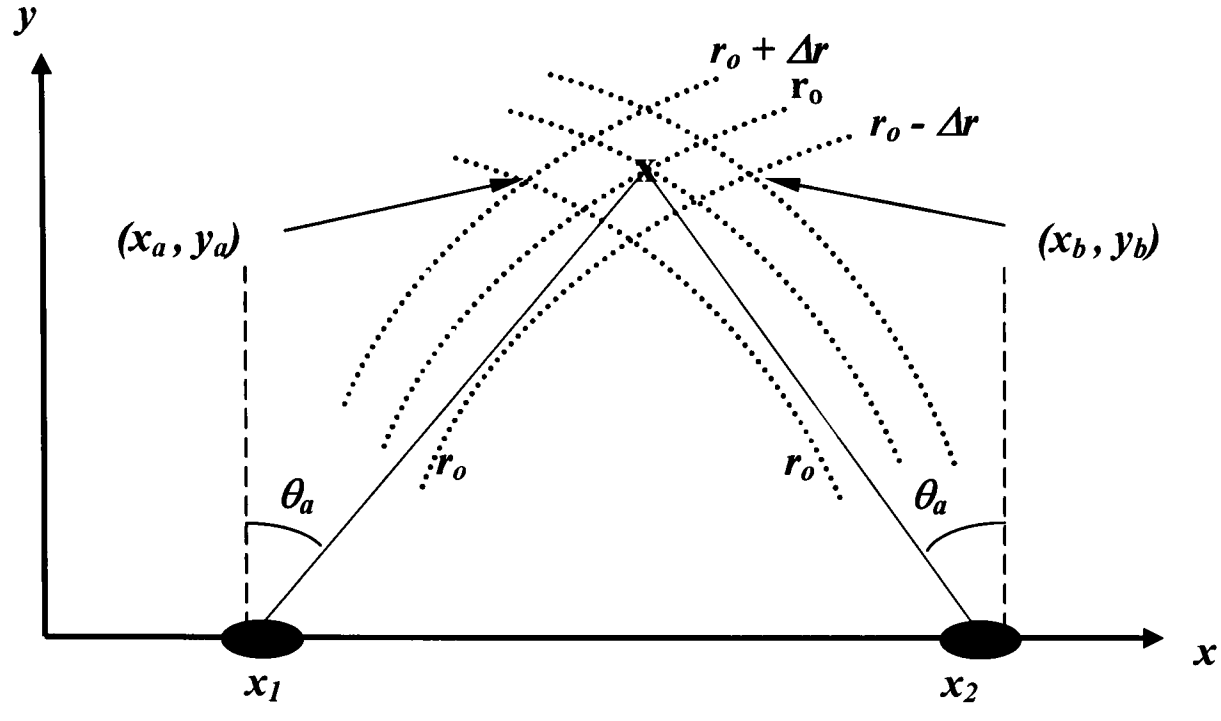


Figure A-1: Geometry for the derivations of along-track resolution in incoherent processing.

For definition, rx_a and rx_b are two transducer positions with beam angle θ_a, and r_0 is the closest path of approach to the target. The dotted lines are range-ambiguity curvatures with respect to the transducer positions, and they correspond to the matched-filtered responses from a point target marked '**x**'. The point target matched-filtered responses range from $-\Delta r$ to Δr.

Let the target be at position (x_T , y_T). Observing from two points, x_1 and x_2 with angular width of θ_a, the detection zone around the target will be from (x_a, y_a) to (x_b, y_b) in the along-track direction. The dotted lines represent the loci of ambiguities crossing the target point. Along with it are the lines that define the width of the range matched-filtered pulse width, ranging from $-\Delta r$ to Δr, and thus the Δr is the range (or cross track) resolution. The azimuth resolution of the system can be defined in terms of the correlation or overlapping of the envelope of the echo return with a replica of the envelope of the transmitted signal. This resolution is taken to be twice the azimuth increment that causes the overlapping to drop to one-half of its maximum value,

considering only a cut *along* the azimuth dimension of the azimuth-range ambiguity function.

By defining Z to be the azimuth (or along track) resolution, it can be expressed as

$$Z = x_b - x_a$$

From the geometry of the diagram,

$$x_a = x2 - (r_o + \Delta r)\sin\theta_a ,$$

$$x_b = x1 + (r_o + \Delta r)\sin\theta_a ,$$

$$\therefore Z = (x1 - x2) + 2(r_o + \Delta r)\sin\theta_a$$

To solve for *Z,* an expression for $(x_1\text{-}x_2)$ needs to be found.

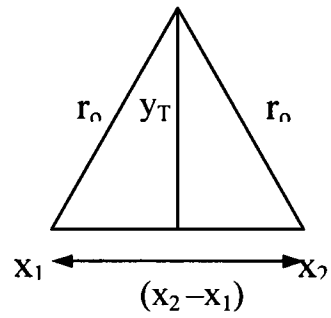


Figure (2)

Referring to Figure (2) derived from Figure (1), an expression for $(x_1\text{-}x_2)$ can be found using Pythagoras theorem, where

$$r_o^2 = y_T^2 + \frac{(x_2 - x_1)^2}{4}$$

Referring back to Figure (1),

$$y_T = (r_o + \Delta r)\cos\theta_a$$

Thus,

$r_o^2 = (r_o + \Delta r)^2 \cos^2\theta_a + \frac{(x2-x1)^2}{4}$, then rearranging,

$$(x_2 - x_1)^2 = 4[r_o^2 - (r_o + \Delta r)^2 \cos^2\theta_a] = 4[(r_o + \Delta r)^2(1 - \cos^2\theta_a) - 2\Delta r r_o - \Delta r^2],$$

$$(x_2 - x_1)^2 = 4[(r_o + \Delta r)^2(\sin^2\theta_a) - 2\Delta r r_o - \Delta r^2]$$

To obtain a square-root of the expression for $(x_2-x_1)^2$, let $(\alpha+\beta)^2 = \alpha^2+2\alpha\beta+\beta^2$. Then, assuming that $\alpha>>\beta$, $(\alpha+\beta)^2 \approx \alpha^2+2\alpha\beta$. In this case, $\alpha = 2(r_o+\Delta r)\sin\theta_a$ and $2\alpha\beta = -8\Delta r r_o - 4\Delta r^2$

$$\therefore \beta = \frac{-4\Delta r r_o - 2\Delta r^2}{2(r_o + \Delta r)\sin\theta_a} = \frac{-2\Delta r(r_o + \Delta r/2)}{(r_o + \Delta r)\sin\theta_a}$$

and assuming that $r_o>>\Delta r/2$

$$\beta = \frac{-2\Delta r}{\sin\theta_a}$$

Thus,

$$(x_2 - x_1) = 2(r_o + \Delta r)\sin\theta_a - \frac{2\Delta r}{\sin\theta_a}$$

The azimuth resolution, Z, can now be expressed as

$$Z = -2(r_o + \Delta r)\sin\theta_a + \frac{2\Delta r}{\sin\theta_a} + 2(r_o + \Delta r)\sin\theta_a$$

$$\therefore Z = \frac{2\Delta r}{\sin\theta_a}$$

Then, by considering the beampattern of the transducer with beamwidth of θ_a and setting a 3dB effective beamwidth, $\sin\theta_a$ can be expressed as

$$\sin\theta_a = \frac{1.39 \cdot \lambda}{\pi L}$$

where λ is the wavelength and L is the physical dimension of the transducer. Substituting this into the expression for azimuth resolution yields, conservatively,

$$Z = \frac{3 \cdot \Delta r \cdot L}{\lambda}$$

Note: $2\Delta r$ is the range resolution, defined to be half the width between the first zeros of the match-filtered signal in the cross-track dimension.

Appendix B:

K.Y.Foo, P.R.Atkins and T.Collins, "Robust underwater imaging with fast broadband incoherent synthetic aperture sonar," *IEEE Proceedings of ICASSP-03*, vol. 5, pp. v17-v20, Apr. 2003.